DISS. ETH NO. 29343

DEVELOPMENT OF VIRTUAL SENSING TECHNIQUES FOR DYNAMIC VIRTUALIZATION

A thesis submitted to attain the degree of
DOCTOR OF SCIENCES
(Dr. sc. ETH Zurich)

Presented by

SILVIA VETTORI

M.Sc. from University of Rome "La Sapienza"
born on 16.12.1993

Accepted on the recommendation of

Prof. Dr. Eleni Chatzi, examiner
Dr. Emilio Di Lorenzo, co-examiner
Dr. Bart Peeters, co-examiner
Prof. Dr. Costas Papadimitriou, co-examiner
Prof. Dr. David Wagg, co-examiner

2023

ACKNOWLEDGMENTS

During the past four years I found my self thinking at this moment several times. I have imagined the instant at which I would have written the last sentence of this thesis in many different ways: as the final effort of an intense work, as the melancholic conclusion of a professional as well as a personal path, but also as the joyful ending of an enriching journey. Indeed, I have always been certain that my doctoral studies could be not only technically formative, but also fundamental for my personal growth. Now that I have finally reached the conclusion, I can confirm that this path has definitely contributed to make me the person I am today. Therefore, the time has come to put together my thoughts and memories and take this occasion to thank some of the people I crossed paths with during these years.

The completion of this work would not have been possible without the guidance of Prof. Eleni Chatzi, to whom I am extremely grateful for her constant support and precious advice. She has been essential in the definition of my research direction, at the same time allowing me to develop my own research vision. Eleni, I am really happy I had the chance to be part of your research group at ETH.

I would like to express my deepest gratitude to my supervisor at Siemens, Dr. Emilio Di Lorenzo, for his daily mentoring. I am really thankful for the trust you have always placed in me, which I believe it has been the main driver for my professional development. I would like to also thank Dr. Bart Peeters, who has also supported me from the start. Bart and Emilio, you have believed in me from my very first day at Siemens and I would be forever grateful for the enormous opportunity you gave me when you decided to take me on board with you within the DyVirt project.

The DyVirt project has been an exciting and motivating experience. I would like to thank the entire DyVirt network and in particular Prof. Costas Papadimitriou and Prof. David Wagg for taking part to my doctoral committee. Special thanks go to Giancarlo Kosova for sharing this experience with me. It was nice enjoying travels, meetings, trainings (and project reports) together with you.

I would also like to acknowledge the RELIABLADE consortium, Dr. Marcin Luczak and DTU Wind Energy for supporting part of the work developed within this thesis.

At Siemens I met many people, who are not only colleagues but also friends. I would like to start thanking my team mates: Giancarlo, André, Davide, Mattia, Alberto, Ruben, Francesco. Thanks a lot for the interesting (and long) technical discussions, but more importantly for making our team fresh, young and motivated. I would like to extend my thanks to Karl Janssens, Bart Forrier and the entire Test RTD team, it is a pleasure to cooperate and share the office with you.

Working at Siemens and living in Leuven allowed me to meet some very nice people: Roberta C., Adriano, Vincenzo, Claudio, Sara, Antonio, Andrea, Roberta G., thank you for crossing my path and sharing wonderful memories with me. A special mention goes to Maria Lucia, Caterina and Roberto: my life in Leuven would not be the same without you. I really thank you for being by my side whenever needed, for the time spent together and for the interesting exchanges of ideas we always have. My deepest thanks go to Elena for her sincere and authentic friendship. Meeting you has been a precious gift, you have been my home abroad and I am sure you will still be even miles away.

I would like to thank my old and best friends, Ludovica and Giorgia. One of us once said: “we see each other once a year but every time it feels like yesterday”. We have grown a lot since we were at school together and each of us has taken a different path, but when I stop and look around me I always find you. Thanks a lot to you both, I am really grateful to have you.

Vorrei poi ringraziare tutta la mia famiglia, per aver sempre creduto nelle mie capacità e per avermi supportata nel raggiungere i miei obiettivi. Un grazie particolare ai miei genitori, il mio esempio di vita. Grazie papà per i tuoi insegnamenti e la tua pazienza. Grazie mamma per avermi sempre

mostrato la strada, anche quando questa ci allontanava. Un grazie a mia sorella Giulia per essere la parte più irrazionale di me e allo stesso tempo una meravigliosa fonte di ispirazione. Ringrazio poi mia nonna Gina e mia zia Mariarosaria per essere le mie radici. Vi sono immensamente grata per l'affetto che giornalmente mi regalate. Vorrei inoltre ringraziare tutta la famiglia Menicocci, per avermi accolta incondizionatamente dal primo giorno in cui ci siamo incontrati. In ultimo, ma non per importanza, vorrei ringraziare Fabrizio. Ti ringrazio per esserti buttato insieme a me in questa avventura, nonostante la decisione non fosse tua. Grazie per aver supportato le mie scelte, per aver condiviso viaggi, aerei e trasferimenti. Parte di questo lavoro è anche merito tuo perché senza il tuo appoggio niente di tutto ciò sarebbe stato possibile.

Grazie zio per non essertene mai andato. Da qualche parte nell'universo so che ci sei e questo ormai basta a rendermi felice.

SV - Leuven, 9 March 2023

ABSTRACT

Over the last half-century, the economic growth has determined higher standards of living and sustained social progress and development. As a result, the needs of modern society have significantly evolved in several contexts such as transportation, infrastructures, energy production, and communication systems. This social and economic transformation has driven a substantial technological advancement, which in turn has led to new opportunities as well as new attractive challenges. One of these stems from the ever-increasing demand for more efficient, reliable, and sustainable engineering systems, and their resulting ever-growing complexity. Within the structural and mechanical domains, digitalization is key to handling the challenges in design, analysis, and monitoring as it provides tools such as forward simulations, advanced data acquisition technologies, and powerful data processing strategies. More accurate information about the behavior of mechanical and structural components can be gathered through these technologies and used to improve systems design in terms of safety and reliability, as well as for enabling advanced Structural Health Monitoring (SHM) strategies. The latter aim at maximizing systems performance, reducing maintenance costs, and extending their life span. New avenues for the establishment of a permanent performance assessment of structures and mechanical components are opened up by the development of enhanced virtualization strategies aimed at defining the so-called Digital Twins (DTs), i.e., digital mirrored representations of physical systems built with the help of both numerical simulations and real-time collected data. The hereby proposed research focuses on the use of Virtual Sensing (VS) for constructing DTs in structural dynamics, with spacecraft vibration testing and Wind Turbine (WT) blades testing comprising the main application domains. VS consists in inferring Quantities of Interest (QoI) which cannot be physically acquired for time, cost, or accessibility limitations. The so-called "virtual sensors" are built using data assimilation methods that exploit the fusion of physically recorded vibration data with mechanistic models to build a real-time estimate of the QoI, e.g., unmeasured loads or responses. This thesis addresses the existing challenges and limitations arising from the development of VS techniques for joint input-state estimation in structural dynamics. Within this context, a major task stems from seeking representative models for the uncertainty parameters leveraged by the adopted data assimilation strategies. Indeed, these methods lie in a stochastic setting, where modeling and loading conditions uncertainties are taken into account via specific parameters, whose proper selection, essential for the correct functioning of the algorithms, often comprises a complex offline tuning task. This feature unavoidably hinders the real-time applicability of data assimilation strategies, thus limiting their exploitation both during laboratory testing and in operation. Data-driven and adaptive approaches are proposed in this thesis to embed adequate a priori uncertainties representations into the models adopted within the input-state estimation strategies, thus allowing for their real-time and user-independent deployment. The approaches developed within this work are tested and validated for several experimental case studies.

SOMMARIO

La crescita economica avvenuta nell'ultima metà di secolo ha determinato un forte miglioramento del tenore di vita e un conseguente sostenuto progresso e sviluppo sociale, il quale ha portato ad un'evoluzione dei bisogni della società moderna in diversi contesti, come i trasporti, le infrastrutture, la produzione energetica e i sistemi di comunicazione. Tale trasformazione sociale ed economica ha promosso un sostanziale avanzamento tecnologico che, a sua volta, ha introdotto nuove opportunità e, allo stesso tempo, nuove interessanti sfide. Una di queste nasce dalla crescente richiesta di sistemi ingegneristici più efficienti, affidabili e sostenibili e, di conseguenza, dalla loro sempre maggiore complessità. Nell'ambito meccanico e strutturale, l'avvento della digitalizzazione ha giocato un ruolo fondamentale nel gestire le sfide derivanti dal design, l'analisi ed il monitoraggio, grazie a strumenti come simulazioni dirette ed avanzate tecnologie di acquisizione ed elaborazione dei dati. Un'informazione più accurata riguardo il comportamento di componenti meccanici e strutturali può essere ricostruita tramite queste tecnologie e utilizzata per migliorare il design in termini di sicurezza e affidabilità, cosi come per facilitare strategie avanzate di controllo strutturale. Queste ultime ambiscono a massimizzare la performance dei sistemi, riducendone i costi di manutenzione e allungandone la vita utile. Nuovi strumenti per la definizione di un continuo processo di verifica della performance di strutture e componenti meccanici sono forniti dallo sviluppo di metodi potenziati di virtualizzazione, finalizzati alla costruzione dei cosiddetti Digital Twin (DT), ossia delle fedeli rappresentazioni digitali di sistemi fisici ottenuti attraverso l'utilizzo di simulazioni numeriche e dati registrati in tempo reale. La ricerca proposta in questa tesi si focalizza sull'uso di metodi di VS, anche detti metodi di sensorizzazione virtuale, per creare DT nell'ambito della dinamica strutturale e, più specificatamente, nei contesti di test vibrazionali di satelliti e di pale di turbine eoliche. I metodi di Virtual Sensing (VS) consistono nel ricostruire le quantità di interesse che non possono essere acquisite tramite misure fisiche a causa di limitazioni in termini di tempi, costi ed accessibilità. I cosiddetti "sensori virtuali" vengono derivati attraverso metodi di assimilazione dei dati, che sfruttano la combinazione di misure vibrazionali fisiche con modelli meccanistici per calcolare una stima delle quantità di interesse, ad esempio carichi e risposte strutturali non misurati, in tempo reale. Questa tesi affronta le esistenti sfide e limitazioni derivanti dallo sviluppo di tecniche di sensorizzazione virtuale per stime simultanee di carichi e stati del sistema nel dominio della dinamica strutturale. In questo contesto, uno dei compiti principali scaturisce dalla ricerca di modelli rappresentativi per i parametri di incertezza che vengono sfruttati dai metodi di assimilazione dei dati. Tali tecnologie sono infatti caratterizzate da un approccio stocastico, dove le incertezze inerenti ai modelli e alle condizioni di carico sono prese in considerazione tramite parametri specifici, la cui accurata selezione, essenziale per il corretto funzionamento di questi algoritmi, richiede spesso una complessa attività di regolazione offline. Questa caratteristica ostacola inevitabilmente l'applicabilità in tempo reale delle strategie di assimilazione dei dati, limitando conseguentemente il loro utilizzo durante test in laboratorio o misure operazionali. In questa tesi, metodi adattivi e basati sui dati vengono proposti per includere rappresentazioni adeguate delle incertezze all'interno dei modelli impiegati nelle strategie di stima di carichi e stati, quindi garantendone l'implementazione in tempo reale ed in maniera indipendente dall'utilizzatore. Gli approcci sviluppati in questa tesi sono testati e validati attraverso diversi casi studio sperimentali.

CONTENTS

ACRONYMS

A-AKF	Adaptive-noise Augmented Kalman Filter
AKF	Augmented Kalman Filter
AR	Autoregressive
BARC	Box Assembly with Removable Component
BC	Boundary Condition
BCC	Boundary Condition Challenge
BDM	Bayesian Dynamic Model
BM	Brownian Motion
CAD	Computer Aided Design
CMS	Component Mode Synthesis
CMS-ME	Component Mode Synthesis - Modal Expansion
DKF	Dual Kalman Filter
DOF	Degree of Freedom
DT	Digital Twin
EDM	Electrical Discharge Machining
EoM	Equation of Motion
EMA	Experimental Modal Analysis
FE	Finite Element
FT	Fourier Transform
FRAC	Frequency Response Assurance Criterion
GDF	Gillijns De Moor Filter
GP	Gaussian Process
GPLFM	Gaussian Process Latent Force Model
GFRP	Glass Fiber Reinforced Plastic
KF	Kalman Filter
KS	Kalman Smoother
LFM	Latent Force Model
LTI	Linear Time Invariant
LTV	Linear Time Variant
ML	Machine Learning
MAP	Maximum a Posteriori

MCMC	Markov chain Monte Carlo
MAC	Modal Assurance Criterion
ME	Modal Expansion
MOR	Model Order Reduction
NRMSE	Normalized Root Mean Square Error
OMA	Operational Modal Analysis
OSP	Optimal Sensor Placement
PBH	Popov-Belevitch-Hautus
PDE	Partial Differential Equation
PSD	Power Spectral Density
PE	Predictive Engineering
PDF	Probability Density Function
POD	Proper Orthogonal Decomposition
QoI	Quantities of Interest
RIRA	Residual Inertia-Relief Attachment
RB	Reduced Basis
ROM	Reduced Order Model
RTS	Rauch-Tung-Striebel
RW	Random Walk
RBE	Rigid Body Element
RMS	Root Mean Square
RMSE	Root Mean Square Error
SD	Standard Deviation
SDE	Stochastic Differential Equation
SE	Static Error
SHM	Structural Health Monitoring
SISW	Siemens Industry Software
SSM	State-Space Model
STP	Student-t Process
STPLFM	Student-t Process Latent Force Model
TF	Transfer Function
TRAC	Time Response Assurance Criterion
UKF	Unscented Kalman Filter
VS	Virtual Sensing
WT	Wind Turbine

LIST OF FIGURES

LIST OF TABLES

1

INTRODUCTION

Engineering systems are complex, multidisciplinary entities that play an important role in modern society. They must be designed, built, and maintained with a focus on functionality and reliability, as well as safety and sustainability. To address these requirements, attention must be paid to putting in place a controlled management of their life cycle to supervise these systems from their design, through manufacturing and operation to disposal. Knowledge of engineering systems has thus gained crucial importance in recent decades, especially with regard to the design and monitoring phase. Design involves the definition of an initial plan for the system under development, and often includes simulations and testing to ensure that the required system specifications and performance standards are met. Monitoring, on the other hand, involves continuous observation and analysis of the system performance during operation to identify any potential issues or deviations from the expected behavior. This includes the collection and analysis of data, the use of sensors and control systems, and the identification of corrective measures necessary to ensure that the system continues to operate effectively. The combination of effective design and ongoing monitoring of engineering systems helps to improve their performance and reliability and reduces the risk of malfunctions and failures. It also ensures that systems continue to meet the evolving needs and requirements of users as well as changing regulatory and safety standards. In the structural and mechanical domains, the increasing complexity and multidisciplinarity of developed systems and the rapid pace of technological change have increased the need for in-depth knowledge and understanding of the underlying characteristics and phenomena. Moreover, stricter safety and environmental regulations have also incremented the need for detailed knowledge of structures and mechanical components. In this regard, experimental and operational measurements are essential for identifying the structural properties of systems for both design and monitoring. During the design stage, experimental testing is exploited to ensure that structures meet initial design, safety, and performance criteria, as well as for ensuring that they can withstand the loads and conditions they will encounter in service. Data-driven identification methods often referred to as inverse engineering, are in many application cases supported by simulation efforts, i.e., forward engineering, for initial design and prototyping. An iterative process is then installed between testing and simulation for validating the accuracy of source models and implementing potential required modifications according to testing outcomes with the purpose of developing trust in the model through the process of verification and validation. The latter serves to establish a test-validated Digital Twin (DT), i.e., a digital representation featuring encoded information on the structure "as-is". Physical tests can be simplified by extracting information from digital models, e.g. via model-driven data selection or the creation of model-based virtual channels. In the monitoring context, measurements are exploited to evaluate the in-field performance of the structures, identify possible damages, and limit the need for repair efforts by implementing an effective monitoring strategy. The latter is referred to as Structural Health Monitoring (SHM), whose implementation aims to continuously assess the performance level of structures for reducing maintenance time and costs. This process is normally implemented by exploiting on-site monitoring systems to measure Quantities of Interest (QoI) and detect irregularities in the monitored structural behavior. However, the ever-growing systems complexity and the online nature of collected information, which also implies large amounts of data, render the latter difficult to interpret by means of standard system identification techniques. To cope with these restrictions and with the limited in-field accessibility of structures, more articulated SHM strategies have been put in place in recent times with the support of digitalization. Data-driven and physics-based models are being exploited nowadays towards the goal of performing Predictive Engineering (PE), according

to which the system performance can be investigated at any stage of its development, allowing for behavior prediction rather than ad hoc solutions to issues that may arise during operation. With this purpose, DTs developed and validated within the design stage, can be updated throughout the entire life cycle of the system using automated condition monitoring.

1.1 Problem outline and motivation

Design, identification, verification and monitoring comprise primary activities within the life cycle management of mechanical and structural components. Several challenges may arise from the execution of these tasks due to systems complexity, inaccessibility limitations, time and costs constraints and external sources of uncertainties. These aspects can be mitigated by implementing virtualization strategies to be exploited throughout the life span of these components. The goal in this context consists in constructing a DT of the system under study, i.e., a virtual replica of the physical system obtained from a fusion of models and data. The implementation of such strategies in an engineering setting has been facilitated by the digital transformation and technological advancement, which have led to i) increasing computational power and hence more detailed mechanistic models and ii) high levels of sensorization, which imply accessibility to large amounts of data. The main challenge behind the definition of DTs lies in the implementation of reliable methodologies for combining model-based and data-based information to create a predictive tool that can evolve over time. To this end, data assimilation techniques are widely adopted in the structural dynamics context for implementation of Virtual Sensing (VS) strategies, i.e., for inferring QoI such as system responses and/or unknown loads in a dynamic environment. The working principle of these strategies comprises the use of data for reduction of the uncertainties arising from the limitations of mechanistic modeling, which is in turn exploited to expand the available data and gain further knowledge of the system dynamic behavior. Despite VS methods are nowadays recognized as powerful tools for twinning of dynamic systems, several limitations are still to be addressed for improvement of the accuracy and efficiency of the underlying data assimilation process. The major constraints surrounding the applicability of these methods to real-life scenarios derives from modeling inaccuracies and poor data quality. The first can arise from insufficient design data, unsuitable simplifying assumptions used for reducing models computational complexity, parameters uncertainties or numerical errors. The latter is instead related to the correctness and completeness of the information conveyed by physically recorded data, which can often be contaminated by noise, insufficient or sparsely sampled. Despite the effect of these aspects can be controlled and mitigated by means of uncertainties quantification approaches, the latter often require regular offline calibration, thus hindering the real-time applicability and user-independence of these methods.

In this framework, the main motivation of the work presented in this dissertation stems from the existing challenges in the implementation and deployment of a real-time predictive framework for virtualization of dynamic systems. To this end, this thesis proposes novel approaches to limit the necessity of offline user-dependent calibration of data assimilation methods by i) adaptive noise parameters tuning and ii) employment of data-driven a priori models within existing VS algorithms.

1.2 State of the art

The deployment of dynamic virtualization strategies for structures is addressed in this thesis by exploiting VS techniques defined either in a deterministic or in a stochastic framework. These methods combine a limited set of measurements with a validated model in order to infer QoI such as responses at unmeasured locations, unknown loads or system parameters. The task of building "virtual sensors" is often addressed by implementing data assimilation strategies, i.e., by assimilating physically recorded data into a model of the system to merge measured and synthetic information.

The model employed within VS approaches can be i) extrapolated from measured data via inverse engineering methods such as **system identification** techniques [1, 2, 3, 4] or ii) obtained as a physics-based representation of the system, e.g. Finite Element (FE) models [5]. This dissertation

is focused on employing VS methods constructed on the use of the latter class of models. The objective of this methods lies indeed in exploiting mechanistic assumptions for augmenting the information available from data recorded by physical sensors. On the other hand, acquired vibration data is used to contain the uncertainties derived from approximated physics-based modeling, which often feature a too high level of discretization with respect to systems actual behavior. Nevertheless, data-driven system identification techniques are exploited for assessment of the proper characteristics of the structure, e.g, its modal parameters. Data is recorded during experimental or operational measurements and structural features, e.g. modal parameters of the structure, are extrapolated via Experimental Modal Analysis (EMA) and Operational Modal Analysis (OMA) methods respectively. Several enhanced strategies are being developed nowadays to cope with the challenges arising from OMA and SHM, namely the transient response characterizing operational conditions [6, 7] and the effects of fatigue on operating structures, which causes structural parameters variability and eventually damages [8, 9, 10, 11]. On the other hand, many novel strategies have been proposed in the context of EMA, where particular attention has been shed on nonlinearities which may arise, e.g. for large and flexible structures [9, 12, 13, 14]. System parameters extrapolated via data-driven system identification techniques are then referenced to verify, validate and update available FE models, thus allowing their employment within the analyzed VS strategies. Common techniques for **model updating** rely on FE models parameterization and seek for point-estimates of the parameters, e.g. the material properties, by minimizing the difference between the numerical and the experimental dynamic properties. Several metrics sensitive to model parameters change can be adopted for optimization. Most traditional ones [15, 16, 17, 18], which we found implemented in commercial software, comprise non-probabilistic methods which do not account for model uncertainties, noise affecting measured data and material and manufacturing variability [19]. These effects are instead taken into consideration in probabilistic approaches to model update [20, 21, 22]. Popular model updating techniques however, require a large number of analyses of FE models. This gives rise to significant computational efforts, especially when large structures featuring a high number of Degree of Freedoms (DOFs) are analyzed. To mitigate the challenges derived by model updating of high-dimensional FE models, several studies have integrated Reduced Order Models (ROMs) within model updating strategies [23, 24, 25]. Model Order Reduction (MOR) techniques such as Component Mode Synthesis (CMS) [26], i.e., synthetic representation of structural components by means of their vibration modes, Proper Orthogonal Decomposition (POD) [27, 28] or Reduced Basis (RB) methods [29], are indeed commonly used for dimensionality reduction of FE models, thus also allowing for a lower computational effort when making use of these models in processing algorithms such as the ones adopted for VS. Indeed, a crucial advantage of the data assimilation methods explored within this thesis lies in their recursive nature, which implies real-time applicability. The online deployment of "virtual sensors" comprise an attractive feature in the field of structural testing and monitoring, and particularly for spacecraft and Wind Turbine (WT) blade testing, which comprise the two main application fields in this thesis, as well as WT operational measurements. **MOR** is often adopted as solution to the challenges posed by the real-time performance of linear or even nonlinear high-dimensional models. Analyzing systems of high complexity such as the ones featuring nonlinear behavior due to nonlinear materials or large deformations, require high modeling precision and therefore larger computational efforts. To this end, several machine learning algorithms allowing for dimensionality reduction of nonlinear systems for their real-time deployment have been proposed in literature[30, 31, 32, 33].

In specific cases in which the VS main focus is on structural response reconstruction, Modal Expansion (ME) can be applied for **data assimilation** to predict real-time operating data at unmeasured locations by mapping the measured responses through numerical normal modes. The prediction relies upon a modal decomposition of the measured responses to obtain the modal coordinates, which are expanded to the unmeasured DOFs through the FE model mode shapes. This type of deterministic approach has been shown to provide robust predictions when applied on displacement or strain data acquired on simple structures, e.g. Base-Upright [34] and square plate

[35] structures, while further demonstrated for a WT application on a purely accelerations-based dataset [36]. The latter has been also adopted in [37] for building virtual strain sensors for fatigue analysis of an offshore oil platform scaled mockup. Additionally, ME has been tested on both pure acceleration data and a mixed acceleration-strain data set with the purpose of strain-stress estimation for fatigue-life prediction of an offshore monopile WT [38]. As an alternative to ME, Bayesian filtering has also been extensively adopted in the recent years for the purpose of VS [39, 40, 41, 42, 43, 44, 45]. In particular, Kalman-type filters were initially adopted for real-time state estimation under the assumption of complete knowledge of the loads acting on linear or even nonlinear structures [46, 47, 48]. Several extensions of the original algorithm have been proposed for linear dynamic systems in order to simultaneously tackle **response prediction** and inverse **load identification** in a stochastic setting. The so-called Augmented Kalman Filter (AKF) consists in including the unknown input within a new augmented state vector by assuming a pure Random Walk (RW) model for its dynamics. The algorithm and its applicability to structural dynamics have been proposed in [49]. The AKF instability issues have been investigated in [50], where dummy measurements are adopted to overcome the un-observability of the augmented system matrix, which appears when acceleration measurements are exclusively considered. Numerical issues due to un-observability exhibited by the AKF have been resolved by an alternative algorithm for joint input-state estimation, commonly referred as the Dual Kalman Filter (DKF). The DKF, consisting in approaching the input and states prediction into two sequential stages under the assumption that the input follows a pure RW model, has been presented in [51] and tested in [52]. Several additional algorithms have been proposed for joint input-state estimation with a time-delayed scheme [53, 54, 55]. It has been proved in [55] that these approaches, classified as smoothing, allow to significantly reduce the estimation uncertainty due to measurement noise when measurements collocated with the estimated forces are not available. The challenges derived from instantaneous system inversion for load identification within input-state estimation algorithms have been investigated in [56], where the requirements in terms of sensors quantity and type are investigated. In this sense, an ad hoc Optimal Sensor Placement (OSP) strategy has been developed in [57, 58] for input-state estimation using the AKF, while a more extended framework based on information theory is proposed in [35, 59, 60].

A more generic model for the input, i.e., a first order stationary autoregressive process, has been used in [39] to address joint input-state-parameter estimation via a combination of the DKF and the Unscented Kalman Filter (UKF) [61, 62, 63, 64]. Although the RW model and its adaptations are widely adopted as prior input information in generic circumstances when applying joint input-state estimation schemes, it is sometimes not representative of the actual loading conditions. As such, imposing an a priori RW model for estimating loads in any laboratory or operational condition often negatively influences the prediction accuracy. To this end, Machine Learning (ML) approaches such as Gaussian Process (GP) regression [65] have been exploited to construct more comprehensive **models for the unknown input**. A state-space representation for GP models has been proposed in [66, 67], where a recursive regression solution has been implemented using a combination of Kalman filtering and smoothing. The sequential GP regression solution has been used to construct Gaussian Process Latent Force Models (GPLFMs) with applications in several domains [68, 69, 70]. In [71], GPLFMs have been introduced as flexible alternatives for unknown input modeling in the framework of joint input-state estimation of structures. With this purpose, a GPLFM with a Matérn kernel is used in combination with the Bayesian Dynamic Model (BDM) of the system for joint input-state prediction via Kalman filtering and smoothing. Besides its higher flexibility, it has been demonstrated in [71] that this method overcomes the un-observability issues arising from the use of the AKF with acceleration-only data sets. The GPLFM has been further exploited for input-state-parameter estimation in [72]. Additionally, GP regression has been implemented in both time and space dimensions for recursive distributed load prediction in [73]. The need of an a priori assumption regarding the input dynamics has been overcome in [74] by the so-called Gillijns De Moor Filter (GDF). This estimator has been derived on the basis of the Kitanidis filter [75, 76], a

linear state estimator operating in presence of unknown inputs which do not affect the produced state estimation. Under this assumption, the coupled input-state estimation can be perfomed via the GDF algorithm, in which the input true values are substituted by their optimal estimates. The GDF has been extended for systems with a direct transmission term in [77], while an improvement of the method regarding instabilities due to the number of adopted sensors exceeding the model order has been suggested in [78]. The input-state prediction through Bayesian VS often implies significant challenges when applied to complex systems subjected to uncertain loading conditions such as WTs. In order to address the reduction of these uncertainties, a substructure approach for input-state estimation has been proposed in [79] and validated on real-life data from an offshore WT in [80]. Recently, Bayesian filtering and ME have been combined via the so-called ME-AKF method. The latter consists in implementing strain responses predicted via ME into the AKF in order to enhance the online estimation results. The method has been proposed and tested on a full-scale rollercoaster structure in [81].

Within the context of Bayesian filtering, the assumption of a priori knowledge of the **process and measurement noise statistics** is placed. The process and measurement noise terms are used in a stochastic framework to reflect the uncertainties that stem from modeling errors/approximations, input uncertainty and measurement noise in the system representation. These two noise variables are commonly assumed to be independent, zero-mean white noise processes and the corresponding covariance matrices are treated as time-invariant quantities. The adoption of incorrect values for the process noise and measurement noise covariance matrices can lead to large estimation errors. In many cases, these values are not known exactly and offline tuning procedures are put in place [82, 83, 84, 39, 51, 52]. In an effort to handle this, a common approach is to prescribe the measurement noise covariance by exploiting the available physical sensors specifications. Then, an optimization procedure regarding the process noise term is carried out in a rather heuristic manner, i.e., either by trial and error or by means of regularization metrics, such as the L-curve [85]. Besides its offline nature, this method often generates a plot which does not appear as a perfect L-shape. This renders the regularization parameter choice not straightforward for several Kalman-type filters, e.g. the AKF [49] and the DKF [52]. The application of regularization schemes is also limited to the condition in which only one parameter is to be calibrated. The working principle behind the L-curve has been adapted and used for simultaneously tuning more than one term in [86, 41]. An online alternative to the previously mentioned methods for identifying the disturbances consists in using adaptive filtering techniques. These strategies have been applied for both the process and measurement noise terms [43] and they can be classified into four main categories [87]: Bayesian [88], maximum-likelihood estimation [89], correlation [90, 91, 92, 93] and covariance matching [94] methods. These approaches describe generic adaptive filtering schemes, which are typically characterized by excessive computational times. Moreover, the majority of these techniques are based on seeking the most suitable process and measurement noise covariance matrices steady-state estimates, rather then their current optimal values.

1.3 Case studies

Focus will be shed in this dissertation onto the development of dynamic virtualization strategies, i.e., methodologies aimed at creating DTs of dynamic systems by augmenting numerical models using data. Two major application domains will be investigated by means of the analyzed case studies: spacecrafts and WT blades testing. Within both contexts, enhanced tools will be provided for installing a real-time dynamic virtualization process by blending the margins between testing and simulation. In this respect, a hybrid approach is developed by exploiting VS technologies aimed at the fusion of physically acquired vibration data with artificial information produced by mechanistic or data-driven models.

1.3.1 Dynamic virtualization for spacecraft environmental testing

Environmental testing is a crucial step in the development of spacecrafts as it helps to ensure that they can withstand the harsh conditions of space. This includes testing the spacecraft ability to resist to extreme temperatures, vacuum conditions, and high levels of radiation. Environmental testing is

also important for verifying the reliability of the spacecraft electrical and mechanical components to the dynamical launch environment, where the most extreme excitation conditions occur. One of the main objectives of environmental testing thus consists in verifying the resistance of the system and its sub-components to the vibration environment these are subjected to during the launch phase. To this end, during environmental testing campaigns such as the one represented in Fig. 1.1, spacecrafts are positioned on a large scale electrodynamic or hydraulic shaker testing facility, which provides a controlled excitation with the purpose of replicating the in-service structural response of the tested structure.

Figure 1.1: The BepiColombo spacecraft stack undergoing vibration tests at the European Space Agency. Credit: ESA - European Space Agency, CC BY-SA 3.0 IGO.

Due to prohibitive costs of testing entire complex systems as spacecrafts, it is common practice to perform vibration control tests at a component level. To this end, the component of interest is typically attached to the shaker via a rigid fixture [95] and excitation is provided in its main axes of vibration. The most critical aspect in the execution of these tests is related to the erroneous representation of the operational environment due to limitations in vibration control strategies and in the Boundary Conditions (BCs) replication [96, 97]. Indeed, commonly adopted fixtures often recreate incorrect interaction between the tested article and the shaker, thus producing side effects as i) unplanned over- or under-testing, ii) incorrect estimation of remaining life time and iii) damage. Motivated by the above, the testing community has defined a Boundary Condition Challenge (BCC), whose goal is to improve the in-service environment replication at component level during environmental testing. The BCC has built a collaborative environment for investigating alternative approaches [98, 99, 100, 101, 102] for environmental testing of the Box Assembly with Removable Component (BARC) setup shown in Fig. 1.2 [103].

Figure 1.2: The Box Assembly with Removable Component

Under this perspective, dynamic virtualization offers powerful tools for gaining better understanding of the structural behavior of the component under test, thus facilitating the improvement of in-service response replication during vibration tests. In this respect, a real-time hybrid framework can be installed for spacecraft components virtualization exploiting virtual sensors built by combining model-based information and vibration response measurements. VS techniques can be employed in environmental testing applications to retrieve the complete strain field on the tested component, allowing for a more complete understanding of its structural behavior. Entire stress fields can be derived from strain information, based on which component failure can be predicted. Real-time virtual channels can be also exploited within vibration control strategies in order to ensure safety and allow replication of several testing scenarios. Moreover, these methods can be used to retrieve loads acting on the tested structure as such relevant quantities are not typically measured during environmental tests.

1.3.2 Dynamic virtualization for wind turbine blades testing

Wind energy infrastructure represents an active area of research on multiple fronts, but particularly within the structural dynamics domain, where multiple challenges arise due to the stochastic nature of the loads these systems are exposed to and the inaccessibility of components after their installation. In view of the increasing industrial need of reducing WTs operational costs, improved SHM strategies are nowadays exploited and further boosted through innovative digitalization processes [104]. The aim of these schemes consists in tracking and supporting blades status assessment not only in the field, but also from conceptualization, through certification tests, all the way to operation and end-of-life. Blades comprise WT components of elevated importance and complexity. Extensive testing is usually performed on blades in order to build a test-validated DT and to prove that these can withstand the anticipated loads in field conditions [105]. Although more attention is usually placed on static [106, 107] and fatigue tests [108, 109, 110, 111, 112], dynamic tests are also adopted for identifying basic dynamic properties, essential for the structural integrity of the entire WT. Dynamic tests [113, 114, 115, 116, 117, 118] require a vibration source, which could be achieved via use of a shaker or by hammer tests, with the blade typically positioned in free-free or clamped-free boundary conditions as in Fig. 1.3, as well as the so-called pull and release tests [119, 120, 121], where the blade is in clamped-free conditions and it is pulled close to the free-end before being released to be able to measure its free-vibrations. The latter class involves output-only measurements with the purpose of collecting as much information as possible regarding the operational response of the structure.

Figure 1.3: A 14.3 m long research WT blade manufactured by Olsen Wings and tested by DTU Wind Energy at the DTU Large Scale Facility. Credit: DTU Wind Energy.

Implementation of a thorough monitoring at a dense set of structural locations, even those that are considered as hot spots, is often hindered by the inaccessibility of certain locations and the costs of sensors required, which might often limit the assessment procedure. VS can be exploited for

estimating the response of the monitored blade at locations that are not instrumented for accessibility, time and costs limitations [122, 123, 124]. The resulting "enriched" data, e.g, full-field deformation, can be used to build a true-to-life DT, able to reproduce representative dynamic response in operational circumstances. The constantly updated high-fidelity models can be then employed for refined condition assessment. Besides representing a valid solution for bulding vibrational response "virtual sensors", these methods can be used for prediction of additional QoI such as unknown loads acting on blades both in operation and during laboratory testing.

1.4 Objectives and contributions

In this thesis, focus is placed on the development of VS techniques for dynamic virtualization of structures, with spacecrafts components and WT blades testing comprising the two main implementation case studies. The construction of "virtual sensors" is hereby addressed via state-of-the-art and newly developed data assimilation methods designed for simultaneous real-time structural response and unknown loads prediction. Within this framework, the major objectives and contributions of this dissertation can be summarized as follows.

Deterministic structural response estimation

The problem of structural response estimation, i.e., real-time prediction of mainly strains and accelerations, is treated by means of both stochastic and deterministic approaches. Within the context of deterministic response estimation, the "enriched" response information can be obtained via ME methods, which map the available limited set of recorded measurements through numerical normal modes. These strategies assume that the employed FE model captures the complete physics of the system under study, i.e., they do not account for modeling errors or uncertainties, as well as local deformations under the analyzed loading conditions. To cope with this latter aspect, the Component Mode Synthesis - Modal Expansion (CMS-ME) approach is derived from the combination of ME with a CMS technique aimed at providing a more complete structural reduced space representation of the system by including static deformations in the numerical reduction basis.

Bayesian joint input-state estimation: adaptive uncertainties modeling

A major challenge in the use of Kalman-based estimators for joint input-state estimation, i.e., for simultaneous prediction of unknown loads and responses, comprise modeling of the uncertainties involved in the estimation. These are grouped within the measurement and process noise terms, which respectively quantify noise affecting observations and uncertainties in the physics-based model adopted for data assimilation. While measurement noise is a more concrete entity as it can be linked to physically recorded signals, the process noise term often acts as an abstract parameter whose numerical value heavily affects the estimator results. An intuitive approach is proposed in this thesis for adaptive process noise covariance matrix tuning for joint input-state estimation using the AKF. In this context, both the uncertainties related to the unknown input and system states, i.e., modeling errors, are taken into account for optimization. The covariance matrix of the "augmented" process noise is considered to be time-variant, since the modeling uncertainty and the dynamic characteristics of the input (load) may vary in time. The newly proposed method, addressed as Adaptive-noise Augmented Kalman Filter (A-AKF), is based on reference response estimates computed using the hereby proposed CMS-ME approach.

Bayesian joint input-state estimation: unknown input modeling

The joint input-state estimation performed via Kalman-type filters requires the definition of an a priori time evolution model for the unknown loads. A common approach consists in imposing a RW equation to shape the unknown input dynamics, which is then coupled with the mechanistic time-domain model of the structure for simultaneously estimating its responses at unmeasured locations and the loads it is subjected to. This assumption is adopted within state-of-the-art schemes such as the AKF and the DKF and often employed to infer inputs and system states in several loading scenarios. However, this assumption results in a too strict simplification, especially for loads which

deviate from the popular ambient noise excitation scheme. This leads to challenging tuning efforts of the estimators and difficulties in providing reliable loading predictions in generic circumstances. This dissertation explores the use of stochastic processes (GP and Student-t Process (STP)) Latent Force Models (LFMs) for constructing the unknown input state-space representation within a joint input-state estimation logic.

GP regression for unknown input modeling

GP regression is adopted for defining LFMs to be employed within joint input-state estimation strategies. A critical review on the necessary tools for building a state-space representation of a GP is presented. Specifically, a detailed analysis of conventional and non-conventional GP covariance functions in structural dynamics is offered, along with the derivation of their Stochastic Differential Equation (SDE) representations. The latters have been analyzed by means of an analogy with the harmonic oscillators theory, which has served to identify the inner dynamic features of each investigated covariance function. This thesis proposes the use of ad hoc covariance functions according to the analyzed experimental case study in order to maximize the joint input-state estimation performance. To this end, the theoretical study has been complemented with a simulated example concerning a 3 DOFs system subjected to an array of different loading conditions.

Experimental validation

An extensive experimental validation of both state-of-the-art and newly developed VS methods is provided in this thesis. These approaches are tested using data sets acquired during testing of i) spacecrafts mechanical components, ii) small scale WT blades (isotropic and composite) and iii) large scale composite WT blades. The analyzed experimental applications introduce several modeling challenges linked to BCs and material uncertainties, which have been treated by employing specific MOR and model updating strategies. Within this context, the analyzed estimators are tested and compared for several loading conditions. Additionally, their performance variability with the type of installed sensors is investigated.

1.5 Organization of the text

This chapter (**Chapter 1**) provides an introduction to the context of dynamic virtualization by outlining the problem and motivating the work documented in this thesis. After a presentation of the current state of the art and a description of the analyzed case studies, the thesis objectives and main contributions are highlighted. The remainder of the thesis is structured as follows: Chapters 2-5 provide the required theoretical background along with a description of the developed methodological tools, while Chapters 6-9 report on the experimental validation of the state-of-the-art and newly developed approaches by means of several case studies.

Chapter 2 introduces the necessary tools for constructing the dynamic system models used in the VS strategies developed in this thesis. It starts from presenting the state-space representation and the MOR techniques adopted in this thesis to build initial deterministic physics-based models. Next, the stochastic framework forming the core of the presented data assimilation strategies is offered. This chapter also focuses on data-driven methods for building dynamic models from observations-only by means of stochastic processes regression tools. Specifically, it reports on GP regression and on the conventional covariance functions adopted in structural dynamics. Alternative covariance functions are also proposed and a thorough analysis of the SDE representation of the stochastic process obtained when different covariance functions are adopted is offered. This chapter also proposes the analysis of a second regression scheme, the STP regression, more suitable for training data containing outliers.

Chapter 3 summarizes the data assimilation methods exploited in this thesis for VS in structural dynamics. The first part of the chapter deals with the problem of response estimation in a deterministic setting by describing the ME approach and proposing an improvement of the method, i.e., the so-called CMS-ME approach. Next, the Kitadininis and the GDF algorithms are proposed.

The chapter also reports on the AKF and DKF algorithms as state-of-the-art Bayesian estimators of input and states.

Chapter 4 pertains to the problem of uncertainties modeling in Bayesian filtering. Uncertainties arising from modeling errors and measurement noise are indeed embedded into two noise terms, i.e., the process and measurement noise respectively, within Bayesian estimators such as the Kalman Filter (KF). These terms, which are introduced in Section 2.2, robustly control the accuracy of Kalman-based filters. Chapter 4 first describes the effect of the selected noise terms on Kalman-based filters accuracy. Next, the use of conventional methods for process noise covariance tuning in an input-state estimation framework are presented. Finally, a newly developed approach is proposed in this chapter for adaptive tuning of the time-variant process noise covariance matrix using the AKF. The method, addressed as A-AKF, is based on reference response estimates computed via the CMS-ME approach introduced in Chapter 2.

Chapter 5 focuses on the necessary input modeling efforts within the context of input-state estimation via Bayesian filtering. Initially, the conventional RW transition model is described, along with a detailed analysis of the limitations derived from its employment. This chapter then proposes a prior unknown input transition model constructed via a LFM derived from the regression concepts proposed in Chapter 2. The applicability to several loading conditions of the LFM obtained when different covariance functions are adopted is tested by means of a simulated example.

Chapter 6 treats the use of VS strategies for estimating unknown loads and augmenting the response measured during environmental tests on the BARC setup. As such, this chapter provides a primary description of the main necessary steps for implementation of conventional VS methods in real-life scenarios. The main challenges derived from practical use of such methods, i.e., necessary modeling accuracy, sensors fusion and estimators tuning, are thus introduced within this chapter. After a description of the BARC, the FE model is presented along with the details of its model updating process. Secondly, the environmental testing campaign carried out on the BARC is described and the constructed ROM is presented. The remainder of this chapter documents the prediction results obtained from the use of Kalman-type filters during environmental tests on the BARC. Specifically, the responses and loads inferred via the AKF are first assessed under the assumption of strains-only or mixed observations set. The use of a conventionally constructed GPLFM for input-state estimation on the BARC is also tested.

Chapter 7 tackles the challenge of conventional Kalman-based estimators tuning by proposing an experimental validation of the adaptive noise modeling approach presented in Chapter 4. Specifically, this chapter focuses on output-only measurements performed on a large-scale WT blade. A summary of the measurement campaign is initially reported, along with a description of the blade FE model and its validation results. First, this case study is used to validate the CMS-ME approach proposed in Chapter 2 by comparing the response estimation results with the standard ME results. This chapter continues with a parametric analysis of the input-response predictions achieved by the state-of-the-art AKF for several choices of the time-invariant process noise covariance associated to the unknown input. This analysis is then used for proving the validity of the input-response predictions produced by the A-AKF during pull and release tests on the blade under study. Finally, a parametric assessment of the A-AKF and a comparison with the results achieved via the conventional AKF and the CMS-ME approach are provided.

Chapter 8 extends the A-AKF validation provided in Chapter 7 to a random excitation scenario by employing the A-AKF for input-state estimation during random tests of a 3D-printed scaled blade. The WT blade test campaign replicated on the 3D-printed scaled blade is first described. The FE model, its validation and update results are then presented. The case study analyzed within this chapter is then exploited for providing additional validation of the GP-based approach with conventional Matérn covariance function, introduced in Chapter 5 and previously validated for the BARC in Chapter 6. Specifically, a comparison of the AKF and the GP-based approach with conventional Matérn covariance function is proposed for the random tests under both the assumptions of available strain and acceleration measurements or acceleration-only measurements.

This chapter also provides additional assessment of the GP-based method for a different excitation scenario by analyzing the pull and release tests performed on the 3D-printed scaled blade. During the latter, the AKF, DKF and GP-based approach with conventional Matérn covariance function are tested for input-response prediction. Finally, the use of ad hoc covariance functions for input-state prediction via the GPLFMs conceptualized in Chapter 5 is tested on the 3D-printed WT blade under different loading conditions.

Chapter 9 further explores the use of ad hoc covariance functions for a case study concerning a scaled WT blade made of Glass Fiber Reinforced Plastics (GFRPs) undergoing laboratory testing. Additionally, the adoption of alternative stochastic processes is hereby proposed via application of the Student-t Process Latent Force Model (STPLFM). The latter is tested in combination with a Wiener covariance function on the task of input-state prediction in presence of noise contaminated data due to the GFRPs high flexibility. The estimator performance is evaluated by comparing it against the GPLFM with the same covariance function and the state-of-the-art AKF. The proposed case study is first addressed through a description of the measurement campaign, the FE model and its validation and update results. VS results from the use of the mentioned data assimilation methods during shaker testing are then reported.

Chapter 10 presents the closing remarks for this thesis and provides recommendations for further research.

2

DYNAMIC SYSTEM MODELS

A model is defined as an abstract representation of a real situation that can be manipulated to predict the expected results for different types of inputs in real life [125]. Exploiting physics knowledge, engineers create mechanistic models to predict real-life situations, turning physical problems into analytical models typically represented with a set of differential equations. In a deterministic setting, physics-based models provide specific values for output variables of the system for any input provided. However, due to systems complexity, the predicted "output" may not necessarily correspond to the "correct value". As a result, it is common practice to account for certain levels of unpredictability or randomness via the adoption of stochastic models. It is also worth noting that, even if all the physical underlying processes can be adequately described in a stochastic setting, the resulting model can be extremely complex due to the numerous interactions that need to be modeled. To solve this issue, data-driven approaches are often employed to: i) identify dynamic systems from vibration measurements, also with the purpose of validating and update available physics-based models, ii) infer predictions purely relying on data analysis and interpretation.
This chapter reports on the basic concepts adopted in this dissertation to build dynamic system models and it is divided into three units. The first one treats the mechanistic approaches of interest, mainly focusing on MOR and state-space representation, which build the dynamic models formulation adopted in the following sections and chapters. The second one deals with Bayesian modeling, presenting the stochastic framework which forms the basis for the algorithms adopted within this dissertation. The third one focuses on data-driven methods proposing Bayesian regression tools for performing predictions by means of observations-only.

2.1 Mechanistic forward modeling

Mechanistic models make use of a fairly well characterized physical process that underpins the system to describe its physics via a set of differential equations. Despite these types of models typically result in rather discrete representations of real-life systems due to the complexity of the modeled physical processes, they still maintain their usefulness as they enable predictions even in regions where there may be no available observations. An example in structural mechanics lies in FE models of complex structures, which undergo a "discretization" process through elements and nodes. The resulting representation is then complemented with the known physical properties of the system and responses to the physically meaningful inputs are obtained by solving a set of Partial Differential Equations (PDEs). FE models of large and complex structures typically feature high computational cost. In view of mitigating this cost, therefore addressing the increasing need of lighter virtual models to be deployed in real-time, the present section reports on the basic concepts for the MOR methods adopted within this dissertation. Subsequently, the time-domain state-space formulation, which will serve as link with the following chapters, will be introduced.

2.1.1 Model Order Reduction via Component Mode Synthesis

The Equation of Motion (EoM) of a linear structural system, which is usually simulated via use of a FE model, may be formulated as a second order vector differential equation of the form:

$$\mathbf{M}\ddot{\mathbf{z}}(t) + \mathbf{D}\dot{\mathbf{z}}(t) + \mathbf{K}\mathbf{z}(t) = \mathbf{S}_i\mathbf{u}(t) \tag{2.1}$$

where $\mathbf{z}(t) \in \mathbb{R}^{n_{dof}}$ is the vector of displacements, corresponding to the FE model DOFs, $\mathbf{M} \in \mathbb{R}^{n_{dof} \times n_{dof}}$, $\mathbf{D} \in \mathbb{R}^{n_{dof} \times n_{dof}}$ and $\mathbf{K} \in \mathbb{R}^{n_{dof} \times n_{dof}}$ denote the mass, damping and stiffness matrices respectively; $\mathbf{u}(t) \in \mathbb{R}^{n_i}$ (with n_i representing the number of loads) is the input vector and $\mathbf{S}_i \in \mathbb{R}^{n_{dof} \times n_i}$ is the Boolean input shape matrix that selects the DOFs where loads (inputs) are applied. A MOR technique relying on CMS can be applied to reduce the model size. CMS is a widely applied method in substructures coupling analysis, where it is adopted to provide a synthetic representation of structural components via their vibration modes [26]. In this dissertation, a time-domain CMS approach will be exploited to model the analyzed systems as single structures. According to this method, the dynamic behavior of a structure can be formulated as a superposition of modal contributions:

$$\mathbf{z} \approx \mathbf{\Psi p} \tag{2.2}$$

where $\mathbf{\Psi} \in \mathbb{R}^{n_{dof} \times n_r}$ is the reduction basis and $\mathbf{p} \in \mathbb{R}^{n_r}$ is the vector of the generalized coordinates of the system, with n_r being the dimension of the reduced coordinates. Inserting the reduction basis into Eq. 2.1 and premultiplying each term by $\mathbf{\Psi}^T$, the resulting equation is of the form:

$$\mathbf{M}_r \ddot{\mathbf{p}}(t) + \mathbf{D}_r \dot{\mathbf{p}}(t) + \mathbf{K}_r \mathbf{p}(t) = \mathbf{S}_r \mathbf{u}(t) \tag{2.3}$$

where the mass, damping, stiffness and input shape matrices of the reduced system are respectively $\mathbf{M}_r = \mathbf{\Psi}^T \mathbf{M} \mathbf{\Psi}$, $\mathbf{D}_r = \mathbf{\Psi}^T \mathbf{D} \mathbf{\Psi}$, $\mathbf{K}_r = \mathbf{\Psi}^T \mathbf{K} \mathbf{\Psi}$ and $\mathbf{S}_r = \mathbf{\Psi}^T \mathbf{S}_i$. The adopted reduction basis can be expressed as:

$$\mathbf{\Psi} = \begin{bmatrix} \mathbf{\Psi}_n & \mathbf{\Psi}_\alpha \end{bmatrix}; \tag{2.4}$$

where $\mathbf{\Psi}_n \in \mathbb{R}^{n_{dof} \times n_k}$ is the matrix of the numerical normal modes to be included in the Reduced Order Model (ROM), i.e., the eigenmodes of the entire structure in the frequency range of interest, and $\mathbf{\Psi}_\alpha \in \mathbb{R}^{n_{dof} \times n_\alpha}$ is the residual attachment modes matrix. The residual attachment modes are usually inserted in this kind of reduction bases in order to include a representation of the static response of the structure to an input at a specific DOF. Typically, for each load acting on the structure, the relative residual attachment mode is included in the basis. The latter is computed as a mode of the structure under application of a unitary static input applied at the actual input DOF. Therefore, n_α is equal to the number of loads applied to the system and $n_r = n_k + n_\alpha$.

2.1.1.1 Residual Inertia-Relief Attachment modes

In situations in which no fixed constraint is provided in the global frame, rigid body motion is present and, as a consequence, the static solution, and hence the residual attachment modes, can not be computed. A workaround to this issue consists in making use of the Residual Inertia-Relief Attachment (RIRA) modes [26, 126], i.e., specific attachment modes computed through the following steps:

1. Constrain the minimum number of random DOFs needed for having $\mathbf{K}$ non-singular;
2. Compute the static solution, i.e., obtain the Inertia-Relief Attachment modes $\mathbf{\Psi}_{IRA}$ as:

$$\mathbf{K} \mathbf{\Psi}_{IRA} = \mathbf{Pr} \mathbf{S}_i \tag{2.5}$$

   where $\mathbf{Pr} = \mathbf{I} - \mathbf{M} \mathbf{\Psi}_{RB} \mathbf{\Psi}_{RB}^T$ is the so called inertia-relief projector, i.e., a matrix used to re-equilibrate the applied unitary forces with a set of inertial forces that are manifested because of the presence of the rigid body modes in $\mathbf{\Psi}_{RB}$. This operation allows to obtain the net force causing flexible motion;
3. Make $\mathbf{\Psi}_{IRA}$ residual with respect to normal modes $\mathbf{\Psi}_n$ included in the basis, thereby obtaining the $\mathbf{\Psi}_{RIRA}$ as:

$$\mathbf{\Psi}_{RIRA} = \mathbf{Pr}^T \mathbf{\Psi}_{IRA} - \mathbf{\Psi}_n \mathbf{\Lambda}^{-1} \mathbf{\Psi}_n^T \mathbf{S}_i \tag{2.6}$$

   where $\mathbf{\Lambda} = \mathbf{\Psi}_n^T \mathbf{K} \mathbf{\Psi}_n$ is the diagonal reduced stiffness matrix. In Eq. 2.6, the first term renders matrix $\mathbf{\Psi}_{IRA}$ orthogonal to $\mathbf{\Psi}_{RB}$, while the second term makes them independent with respect to the normal modes matrix $\mathbf{\Psi}_n$. Indeed, the latter already includes part of the static deformation, which should be therefore excluded from the residual attachment modes.

2.1.2 State-Space modeling

Physics-based models typically result in a set of differential equations which can be more or less complex according to the complexity of the underlying system behavior which is being modeled. It is a common approach to transform this set of high-order differential equations to lower order State-Space Models (SSMs) which shape the system dynamics via a set of state variables, i.e., variables that fully describe the underlying system dynamics. In a more broad perspective, SSMs are flexible time series models which allow to recover time values of specific QoI based on the system history, i.e., to link current values of the so-called observations to past values of the system states. In particular, SSMs are built by enforcing the dependence of the current state only on the direct previous instant of time (Markov property). The dependence of the observation $\mathbf{y}_k$ at the current k-th time instant on the system states at $k-1$ is postulated by coupling the so-called observation and transition models. The first describes how the underlying dynamics can be superposed to generate the observations, while the latter shows how these dynamics evolve through time. This results into two separate equations building the conventional state-space formulation:

$$\begin{aligned} \mathbf{x}_k &= f(\mathbf{x}_{k-1}) \\ \mathbf{y}_k &= h(\mathbf{x}_k) \end{aligned} \tag{2.7}$$

where f is the function defining the transition model by embedding the relationship between current states $\mathbf{x}_k$ and previous states $\mathbf{x}_{k-1}$, and h maps the current states $\mathbf{x}_k$ in the current observations $\mathbf{y}_k$. The behavior postulated by Eq. 2.7 can be repeated recursively, thus allowing full time series modeling. In this section, the state-space formulation for linear structural systems will be presented under the deterministic assumption, i.e., by assuming that exact values of the involved variables can be calculated in a unique manner. Section 2.2 will later introduce BDMs as special case of SSMs defined in a stochastic framework, which builds the core of this dissertation. In a structural dynamics setting, SSMs simplify the analysis of systems dynamic behavior by reducing second-order differential equations to first-order time models. The EoM of a linear reduced-order structural system postulated in Eq. 2.3 can be formulated via a continuous-time deterministic state-space representation as:

$$\begin{cases} \dot{\mathbf{x}}(t) = \mathbf{A}\mathbf{x}(t) + \mathbf{B}\mathbf{u}(t) \\ \mathbf{y}(t) = \mathbf{C}\mathbf{x}(t) + \mathbf{G}\mathbf{u}(t) \end{cases} \tag{2.8}$$

where the state vector $\mathbf{x} = \begin{bmatrix} \mathbf{p} & \dot{\mathbf{p}} \end{bmatrix}^T \in \mathbb{R}^{2n_r}$ groups the generalized coordinates vector $\mathbf{p}$ (modal displacements) and its first derivative $\dot{\mathbf{p}}$ (modal velocities). The first equation in Eq. 2.8, i.e., the transition model or state equation, defines the state vector change in time as a function of the current state vector and the external inputs $\mathbf{u}$ acting on the system. Matrices $\mathbf{A}$ and $\mathbf{B}$ are computed as functions of $\mathbf{M}_r$,$\mathbf{K}_r$ and $\mathbf{D}_r$ presented in Subsection 2.1.1:

$$\mathbf{A} = \begin{bmatrix} \mathbf{0}_{n_r} & \mathbf{I}_{n_r} \\ -\mathbf{M}_r^{-1}\mathbf{K}_r & -\mathbf{M}_r^{-1}\mathbf{D}_r \end{bmatrix}, \qquad \mathbf{B} = \begin{bmatrix} \mathbf{0}_{n_r \times n_i} \\ \mathbf{M}_r^{-1}\mathbf{S}_r \end{bmatrix}. \tag{2.9}$$

The second equation of Eq. 2.8 defines the system measurements, i.e., the observations model, with $\mathbf{y} \in \mathbb{R}^{n_o}$ representing the observations vector, while the time-invariant matrices $\mathbf{C} \in \mathbb{R}^{n_o \times 2n_r}$ and $\mathbf{G} \in \mathbb{R}^{n_o \times n_i}$ are constructed as follows:

$$\mathbf{C} = \begin{bmatrix} \mathbf{S}_d & \mathbf{0}_{n_d \times n_r} \\ \mathbf{0}_{n_v \times n_r} & \mathbf{S}_v \\ -\mathbf{S}_a\mathbf{M}_r^{-1}\mathbf{K}_r & -\mathbf{S}_a\mathbf{M}_r^{-1}\mathbf{D}_r \end{bmatrix}, \qquad \mathbf{G} = \begin{bmatrix} \mathbf{0}_{n_d \times n_i} \\ \mathbf{0}_{n_v \times n_i} \\ \mathbf{S}_a\mathbf{M}_r^{-1}\mathbf{S}_r \end{bmatrix}, \tag{2.10}$$

In a structural dynamics context, the output vector $\mathbf{y}$ may contain n_d displacement or strain, n_v velocity and n_a acceleration measurements at specific DOFs, which are respectively selected via the matrices $\mathbf{S}_d \in \mathbb{R}^{n_d \times n_r}$, $\mathbf{S}_v \in \mathbb{R}^{n_v \times n_r}$, and $\mathbf{S}_a \in \mathbb{R}^{n_a \times n_r}$. For strain measurements, the $\mathbf{S}_d$ matrix is constructed through a combination of DOFs. Using the FE formulation, the strain vector $\boldsymbol{\varepsilon}$ at any

point of an element can be expressed as a function of the displacement vector $\mathbf{z}$ via the following formula:

$$\boldsymbol{\varepsilon} = S\mathbf{z} \tag{2.11}$$

where S is a differential operator defined as follows:

$$S = \begin{bmatrix} \frac{\partial}{\partial x} & 0 & 0 \\ 0 & \frac{\partial}{\partial y} & 0 \\ 0 & 0 & \frac{\partial}{\partial z} \\ \frac{\partial}{\partial y} & \frac{\partial}{\partial x} & 0 \\ 0 & \frac{\partial}{\partial z} & \frac{\partial}{\partial y} \\ \frac{\partial}{\partial z} & 0 & \frac{\partial}{\partial x} \end{bmatrix}. \tag{2.12}$$

The displacement vector $\mathbf{z}$ at each element point can be discretized as follows:

$$\mathbf{z} \approx \sum_a N^a \mathbf{z}^a \tag{2.13}$$

where $\mathbf{z}^a$ is the displacement vector at the a^{th} node of the element and N^a are the element shape functions. By introducing Eqs. 2.13 and 2.2 into Eq. 2.11, the following expression for the strain vector is obtained:

$$\boldsymbol{\varepsilon} = \sum_a \mathbf{B}^a \boldsymbol{\Psi}^a \mathbf{p} \tag{2.14}$$

where $\boldsymbol{\Psi}^a$ is the reduction basis computed at the element nodal DOFs and $\mathbf{B}^a$ contains the shape functions derivatives:

$$\mathbf{B}^a = \begin{bmatrix} \frac{\partial N^a}{\partial x} & 0 & 0 \\ 0 & \frac{\partial N^a}{\partial y} & 0 \\ 0 & 0 & \frac{\partial N^a}{\partial z} \\ \frac{\partial N^a}{\partial y} & \frac{\partial N^a}{\partial x} & 0 \\ 0 & \frac{\partial N^a}{\partial z} & \frac{\partial N^a}{\partial y} \\ \frac{\partial N^a}{\partial z} & 0 & \frac{\partial N^a}{\partial x} \end{bmatrix}. \tag{2.15}$$

Therefore, when the output vector $\mathbf{y}$ contains strain measurements, the selection matrix $\mathbf{S}_d$ is obtained evaluating the matrix $\sum_a \mathbf{B}^a \boldsymbol{\Psi}^a$ at the strain vector components corresponding to the measured strain quantity.
In order to ensure consistency with the discrete nature of real-life measurements, Eq. 2.8 should be transferred to its discrete-time representation:

$$\begin{cases} \mathbf{x}_k &= \mathbf{A}_d \mathbf{x}_{k-1} + \mathbf{B}_d \mathbf{u}_{k-1} \\ \mathbf{y}_k &= \mathbf{C}\mathbf{x}_k + \mathbf{G}\mathbf{u}_k \end{cases}. \tag{2.16}$$

where the superscript $\square_k$ indicates the time instant $t = k\Delta t$ when Δt is the time step. Matrices $\mathbf{A}_d, \mathbf{B}_d, \mathbf{C}$ and $\mathbf{G}$ are the discrete-time versions of $\mathbf{A}, \mathbf{B}, \mathbf{C}, \mathbf{G}$ respectively. Equation 2.16 is hereby derived by imposing a zero-order hold assumption on the input vector, i.e., by assuming a constant intersample behavior for the input. While matrices $\mathbf{A}$ and $\mathbf{B}$, which describe the transition model, are discretized following this logic, matrices $\mathbf{C}$ and $\mathbf{G}$ do not require discretization as they already model discrete observations, i.e., time derivation is not involved in the output equation. In this dissertation, the following exponential-time discretization scheme [127] is adopted according to the zero-order hold assumption:

$$\begin{aligned} \mathbf{A}_d &= e^{\mathbf{A}\Delta t} \\ \mathbf{B}_d &= \mathbf{A}_d^{-1}[\mathbf{A} - \mathbf{I}]\mathbf{B}. \end{aligned} \tag{2.17}$$

2.2 Bayesian dynamic modeling for data assimilation

Bayesian modeling provides mathematical tools, e.g. probability distributions and rules of probability calculus, that can be used for modeling systems under stochastic assumptions, i.e., by taking into account the uncertainties and randomness. In this context, a BDM can be defined as a special case of SSM where the evolution of states over time is assumed to follow a stochastic process with Gaussian errors modeling uncertainties on both the transition and observation equations:

$$\begin{cases} \mathbf{x}_k = \mathbf{A}_d \mathbf{x}_{k-1} + \mathbf{B}_d \mathbf{u}_{k-1} + \mathbf{w}_{k-1} \\ \mathbf{y}_k = \mathbf{C}\mathbf{x}_k + \mathbf{G}\mathbf{u}_k + \mathbf{v}_k. \end{cases} \tag{2.18}$$

In Eq. 2.18, the state vector is described by a Gaussian distribution with mean $\hat{\mathbf{x}}_k \in \mathbb{R}^{2n_r}$ and covariance matrix $\mathbf{P}_k \in \mathbb{R}^{2n_r \times 2n_r}$. Stationary zero-mean white noises $\mathbf{w}$ and $\mathbf{v}$ have been introduced to respectively take into account model uncertainties and measurement noise. The whiteness assumption for $\mathbf{w}$ (process noise) and $\mathbf{v}$ (measurement noise) excludes the presence of systematic uncertainties affecting the state vector, i.e., the model, and the measurements, respectively. The covariance matrices associated to $\mathbf{v}$ and $\mathbf{w}$ are denoted as $\mathbf{R} \in \mathbb{R}^{n_o \times n_o}$, $\mathbf{Q} \in \mathbb{R}^{2n_r \times 2n_r}$ and $\mathbf{S} \in \mathbb{R}^{2n_r \times n_o}$, such that:

$$\mathbb{E}\left\{ \begin{pmatrix} \mathbf{w}_k \\ \mathbf{v}_k \end{pmatrix} \quad \begin{pmatrix} {\mathbf{w}_l}^T & {\mathbf{v}_l}^T \end{pmatrix} \right\} = \begin{bmatrix} \mathbf{Q} & \mathbf{S} \\ \mathbf{S}^T & \mathbf{R} \end{bmatrix} \delta_{kl} \tag{2.19}$$

where δ_{kl} is the Kronecker delta function and the autocovariance terms $\mathbf{Q}$ and $\mathbf{R}$ represent the covariance matrices of $\mathbf{w}$ and $\mathbf{v}$, respectively. $\mathbf{S}$ depicts instead the mutual correlation of these processes. For simplicity, the assumption of mutually uncorrelated process and measurement noise, i.e., $\mathbf{S} = \mathbf{0}$, is adopted in this dissertation. Additionally, in exploiting BDMs for the case studies presented in this dissertation, further simplification will be introduced via the assumption of uncorrelated process noise sources, i.e. diagonal $\mathbf{Q}$, and uncorrelated measurement noise sources, i.e., diagonal $\mathbf{R}$.

Within the context of dynamic problems expressed through BDMs, the objective lies in the estimation of the state vector from the transition model and the observed outputs of the system modeled by the measurement equation. This process, often referred as data assimilation, is typically performed via Bayesian estimators, which allow combination of physics-based paradigms and response measurements to generate predictions of the posterior Probability Density Function (PDF) of the model conditioned on the available observations. The posterior PDF can then be used to derive the optimal state estimate according to the selected QoI. The first two statistical moments, i.e., the mean and the covariance, are usually adopted within the structural dynamics framework:

$$\begin{aligned} &\text{Mean:} \quad \hat{\mathbf{x}} = \mathbb{E}\left[\mathbf{x}\right] \\ &\text{Covariance:} \quad \mathbf{P} = \mathbb{E}\left[\left(\mathbf{x} - \hat{\mathbf{x}}\right) \left(\mathbf{x} - \hat{\mathbf{x}}\right)^T \right]. \end{aligned} \tag{2.20}$$

2.2.1 Bayesian inference

Bayesian inference constitutes the underlying process for the Bayesian tools adopted within this dissertation for data assimilation, i.e., combination of a physics-based model with observations to estimate the states of the system as it evolves in time. Indeed, Bayesian inference consists in updating prior hypotheses about models as more information becomes available from data. It is worth noting that the Bayesian approach to statistics differs from the conventional frequentist approach for the assumption of past knowledge encoded in the prior. Indeed, while the frequentist methods formulate predictions only relying on data from the current experiment and do not require formulation of a prior, Bayesian approaches employ hypotheses and make use of their probabilities in conjunction with the probability of the observed data. The key tool for Bayesian inference is Bayes' rule:

$$\text{posterior probability} = \frac{\text{likelihood x prior probability}}{\text{marginal likelihood}} \tag{2.21}$$

which can be expressed analytically as:

$$p(\boldsymbol{\theta}|\mathbf{y}) = \frac{p(\mathbf{y}|\boldsymbol{\theta})p(\boldsymbol{\theta})}{p(\mathbf{y})} \tag{2.22}$$

where the marginal likelihood $p(\mathbf{y})$ is defined as:

$$p\left(\mathbf{y}\right) = \int p(\mathbf{y}|\boldsymbol{\theta})p(\boldsymbol{\theta})d\boldsymbol{\theta} \tag{2.23}$$

and acts as a normalizing constant. Hence, according to Bayes' rule, the posterior distribution of a model is proportional to the product of the model prior belief $p\left(\boldsymbol{\theta}\right)$ and the likelihood of the observed data given the model $p(\mathbf{y}|\boldsymbol{\theta})$. Bayesian inference can be performed alternatively via a batch or a recursive solution, with the same objective of inferring the model posterior distribution from a prior and observed data. However, while for the batch approach the entire time history of the observed data is used to formulate the joint posterior distribution of all states, the recursive method computes the posterior distribution at each time instant by adopting the posterior distribution of the previous time step as a prior. The batch and recursive solutions for Bayesian inference are respectively reported in Algs. 1 and 2.

Algorithm 1 Bayesian inference: batch solution

1: Encode prior information about the model parameters in $p(\boldsymbol{\theta})$
2: Determine the measurement model likelihood $p(\mathbf{y}_{1:n}|\boldsymbol{\theta})$ given $\boldsymbol{\theta}$ by assuming conditionally independent measurements, i.e., $p(\mathbf{y}_{1:n}|\boldsymbol{\theta})$ is the product of individual measurements distributions:

$$p(\mathbf{y}_{1:n}|\boldsymbol{\theta}) = \prod_{k=1}^{n} p(\mathbf{y}_k|\boldsymbol{\theta})$$

3: Get the observations data set: $\mathcal{D} = \{(t_1, \mathbf{y}_1), \cdots, (t_n, \mathbf{y}_n)\}$
4: Applying Bayes' Rule, calculate the posterior distribution of the problem:

$$p(\boldsymbol{\theta}|\mathbf{y}_{1:n}) = \frac{1}{p(\mathbf{y}_{1:n})} p(\boldsymbol{\theta}) \prod_{k=1}^{n} p(\mathbf{y}_k|\boldsymbol{\theta}).$$

Algorithm 2 Bayesian inference: recursive solution

1: Define:

$$\text{Prior Distribution} = \begin{cases} p(\boldsymbol{\theta}), & \text{if } k = 1 \\ p(\boldsymbol{\theta}|\mathbf{y}_{k-1}) & \text{if } 2 \leq k \leq n \end{cases}$$

2: Compute the likelihood function of the measurement model at each time step: $p(\mathbf{y}_k|\boldsymbol{\theta}), \quad k = 1, \cdots, n$
3: Calculate the posterior distribution recursively by relying on the information from the previous time step:

$$\begin{aligned} p\left(\boldsymbol{\theta} \mid \mathbf{y}_1\right) &= \frac{1}{p(\mathbf{y}_1)} p\left(\mathbf{y}_1 \mid \boldsymbol{\theta}\right) p(\boldsymbol{\theta}) \\ p\left(\boldsymbol{\theta} \mid \mathbf{y}_{1:2}\right) &= \frac{1}{p(\mathbf{y}_2)} p\left(\mathbf{y}_2 \mid \boldsymbol{\theta}\right) p\left(\boldsymbol{\theta} \mid \mathbf{y}_1\right) \\ p\left(\boldsymbol{\theta} \mid \mathbf{y}_{1:3}\right) &= \frac{1}{p(\mathbf{y}_3)} p\left(\mathbf{y}_3 \mid \boldsymbol{\theta}\right) p\left(\boldsymbol{\theta} \mid \mathbf{y}_{1:2}\right) \\ &\vdots \\ p\left(\boldsymbol{\theta} \mid \mathbf{y}_{1:n}\right) &= \frac{1}{p(\mathbf{y}_n)}) p\left(\mathbf{y}_n \mid \boldsymbol{\theta}\right) p\left(\boldsymbol{\theta} \mid \mathbf{y}_{1:n-1}\right). \end{aligned}$$

The main disadvantage of the batch solution is that the full posterior formulation has to be recomputed as soon as a new measurement is observed. This may result in a problem when the variables that are being estimated, vary dynamically. To the contrary, the recursive solution can be used for real-time estimation, where the estimated parameters are updated as new measurements are

obtained, thus allowing to track their variability with time. Additionally, the posterior distribution dimensionality is kept constant when the recursive solution is adopted, i.e., the computational complexity does not increase at each time step. Given these advantages, within this dissertation focus will be placed on tools that exploit Bayesian recursive inference for predicting the optimal state vector of BDMs at each time step. Within this logic, the formulation proposed in Alg. 2 can be tailored to instantaneous estimation of the BDM state vector $\mathbf{x}_{k|k}$ posterior PDF given the observations $\mathbf{y}_{1:k}$ up to the current time step k. More specifically, Bayes' rule can be used to condition the prior probability $p\left(\mathbf{x}_k|\mathbf{y}_{1:k-1}\right)$ on the current observations $\mathbf{y}_k$:

$$p\left(\mathbf{x}_k|\mathbf{y}_k\right) = p\left(\mathbf{x}_k|\mathbf{y}_k, \mathbf{y}_{1:k-1}\right) = \frac{p\left(\mathbf{y}_k|\mathbf{x}_k\right) p\left(\mathbf{x}_k|\mathbf{y}_{1:k-1}\right)}{p\left(\mathbf{y}_k|\mathbf{y}_{1:k-1}\right)} \tag{2.24}$$

where the prior probability $p\left(\mathbf{x}_k|\mathbf{y}_{1:k-1}\right)$ is derived by propagating the available PDF $p\left(\mathbf{x}_{k-1}|\mathbf{y}_{1:k-1}\right)$ through the Chapman-Kolmogorov equation, which governs transition probabilities by exploiting the Markov assumption on which BDMs rely:

$$p\left(\mathbf{x}_k|\mathbf{y}_{1:k-1}\right) = \int p\left(\mathbf{x}_k|\mathbf{x}_{k-1}\right) p\left(\mathbf{x}_{k-1}|\mathbf{y}_{1:k-1}\right) d\mathbf{x}_{k-1}. \tag{2.25}$$

In Eq. 2.25, the transitional density $p\left(\mathbf{x}_k|\mathbf{x}_{k-1}\right)$ defines the state evolution and it is therefore controlled, for BDMs, by the transition model in Eq. 2.18. The likelihood function in Eq. 2.24 is instead governed by the measurement model in Eq. 2.18. When dealing with linear BDMs, Eqs. 2.25 and 2.24 can be expressed in an analytic form, leading to the time prediction and measurement update steps of the well-known KF algorithm.

2.2.2 Kalman filter

The KF was introduced by R. Kalman in 1960 [128] and it is commonly adopted nowadays for estimation of a wide range of processes when a linear dynamic model and a limited number of observations are available. In this dissertation, the KF forms the basis for all the Bayesian filtering schemes adopted for input-state estimation of the analyzed case studies. As explained previously in this section, the QoI for the KF predictions in a structural dynamics context are the states of the BDM under study, which can be derived from the discrete-time state-space representation of the EoM in Eq. 2.1.
The application of the KF algorithm for state estimation of a BDM follows three main steps:

- **Initialization**:
  The initial values for the state mean $\hat{\mathbf{x}}_{0|0}$ and the state covariance $\mathbf{P}_{0|0}$ need to be defined using previous knowledge about the system dynamic behavior. Additionally, the time-invariant process and measurement noise covariance matrices $\mathbf{Q}$ and $\mathbf{R}$ must be selected. These values substantially influence the prediction accuracy achieved via the KF. Therefore, a detailed investigation of their role in the estimation will be presented in Chapter 4.

- **Prediction**:
  The initial system state $\hat{\mathbf{x}}_{0|0}$ is propagated through the transition model of Eq. 2.18 to obtain the state prediction at $k = 1$. By exploiting the Gaussian assumption for $\hat{\mathbf{x}}$ and $\mathbf{w}$ and time-invariance for $\mathbf{A}_d$ and $\mathbf{B}_d$, the linear transformation of Gaussian distributions can be applied to obtain the predictions of both the state mean $\hat{\mathbf{x}}_{1|0}$ and covariance $\mathbf{P}_{1|0}$:

  $$\begin{aligned} \hat{\mathbf{x}}_{1|0} &= \mathbf{A}_d \hat{\mathbf{x}}_{0|0} + \mathbf{B}_d \mathbf{u}_0 \\ \mathbf{P}_{1|0} &= \mathbf{A}_d \hat{\mathbf{x}}_{0|0} \mathbf{A}_d^T + \mathbf{Q}. \end{aligned} \tag{2.26}$$

  The state mean and covariance predicted in this step correspond to the prior probability in Eq. 2.24.

- **Update**:
  The prior probability obtained at the previous step needs to be updated with the current

available measurements to obtain the posterior distribution via Eq. 2.24. To implement so, a first transformation of Eq. 2.26 from the state space to the observation space needs to be performed:

$$\begin{aligned} \hat{\mathbf{y}}_{1|0} &= \mathbf{C}\hat{\mathbf{x}}_{1|0} + \mathbf{G}\mathbf{u}_1 \\ \mathbb{E}\left[\left(\mathbf{y}_{1|0} - \hat{\mathbf{y}}_{1|0}\right)\left(\mathbf{y}_{1|0} - \hat{\mathbf{y}}_{1|0}\right)^T\right] &= \mathbf{C}\mathbf{P}_{1|0}\mathbf{C}^T. \end{aligned} \tag{2.27}$$

The prior probability in the observations space in Eq. 2.27 is then employed within Bayes' rule to obtain the posterior probability, i.e., the posterior mean and covariance in the observations space:

$$\begin{aligned} \mathbf{C}\hat{\mathbf{x}}_{1|1} + \mathbf{G}\mathbf{u}_1 &= \mathbf{C}\hat{\mathbf{x}}_{1|0} + \mathbf{G}\mathbf{u}_1 + \mathbf{K}(\mathbf{y}_1 - \mathbf{C}\hat{\mathbf{x}}_{1|0} - \mathbf{G}\mathbf{u}_1) \\ \mathbf{C}\mathbf{P}_{1|1}\mathbf{C}^T &= \mathbf{C}\hat{\mathbf{x}}_{1|0}\mathbf{C}^T - \mathbf{K}\mathbf{C}\mathbf{P}_{1|0}\mathbf{C}^T \end{aligned} \tag{2.28}$$

where the adopted likelihood comes from the measurements at $k = 1$: $\mathcal{N}(\mathbf{y}_1, \mathbf{R})$ and $\mathbf{K}$ has been defined as $\mathbf{K} = \mathbf{C}\mathbf{P}_{1|0}\mathbf{C}^T(\mathbf{C}\mathbf{P}_{1|0}\mathbf{C}^T + \mathbf{R})^{-1}$. By introducing the Kalman gain $\mathbf{Kg}$ such that $\mathbf{K} = \mathbf{H}\mathbf{K}\mathbf{g}$, subtracting the term $\mathbf{G}\mathbf{u}_1$ and rearranging the resulting equations, the posterior mean and covariance in the observations space can be derived:

$$\begin{aligned} \mathbf{K}\mathbf{g} &= \mathbf{P}_{1|0}\mathbf{C}^T(\mathbf{C}\mathbf{P}_{1|0}\mathbf{C}^T + \mathbf{R})^{-1} \\ \hat{\mathbf{x}}_{1|1} &= \hat{\mathbf{x}}_{1|0} + \mathbf{K}\mathbf{g}(\mathbf{y}_1 - \mathbf{C}\hat{\mathbf{x}}_{1|0} - \mathbf{G}\mathbf{u}_1) \\ \mathbf{P}_{1|1} &= \mathbf{P}_{1|0} - \mathbf{C}\mathbf{K}\mathbf{g}\mathbf{P}_{1|0}. \end{aligned} \tag{2.29}$$

Equation 2.29 builds the update step of the KF algorithm. The resulting posterior mean $\hat{\mathbf{x}}_{1|1}$ and covariance $\mathbf{P}_{1|1}$ are then employed as prior estimates for predictions at $k = 2$.

The prediction and update steps are recursively computed for $k = 1, \cdots, n$ where n is the number of available data points. The resulting KF algorithm is reported in Alg. 3 and presented in Fig. 2.1 through a block diagram scheme. Here, the time prediction is shown to propagate the state vector and the error covariance matrix from $k-1$ to k through the system transition model, which can be retrieved from the structure FE model. The resulting prediction is then corrected by the measurement update step, which uses information given by the available observations at time step k to build the state vector posterior estimate and the corresponding posterior estimate covariance matrix. Once the estimated state vector has been obtained, it can be used for predicting the current vector $\hat{\mathbf{y}}_k^e$ of the n_e unmeasured responses using the following formula:

$$\hat{\mathbf{y}}_{k|k}^e = \mathbf{C}_e\hat{\mathbf{x}}_{k|k} + \mathbf{G}_e\mathbf{u}_k \tag{2.30}$$

where $\mathbf{C}_e$ and $\mathbf{G}_e$ are respectively the output and feed-forward matrix computed at the DOFs where the response has to be estimated.

Algorithm 3 KF algorithm

for $k = 1, 2, ..., n$ **do**
  (a) Kalman prediction:
  $\hat{\mathbf{x}}_{k|k-1} = \mathbf{A}_d\hat{\mathbf{x}}_{k-1|k-1} + \mathbf{B}_d\mathbf{u}_{k-1}$
  $\mathbf{P}_{k|k-1} = \mathbf{A}_d\mathbf{P}_{k-1|k-1}\mathbf{A}_d^T + \mathbf{Q}$
  (b) Kalman update:
  $\mathbf{In}_k = \mathbf{y}_k - \mathbf{C}\hat{\mathbf{x}}_{k|k-1} - \mathbf{G}\mathbf{u}_k$
  $\mathbf{S}_k = \mathbf{C}\mathbf{P}_{k|k-1}\mathbf{C}^T$
  $\mathbf{K}\mathbf{g}_k = \mathbf{P}_{k|k-1}\mathbf{C}^T\mathbf{S}_k^{-1}$
  $\hat{\mathbf{x}}_{k|k} = \hat{\mathbf{x}}_{k|k-1} + \mathbf{K}\mathbf{g}_k\mathbf{In}_k$
  $\mathbf{P}_{k|k} = \mathbf{P}_{k|k-1} - \mathbf{K}\mathbf{g}_k\mathbf{S}_k\mathbf{K}\mathbf{g}_k^T$
end for

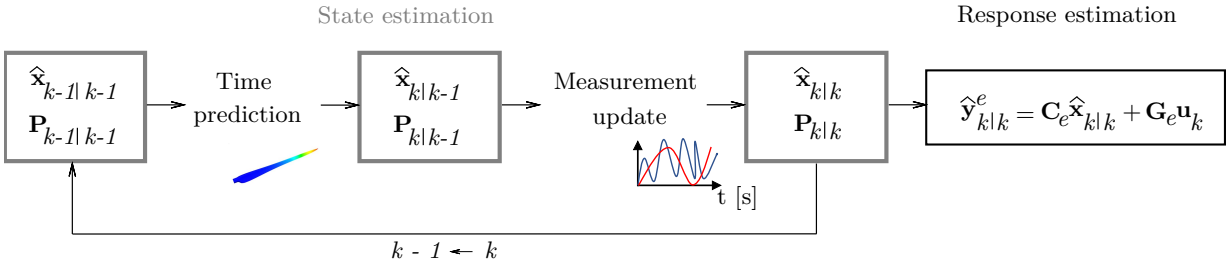

Figure 2.1: KF algorithm scheme

2.2.3 *Kalman smoother*

The KF is an analytical tool for computing the posterior PDF of the state of a BDM at time k by conditioning its prior probability to available data up to time k. To the contrary, the smoothing problem deals with the posterior PDF estimation using future data, i.e., conditioning to data up to time $n > k$. Specifically, the Kalman Smoother (KS) or Rauch-Tung-Striebel (RTS) smoother aims at sequentially calculating $\hat{\mathbf{x}}_{k|n}$ and $\mathbf{P}_{k|n}$ for $k = n, n-1, \cdots, 1$ in reverse order. To do so, the algorithm foresees a forward-backward pass. In the forward pass, a KF computes $\hat{\mathbf{x}}_{k|k}$ and $\mathbf{P}_{k|k}$ and propagates them through the BDM transition model yielding $\hat{\mathbf{x}}_{k+1|k}$ and $\mathbf{P}_{k+1|k}$. The prediction is then "smoothed" in the backward pass using data up to $n > k$ to get $\hat{\mathbf{x}}_{k|n}$ and $\mathbf{P}_{k|n}$ from:

$$p(\mathbf{x}_k|\mathbf{y}_{1:n}) \propto p(\mathbf{x}_k|\mathbf{y}_{1:k})p(\mathbf{y}_{k+1:n}|\mathbf{x}_k) \tag{2.31}$$

where $p(\mathbf{x}_k|\mathbf{y}_{1:k})$ can be obtained by Kalman filtering and $p(\mathbf{y}_{k+1:n}|\mathbf{x}_k)$ can be computed by conditioning on $p(\mathbf{x}_{k+1})$:

$$\begin{aligned} p(\mathbf{y}_{k+1:n}|\mathbf{x}_k) &= \int p(\mathbf{y}_{k+1:n}|\mathbf{x}_k|\mathbf{x}_{k+1})p(\mathbf{x}_{k+1}|\mathbf{x}_k)d\mathbf{x}_{k+1} \\ &= \int p(\mathbf{y}_{k+1}|\mathbf{x}_{k+1})p(\mathbf{y}_{k+2:n}|\mathbf{x}_{k+1})p(\mathbf{x}_{k+1}|\mathbf{x}_k)d\mathbf{x}_{k+1}. \end{aligned} \tag{2.32}$$

The second equation in Eq. 2.32 can be derived from the first by exploiting the sum and product rules and the conditional independence relations of $p(\mathbf{y}_k)$ from $p(\mathbf{y}_{1:k-1}|\mathbf{x}_{k-1})$ and $p(\mathbf{x}_{1:k-1}|\mathbf{x}_k)$. The first term is obtained from the sensor model, the second one is computed recursively backwards in time and the third one follows from the transition model. As reported for the KF in Subsection 2.2.2, Eqs. 2.31 and 2.32 can be tailored to the BDM in Eq. 2.18 to find the linear analytic equations of the RTS smoother presented in Alg. 4, where $\hat{\mathbf{x}}_{k|k}$ is the KF estimate at time step k.

Algorithm 4 RTS smoother algorithm

1: **for** $k = n-1, n-2, ..., 1$ **do**
2: (a) RTS prediction:
3: $\hat{\mathbf{x}}_{k+1|k} = \mathbf{A}_d\hat{\mathbf{x}}_{k|k} + \mathbf{B}_d\mathbf{u}_k$
4: $\mathbf{P}_{k+1|k} = \mathbf{A}_d\mathbf{P}_{k|k}\mathbf{A}_d^T + \mathbf{Q}$
5: (b) RTS update:
6: $\mathbf{Rg}_k = \mathbf{P}_{k|k}\mathbf{A}_d^T\mathbf{P}^{-1}_{k+1|k}$
7: $\hat{\mathbf{x}}_{k|n} = \hat{\mathbf{x}}_{k|k} + \mathbf{Rg}_k\left(\hat{\mathbf{x}}_{k+1|n} - \hat{\mathbf{x}}_{k+1|k}\right)$
8: $\mathbf{P}_{k|n} = \mathbf{P}_{k|k} - \mathbf{Rg}_k\left(\mathbf{P}_{k+1|n} - \mathbf{P}_{k+1|k}\right)\mathbf{Rg}_k^T$
9: **end for**

The RTS algorithm can be interpreted as improving the KF estimate of the state using the additional data observed at time steps $k+1, \cdots, n$. A block diagram scheme of the RTS algorithm is presented in Fig. 2.2.

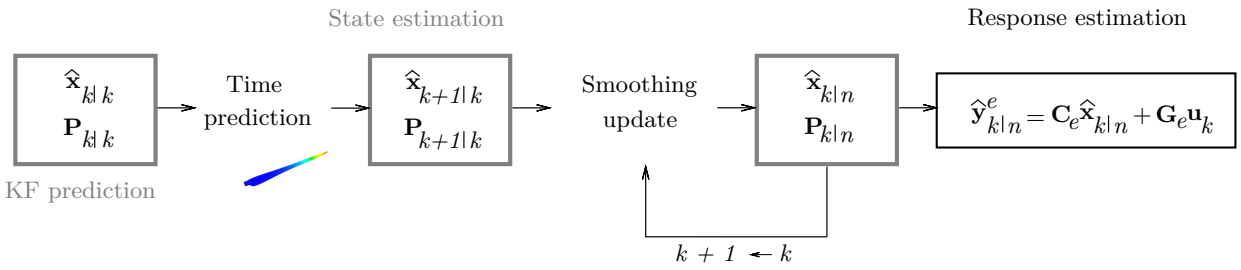

Figure 2.2: RTS smoother algorithm

2.3 Data-driven modeling

In opposition to the methods proposed in Section 2.1, which are based on providing models inspired by the underlying physical knowledge of the system, this section introduces techniques designed to generate models via data-driven paradigms. These methods are widely adopted to gain insights into the overall input-output process behavior constructing the so-called black-box model, i.e., a model which does not rely on assumptions derived from complex physics formulation but exclusively on experimental observations. Data-driven approaches are often referred as ML methods, which stands for the machine ability to learn from data without being explicitly programmed. ML can be classified into four main categories:

- *Supervised learning*:
  Given labeled training data sampled independently, the algorithm learns about the latent data input-output relationships.
- *Semi-supervised learning*:
  Similar to supervised learning but the latent process is determined exploiting both labeled and unlabeled data.
- *Unsupervised learning*:
  The algorithm identifies relationships between data as hidden and abstract structures since training data is unlabeled.
- *Reinforcement learning*:
  The algorithm perceives and interpret its environment taking actions and learning via trial and error. In doing so, favorable outputs are "reinforced" and non-favorable outputs are "punished". The adopted observed data is dependent on the played actions.

This section formulates the necessary basic knowledge regarding supervised learning to link with the content of Chapter 5, where these concepts will be exploited for providing alternative schemes to model unknown inputs in the context of Kalman-based input-state estimation in structural dynamics.

2.3.1 Regression: from weight space to function space

Linear regression is the simplest supervised learning problem, where a linear relationship is assumed between outputs and inputs of the underlying function. However, linear regression forms the basis for more general types of regression problems. According to the Bayesian treatment of linear regression, given the input vector $\mathbf{x}$, the goal is to identify a function $f(\mathbf{x})$ such that:

$$f(\mathbf{x}) = \mathbf{x}^T\mathbf{w}, \quad y = f(\mathbf{x}) + \varepsilon \tag{2.33}$$

where y contains the observed outputs, which differ from the latent function $f(\mathbf{x})$ by a zero-mean Gaussian noise with variance σ_n^2: $\varepsilon = \mathcal{N}(0, \sigma_n^2)$. The $\mathbf{w}$ vector contains the weights of the linear model, for which a zero mean Gaussian prior with covariance Σ_p is placed: $\mathbf{w} = \mathcal{N}(0, \Sigma_p)$. The

inference purpose is to identify the posterior distribution over the weights given a training data set of observations $D = \{\{\tilde{x_1}, \tilde{y_1}\}, \{\tilde{x_2}, \tilde{y_2}\}, ..., \{\tilde{x_n}, \tilde{y_n}\}\}$. This operation can be put in place by writing Bayes' rule (Eq. 2.21) for the weights:

$$p(\mathbf{w}|\mathbf{y}, \mathbf{X}) = \frac{p(\mathbf{y}|\mathbf{X}, \mathbf{w})p(\mathbf{w})}{p(\mathbf{y}|\mathbf{X})} \tag{2.34}$$

where the likelihood is expressed as the probability density of the observations given the weights. The likelihood can be factored over the data if we assume that data is conditionally independent given the underlying model:

$$\begin{aligned} p(\mathbf{y}|\mathbf{X}, \mathbf{w}) = \prod_{i=1}^{n} p(y_i|\mathbf{x}_i, \mathbf{w}) &= \prod_{i=1}^{n} \frac{1}{\sqrt{2\pi}\sigma_n} exp\left(-\frac{(y_i - \mathbf{x}_i^T\mathbf{w})^2}{2\sigma_n^2}\right) \\ &= \frac{1}{(2\pi\sigma_n^2)^{n/2}} exp\left(-\frac{1}{2\sigma_n^2}|\mathbf{y} - \mathbf{X}^T\mathbf{w}|^2\right). \end{aligned} \tag{2.35}$$

In Eq. 2.35, each term within the product has been assumed to be Gaussian $\mathcal{N}(\mathbf{x}_i^T\mathbf{w}, \sigma_n^2)$. As a result, the likelihood has as well a Gaussian distribution $\mathcal{N}(\mathbf{X}^T\mathbf{w}, \sigma_n^2 I)$. The marginal likelihood in Eq. 2.34 expresses the observations likelihood independently from the weights, i.e., "marginalizing" over the latent function. It is indeed computed as the integral over the weights of the likelihood and prior product:

$$p(\mathbf{y}|\mathbf{X}) = \int p(\mathbf{y}|\mathbf{X}, \mathbf{w})p(\mathbf{w})d\mathbf{w}. \tag{2.36}$$

By plugging Eq. 2.35 into Eq. 2.34 and expressing the Gaussian analytical form for the prior, the posterior over the weights is obtained:

$$\begin{aligned} p(\mathbf{w}|\mathbf{X}, \mathbf{y}) &\propto exp\left(-\frac{1}{2\sigma_n^2}|\mathbf{y} - \mathbf{X}^T\mathbf{w}|^2\right) exp\left(-\frac{1}{2}\mathbf{w}^T\Sigma_p^{-1}\mathbf{w}\right) \\ &\propto exp\left(-\frac{1}{2}\left(\mathbf{w} - \bar{\mathbf{w}}\right)^T\left(\frac{1}{\sigma_n^2}\mathbf{X}\mathbf{X}^T + \Sigma_p^{-1}\right)\left(\mathbf{w} - \bar{\mathbf{w}}\right)\right), \end{aligned} \tag{2.37}$$

where $\bar{\mathbf{w}} = \sigma_n^{-2}(\sigma_n^{-2}\mathbf{X}\mathbf{X}^T + \Sigma_p^{-1})^{-1}\mathbf{X}\mathbf{y}$. From Eq. 2.37, it can be concluded that the posterior distribution is a Gaussian with mean $\bar{\mathbf{w}}$ and covariance $\bar{\Sigma} = \sigma_n^{-2}\mathbf{X}\mathbf{X}^T + \Sigma_p^{-1}$. The posterior mean $\bar{\mathbf{w}}$ corresponds to the mode of the distribution, also called Maximum a Posteriori (MAP) estimate, and can be also obtained as the solution of ridge regression, i.e., linear regression optimization problem featuring a closed deterministic form solution (in a non-Bayesian setting). In order to make predictions about the latent linear function at a test point x_*, the probability distribution of f_* can be computed by averaging out all the possible models, i.e., by integrating over all the possible weight values and weighting their contributions via their posterior probability:

$$p(f_*|\mathbf{x}_*, \mathbf{X}, \mathbf{y}) = \int p(f_*|\mathbf{x}_*, \mathbf{w})p(\mathbf{w}|\mathbf{X}, \mathbf{y})d\mathbf{w} \quad = \int \mathbf{x}_*^T\mathbf{w}p(\mathbf{w}|\mathbf{X}, \mathbf{y})d\mathbf{w}, \tag{2.38}$$

where Eq. 2.33 evaluated at $\mathbf{x}_*$ has been substituted. The resulting prediction distribution is a Gaussian with mean $\mathbf{x}_*\bar{\mathbf{w}}$ and covariance $\mathbf{x}_*^T\bar{\Sigma}^{-1}\mathbf{x}_*$. However, this simple model is often not suitable for real-life problems, for which often outputs cannot be computed as a linear combination of inputs. A method to add flexibility to regression consists in projecting the D-dimensional inputs $\mathbf{x}$ into an N dimensional space using basis functions $\boldsymbol{\phi}(\mathbf{x})$ and apply the linear transformation on this space rather than on the inputs. The problem, still linear in the weights, is reformulated as:

$$f(\mathbf{x}) = \boldsymbol{\phi}(\mathbf{x})^T\mathbf{w}, \tag{2.39}$$

where $\mathbf{w}$ has length N. The resulting predictive distribution is:

$$p(f_*|\mathbf{x}_*, \mathbf{X}, \mathbf{y}) \sim \mathcal{N}\left(\frac{1}{\sigma_n^2}\boldsymbol{\phi}(\mathbf{x}_*)^T\tilde{\Sigma}^{-1}\boldsymbol{\Phi}\mathbf{y}, \boldsymbol{\phi}(\mathbf{x}_*)^T\tilde{\Sigma}^{-1}\boldsymbol{\phi}(\mathbf{x}_*)\right), \tag{2.40}$$

where $\mathbf{\Phi} = \mathbf{\Phi}(\mathbf{X})$ groups the columns $\boldsymbol{\phi}(\mathbf{x})$ for all the training set cases and $\tilde{\Sigma} = \sigma_n^{-2}\mathbf{\Phi}\mathbf{\Phi}^T + \Sigma_p^{-1}$. Equation 2.40 involves the inversion of the $\tilde{\Sigma} \in N \times N$ for computing predictions. In order to reduce the computational complexity of this operation, Eq. 2.40 can be manipulated and rewritten as:

$$p(f_*|\mathbf{x}_*, \mathbf{X}, \mathbf{y}) \sim \mathcal{N}(\boldsymbol{\phi}_*^T\Sigma_p\mathbf{\Phi}(K + \sigma_n^2 I)^{-1}\mathbf{y}, \boldsymbol{\phi}_*^T\Sigma_p\boldsymbol{\phi}_* - \boldsymbol{\phi}_*^T\Sigma_p\mathbf{\Phi}(K + \sigma_n^2 I)^{-1}\mathbf{\Phi}^T\Sigma_p\boldsymbol{\phi}_*) \tag{2.41}$$

where $\boldsymbol{\phi}_* = \boldsymbol{\phi}(\mathbf{x}_*)$ and $K = \mathbf{\Phi}^T\Sigma_p\mathbf{\Phi}$. Equation 2.41 now only involves inversion of matrices of size $n \times n$, where n is the number of data points, normally lower than N. Additionally, the feature space appears in Eq. 2.41 only via inner products and, if Σ_p is positive definite, the product $\boldsymbol{\psi}(\mathbf{x}) = \Sigma_p^{1/2}\boldsymbol{\phi}(\mathbf{x})$ can be introduced in order to define the so-called kernel or covariance function $k(\mathbf{x}, \mathbf{x}') = \boldsymbol{\phi}(\mathbf{x})^T\Sigma_p\boldsymbol{\phi}(\mathbf{x}') = \boldsymbol{\psi}(\mathbf{x}) \cdot \boldsymbol{\psi}(\mathbf{x}')$. Replacing inner products in input space with kernels for problems where data only appear through inner products allows to more efficiently compute solutions. This is the so-called kernel trick.

When inference is directly performed in the function space instead of the weight space, distributions over functions must be taken into consideration to generalize the previously presented concepts to infinitely large domains. Stochastic processes are widely adopted to model functions distributions for randomly varying phenomena in many areas, such as finance, chemistry, biology, physics, control theory, telecommunications and signal processing. A stochastic process is a collection of random variables $Y = Y_x : x \in P$ with values in a common set S, i.e., the state space, and indexed by a set P, i.e., the parameter space, usually representing time (either continuous or discrete). Stochastic processes thus comprise a generalization of random vectors to the function space and can be as such defined by statistical moments:

$$\mu_Y(x) = \mathbb{E}[\ Y(x)]\ ; \quad K_Y(x_p, x_q) = \mathbb{E}[\ (Y(x_p) - \mu_Y(x_p))(Y(x_q) - \mu_Y(x_q))] \tag{2.42}$$

where $\mu_Y(x)$ is the mean function and $K_Y(x)$ is the covariance function of the stochastic process. The latter specifies the covariance between pairs of random variables. Due to its random nature, a stochastic process may have many outcomes. A unique outcome of a stochastic process is defined as sample function or realization. A stochastic process can be also seen as a probability distribution over a space of sample functions.

Classification of stochastic processes can be based on several criteria, e.g. its parameter space, its state space or the type of dependence among the random variables. Common known stochastic processes are RWs, Markov processes, Wiener processes, Bernoulli processes, Gaussian and Student-t processes. This section will present the last two classes, which will see their application in this work in a LFM framework for joint input-state estimation in structural dynamics.

2.3.1.1 Gaussian Process

A stochastic process $Y(x)$ is Gaussian if for each subset of parameters $x_1, ..., x_n$ the random vector $(Y(x_1), \ldots, Y(x_n))^T$ is Gaussian. Therefore, a GP is a stochastic process for which any finite number of variables have a joint Gaussian distribution [65]. A GP can be defined by its mean function $\mu(\mathbf{x}) = \mathbb{E}[\ f(\mathbf{x})]$ and covariance function $k(\mathbf{x}, \mathbf{x}') = \mathbb{E}[\ (f(\mathbf{x}) - \mu(\mathbf{x}))(f(\mathbf{x}') - \mu(\mathbf{x}'))]$ as:

$$f(\mathbf{x}) \sim \mathcal{GP}(\mu(\mathbf{x}), k(\mathbf{x}, \mathbf{x}')). \tag{2.43}$$

It is worth noting that the regression problem in the weight space reported in Eq. 2.39 is a simple example of GP in the function space for which the kernel $k(\mathbf{x}, \mathbf{x}') = \boldsymbol{\phi}(\mathbf{x})^T\Sigma_p\boldsymbol{\phi}(\mathbf{x}')$ is set as covariance function.

A defining property of GPs is the so-called consistency or marginalization property. This property implies that examining the function at a finite subset of points would give the same results as if the infinite number of other points would have been taken into account. Since in practice only finite dimensional data can be adopted, this property allows the use of infinite dimension objects such as the GPs for real-life applications. For GPs, finite marginals are multivariate Gaussian distributions with covariance $k(x_i, x_j) = \mathbb{E}[\ (f(x_i) - \mu(x_i))(f(x_j) - \mu(x_j))]$. The latter is shaped such that the covariance decreases as x_i and x_j become further apart, i.e., the further the two test points are,

the lower will be the correlation. For simplification, Fig. 2.3 shows a representation of a univariate marginal distribution drawn from a certain GP at a given test point x_*.

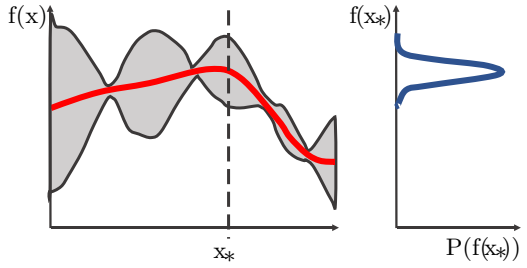

Figure 2.3: GP posterior (left). The gray area represents the mean (red solid curve) plus and minus two times the standard deviation for each input value. Univariate Gaussian marginal distribution at test point x_* (right).

As visible in Fig. 2.3, the resulting marginal distribution is a univariate Gaussian distribution with mean and variance obtained evaluating the GP mean $\mu(x_*)$ and covariance function $k(x_*, x_*)$ at x_*:

$$P(f(x_*)) = \mathcal{N}(f(x_*); \mu(x_*); k(x_*, x_*)). \tag{2.44}$$

A common convention consists in adopting GPs with zero prior mean, i.e., $\mu = 0$:

$$f(\mathbf{x}) \sim \mathcal{GP}(\mathbf{0}, k(\mathbf{x}, \mathbf{x}')). \tag{2.45}$$

This assumption allows to simplify the notation without loss of generality since a realization of a GP with a non-zero mean function $\mu(x)$ can be retrieved from a function drawn from a zero-mean GP with the same covariance by adding the mean function. Given a training data set of n observations $D = \{\{\tilde{x_1}, \tilde{y_1}\}, \{\tilde{x_2}, \tilde{y_2}\}, ..., \{\tilde{x_n}, \tilde{y_n}\}\}$ and a GP mean (conventionally 0) and covariance prior, GP regression consists in obtaining the latent function at unobserved test points. For GPs, the posterior, i.e., the distribution of the latent function at the unobserved locations given the n data points available in D, is a $(n+1)$-dimensional Gaussian distribution with mean and covariance of the following closed-form:

$$\begin{aligned} \hat{\boldsymbol{\mu}} &= \mathbf{K}_{\mathbf{x},\mathbf{x}} \left(\mathbf{K}_{\tilde{\mathbf{x}},\tilde{\mathbf{x}}} + \sigma_n^2 \mathbf{I} \right)^{-1} \tilde{\mathbf{y}}; \\ \hat{\mathbf{K}} &= \mathbf{K}_{\mathbf{x},\mathbf{x}} - \mathbf{K}_{\mathbf{x},\tilde{\mathbf{x}}} \left(\mathbf{K}_{\tilde{\mathbf{x}},\tilde{\mathbf{x}}} + \sigma_n^2 \mathbf{I} \right)^{-1} \mathbf{K}_{\tilde{\mathbf{x}},\mathbf{x}} \end{aligned} \tag{2.46}$$

where $\mathbf{K}_{\tilde{\mathbf{x}},\tilde{\mathbf{x}}}$ is the covariance matrix between the observations in D, $\mathbf{K}_{\mathbf{x},\mathbf{x}}$ is the covariance matrix between the unobserved test points and $\mathbf{K}_{\tilde{\mathbf{x}},\mathbf{x}}$ is the covariance matrix between the observations and the unobserved test points. Equation 2.46 is obtained by conditioning the joint Gaussian distribution on the observations in D. In Eq. 2.46, the posterior mean is obtained as a linear combination of the observations, which are weighted according to how much the data are relevant with respect to the test point. Within the correction term, an independent Gaussian noise ε with variance σ_n^2 has been added as in Eq. 2.33 to account for noisy measurements. The same correction term is used in the posterior covariance expression, where the prior covariance, i.e., the uncertainty, is reduced by a term which is proportional to the correlation between the available data points and the test point. The posterior computation features a computational cost that scales with $O(n^3)$ because of the term $\left(\mathbf{K}_{\tilde{\mathbf{x}},\tilde{\mathbf{x}}} + \sigma_n^2 \mathbf{I}\right)^{-1}$.

Realizations of a GP with mean and covariance expressed by Eq. 2.46 at a chosen number of test points are generated by applying the steps listed in Alg. 5. The results of a one-dimensional GP regression example are reported in Fig. 2.5 (left, GP prior) and Fig. 2.6 (left, GP posterior).

Following Eq. 2.36, the marginal likelihood for GPs can be written as:

$$p(\mathbf{y}|\mathbf{X}) = \int p(\mathbf{y}|\mathbf{f}, \mathbf{X}) p(\mathbf{f}|\mathbf{X}) d\mathbf{f} \tag{2.47}$$

where the likelihood is a factorized Gaussian $p(\mathbf{y}|\mathbf{f}, \mathbf{X}) \sim \mathcal{N}(\mathbf{f}, \sigma_n^2 \mathbf{I})$ and the prior is a Gaussian with zero mean and covariance matrix $\mathbf{K}$ obtained from the prior covariance function $k(\mathbf{x}, \mathbf{x}')$:

Algorithm 5 GP sampling

1: Compute Cholesky decomposition $\mathbf{L}$ of matrix $\hat{\mathbf{K}} = \mathbf{L}\mathbf{L}^T$
2: Generate $\mathbf{u} \sim \mathcal{N}(\mathbf{0}, \mathbf{I})$
3: Compute $\mathbf{f}_* = \hat{\boldsymbol{\mu}} + \mathbf{L}\mathbf{u}$, i.e., a Gaussian distribution with mean $\hat{\boldsymbol{\mu}}$ and covariance $\mathbf{L}\mathbb{E}[\mathbf{u}\mathbf{u}^T]\mathbf{L}^T = \mathbf{L}\mathbf{L}^T = \mathbf{K}$

$p(\mathbf{f}|\mathbf{X}) \sim \mathcal{N}(\mathbf{0}, \mathbf{K})$. Therefore, the marginal likelihood will also result in a Gaussian with the following analytical expression:

$$\mathcal{N}(\mathbf{0}, \mathbf{K} + \sigma_n^2\mathbf{I}) = \frac{1}{\sqrt{(2\pi)^n|\mathbf{K} + \sigma_n^2\mathbf{I}|}} exp(-\frac{1}{2}\mathbf{y}^T(\mathbf{K} + \sigma_n^2\mathbf{I})\mathbf{y}). \tag{2.48}$$

By evaluating the logarithm of Eq. 2.48, the following simplified result is achieved:

$$logp(\mathbf{y}|\mathbf{X}) = -\frac{n}{2}log2\pi - \frac{1}{2}log|\mathbf{K} + \sigma_n^2\mathbf{I}| - \frac{1}{2}\mathbf{y}^T(\mathbf{K} + \sigma_n^2\mathbf{I})^{-1}\mathbf{y}. \tag{2.49}$$

The first term in Eq. 2.49 is a normalization constant, while the second term is a complexity penalty which depends on the covariance function and the inputs only. The last term instead quantifies the goodness of fit, i.e, the alignment of $\mathbf{y}$ with the covariance matrix $\mathbf{K} + \sigma_n^2\mathbf{I}$.

Since this dissertation will treat signals evolution in time domain, it is convenient to introduce the definition of a one-dimensional GP defined over time:

$$f(t) \sim \mathcal{GP}(0, k(t, t')). \tag{2.50}$$

2.3.1.2 Student-t Process

A Student-t Process (STP) is a stochastic process with a marginal distribution described by a multivariate Student-t distribution:

$$f(\mathbf{x}) \sim \mathcal{STP}(\mu(\mathbf{x}), k(\mathbf{x}, \mathbf{x}'), \nu). \tag{2.51}$$

The probability density of a multivariate Student-t distribution with dimension d, i.e. $\mathbf{x} \in \mathbb{R}^d$, is:

$$\mathcal{T}(\mathbf{x}|\boldsymbol{\mu}, \mathbf{K}, \nu)(x) = \frac{\Gamma((\nu + d)/2)}{\Gamma(\nu/2)((\nu - 2)\pi)^{d/2}|\mathbf{K}|^{1/2}} \left(1 + \frac{1}{\nu - 2}(\mathbf{x} - \boldsymbol{\mu})^T\mathbf{K}^{-1}(\mathbf{x} - \boldsymbol{\mu})\right)^{-(\nu+d)/2}. \tag{2.52}$$

From Eq. 2.52, it can be concluded that for $\nu \to \infty$, a multivariate Gaussian distribution with mean $\boldsymbol{\mu}$ and covariance $\mathbf{K}$ is recovered. Hence, a Student-t distribution consists in a generalization of the Gaussian distribution with an additional parameter $\nu > 2$ describing the DOFs of the distribution. A simplified visual representation of this concept is proposed in Fig. 2.4, which reports a zero-mean uni-variate Student-t distribution at increasing ν and compares it to a zero-mean uni-variate Gaussian distribution. The reported comparison confirms that for $\nu \to \infty$, the Student-t distribution matches a Gaussian distribution with the same mean. Additionally, Fig. 2.4 also highlights that a Student-t distribution normally features heavy tails. The"tailedness" of a probability distribution is often measured via the so-called kurtosis, i.e., the fourth standardized moment of the distribution. The latter has the following expression for a uni-variate distribution:

$$Kurt[x] = \mathbb{E}\left[\left(\frac{x - \mu}{\sigma}\right)^4\right]. \tag{2.53}$$

For a Student-t distribution, the kurtosis is controlled by the ν parameter: higher kurtosis values are reached when ν is smaller, i.e., smaller values of ν give rise to heavier tails. STPs have been derived in [129] as a mixture of GPs by placing an inverse Wishart random variable as the scaling distribution. As a result, it has been demonstrated that STPs are the most general elliptic processes for which an analytical expression can be retrieved for the marginal and predictive distributions. This property is retained from GPs, together with the facilitated model selection via a kernel choice. However, STPs have been found to provide more flexibility thanks to the scale mixture connection

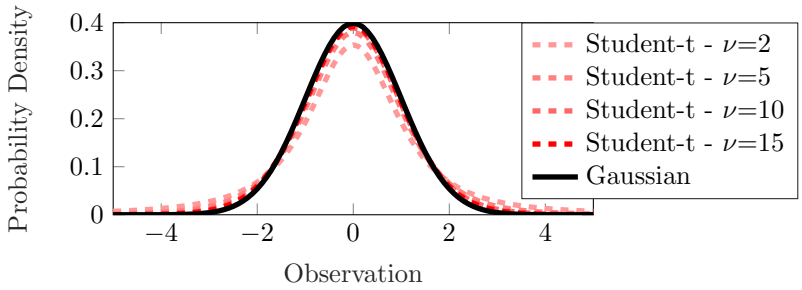

Figure 2.4: Student-t univariate distribution at several values of ν

to GPs. A further benefit of STPs generates from their heavy tailed density, which introduces more robustness to model errors thanks to an easier detectability of outliers. Additionally, while the predictive mean of a STP has the same form of a GP predictive mean with the same kernel, the predictive covariances of a GP and a STP differ. Indeed, while GPs predictive covariance do not depend on training observations, STPs ones explicitly depend on the values of the training observations. This concept can be clarified by considering a STP regression problem for which, given a training data set of n observations $D = \{\{\tilde{x_1}, \tilde{y_1}\}, \{\tilde{x_2}, \tilde{y_2}\}, ..., \{\tilde{x_n}, \tilde{y_n}\}\}$, the latent function needs to be identified at test points of interest from a STP prior. Following the same approach adopted for GPs, a zero-mean prior can be chosen to simplify calculations without loss of generality:

$$f(\mathbf{x}) \sim \mathcal{STP}(\mathbf{0}, k(\mathbf{x}, \mathbf{x}'), \nu). \tag{2.54}$$

Assuming noise-free observations, STPs posterior mean and covariance can be easily computed in closed-form as:

$$\begin{aligned} \hat{\mu} &= \mathbf{K}_{\mathbf{x},\mathbf{x}} \mathbf{K}_{\tilde{x},\tilde{x}}^{-1} \tilde{\mathbf{y}}; \\ \hat{K} &= \frac{\nu + \tilde{\mathbf{y}}^T \mathbf{K}_{\tilde{\mathbf{x}},\tilde{\mathbf{x}}}{}^{-1} \tilde{\mathbf{y}} - 2}{\nu + n - 2} \left(\mathbf{K}_{\mathbf{x},\mathbf{x}} - \mathbf{K}_{\mathbf{x},\tilde{\mathbf{x}}} \mathbf{K}_{\tilde{\mathbf{x}},\tilde{\mathbf{x}}}{}^{-1} \mathbf{K}_{\tilde{\mathbf{x}},\mathbf{x}} \right). \end{aligned} \tag{2.55}$$

Equation 2.55 confirms that the STP posterior mean has equivalent form of a GP with the same prior covariance. To the contrary, the STP posterior covariance in Eq. 2.55 features an additional term, not appearing in Eq. 2.46, which depends on the observations $\tilde{\mathbf{y}}$. As reported in the previous paragraphs of this section, when noisy processes are treated, outputs are commonly assumed as the sum of the latent GP and independent Gaussian noise ε. This approach cannot be implemented for STPs since the problem would not be analytically treatable due this type of processes not being closed under summation. An approach has been proposed in [129] to allow for analytic tractability of STPs for noisy functions by including the noise model in the covariance function as $k = k_\theta + \sigma_n^2 \delta_{ij}$. This allows to model uncorrelated noise with respect to the latent function but not independent. When $\nu \to \infty$, the proposed scheme turns into a conventional GP with independent Gaussian noise. Given the same adopted kernel, the deviation of the STP posterior covariance with respect to the GP posterior covariance depends on how much the ratio $(\tilde{\mathbf{y}}^T \mathbf{K}_{\tilde{\mathbf{x}},\tilde{\mathbf{x}}}{}^{-1} \tilde{\mathbf{y}})/n$ deviates from unity. It is worth noting that the value of this ratio plays a meaningless role in the STP $\hat{\mathbf{K}}$ when the DOF parameter ν is very high. This reflects the assumption made above according to which a GP can be obtained from a STP for $\nu \to \infty$. The difference between GP and STP is therefore more evident for small ν values. The use of STPs instead of GPs comes with no additional computational costs. Indeed, once the common terms of Eqs. 2.55 and 2.46 are computed, the additional factor calculation only scales with $O(n)$.

Realizations of the STP with mean and covariance expressed by Eq. 2.55 at a chosen number of test points are generated by applying the steps listed in Alg. 6. Figures 2.5 and 2.6 respectively compare random realizations (in gray) from a GP and a STP prior and posterior. For both the GP and the STP, a prior zero mean and a commonly adopted (Matérn) covariance function have been selected. The STP DOF parameter has been set to $\nu = 2.5$. Figure 2.5 demonstrates that the STP prior more likely foresees outliers with respect to a GP with the same mean and covariance

functions. The same behavior is encountered when analyzing the GP and STP posteriors under the adoption of the same observations set (black dots) in Fig. 2.6: outliers are more likely in the STP posterior, where the number of realizations exceeding the confidence bounds in regions close to observations is higher. Moreover, the uncertainty bounds are generally broader for the STP.

Algorithm 6 STP sampling

1: Generate $\mathbf{s} = \frac{1}{\nu}\mathbf{u} \sim \Gamma(\nu/2, 2/\nu)$, so that $\mathbf{u} \sim \chi^2_\nu$ given $\frac{1}{\nu} > 0$
2: Generate $\mathbf{r} \sim \mathcal{N}(\mathbf{0}, \hat{\mathbf{K}})$
3: Compute $\mathbf{f}_* = \hat{\boldsymbol{\mu}} + \mathbf{r}/\sqrt{\frac{1}{\nu}\mathbf{u}} = \hat{\boldsymbol{\mu}} + \mathbf{r}/\sqrt{\mathbf{s}}$

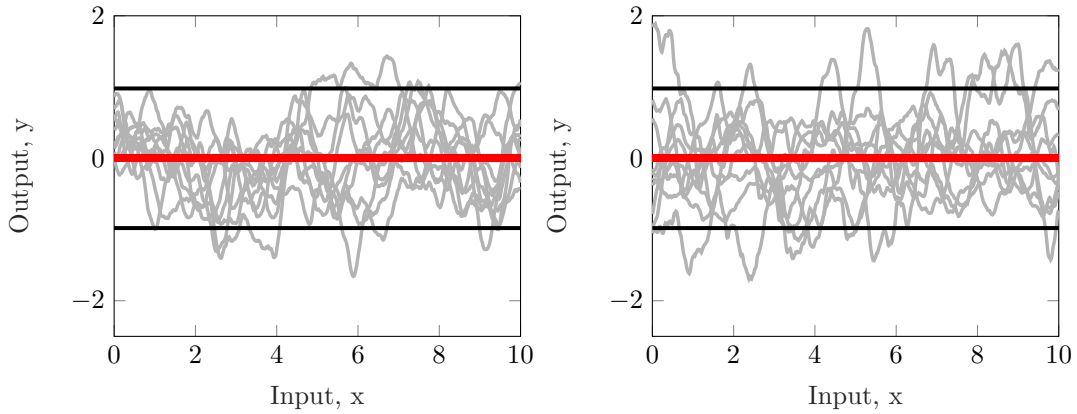

Figure 2.5: GP prior (left) and STP prior (right) comparison for the same mean (zero) and covariance functions. Mean functions are reported in red, realizations of the processes in gray. Black lines denote the 95% confidence intervals.

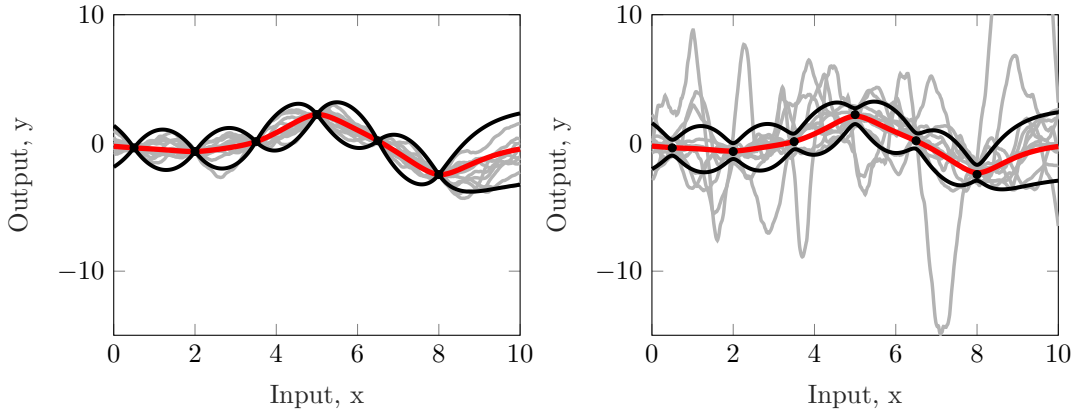

Figure 2.6: GP posterior (left) and STP posterior (right) comparison for the same mean (zero) and covariance functions. Mean functions are reported in red, realizations of the processes in gray. Black lines denote the 95% confidence intervals. Regression is performed using the same training data set D for both GP and STP. Observations in D are shown via black dots.

Following the same procedure adopted in Subsubsection 2.3.1.1, the logarithmic marginal likelihood for STPs can be derived:

$$logp(\mathbf{y}|\mathbf{X}) = -\frac{n}{2}log((\nu-2)\pi) - \frac{1}{2}log|\mathbf{K}| + log\Gamma(\frac{\nu+n}{2}) - log\Gamma\left(\frac{\nu}{2}\right) - \frac{\nu+n}{2}log\left(1 + \frac{\mathbf{y}^T\mathbf{K}^{-1}\mathbf{y}}{\nu-2}\right). \tag{2.56}$$

For facilitating the following applications, it is convenient to express the definition of a one-dimensional zero-mean STP defined over time:

$$f(t) \sim \mathcal{STP}(0, k(t,t'), \nu). \tag{2.57}$$

2.3.1.3 Covariance functions for regression via stochastic processes

The covariance function is a key tool for regression via stochastic processes since it embeds any prior knowledge about the sought-after latent function. Validity of covariance functions for stochastic processes theory is subject to some specific indications. An arbitrary function k of input pairs $\mathbf{x}$ and $\mathbf{x}'$ is a valid covariance (kernel) function if it satisfies the following properties:

- *Symmetry*:
  $k(\mathbf{x}, \mathbf{x}') = k(\mathbf{x}', \mathbf{x})$ for all $\mathbf{x}, \mathbf{x}'$
- *Positive semi-definiteness*:
  Given a set of input points $\mathbf{x} = x_i | i = 1, ..., n$, the matrix $\mathbf{K} = K_{ij} = k(\mathbf{x}_i, \mathbf{x}_j)$ is the so-called covariance matrix. $\mathbf{K}$ is positive semi-definite for all $\mathbf{v} \in \mathbb{R}^n$ if $\mathbf{v}^T\mathbf{K}\mathbf{v} \geq 0$. In particular, a symmetric matrix is positive semi-definite if and only if its eigenvalues are non-negative.

Valid covariance functions can be manipulated to construct more complex versions by exploiting the following composition rules:

- *sum rule*:
  $k(\mathbf{x}, \mathbf{x}') = k_1(\mathbf{x}, \mathbf{x}') + k_2(\mathbf{x}, \mathbf{x}')$
- *product rule*:
  $k(\mathbf{x}, \mathbf{x}') = k_1(\mathbf{x}, \mathbf{x}')k_2(\mathbf{x}, \mathbf{x}')$
- *scaling rule*:
  $k(\mathbf{x}, \mathbf{x}') = ck_1(\mathbf{x}, \mathbf{x}')$ for $c > 0$
- *general rule*:
  $k(\mathbf{x}, \mathbf{x}') = f(k_1(\mathbf{x}, \mathbf{x}'))$.

Additional properties of valid covariance functions are:

- *Stationarity*:
  $k(\mathbf{x}, \mathbf{x}') = k(\mathbf{x} - \mathbf{x}') = k(\mathbf{r})$ with $\mathbf{r} = \mathbf{x} - \mathbf{x}'$
- *Isotropy*:
  $k(\mathbf{x}, \mathbf{x}') = k(||\mathbf{x} - \mathbf{x}'||_2) = k(\boldsymbol{\tau})$ with $\boldsymbol{\tau} = ||\mathbf{x} - \mathbf{x}'||_2$.

Conventional covariance functions in structural dynamics

Isotropic covariance functions are commonly adopted for regression via stochastic processes. These covariance functions depend on the so-called hyperparameters, i.e., parameters of a non-parametric model. Indeed, the underlying model parameters, i.e., the weights, have been integrated out according to Subsection 2.3.1. The most common types of covariance functions are reported below for one-dimensional stochastic processes.

- *Squared exponential:*

$$k(\tau) = \sigma^2 exp\left(-\frac{\tau^2}{2l^2}\right), \quad \tau = |x - x'| \tag{2.58}$$

  where τ is the characteristic length-scale controlling the bandwidth of the resulting process and σ is the signal variance controlling the magnitude of the process. This covariance function is infinitely differentiable, which implies infinite mean square differentiability of the stochastic process with a squared exponential covariance function. The latter is therefore very smooth.

- *Exponential:*

$$k(\tau) = \sigma^2 exp\left(-\frac{\tau}{2l}\right), \quad \tau = |x - x'| \tag{2.59}$$

where τ is the characteristic length-scale and σ is the magnitude-scale. This type of functions generate mean square continuous but not mean square differentiable stochastic processes, which thus have a non-smooth shape.

- *Matérn class:*

$$k(\tau; \nu, \sigma, l) = \sigma^2 \frac{2^{1-\nu}}{\Gamma(\nu)} \left(\frac{\sqrt{2\nu}}{l}\tau\right)^{\nu} \mathrm{K}_{\nu}\left(\frac{\sqrt{2\nu}}{l}\tau\right), \quad \tau = |x - x'| \tag{2.60}$$

where l is the length-scale hyperparameter, σ is the magnitude-scale hyperparameter, ν is the smoothness parameter, $\Gamma(\nu)$ is the Gamma function and K_ν is a modified Bessel function of second kind. For half-integer values of ν, i.e., non-negative integer values of $p = \nu - \frac{1}{2}$, the covariance function can be written as the product of a decaying exponential and a polynomial of order p:

$$k_{\nu=p+1/2} = \sigma^2 exp(\frac{-\sqrt{2\nu}\tau}{l}) \frac{\Gamma(p+1)}{\Gamma(2p+1)} \sum_{i=0}^{p} \frac{(p+i)!}{i!(p-1)!} (\frac{\sqrt{8\nu}\tau}{l})^{p-i}. \tag{2.61}$$

The smoothness parameter ν determines the decaying rate of the covariance function, its differentiability and the mean square differentiability of the corresponding stochastic process. For $p = 0$ ($\nu = 0.5$), the Matérn covariance function corresponds to an exponential covariance function, i.e., it is continuous but not differentiable. For $\nu \to \infty$, the function converges to a squared exponential covariance function, i.e., it is infinitely differentiable. More generally, Matérn covariance functions generate stochastic processes that are $\nu - 1$ times mean square differentiable [65]. These concepts are visually demonstrated by Fig. 2.7, which displays Matérn covariance functions with assigned l and σ for different ν values (left) and corresponding random GP realizations (right). Figure 2.7 reports the square exponential and the exponential covariance functions as limit cases for the Matérn class, respectively achieved for $\nu = 0.5$ and $\nu \to \infty$. Additionally, Fig. 2.7 provides a visible insight regarding the functions differentiability scaling with ν.

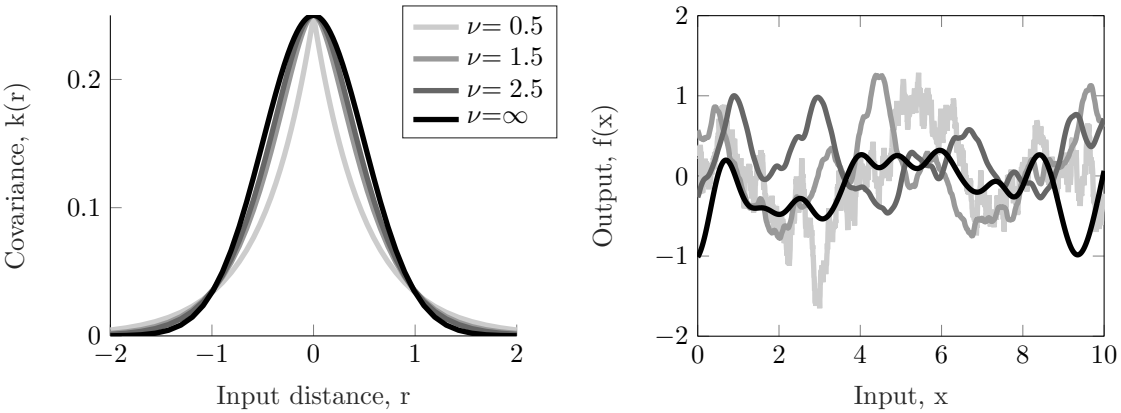

Figure 2.7: Matérn covariance functions with $\sigma = l = 0.5$ for different values of ν (left). Realizations drawn from GPs with Matérn covariance functions ($\sigma = l = 0.5$) for different values of ν (right).

Periodic covariance functions

Periodic stationary covariance functions can be derived via the so-called warping method, i.e., introducing a periodic mapping $u(t)$ of the input t and using a stationary covariance function in

the u space [130]. A typical choice for the periodic function is $u = (sin(t), cos(t))^T$, for which the following stationary property holds:

$$||u(t) - u(t')||^2 = (sin(t) - sin(t'))^2 + (cos(t) - cos(t'))^2 + 4sin^2\left(\frac{t-t'}{2}\right). \tag{2.62}$$

A commonly adopted periodic covariance function is the so-called canonical periodic covariance function, which is derived as a squared exponential covariance in the previously introduced u space:

$$k(\tau; \sigma, l, \omega_0) = \sigma^2 exp\left(-\frac{2sin^2\left(\frac{\omega_0 \tau}{2}\right)}{l^2}\right) \tag{2.63}$$

where $\tau = |t - t'|$, l = length-scale hyperparameter, σ = magnitude-scale hyperparameter, ω_0 = frequency. It is common practice to use the period length parameter, i.e., $t_{period} = 2\pi/\omega_0$, rather than the frequency. Figure 2.8 illustrates a representation of the canonical periodic covariance function (left) and corresponding GP realization at several values of t_{period}.

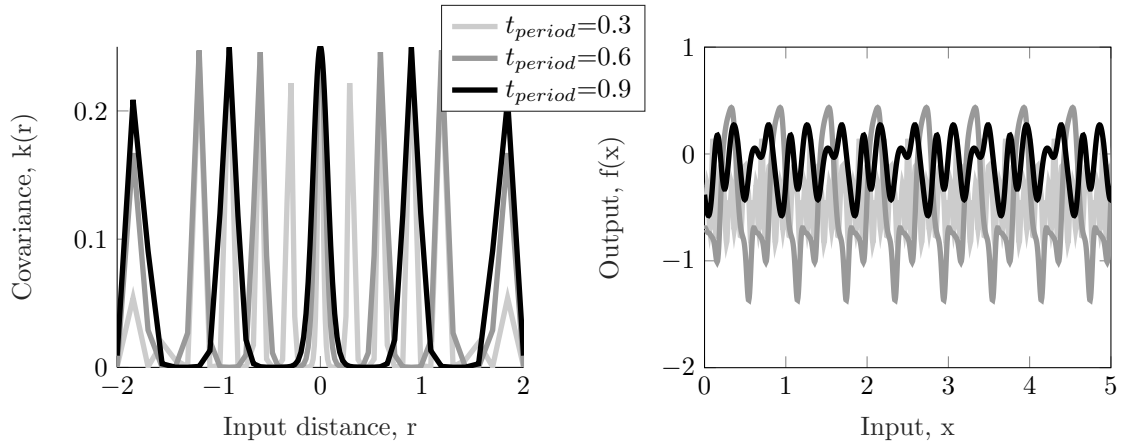

Figure 2.8: Periodic covariance functions with $\sigma = l = 0.5$ for different values of t_{period} (left). Realizations drawn from GPs with periodic covariance functions ($\sigma = l = 0.5$) for different values of t_{period} (right).

Quasiperiodic covariance functions

In practical applications, using a periodic covariance function may result in a too strict assumption. To account for variability effects, a quasiperiodic covariance function can be adopted. This type of covariance function is obtained from the product of a periodic covariance function and a covariance function with long characteristic length scale, i.e., Matérn covariance functions. This feature allows for the introduction of a slow decay effect, i.e., damping effect, which is controlled by the smoothness parameter of the Matérn covariance function as described in Fig. 2.7. Figure 2.9 (left) shows a representation of the a quasiperiodic covariance function obtained from the product of a canonical periodic function and a squared exponential covariance function (Matérn with $\nu \to \infty$) for several values of t_{period}. The relative GP realizations are reported in Figure 2.9 (right). The visual information provided by Fig. 2.9 proves that the quasiperiodic covariance function is a damped version (with damping dependent on the smoothness of the Matérn covariance function) of the periodic covariance function.

Constant covariance functions

Constant covariance functions are conventionally adopted to model biases in stochastic processes. A constant covariance function is defined as:

$$k(t, t') = \sigma^2 \tag{2.64}$$

where σ is the magnitude-scale hyperparameter. Figure 2.10 depicts constant covariance functions and relative GP realizations for several values of the magnitude scale hyperparameter.

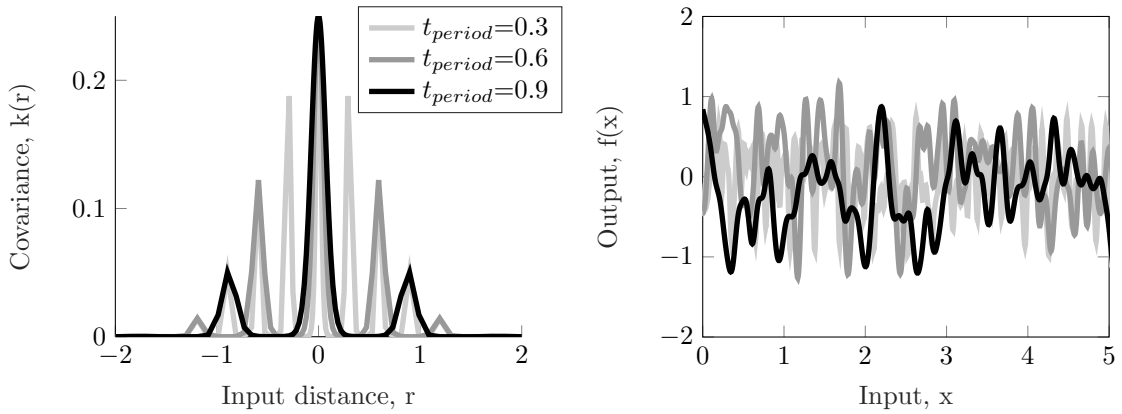

Figure 2.9: Quasiperiodic covariance functions with $\sigma_{per} = l_{per} = \sigma_{se} = l_{se} = 0.5$ for different values of t_{period} (left). Realizations drawn from GPs with periodic covariance functions ($\sigma_{per} = l_{per} = \sigma_{se} = l_{se} = 0.5$) for different values of t_{period} (right).

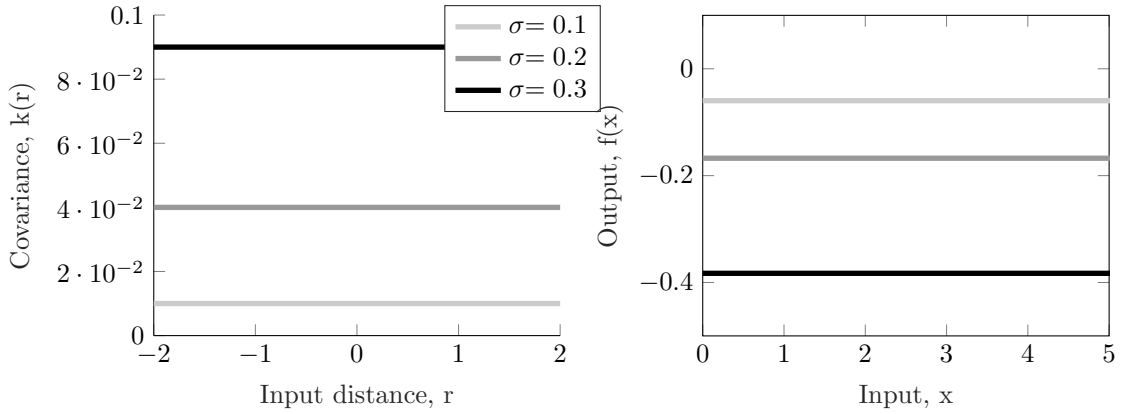

Figure 2.10: Constant covariance functions for different values of σ (left). Realizations drawn from GPs with constant covariance functions for different values of σ (right).

Biased quasiperiodic covariance functions

A biased quasiperiodic covariance function is obtained from a constant and a quasiperiodic covariance function as:

$$k = k_{constant} + k_{quasiperiodic}. \tag{2.65}$$

The sum rule is thus exploited to build a more complex covariance function in which a constant offset in added on top of the dynamics, which are fully modeled via the quasiperiodic function. This operation is commonly adopted in regression problems where data are distributed around a bias, which would not be detected without the introduction of a static term via the constant covariance function. A visualization of the biased quasiperiodic covariance function for several values of the constant covariance magnitude-scale is reported in Fig. 2.11 (left), while Fig. 2.11 (right) displays the respective GP realizations.

Linear covariance functions

Linear covariance functions can be adopted for regression via stochastic processes to model linear trends in data. A linear covariance function is defined as:

$$k(t, t') = \sigma^2 t t' \tag{2.66}$$

where σ is the magnitude-scale hyperparameter. Figure 2.12 illustrates linear covariance functions and relative GP realizations for several values of the magnitude-scale hyperparameter.

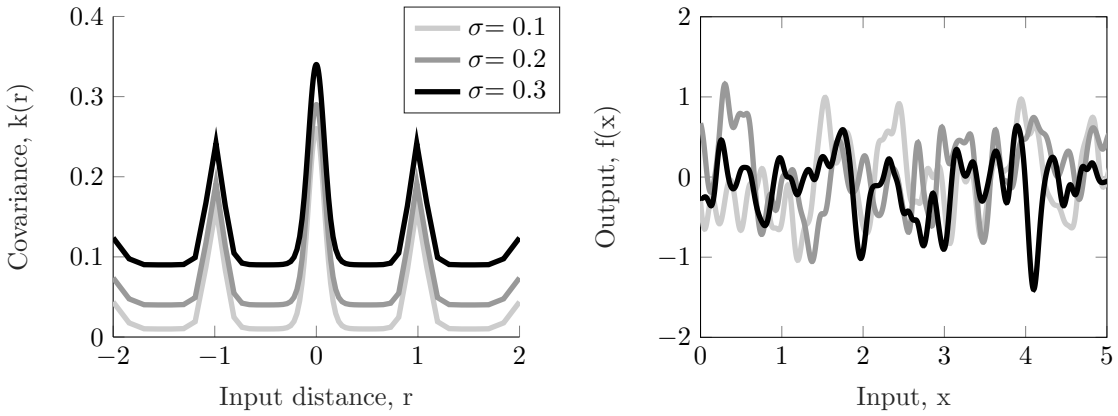

Figure 2.11: Biased quasiperiodic covariance functions for different values of $\sigma_{constant}$ (left). Realizations drawn from GPs with biased quasiperiodic covariance functions for different values of $\sigma_{constant}$ (right).

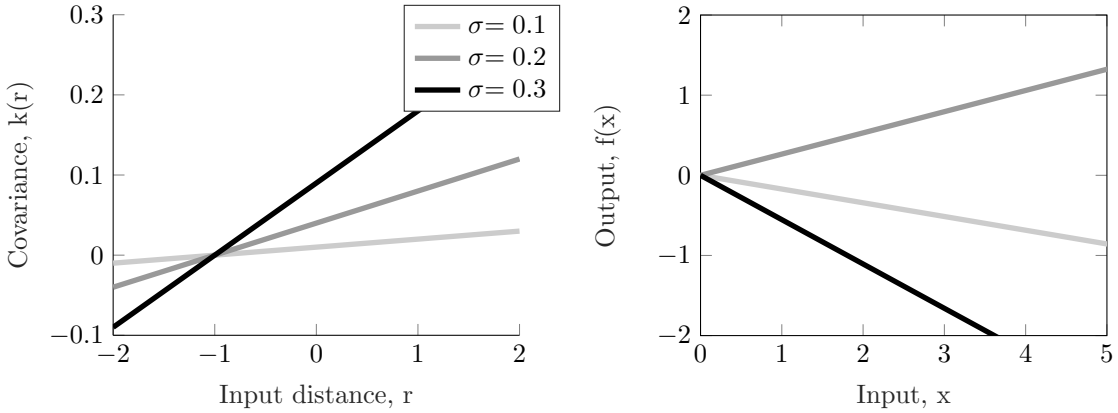

Figure 2.12: Linear covariance functions for different values of σ (left). Realizations drawn from GPs with linear covariance functions for different values of σ (right).

Wiener covariance functions

The Wiener process, i.e., a Brownian Motion (BM), is a widely adopted non-stationary process. Its covariance function is defined as:

$$k(t, t') = \sigma^2 min(t, t') \tag{2.67}$$

valid for $t, t' \geq 0$, with σ being the magnitude-scale hyperparameter. A representation of the Wiener covariance function and relative GP realizations for several values of σ is provided in Fig. 2.13. Figure 2.13 (right) proves that a covariance function such as Eq. 2.67 generates GP samples that are in the form of RW models. The latter will be further treated in Chapter 5, where they will be introduced as the basic unknown input model for input-state Kalman-based estimators. In this sense, a GP with a Wiener covariance function is an alternative to the direct RW expression adopted for input-state estimation via Kalman filtering.

2.3.1.4 Bayesian model selection in stochastic process regression

An important step in the use of stochastic processes for prediction consists in the selection of the a priori model to be employed for regression given a set of available measurements. This choice builds the starting point and substantially determines the outcome quality of regression via stochastic processes. Model selection can be intended as the set of a priori decisions taken as input for regression, e.g. choice of the covariance form, selection of the kernel hyperperameters. While the first is essentially a discrete choice of the user which can rely of any available prior knowledge regarding the nature of the analyzed data, the selection of hyperparameters needs to

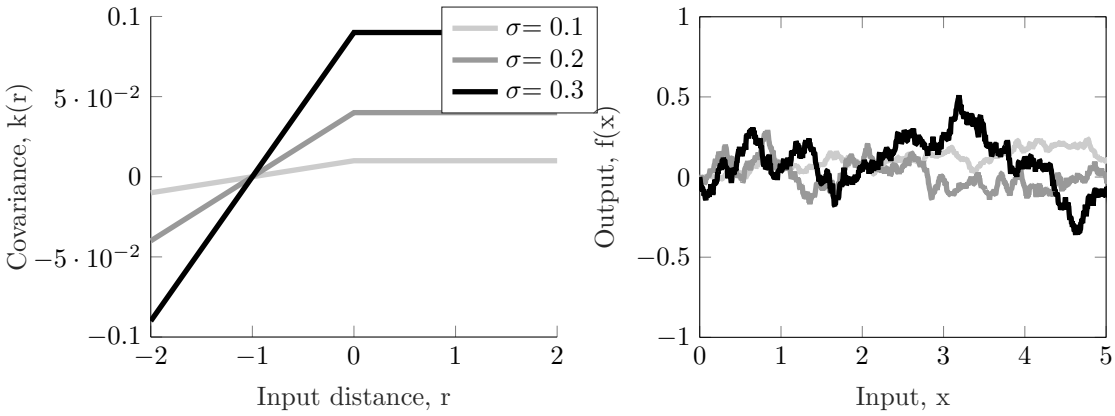

Figure 2.13: Wiener covariance functions for different values of σ (left). Realizations drawn from GPs with Wiener covariance functions for different values of σ (right).

be performed via ad hoc algorithms. In a non-Bayesian perspective, cross-validation on predictive performance could be employed for this purpose. According to this method, the best model could be selected via a training data set and evaluations regarding its performance are then taken on a validation set. This approach is known to be prone to over-fitting and often requires the use of several validation sets. In a Bayesian inference scheme instead, model selection can be performed by making use of just a training data set since it does not involve evaluation of the latent function point estimates but rather foresees averaging over it. This concept translates in estimating the covariance function hyperparameters via a training data set instead of punctual values of the latent function. A first approach to perform this estimation consists in evaluating the hyperparameters posterior in a hierarchical setting, which would require evaluation of complex integrals via analytical approximations or Markov chain Monte Carlo (MCMC) methods. A much more efficient option consists in maximizing the marginal likelihood, i.e., maximizing the probability of the data given the model, w.r.t the hyperparameters:

$$\underset{\boldsymbol{\theta}}{\text{argmax}} \quad p(\mathbf{y}|\mathbf{X},\boldsymbol{\theta}) = \underset{\boldsymbol{\theta}}{\text{argmax}} \quad \int p(\mathbf{y}|\mathbf{f},\mathbf{X},\boldsymbol{\theta})p(\mathbf{f}|\boldsymbol{\theta})d\mathbf{f}. \tag{2.68}$$

Following this method, values of the covariance hyperparameters are chosen such that the likelihood of the data is maximized when marginalizing, i.e., averaging, over all the possible realizations of the adopted stochastic process (GP, STP, etc.).
When GPs or STPs are adopted for regression, the marginal likelihood has an easy and analytically tractable expression (see Eqs. 2.49 and 2.56 respectively), which renders its optimization computationally attractive. For the sake of simplicity, it is common choice to convert maximization of the marginal likelihood into minimization of the negative logarithmic marginal likelihood. The resulting optimization problem is reported in Eqs. 2.69 and 2.70 respectively for a GP and a STP:

$$\underset{\boldsymbol{\theta}}{\text{argmin}} \; -log \quad p(\mathbf{y}|\mathbf{X},\boldsymbol{\theta}) = \underset{\boldsymbol{\theta}}{\text{argmin}} \quad \frac{n}{2}log2\pi + \frac{1}{2}log|\mathbf{K}+\sigma_n^2\mathbf{I}| + \frac{1}{2}\mathbf{y}^T(\mathbf{K}+\sigma_n^2\mathbf{I})^{-1}\mathbf{y} \tag{2.69}$$

$$\begin{aligned}\underset{\boldsymbol{\theta}}{\text{argmin}} \quad -log\, p(\mathbf{y}|\mathbf{X},\boldsymbol{\theta}) = \underset{\boldsymbol{\theta}}{\text{argmin}} \quad & \frac{n}{2}log((\nu-2)\pi) + \frac{1}{2}log|\mathbf{K}| - log\Gamma(\frac{\nu+n}{2}) + \\ & log\Gamma\left(\frac{\nu}{2}\right) + \frac{\nu+n}{2}log\left(1+\frac{\mathbf{y}^T\mathbf{K}^{-1}\mathbf{y}}{\nu-2}\right).\end{aligned} \tag{2.70}$$

For solving the optimization problem in a GP or STP regression setting, gradient-based optimization is widely exploited since derivatives of Eqs. 2.69 and 2.70 can be easily computed. This comprises another advantage of regression via stochastic processes w.r.t. other methods, e.g. MAP estimation. This type of methods can easily incur in local minima when the adopted cost functions, such as the

ones in Eqs. 2.69 and 2.70, are non-convex. As a result, different initial guess on the hyperparameters may be tested to avoid deterioration of the training outcome. With regards to computational complexity, derivatives computation requires time $O(n^2)$ per hyperparameter (if n is the number of data points, i.e. the dimension of the covariance matrix is $n \times n$). Therefore, the most substantial contribution is provided by the inversion of the positive definite covariance matrix, which scales cubically with n.

2.3.2 Regression in state-space

The main drawback of the direct solution for regression via both GPs and STPs consists in the computational complexity scaling as $O(n^3)$, where n is the number of data points. As this paragraph will treat one-dimensional stochastic processes defined over time (see Eqs. 2.50 and 2.57), n will correspond to the number of time samples in the observations used for regression. In real-life measurements, time instances of collected data is relatively high, resulting in a large amount of time needed to perform GP or STP regression. To remedy this problem, a sequential inference scheme, whose computational complexity scales linearly with n, can be implemented using Kalman filtering and smoothing [66], whose working principle will be thoroughly presented in Chapter 3. In view of adopting a sequential approach, the stochastic process under consideration needs to be formulated as a dynamical system rather than adopting the conventional kernel formalism. This consists in expressing a stochastic process as a solution of the following m^{th} order Linear Time Invariant (LTI) SDE:

$$\frac{d^m f(t)}{dt^m} + a_{m-1}\frac{d^{m-1} f(t)}{dt^{m-1}} + \cdots + a_1 \frac{df(t)}{dt} + a_0 f(t) = w(t) \tag{2.71}$$

where w is a zero-mean continuous-time white noise process. Every solution $f(t)$ of Eq. 2.71 is a sample function of a stochastic process defined by a certain covariance function k. Collecting the derivative terms in Eq. 2.71 builds the so-called companion form, i.e., a linear SSM to be employed in the recursive inference scheme:

$$\begin{cases} \dot{\mathbf{z}}(t) &= \mathbf{F}\mathbf{z}(t) + \mathbf{L}w(t) \\ f(t) &= \mathbf{H}\mathbf{z}(t) \end{cases} \tag{2.72}$$

where the input state $\mathbf{z} \in \mathbb{R}^m$ and the matrices $\mathbf{F} \in \mathbb{R}^{m \times m}$, $\mathbf{L} \in \mathbb{R}^{m \times 1}$ and $\mathbf{H} \in \mathbb{R}^{1 \times m}$ are given by:

$$\mathbf{z}(t) = \begin{bmatrix} f(t) \\ \frac{df(t)}{dt} \\ \vdots \\ \frac{d^{m-2} f(t)}{dt^{m-2}} \\ \frac{d^{m-1} f(t)}{dt^{m-1}} \end{bmatrix}, \quad \mathbf{F} = \begin{bmatrix} 0 & 1 & 0 & \dots & 0 \\ 0 & 0 & 1 & \dots & 0 \\ \vdots & \vdots & \vdots & \ddots & \vdots \\ 0 & 0 & 0 & \dots & 1 \\ -a_0 & -a_1 & \dots & \dots & -a_{m-1} \end{bmatrix}, \quad \mathbf{L} = \begin{bmatrix} 0 \\ 0 \\ \vdots \\ 0 \\ 1 \end{bmatrix}, \quad \mathbf{H} = \begin{bmatrix} 1 & 0 & \dots & 0 & 0 \end{bmatrix}. \tag{2.73}$$

2.3.2.1 Gaussian Process

To be employed for GP sequential inference, the first equation in Eq. 2.72 must be transformed in a discrete-time model of the form:

$$\mathbf{z}_k = \mathbf{F}_{d_{k-1}} \mathbf{z}_{k-1} + \mathbf{q}_{k-1}, \quad \mathbf{q}_{k-1} \sim \mathcal{N}(\mathbf{0}, \mathbf{Q}_{k-1}) \tag{2.74}$$

where the state transition and process noise covariance matrices can be calculated analytically as:

$$\begin{aligned} \mathbf{F}_{d_{k-1}} &= exp(\mathbf{F}\Delta t) \\ \mathbf{Q}_{k-1} &= \int_0^{\Delta t} exp(\mathbf{F}(\Delta t - \tau)) \mathbf{L} q_c \mathbf{L}^T exp(\mathbf{F}^T(\Delta t - \tau)) d\tau \end{aligned} \tag{2.75}$$

where $\Delta t = t_k - t_{k-1}$. The second equation in Eq. 2.72 instead represents the intrinsically discrete measurement model, on top of which the noise term ε_k must be added to account for noisy observations:

$$f_k = \mathbf{H}\mathbf{z}_k + \varepsilon_k, \quad \varepsilon_k \sim \mathcal{N}(0, \sigma_n^2). \tag{2.76}$$

Given the model postulated by Eqs. 2.74 and 2.76, GP sequential inference consists in estimating the state vector $\mathbf{z}_k$ at any k given the available measurements for $k = 0 : \Delta t : T$. This operation can be performed in two sequential steps: the filtered posterior distribution $p(\mathbf{z}_n|y_{1:n}, \boldsymbol{\theta}) = \mathcal{N}(\mathbf{m}_k, \mathbf{P}_k)$ is computed via the KF in Alg. 7, then the RTS smoother in Alg. 8 is employed to evaluate the smoothing distribution $p(\mathbf{z}_n|y_{1:T}, \boldsymbol{\theta}) = \mathcal{N}(\tilde{\mathbf{m}}_k, \tilde{\mathbf{P}}_k)$.
For replicating the naive GP regression results in Eq. 2.46, the initial condition for the estimation should be $p(\mathbf{z}_0) = \mathcal{N}(\mathbf{0}, \mathbf{P}_\infty)$, where $\mathbf{P}_\infty$ is the stationary covariance of the state vector, given by the Riccati equation:

$$\frac{d\mathbf{P}}{dt} = \mathbf{F}\mathbf{P} + \mathbf{P}\mathbf{F}^{\mathbf{T}} + \mathbf{L}q\mathbf{L}^T = 0. \tag{2.77}$$

Algorithm 7 KF for GP regression

for $k = 1, 2, ..., n$ **do**
  (a) Kalman prediction:
  $\mathbf{m}_{k|k-1} = \mathbf{F}_{d_{k-1}} \mathbf{m}_{k-1|k-1}$
  $\mathbf{P}_{k|k-1} = \mathbf{F}_{d_{k-1}} \mathbf{P}_{k-1|k-1} \mathbf{F}_{d_{k-1}}^T + \mathbf{Q}_{k-1}$
  (b) Kalman update:
  $\mathbf{v}_k = \mathbf{y}_k - \mathbf{H}_k \mathbf{m}_{k|k-1}$
  $\mathbf{S}_k = \mathbf{H}_k \mathbf{P}_{k|k-1} \mathbf{H}_k^T + \sigma_n^2 \mathbf{I}$
  $\mathbf{Kg}_k = \mathbf{P}_{k|k-1} \mathbf{H}_k^T \mathbf{S}_k^{-1}$
  $\mathbf{m}_{k|k} = \mathbf{m}_{k|k-1} + \mathbf{Kg}_k \mathbf{v}_k$
  $\mathbf{P}_{k|k} = \mathbf{P}_{k|k-1} - \mathbf{Kg}_k \mathbf{S}_k \mathbf{Kg}_k^T$
end for

Algorithm 8 RTS smoother for GP regression

for $k = n-1, n-2, ..., 1$ **do**
  (a) RTS prediction:
  $\mathbf{m}_{k+1|k} = \mathbf{F}_{d_k} \mathbf{m}_{k|k}$
  $\mathbf{P}_{k+1|k} = \mathbf{F}_{d_k} \mathbf{P}_{k|k} \mathbf{F}_{d_k}^T + \mathbf{Q}_k$
  (b) RTS update:
  $\mathbf{Rg}_k = \mathbf{P}_{k|k} \mathbf{F}_{d_k}^T \mathbf{P}_{k+1|k}^{-1}$
  $\mathbf{m}_{k|n} = \mathbf{m}_{k|k} + \mathbf{Rg}_k \left(\mathbf{m}_{k+1|n} - \mathbf{m}_{k+1|k}\right)$
  $\mathbf{P}_{k|n} = \mathbf{P}_{k|k} - \mathbf{Rg}_k \left(\mathbf{P}_{k+1|n} - \mathbf{P}_{k+1|k}\right) \mathbf{Rg}_k^T$
end for

Both the KF and the RTS smoother algorithms scale with $O(m^3 n)$ in computational complexity. In this context, the state vector dimension m corresponds to the order of the LTI SDE in Eq. 2.71, which is usually pretty small and constant with respect to n. It can be therefore concluded that GP sequential inference scales linearly with the number of samples in the observations, hence allowing for substantial computational time reduction with respect to GP regression naive implementation. The same time efficiency can be achieved for covariance hyperparameters optimization via the minimization of the negative log-likelihood presented in Subsubsection 2.3.1.4 since the marginal likelihood in Eq. 2.49 can be sequentially evaluated as a by-product of the KF update:

$$p(y_{1:n}|\boldsymbol{\theta}) = -\frac{1}{2} \sum_{k=1}^{n} log|2\pi \mathbf{S}_k| + \mathbf{v}_k^T \left(\mathbf{S}_k + \sigma_n^2\right)^{-1} \mathbf{v}_k \tag{2.78}$$

where $\mathbf{v}_k$ and $\mathbf{S}_k$ are respectively the innovation mean and covariance evaluated by the KF measurement update step. Additional computational improvement is introduced when computing the marginal likelihood terms since the smoothing step is not required. The partial derivatives involved in the optimization can also be computed recursively.

2.3.2.2 Student-t Process

The GP sequential inference scheme proposed in the previous paragraph can be adapted for STP regression under the assumption that STPs can be derived as a scale mixture of GPs [131]. The latter hypothesis validates the use of the SSM in Eq. 2.72 as an alternative STP representation in the specific circumstances in which the spectral density is set to γq_c, where γ is an inverse gamma random variable. This implies that Eqs. 2.74 and 2.75 holding for GPs can also be employed for STP sequential inference, with the only difference lying in the expressions for the initial state vector $p(\mathbf{z}_0) = \mathcal{N}(\mathbf{0}, \gamma\mathbf{P}_\infty)$ and the process noise $\mathbf{q}_{k-1} \sim \mathcal{N}(\mathbf{0}, \gamma\mathbf{Q}_{k-1})$. For what concerns the measurement noise, a valid approach consists in including the noise term in the adopted covariance function as described in Subsubsection 2.3.1.2. Since summation of covariance function under the kernel representation corresponds to stacking state variables in the state-space model, the measurement noise contribution can be accounted by augmenting the state vector with the white noise process of variance σ_n^2. Along the lines of GPs, STP regression can be solved sequentially by implementing a forward filtering problem as in Alg. 9 and using a smoother as in Alg. 10 to update the filtering outcome. The DOF parameter is updated as $\nu_k = \nu_{k-1} + n_k$, where $n_k = 1$, if there is an update on time-step k, and $n_k = 0$ otherwise (for prediction of test points). It is clear that for $\nu \to \infty$, Algs. 9 and 10 respectively revert to the KF and RTS smoother adopted for GPs.

Algorithm 9 Student-t filter

for $k = 1, 2, ..., n$ **do**
  (a) Kalman prediction:
  $\mathbf{m}_{k|k-1} = \mathbf{F}_{d_{k-1}} \mathbf{m}_{k-1|k-1}$
  $\mathbf{P}_{k|k-1} = \mathbf{F}_{d_{k-1}} \mathbf{P}_{k-1|k-1} \mathbf{F}_{d_{k-1}}^T + \gamma_{k-1}\mathbf{Q}_{k-1}$
  (b) Kalman update:
  $\mathbf{v}_k = \mathbf{y}_k - \mathbf{H}_k \mathbf{m}_{k|k-1}$
  $\mathbf{S}_k = \mathbf{H}_k \mathbf{P}_{k|k-1} \mathbf{H}_k^T + \sigma_n^2 \mathbf{I}$
  $\gamma_k = \frac{\gamma_{k-1}}{\nu_k - 2} \left(\nu_{k-1} - 2 + \mathbf{v}_k^T \mathbf{S}_k^{-1} \mathbf{v}_k \right)$
  $\mathbf{Kg}_k = \mathbf{P}_{k|k-1} \mathbf{H}_k^T \mathbf{S}_k^{-1}$
  $\mathbf{m}_{k|k} = \mathbf{m}_{k|k-1} + \mathbf{Kg}_k \mathbf{v}_k$
  $\mathbf{P}_{k|k} = \frac{\gamma_k}{\gamma_{k-1}} \left(\mathbf{P}_{k|k-1} - \mathbf{Kg}_k \mathbf{S}_k \mathbf{Kg}_k^T \right)$
end for

Algorithm 10 Student-t smoother

for $k = n-1, n-2, ..., 1$ **do**
  (a) RTS prediction:
  $\mathbf{m}_{k+1|k} = \mathbf{F}_{d_k} \mathbf{m}_{k|k}$
  $\mathbf{P}_{k+1|k} = \mathbf{F}_{d_k} \mathbf{P}_{k|k} \mathbf{F}_{d_k}^T + \gamma_k \mathbf{Q}_k$
  (b) RTS update:
  $\mathbf{Rg}_k = \mathbf{P}_{k|k} \mathbf{F}_{d_k}^T \mathbf{P}_{k+1|k}^{-1}$
  $\mathbf{m}_{k|n} = \mathbf{m}_{k|k} + \mathbf{Rg}_k \left(\mathbf{m}_{k+1|n} - \mathbf{m}_{k+1|k} \right)$
  $\mathbf{P}_{k|n} = \frac{\gamma_n}{\gamma_k} \left(\mathbf{P}_{k|k} - \mathbf{Rg}_k \mathbf{P}_{k+1|k} \mathbf{Rg}_k^T \right) + \mathbf{G}_k \mathbf{P}_{k+1|n} \mathbf{G}_k^T$
end for

For covariance hyperparameters optimization, the negative log marginal likelihood can be sequentially evaluated as a by-product of the filtering recursion in Alg. 9 as:

$$p(y_{1:n}|\boldsymbol{\theta}) = \sum_{k=1}^{n} \frac{1}{2} log((\nu-2)\pi) + \frac{1}{2} log|\mathbf{S}_k| + log\Gamma\left(\frac{\nu_{k-1}}{2}\right) - log\Gamma\left(\frac{\nu_k}{2}\right) + \frac{1}{2} log\left(\frac{\nu_{k-1}-2}{\nu-2}\right) + \frac{\nu_k}{2} log\left(1 + \frac{\mathbf{v}_k^T \mathbf{S}_k^{-1} \mathbf{v}_k}{\nu_{k-1}-2}\right). \quad (2.79)$$

2.3.2.3 Covariance functions as state-space models

The SDE representation of stochastic processes in Eq. 2.71 is determined by the covariance function defining the stochastic process. According to the adopted class of covariance function, either an exact LTI state-space SDE representation or an approximated version can be retrieved. A collection of state-space SDE representations for the covariance functions presented in Subsubsection 2.3.1.3 is reported in the following.

Matèrn class

For stochastic processes with a covariance function of the Matérn type, an exact state-space representation can be extracted following the rational spectrum approach. The latter derives from the assumption of a rational spectral density for this class of covariance functions. In order to introduce the concept of spectral density, it is convenient to define covariance functions for zero-mean complex-valued stochastic processes: $k(\mathbf{x},\mathbf{x}') = \mathbb{E}\left[f(\mathbf{x})f^*(\mathbf{x}')\right]$ with $\mathbf{x},\mathbf{x}' \in \mathbb{C}^n$. Bochner's theorem [65, 132] states that a complex-valued function k defined on $\mathbb{R}^D$ is the covariance function of a weakly stationary square continuous complex-valued stochastic process in $\mathbb{R}^D$ if and only if it can be represented as:

$$k(\boldsymbol{\tau}) = \int_{\mathbb{R}^d} e^{2\pi i \mathbf{f}\cdot\boldsymbol{\tau}} \mu(d\mathbf{f}) = \int_{\mathbb{R}^d} e^{2\pi i \mathbf{f}\cdot\boldsymbol{\tau}} dF(\mathbf{f}) \tag{2.80}$$

where $\boldsymbol{\tau} = \mathbf{x} - \mathbf{x}'$, μ is a positive finite measure and $F(\mathbf{f})$ is defined such that $\mu(d\mathbf{f}) = dF(\mathbf{f})$. If μ is absolutely continuous, then F is differentiable almost everywhere and $\mu(d\mathbf{f}) = S(\mathbf{f})d\mathbf{f}$, where $S(\mathbf{f})$ is defined as the spectral density or power spectrum corresponding to k. Introducing $S(\mathbf{f})$ into Eq. 2.80 and exploiting Wiener-Khintchine theorem [133], k and $S(\mathbf{f})$ can be defined as Fourier duals:

$$k(\boldsymbol{\tau}) = \int S(\mathbf{f}) e^{2\pi i \mathbf{f}\cdot\boldsymbol{\tau}} d\mathbf{f}, \quad S(\mathbf{f}) = \int k(\boldsymbol{\tau}) e^{-2\pi i \mathbf{f}\cdot\boldsymbol{\tau}} d\boldsymbol{\tau}. \tag{2.81}$$

The relationships in Eq. 2.81 can be expressed for a one-dimensional temporal problem (with $\tau = t - t'$) as:

$$k(\tau) = \int S(f) e^{2\pi i f\cdot\tau} df, \quad S(f) = \int k(\tau) e^{-2\pi i f\cdot\tau} d\tau, \quad f = \frac{\omega}{2\pi}. \tag{2.82}$$

Following Eq. 2.82, this paragraph will make use of the Fourier Transform (FT) to link time and frequency domains and compute the spectral density for a Matérn covariance function. In particular, when k falls in the Matérn class of functions, its FT yields:

$$S(\omega) = \sigma^2 \frac{2\pi^{1/2}\Gamma(\nu+1/2)}{\Gamma(\nu)} \lambda^{2\nu} (\lambda^2+\omega^2)^{-(\nu+1/2)}, \quad \lambda = \frac{\sqrt{2\nu}}{l} = \frac{\sqrt{2(p+1)}}{l}. \tag{2.83}$$

Under the assumption of ν being a half-integer, the spectral density can be reformulated as:

$$S(\omega) = \sigma^2 \frac{2\pi^{1/2}\Gamma(p+1)}{\Gamma(p+1/2)} \lambda^{2p+1} (\lambda^2+\omega^2)^{-(p+1)}. \tag{2.84}$$

After grouping all constant terms in a single constant q_c, the spectral density can be factorized in a rational fraction form:

$$S(\omega) = q_c(\lambda^2+\omega^2)^{-(p+1)} = q_c(\lambda+i\omega)^{-(p+1)}(\lambda-i\omega)^{-(p+1)} = q_c G(i\omega)G(-i\omega). \tag{2.85}$$

Equation 2.85 can be interpreted as the spectral density of the output of a system with Transfer Function (TF) $G(i\omega) = (\lambda+i\omega)^{-(p+1)}$, excited by an input $w(t)$ (white noise with spectral density q_c):

$$F(\omega) = G(i\omega)W(\omega). \tag{2.86}$$

In Eq. 2.86, $F(\omega)$ (FT of $f(t)$) is the output of the spectral density $S(\omega)$ and $W(\omega)$ is the FT of the exciting term $w(t)$, i.e., $W = \sqrt{(q_c)}$. The function $f(t)$ is the GP with Matérn covariance function k, i.e., with desired spectral density $S(\omega)$. For the Matérn class of covariance functions, the

TF $G(i\omega)$ has a rational form of the type $G(i\omega) = ((i\omega)^m + a_{m-1}(i\omega)^{m-1} + ... + a_0)^{-1}$. Hence, Eq. 2.86 can be reformulated as:

$$F(\omega)[(i\omega)^m + a_{m-1}(i\omega)^{m-1} + ... + a_0] = W(\omega). \tag{2.87}$$

The inverse FT of Eq. 2.87 provides the LTI SDE in Eq. 2.71. It has been therefore demonstrated that the GP with covariance function k given by Eq. 2.61 is the output of the LTI SDE postulated by Eq. 2.71, i.e., the LTI SDE provides the evolution in time of sample functions drawn from a GP with covariance k [66]. The coefficients in Eq. 2.71 can be easily determined by analyzing the form of the Matérn covariance functions TF:

$$G(i\omega) = \frac{1}{(\lambda + i\omega)^{p+1}}. \tag{2.88}$$

For example, Eq. 2.88 for $\nu = \frac{5}{2}$ $(p = 2)$ has the form:

$$G(i\omega) = \frac{1}{(\lambda + i\omega)^3} \tag{2.89}$$

where the denominator can be rewritten as $\lambda^3 + (i\omega)^3 + 3\lambda^2(i\omega) + 3\lambda(i\omega)^2$. Hence, the coefficients $a_m, \ldots, a_0$ with $m = 3$ are: $a_3 = 1, a_2 = 3\lambda, a_1 = 3\lambda^2, a_0 = \lambda^3$ and the resulting SDE is:

$$\frac{d^3 f(t)}{dt^3} + 3\lambda \frac{d^2 f(t)}{dt^2} + 3\lambda^2 \frac{df(t)}{dt} + \lambda^3 f(t) = w(t). \tag{2.90}$$

The roots of this SDE are real and coincident with multiplicity equal to 3: $\omega_1 = \omega_2 = \omega_3 = -\lambda$. These correspond to the poles of the system with TF postulated by Eq. 2.89, whose bode plot is displayed in Fig. 2.14.

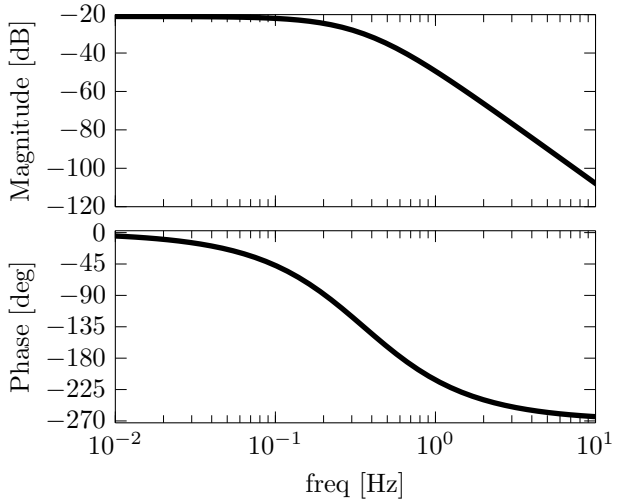

Figure 2.14: GP with Matérn covariance function: TF of the equivalent SDE system

The system poles can be computed by setting the denominator of Eq. 2.89 equal to zero and solve the so-called characteristic equation. This result can be extended to all orders: roots are always $= -\lambda$ with multiplicity equal to $p + 1$. Therefore, the system with TF in Eq. 2.88 is "critically damped" for any integer p, i.e., the time waveform is an exponentially decaying function with a decaying rate driven by the value of $\lambda = \frac{\sqrt{2\nu}}{l} = \frac{\sqrt{2(p+1)}}{l}$. This result is confirmed by the TF shape visible in Fig. 2.14 for $p = 2$. The higher λ (and ν) is, the faster will be the decay. A mathematical proof to this is provided by the homogeneous solution for Eq. 2.90, which could only correspond to:

$$g(t) = \tilde{g}\, e^{\{-\lambda t\}} \tag{2.91}$$

where $\tilde{g}$ can be determined by substituting this expression into the unforced SDE, yielding (for $p = 2$):

$$\frac{d^3\tilde{g}}{dt^3}e^{-\lambda t} = 0. \tag{2.92}$$

Since the exponential function never equals 0, the only possible solution for Eq. 2.92 is given by $\frac{d^3\tilde{g}}{dt^3} = 0$. This expression can be double integrated to get $\tilde{g} = c_1 + c_2 t + c_3 t^2$. Therefore, the explicit form of Eq. 2.92 is given by:

$$g = (c_1 + c_2 t + c_3 t^2)e^{-\lambda t} \tag{2.93}$$

where constants can be determined by applying the initial conditions on $g, \frac{d\,g}{d\,t}, \frac{d^2 g}{d\,t^2}$. This homogeneous solution should be convoluted with the forcing term $w(t)$ to get the forced response of the system with TF $G(i\omega)$: $f(t) = g(t) * w(t)$ [134]. The same result could also be obtained by exploiting partial fraction expansion from control theory to manipulate the TF $G(\omega)$.

Periodic class

A periodic and symmetric covariance function can be expanded into a convergent Fourier series of the form:

$$k(\tau) = \sum_{j=0}^{\infty} q_j^2 cos(j\omega_0\tau). \tag{2.94}$$

The spectral density corresponding to Eq. 2.94 consists of delta peaks at the harmonic frequencies defined by ω_0, i.e., the angular frequency defining the periodicity of the function:

$$S_p(\omega) = \sum_{j=0}^{\infty} q_j^2 \pi \left[\delta(\omega - j\omega_0) + \delta(\omega + j\omega_0)\right]. \tag{2.95}$$

This spectral density does not exhibit a rational form, thus implying that the procedure adopted for Matérn covariance functions can not be used for building the state-space representation of a stochastic process with a periodic covariance function. However, each j^{th} term in Eq. 2.94 can be seen as the covariance function of the sum of statistically independent resonators $\sum_{j=0}^{\infty} x_j(t)$ such that:

$$f_j(t) = (x_j(t), y_j(t))^T \tag{2.96}$$

with the initial condition $f_j(0) \sim \mathcal{N}\left(0, q_j^2 I\right)$ and the following differential equations defining the harmonic oscillator:

$$\begin{aligned} \frac{dx_j(t)}{dt} &= -j\omega_0 y_j(t) \\ \frac{dy_j(t)}{dt} &= j\omega_0 x_j(t). \end{aligned} \tag{2.97}$$

Solving Eq. 2.97 yields:

$$x_j(t) = x_j(0)cos(\omega_0 jt) - y_j(0)sin(\omega_0 jt) \tag{2.98}$$

with associated covariance $\mathbb{E}\left[x_j(t)x_j(t+\tau)\right] = q_j^2 cos(j\omega_0\tau)$. As a result, these processes are deterministic with initial state drawn from a Gaussian distribution. The corresponding state-space formulation features block diagonal matrices composed of J matrices as the following:

- Feedback matrices:

$$F_j = \begin{bmatrix} 0 & -\omega_0\, j \\ \omega_0\, j & 0 \end{bmatrix} \tag{2.99}$$

- Noise effect matrices:

$$L_j = I_2 \tag{2.100}$$

- Stationary covariances:

$$P_{\infty,j} = q_j^2 I_2 \tag{2.101}$$

- Noise effect matrices:

$$Q_c = 0 \tag{2.102}$$

since the process does not have a diffusion term.

- Measurement matrices:

$$H_j = \begin{bmatrix} 1 & 0 \end{bmatrix}. \tag{2.103}$$

In order to retrieve the form in Eq. 2.94 for the canonical covariance function in Eq. 2.63, the relation $2\sin^2\left(\frac{\tau}{2}\right) = 1 - \cos(\tau)$ must be substituted in the canonical covariance function expression. After expanding the exponential function via a Taylor series, the following expression is obtained:

$$k(\tau) = exp(-l^2) \sum_{j=0}^{\infty} \frac{1}{j!} cos^j(\tau). \tag{2.104}$$

This series can be truncated at an order J and the powers of cosines can be written as summation of cosine terms with multiplied angles. This leads to the following expression for the canonical periodic covariance function:

$$k(\tau) = \sum_{j=0}^{J} \hat{q}^2_{j,J} cos(j\tau) \tag{2.105}$$

with coefficients $\hat{q}^2_{j,J} = \frac{2}{exp(l^{-2})} \sum_{i=0}^{\lfloor \frac{J-j}{2} \rfloor} \frac{(2l^2)^{-j-2i}}{(j+i)!i!}$, where $j = 1, \dots J$. An approximation of this expression can be retrieved taking the limit $J \to \infty$ [130]. The eigenvalues associated to the dynamical system corresponding to a GP with covariance function described by Eq. 2.105 are complex conjugates with zero real part (each pair corresponds to the eigenvalues associated to the j^{th} component, with the first two eigenvalues being zero). Referring to the single j^{th} component, a differential equation with imaginary conjugate poles corresponds to an undamped system with frequency specified by the magnitude of the imaginary part. Solving the eigenvalue solution for the reconstructed SSM yields eigenvalues that are multiples of $\omega_0 = 2\pi/t_{period}$. The solution of the j^{th} differential equation is therefore: $x_j(t) = x_j(0)cos(\omega_0 jt) - y_j(0)sin(\omega_0 jt)$, as anticipated in Eq. 2.98. It follows that the resulting stochastic process will be a summation of J harmonic components (harmonics of ω_0). The latter are visible in Fig. 2.15, which shows the bode plot of the TF for the dynamical system associated to a GP with canonical periodic covariance function with $\omega_0 = 1$ and truncation order $J = 6$. Figure 2.15 proves that the TF features a $0Hz$ component and J undamped harmonics (one for each j^{th} component).

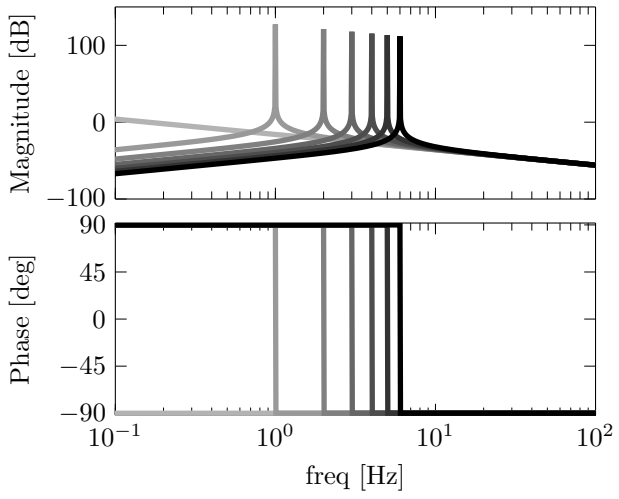

Figure 2.15: GP with periodic covariance function: TFs of the equivalent SDE system

Quasiperiodic class

Following the product rule reported in Subsubsection 2.3.1.3, a quasiperiodic covariance function can be constructed as a product of a periodic and a Matérn covariance function. As a result, the Kronecker product can be exploited as follows to build the related SSM:

$$\begin{aligned} &F_j = F^q \otimes I_2 + I_q \otimes F_j^p, \quad L_j = L^q \otimes L_j^p, \quad Q_{c,j} = Q_c^q \otimes q_j^2 I_2, \\ &P_{\infty,j} = P_\infty^q \otimes P_{\infty,J}^P, \quad H_j = H^q \otimes H_j^P \end{aligned} \tag{2.106}$$

where the p and q notations are respectively used for matrices associated with the periodic and the Matérn covariance function. The eigenvalue solution for the system in Eq. 2.106 provides, for each j^{th} component, complex conjugate pairs of eigenvalues. The dynamical system representing a quasiperiodic covariance function thus corresponds to an underdamped system with solution of the type $x_j(t) = e^{\alpha t}(x_j(0)cos(\omega_0 jt) - y_j(0)sin(\omega_0 jt))$. This is confirmed by the bode plot of the TF reported in Fig. 2.16, which features a $0Hz$ component and J damped harmonics (one for each j^{th} component).

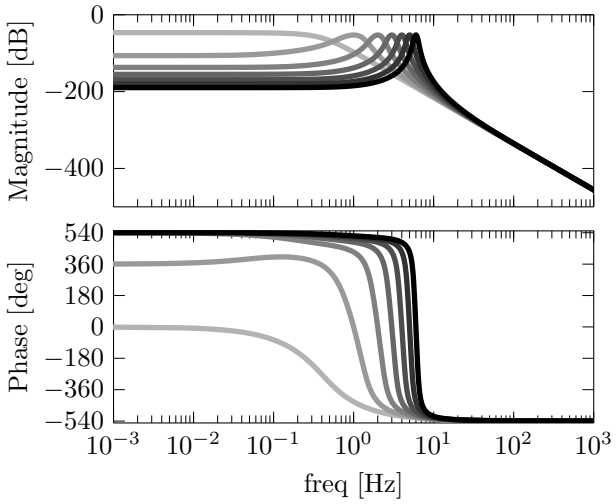

Figure 2.16: GP with quasiperiodic covariance function: TFs of the equivalent SDE system

Constant class

A constant covariance function is degenerate and the corresponding SSM representation is given by the matrices:

$$\begin{aligned} &F = 0, \quad L = 1, \quad Q_c = 0, \\ &H = 1, \quad P_0 = \sigma^2. \end{aligned} \tag{2.107}$$

The bode plot for the TF associated with this model is reported in Fig. 2.17.

Linear class

A linear covariance function is degenerate and the corresponding SSM is defined by the matrices:

$$\begin{aligned} &F = \begin{bmatrix} 0 & 1 \\ 0 & 0 \end{bmatrix}, \quad L = \begin{bmatrix} 0 \\ 1 \end{bmatrix}, \quad Q_c = 0, \\ &H = \begin{bmatrix} 1 & 0 \end{bmatrix}, \quad P_0 = \sigma^2 \begin{bmatrix} t_0^2 & t_0 \\ t_0 & 1 \end{bmatrix}. \end{aligned} \tag{2.108}$$

The bode plot for the TF associated with this model is reported in Fig. 2.18.

Wiener class

The SSM representation of a Wiener process is defined by the matrices:

$$\begin{aligned} &F = 0, \quad L = 1, \quad Q_c = \sigma^2, \\ &H = 1, \quad P_0 = 0. \end{aligned} \tag{2.109}$$

The bode plot for the TF associated with this model is reported in Fig. 2.19.

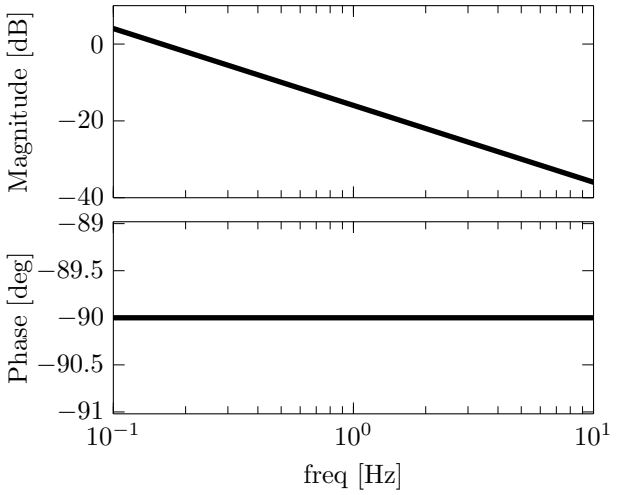

Figure 2.17: GP with constant covariance function: TF of the equivalent SDE system

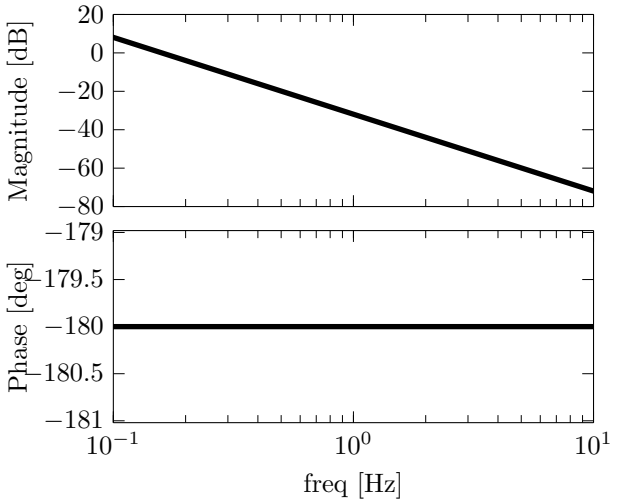

Figure 2.18: GP with linear covariance function: TF of the equivalent SDE system

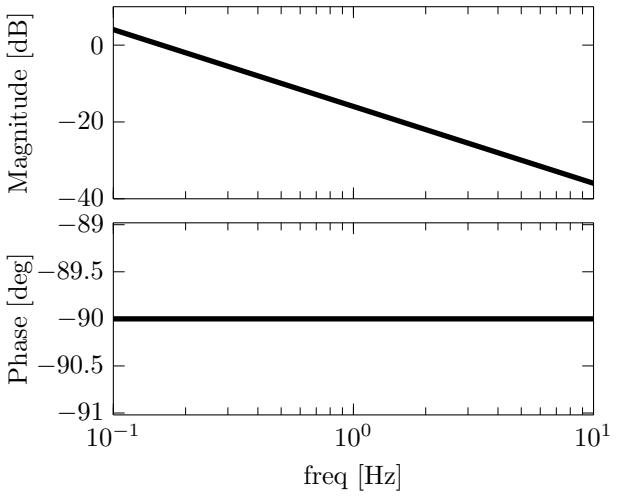

Figure 2.19: GP with Wiener covariance function: TF of the equivalent SDE system

2.4 Summary

This chapter introduces the necessary basic principles for describing the algorithms developed in this thesis. The state-space representation of dynamic system models and the MOR techniques adopted in this thesis are reported in this chapter, along with an introduction to the stochastic framework forming the core of the VS strategies developed within this dissertation. This chapter also focuses on data-driven methods aimed at designing dynamic models from observations-only. Specifically, recursive GP regression is treated and a thorough analysis of the conventional covariance functions adopted in structural dynamics is proposed. Alternative covariance functions are also studied and a second regression scheme, the STP regression, is presented.

3

RESPONSE AND JOINT INPUT-RESPONSE ESTIMATION

The problem of data assimilation has been introduced in Section 2.2 by proposing the KF as an analytic tool for implementation of Bayesian inference. The standard KF can be adopted in structural dynamics for online state, and, therefore, response estimation based on the BDM of the structure and available measurements. When the main focus of data assimilation is only on structural response reconstruction, ME can be applied alternatively to the KF to predict real-time operating data at unmeasured locations by mapping the measured responses through numerical normal modes. The ME approach, which consists in an elementary linear transformation, falls outside the Bayesian framework introduced in Section 2.2 since it is constructed on deterministic assumptions. Nevertheless, ME has proven to generate accurate response prediction in specific circumstances, thus serving as a valid alternative to the KF.
In practical engineering applications, the use of response estimation strategies might be limited by potential uncertainties regarding the loads applied to the system and/or the true parameter values (mass, damping and/or stiffness) of a structure in operational conditions. To tackle this problem, a method for state estimation in presence of unknown or highly non-Gaussian inputs has been developed. This approach, often referred as Kitanidis filter [75], implements linear minimum-variance unbiased state estimation independently of the unknown input that may be acting on the system. In situations in which unknown loads are also of interest, an adaptation of the Kitanidis filter providing input and state estimation concurrently, i.e., the GDF, can be adopted. For the same purpose, several Kalman-based algorithms have been developed relying on the use of an additional SSM. This can be adopted for both unknown loads and/or parameters and it is constructed by coupling the measurement equation of Eq. 2.18 to an a-priori transition model which determines the time evolution of the unknown random process. In this dissertation, the structural parameters of the analyzed system will be treated as known time-invariant quantities and focus will be shed on unknown loads reconstruction. To address joint input-state estimation, Kalman-based approaches, e.g. the AKF and the DKF, have been developed and extensively tested in the structural dynamics field. The first, proposed in [49], relies on augmenting the system state vector with the unknown loads in order to perform simultaneous input-state estimation. To the contrary, the DKF performs joint input-state estimation in two separate stages, as demonstrated in [51].
This chapter first introduces the ME method for deterministic response estimation, further suggesting an improvement by coupling ME to CMS. Secondly, the Kitanidis filter for state estimation in presence of undetermined loads is presented, followed by the description of the GDF algorithm. Ultimately, the Bayesian estimation framework introduced in Section 2.2 is extended to the joint input-state prediction problem by offering the AKF and the DKF algorithms.

3.1 Modal Expansion

ME is a deterministic method specifically constructed for response estimation. The prediction relies upon a modal decomposition of the measured responses to obtain the modal coordinates, which are expanded to the unmeasured DOFs through the FE model mode shapes. For applying

ME, the numerical normal modes matrix $\boldsymbol{\Psi}_n$ must be expressed by distinguishing the measured (observed) and unmeasured (predicted) DOFs as follows:

$$\boldsymbol{\Psi}_n = \begin{bmatrix} \boldsymbol{\Psi}_n^o \\ \boldsymbol{\Psi}_n^p \end{bmatrix}; \tag{3.1}$$

with $\boldsymbol{\Psi}_n^o \in \mathbb{R}^{n_o \times n_k}$ and $\boldsymbol{\Psi}_n^p \in \mathbb{R}^{n_p \times n_k}$, where $n_p = n_{dof} - n_o$. The $\boldsymbol{\Psi}_n^o$ matrix is obtained via the following formulas for displacement or strain, velocity and acceleration measurements, respectively: $\boldsymbol{\Psi}_n^o = \mathbf{S}_d \boldsymbol{\Psi}_n$, $\boldsymbol{\Psi}_n^o = \mathbf{S}_v \boldsymbol{\Psi}_n$ and $\boldsymbol{\Psi}_n^o = \mathbf{S}_a \boldsymbol{\Psi}_n$. When specifically adopted for strain measurements, the selection matrix $\mathbf{S}_d$ is obtained evaluating the matrix $\sum_a \mathbf{B}^a \boldsymbol{\Psi}^a$ in Eq. 2.14 at the strain vector components corresponding to the measured strain quantity.
When a high correlation between the numerical and the experimental mode shapes is available, measured responses can be used to determine the modal displacement (or its first and second derivative in case of velocity and acceleration measurements, respectively) at any DOF of the structure. This approach is valid for any type of response, e.g, displacement, strain, velocity, acceleration. Specifically, it can be adopted for real-time estimation if the measured and estimated quantities are of the same type. If one would use a certain type of measurement, e.g. acceleration, to estimate a different type of response, e.g. displacement, the formulation would require integration or the use of a frequency domain approach via the FT of Eq. 2.10, which would render the method not suitable for real-time prediction. Within this dissertation, only one type of response, i.e., strain, will be used for ME.

By defining the measured DOFs as $\mathbf{z}^o(t)$ and the estimated DOFs as $\mathbf{z}^p(t)$, the relationship in Eq. 2.2 can be written for only the n_o measured DOFs as:

$$\mathbf{z}_k^o = \boldsymbol{\Psi}_n^o \mathbf{p}_k \tag{3.2}$$

where vectors $\mathbf{z}^o(t)$ and $\mathbf{p}(t)$ have been transferred from continuous to discrete-time representation for the sake of consistency with the proposed notation. From 3.2, the modal coordinates vector $\mathbf{p}_k$ can be expressed as:

$$\mathbf{p}_k = (\boldsymbol{\Psi}_n^{oT} \boldsymbol{\Psi}_n^o)^{-1} \boldsymbol{\Psi}_n^{oT} \mathbf{z}_k^o = \boldsymbol{\Psi}_n^{o\dagger} \mathbf{z}_k^o. \tag{3.3}$$

It is worth mentioning that Eq. 3.3 can be solved as a determined (or overdetermined) system only when the number of measurements n_o is equal to (or greater than) the number of modes included in the reduction basis, i.e., n_k. The prediction at unmeasured DOFs can be obtained by expanding the modal coordinates vector computed in Eq. 3.3:

$$\hat{\mathbf{z}}_k^p = \boldsymbol{\Psi}_n^p \mathbf{p}_k = \boldsymbol{\Psi}_n^p \boldsymbol{\Psi}_n^{o\dagger} \mathbf{z}_k^o. \tag{3.4}$$

The ME approach can be adopted for predicting any dynamic response quantity, i.e., displacement, acceleration, or strain, by using an appropriate reduction basis.

3.1.1 Component Mode Synthesis - Modal Expansion

It is worth noting that in Eq. 3.3, the vector $\mathbf{p}_k$ is the modal coordinates vector at the current time step. This differs from the generalized coordinate vector $\mathbf{p}$ introduced in Eq. 2.2, where the augmented reduction basis in Eq. 2.4 has been adopted to express the physical coordinates vector as a function of $\mathbf{p}$. This implies that the conventional ME approach only expands the measured DOFs through the normal modes matrix and does not account for any behavior of different nature. In this dissertation, the use of the generalized coordinates introduced in Eq. 2.2 via use of the CMS reduction basis $\boldsymbol{\Psi}$ is proposed as an alternative to the conventional modal coordinates. In this way, the observed response $\mathbf{z}_k^o$ is interpolated via the augmented reduction basis in Eq. 2.4, which better fits the actual structural behavior of the system by taking into account the presence of static contribution other than the normal one:

$$\mathbf{z}_k^o = \boldsymbol{\Psi}^o \mathbf{p}_k. \tag{3.5}$$

The resulting formulation for the generalized vector is:

$$\mathbf{p}_k = (\mathbf{\Psi}^{oT}\mathbf{\Psi}^o)^{-1}\mathbf{\Psi}^{oT}\mathbf{z}_k^o = \mathbf{\Psi}^{o\dagger}\mathbf{z}_k^o \tag{3.6}$$

and the prediction at unmeasured DOFs can be then computed as:

$$\hat{\mathbf{z}}_k^p = \mathbf{\Psi}^p\mathbf{p}_k = \mathbf{\Psi}^p\mathbf{\Psi}^{o\dagger}\mathbf{z}_k^o. \tag{3.7}$$

This method will be referred in this dissertation as CMS-ME.

3.2 Kitanidis filter

The Kitanidis filter [75, 76] is a linear state estimator which has been conceived to operate in presence of unknown system inputs so that the latter does not affect the produced state estimation. The design of the Kitanidis filter relies on a one-step minimization of the trace of the estimate covariance matrix $\mathbf{P}$ defined in Eq. 2.20. Given the BDM in Eq. 2.18, a distinction between known and unknown input vectors can be made, yielding:

$$\begin{cases} \mathbf{x}_k = \mathbf{A}_d\mathbf{x}_{k-1} + \mathbf{B}_d\mathbf{u}_{k-1} + \mathbf{E}_d\mathbf{f}_{k-1} + \mathbf{w}_{k-1} \\ \mathbf{y}_k = \mathbf{C}\mathbf{x}_k + \mathbf{G}\mathbf{u}_k + \mathbf{v}_k \end{cases} \tag{3.8}$$

where $\mathbf{u}$ and $\mathbf{f}$ are respectively the known and unknown input vectors. It is worth noting that the Kitanidis filter works for Linear Time Variant (LTV) systems, i.e., for BDMs with time-variant matrices. This property allows to adopt this estimator not only in presence of unknown inputs, but also in case unknown parameters are present. As anticipated in the introduction to this chapter, the problem of parameter estimation falls out of the scope of this dissertation and focus is shed on the input prediction problem. For this reason, the state-space matrices in Eq. 3.8 are assumed to be time-invariant. Starting from the system in Eq. 3.8, a generic recursive linear filter can be defined as:

$$\hat{\mathbf{x}}_k^+ = \mathbf{A}_d\hat{\mathbf{x}}_{k-1}^+ + \mathbf{B}_d\mathbf{u}_{k-1} + \mathbf{L}\mathbf{g}_k\left(\mathbf{y}_k - \mathbf{C}\mathbf{A}_d\hat{\mathbf{x}}_{k-1}^+ - \mathbf{C}\mathbf{B}_d\mathbf{u}_{k-1}\right) \tag{3.9}$$

where $\mathbf{Lg}$ is the filter gain matrix and a new notation for the prior/posterior estimates has been adopted for the sake of simplicity. According to this notation, the superscript $\square^-$ denotes the prior estimate of the QoI at the current time-step k, which was previously indicated via the subscript $\square_{k|k-1}$. The superscript $\square^+$ is instead used to denote the posterior estimate at k, previously defined by the subscript $\square_{k|k}$. The Kitanidis filter features a particular gain matrix with sequence $\mathbf{Lg}_{1:k} = (\mathbf{Lg}_1, \mathbf{Lg}_2, \cdots, \mathbf{Lg}_k)$ such that $\mathbf{Lg}_k$ is calculated via the following optimization problem:

$$\begin{aligned} &\mathbf{L}\mathbf{g}_k = \underset{\mathbf{L}\mathbf{g}_k}{\operatorname{argmin}}\, trace\left(\mathbf{P}_k\right) \\ &\mathbb{E}\left[\mathbf{x}_k - \hat{\mathbf{x}}_k\right] = 0 \quad \forall \quad \mathbf{f}_{0:k-1} = \left(\mathbf{f}_0, \cdots, \mathbf{f}_{k-1}\right). \end{aligned} \tag{3.10}$$

The Kitanidis filter can thus be referred to as an unbiased minimum variance filter since it is based on minimizing the trace of the estimate covariance matrix $\mathbf{P}$ under the unbiasedness constraint postulated in Eq. 3.10. The minimization problem in Eq. 3.10 can be expressed analytically by writing $\mathbf{P}_k$ as a function of the state-space matrices:

$$\mathbf{P}_k^+ = \mathbf{L}\mathbf{g}_k\left(\mathbf{C}\mathbf{P}_k^-\mathbf{C}^T + \mathbf{R}\right)\mathbf{L}\mathbf{g}_k^T - \mathbf{P}_k^-\mathbf{C}^T\mathbf{L}\mathbf{g}_k^T - \mathbf{L}\mathbf{g}_k\mathbf{C}\mathbf{P}_k^- + \mathbf{P}_k^-. \tag{3.11}$$

Imposing the derivatives of the trace of Eq. 3.11 equal to zero, the following expression is yielded:

$$2\left(\mathbf{C}\mathbf{P}_k^-\mathbf{C}^T + \mathbf{R}\right)\mathbf{L}\mathbf{g}_k^T - 2\mathbf{C}\mathbf{P}_k - 2\mathbf{C}\mathbf{E}_d\mathbf{\Lambda}_k^T = 0 \tag{3.12}$$

where $\mathbf{\Lambda}$ is the matrix of Lagrangian multipliers. The unbiasedness constraint in Eq. 3.10 can be also postulated as a function of the filter gain:

$$\mathbf{L}\mathbf{g}\mathbf{C}_k\mathbf{E}_{d_{k-1}} - \mathbf{E}_{d_{k-1}} = 0. \tag{3.13}$$

From Eqs. 3.11 and 3.13, the final expressions for the filter gain and the state covariance matrix is obtained:

$$\begin{aligned}\mathbf{Lg}_k =&\mathbf{P}_k^-\mathbf{C}^T\left(\mathbf{C}\mathbf{P}_k^-\mathbf{C}^T+\mathbf{R}\right)^{-1}+\left[\mathbf{E}_d-\mathbf{P}_k^-\mathbf{C}^T\left(\mathbf{C}\mathbf{P}_k^-\mathbf{C}^T+\mathbf{R}\right)^{-1}\mathbf{C}\mathbf{E}_d\right]\\&\times\left[\mathbf{E}_d^T\mathbf{C}^T\left(\mathbf{C}\mathbf{P}_k^-\mathbf{C}^T+\mathbf{R}\right)^{-1}\mathbf{C}\mathbf{E}_d\right]^{-1}\times\mathbf{E}_d^T\mathbf{C}^T\left(\mathbf{C}\mathbf{P}_k^-\mathbf{C}^T+\mathbf{R}\right)^{-1}\end{aligned}\tag{3.14}$$

$$\begin{aligned}\mathbf{P}_k^+ =&\mathbf{P}_k^- -\mathbf{P}_k^-\mathbf{C}^T\times\left(\mathbf{C}\mathbf{P}_k^-\mathbf{C}^T+\mathbf{R}\right)^{-1}\mathbf{C}\mathbf{P}_k^-+\left[\mathbf{E}_d-\mathbf{P}_k^-\mathbf{C}^T\left(\mathbf{C}\mathbf{P}_k^-\mathbf{C}^T+\mathbf{R}\right)^{-1}\mathbf{C}\mathbf{E}_d\right]\\&\times\left[\mathbf{E}_d^T\mathbf{C}^T\times\left(\mathbf{C}\mathbf{P}_k^-\mathbf{C}^T+\mathbf{R}\right)^{-1}\mathbf{C}\mathbf{E}_d\right]^{-1}\times\left[\mathbf{E}_d-\mathbf{P}_k^-\mathbf{C}^T\left(\mathbf{C}\mathbf{P}_k^-\mathbf{C}^T+\mathbf{R}\right)^{-1}\mathbf{C}\mathbf{E}_d\right]^T.\end{aligned}\tag{3.15}$$

3.3 Gillijns De Moor filter

The GDF has been proposed for input-state prediction of systems with no direct feedthrough in [74] and it has been extended for systems with a direct transmission term in [77]. An improvement of the method regarding instabilities due to the number of adopted sensors exceeding the model order has been suggested in [78]. The peculiarity of this estimator, which has been constructed on the basis of the Kitadinis filter, consists in its applicability to any type of load, as it does not require any a priori transition model for the unknown input. The GDF algorithm, which is offered in Alg. 11, operates in three stages: a first input estimation step, a measurement update and a prediction step.

Algorithm 11 GDF algorithm

for $k=1,2,...,n$ **do**
  (a) Input prediction:
  $\tilde{\mathbf{R}}_k=\mathbf{C}\mathbf{P}_{x_k}^-\mathbf{C}^T+\mathbf{R}$
  $\mathbf{Mg}_k=\left(\mathbf{G}^T\tilde{\mathbf{R}}_k^{-1}\mathbf{G}\right)^{-1}\mathbf{G}^T\tilde{\mathbf{R}}_k^{-1}$
  $\hat{\mathbf{x}}_k^-=\mathbf{A}_d\hat{\mathbf{x}}_{k-1}^+ +\mathbf{B}_d\hat{\mathbf{u}}_{k-1}$
  $\hat{\mathbf{u}}_k=\mathbf{Mg}_k\left(\mathbf{y}_k-\mathbf{C}\hat{\mathbf{x}}_k^-\right)$
  $\mathbf{P}_{u_k}^+=\left(\mathbf{G}^T\tilde{\mathbf{R}}_k^{-1}\mathbf{G}\right)^{-1}$
  (b) Measurement update:
  $\mathbf{Lg}_k=\mathbf{P}_{x_k}^-\mathbf{C}^T\tilde{\mathbf{R}}_k^{-1}$
  $\hat{\mathbf{x}}_k^+=\hat{\mathbf{x}}_k^-+\mathbf{Lg}_k\left(\mathbf{y}_k-\mathbf{C}\hat{\mathbf{x}}_k^- -\mathbf{G}\hat{\mathbf{u}}_k^+\right)$
  $\mathbf{P}_{x_k}^+=\mathbf{P}_{x_k}^-+\mathbf{Lg}_k\left(\tilde{\mathbf{R}}_k-\mathbf{G}\mathbf{P}_{u_k}^+\mathbf{G}^T\right)\mathbf{Lg}_k^T$
  $\mathbf{P}_{xu_k}^+=\mathbf{P}_{ux_k}^+=-\mathbf{Lg}_k\mathbf{G}\mathbf{P}_{u_k}^+$
  (c) State prediction:
  $\hat{\mathbf{x}}_{k+1}^-=\mathbf{A}_d\hat{\mathbf{x}}_k^+ +\mathbf{B}_d\hat{\mathbf{u}}_k$
  $\mathbf{P}_{x_{k+1}}^-=\begin{bmatrix}\mathbf{A}_d & \mathbf{B}_d\end{bmatrix}\begin{bmatrix}\mathbf{P}_{x_k}^+ & \mathbf{P}_{xu_k}^+\\ \mathbf{P}_{ux_k}^+ & \mathbf{P}_{u_k}^+\end{bmatrix}\begin{bmatrix}\mathbf{A}_d^T\\ \mathbf{B}_d^T\end{bmatrix}+\mathbf{Q}_k$
end for

In Alg. 11, $\mathbf{P}_{u_k}$ and $\mathbf{P}_{x_k}$ respectively denote the error covariance of the estimated input and state. $\mathbf{P}_{xu_k}$ instead indicates the state-input error cross-covariance.
The potentiality of the GDF has been demonstrated in literature for several structural dynamics applications. However, for the case studies analyzed within this dissertation, input-state estimators derived as direct extensions of the conventional KF, i.e., the AKF and the DKF presented next, have been preferred.

3.4 Augmented Kalman filter

The AKF is an algorithm for joint input-state estimation which relies on the so-called state augmentation, according to which a new augmented state vector is constructed by grouping the

system state vector and the unknown input vector. In doing so, the unknown input excitation can be treated as an additional variable to be estimated via a Kalman filtering scheme. Imposing that the structure is only excited by unknown loads embedded in the vector $\mathbf{u}$, the augmented state vector $\mathbf{x}^a \in \mathbb{R}^{2n_r+n_i}$ can be built as follows:

$$\mathbf{x}^a = \begin{bmatrix} \mathbf{x}^T & \mathbf{u}^T \end{bmatrix}^T. \tag{3.16}$$

In order to shape the unknown loads contained in the input vector $\mathbf{u}$ as states, the augmented representation in Eq. 3.17 is required for the SSM in Eq. 2.8:

$$\begin{cases} \dot{\mathbf{x}}^a(t) = \mathbf{A}^a \mathbf{x}^a(t) \\ \mathbf{y}(t) = \mathbf{C}^a \mathbf{x}^a(t) \end{cases}, \qquad \mathbf{A}^a = \begin{bmatrix} \mathbf{A} & \mathbf{B} \\ \mathbf{0} & \mathbf{I} \end{bmatrix}, \qquad \mathbf{C}^a = \begin{bmatrix} \mathbf{C} & \mathbf{G} \end{bmatrix}, \tag{3.17}$$

where $\mathbf{A}^a \in \mathbb{R}^{n_{aug} \times n_{aug}}$ is the augmented system matrix and $\mathbf{C}^a \in \mathbb{R}^{n_o \times n_{aug}}$ is the augmented output matrix, with $n_{aug} = 2n_r + n_i$. In Eq. 3.17, a RW model [49, 135, 136] has been adopted to model the input dynamics due to lack of prior information regarding the loads acting on the structure. The time-discrete version of the input (load) RW model is:

$$\mathbf{u}_k = \mathbf{u}_{k-1} + \mathbf{w}^u_{k-1} \tag{3.18}$$

where $\mathbf{w}^u$ a vector of zero-mean white uncorrelated processes with associated covariance matrix $\mathbf{Q}^u \in \mathbb{R}^{n_i \times n_i}$. Hence, the diagonal elements of $\mathbf{Q}^u$ represent the variance of the unknown inputs increments in time.
Transforming the continuous SSM in Eq. 3.17 into the time-discrete BDM form, the following formulation can be derived:

$$\begin{cases} \mathbf{x}^a_k = \mathbf{A}^a_d \mathbf{x}^a_{k-1} + \mathbf{w}^a_{k-1} \\ \mathbf{y}_k = \mathbf{C}^a \mathbf{x}^a_k + \mathbf{v}_k. \end{cases} \tag{3.19}$$

In Eq. 3.19, $\mathbf{w}^a = \begin{bmatrix} \mathbf{w}^T & \mathbf{w}^{u^T} \end{bmatrix}^T$ is the augmented process noise vector with associated noise covariance matrix $\mathbf{Q}^a \in \mathbb{R}^{n_{aug} \times n_{aug}} = \mathbb{E}\{\mathbf{w}^a_k \mathbf{w}^{a^T}_l\} = \begin{bmatrix} \mathbf{Q} & \mathbf{0} \\ \mathbf{0} & \mathbf{Q}^u \end{bmatrix} \geq 0$, where $\mathbf{Q} \in \mathbb{R}^{2n_r \times 2n_r} = \mathbb{E}\{\mathbf{w}_k \mathbf{w}^T_l\}$ takes into account uncertainties related to the system states.

Equations 3.16 and 3.19 indicate that the input location has to be known in order to build the augmented state-space representation. In Eq. 3.19, the output matrix is obtained as $\mathbf{C}^a = \begin{bmatrix} \mathbf{C} & \mathbf{G} \end{bmatrix}$, while matrix $\mathbf{A}^a_d$ formulation depends on the chosen discretization scheme. The exponential time integration scheme adopted in Eq. 2.17 for the non-augmented state-space matrices has been also employed for this application.

A KF tailored to the discrete-time BDM in Eq. 3.19, i.e., the AKF, can be built to perform recursive estimation of the augmented state vector mean $\hat{\mathbf{x}}^a$ and covariance $\mathbf{P}_k = \mathbb{E}\{(\mathbf{x}^a_k - \hat{\mathbf{x}}^a_k)(\mathbf{x}^a_k - \hat{\mathbf{x}}^a_k)^T\}$, also known as error covariance matrix. The AKF algorithm in described in Alg. 12 and the working principle of the AKF is presented in Fig. 3.1 through a block diagram scheme.

Algorithm 12 AKF algorithm

1: **for** $k = 1, 2, ..., n$ **do**
2: (a) Kalman prediction:
3: $\hat{\mathbf{x}}^{a-}_k = \mathbf{A}^a_d \hat{\mathbf{x}}^{a+}_{k-1}$
4: $\mathbf{P}^-_k = \mathbf{A}^a_d \mathbf{P}^+_{k-1} \mathbf{A}^{aT}_d + \mathbf{Q}^a$
5: (b) Kalman update:
6: $\mathbf{Kg}_k = \mathbf{P}^-_k \mathbf{C}^{aT} \left(\mathbf{C}^a \mathbf{P}^-_k \mathbf{C}^{aT} + \mathbf{R} \right)^{-1}$
7: $\hat{\mathbf{x}}^{a+}_k = \hat{\mathbf{x}}^{a-}_k + \mathbf{Kg}_k \left(\mathbf{y}_k - \mathbf{C}^a \hat{\mathbf{x}}^{a-}_k \right)$
8: $\mathbf{P}^+_k = \left(\mathbf{I} - \mathbf{Kg}_k \mathbf{C}^a \right) \mathbf{P}^-_k$
9: **end for**

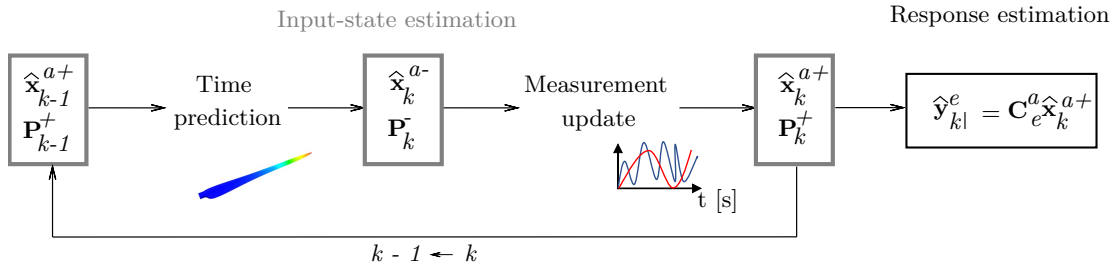

Figure 3.1: AKF algorithm scheme

Once the estimated augmented state vector $\hat{\mathbf{x}}_k^{a+}$ has been obtained, it can be used for predicting the vector $\hat{\mathbf{y}}_k^e$ of the n_e unmeasured responses using the following formula:

$$\hat{\mathbf{y}}_k^e = \mathbf{C}_e^a \hat{\mathbf{x}}_k^{a+} \tag{3.20}$$

where $\mathbf{C}_e^a$ is the augmented output matrix computed at the DOFs where the response has to be estimated.

3.5 Dual Kalman filter

The DKF is an alternative approach for simultaneous input-state estimation which relies on a dual implementation of the standard KF. This results into a separation of the input and state predictions into two different stages. The RW model in Eq. 3.18 is adopted for this purpose and it is joined to the output equation to build a further SSM:

$$\begin{cases} \mathbf{u}_k = \mathbf{u}_{k-1} + \mathbf{w}_{k-1}^u \\ \mathbf{y}_k = \mathbf{C}\mathbf{x}_k + \mathbf{G}\mathbf{u}_k + \mathbf{v}_k. \end{cases} \tag{3.21}$$

In Eq. 3.21, the unknown input $\mathbf{u}_k$ is treated as the state to be estimated via a first KF whereas the system state vector plays the role of a known input to the system. The predicted input vector is used as a known variable to predict the system state in a second KF which is constructed on the SSM in Eq. 2.18. The two prediction steps are performed subsequently at each time step. The DKF algorithm is described in detail in Alg. 13, where the notation for the prior/posterior estimates previously introduced for the AKF is adopted. This procedure needs initialization of both the system state and the input, i.e., expected values for their mean $\hat{\mathbf{x}}_0^-$, $\hat{\mathbf{u}}_0^-$ and covariance $\mathbf{P}_0^-$, $\mathbf{P}_0^{u-}$ must be defined a priori.

Algorithm 13 DKF algorithm

for $k = 1, 2, ..., n$ **do**
  (a) Input prediction:
  $\hat{\mathbf{u}}_k^- = \hat{\mathbf{u}}_{k-1}^+$
  $\mathbf{P}_k^{u-} = \mathbf{P}_{k-1}^{u+} + \mathbf{Q}^u$
  (b) Input update:
  $\mathbf{Kg}_k^u = \mathbf{P}_k^{u-}\mathbf{G}^T\left(\mathbf{G}\mathbf{P}_k^{u-}\mathbf{G}^T + \mathbf{R}\right)^{-1}$
  $\hat{\mathbf{u}}_k^+ = \hat{\mathbf{u}}_k^- + \mathbf{Kg}_k^u\left(\mathbf{y}_k - \mathbf{C}\hat{\mathbf{x}}_{k-1}^+ - \mathbf{G}\mathbf{u}_k^-\right)$
  $\mathbf{P}_k^{u+} = \left(\mathbf{I} - \mathbf{Kg}_k^u\mathbf{G}\right)\mathbf{P}_k^{u-}$
  (c) State prediction:
  $\hat{\mathbf{x}}_k^- = \mathbf{A}_d\hat{\mathbf{x}}_{k-1}^+ + \mathbf{B}_d\hat{\mathbf{u}}_k^+$
  $\mathbf{P}_k^- = \mathbf{A}_d\mathbf{P}_{k-1}^+\mathbf{A}_d^T + \mathbf{Q}$
  (d) State update:
  $\mathbf{Kg}_k^x = \mathbf{P}_k^-\mathbf{C}^T\left(\mathbf{C}\mathbf{P}_k^-\mathbf{C}^T + \mathbf{R}\right)^{-1}$
  $\hat{\mathbf{x}}_k^+ = \hat{\mathbf{x}}_k^- + \mathbf{Kg}_k^x\left(\mathbf{y}_k - \mathbf{C}\hat{\mathbf{x}}_k^- - \mathbf{G}\hat{\mathbf{u}}_k^+\right)$
  $\mathbf{P}_k^+ = \left(\mathbf{I} - \mathbf{Kg}_k^x\mathbf{C}\right)\mathbf{P}_k^-$
end for

Once the estimated state vector $\hat{\mathbf{x}}_k^+$ and unknown input $\hat{\mathbf{u}}_k^+$ have been computed, they can be used for predicting the vector $\hat{\mathbf{y}}_k^e$ of the n_e unmeasured responses using the following formula:

$$\hat{\mathbf{y}}_k^e = \mathbf{C}_e \hat{\mathbf{x}}_k^+ + \mathbf{G}_e \hat{\mathbf{u}}_k^+ \tag{3.22}$$

where $\mathbf{C}_e^a$ is the augmented output matrix computed at the DOFs where the response has to be estimated. A schematic representation of the DKF algorithm is offered in Fig. 3.2.

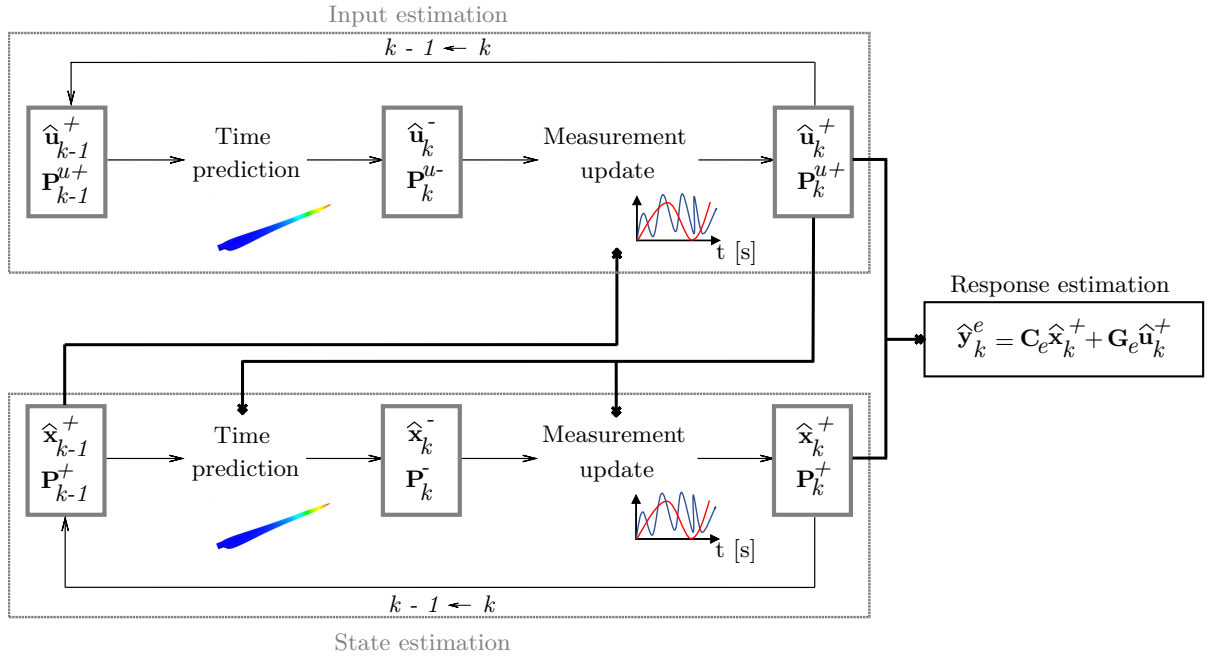

Figure 3.2: DKF algorithm scheme

3.6 Summary

The data assimilation methods exploited in this thesis for VS in structural dynamics are described in this chapter. The problem of response estimation is first treated in a deterministic setting by reporting on the ME approach and proposing an improvement of the method, i.e., the so-called CMS-ME approach. The Kitadininis and the GDF algorithms are then described. This chapter also presents the AKF and DKF algorithms as state-of-the-art Bayesian estimators of inputs and states.

4

ADAPTIVE NOISE MODELING FOR BAYESIAN INPUT-STATE ESTIMATION

Within the context of Bayesian filtering, the assumption of a priori knowledge of the process and measurement noise statistics is commonly placed. These terms, which have been introduced in Section 2.2, are used in a stochastic framework to reflect the uncertainties that stem from modeling errors/approximations and measurement noise in the system representation. Additionally, for specific cases in which response estimation is coupled with input prediction, the process noise term also embeds uncertainty regarding the loading conditions. These two noise variables are commonly assumed to be independent, zero-mean white noise processes and the corresponding covariance matrices are treated as time-invariant quantities. The selection of erroneous values for the process and measurement noise covariance matrices can produce a large drop in the estimators accuracy. These values are typically not known and offline tuning procedures are adopted to select them [82, 83, 84, 39, 51, 52]. Within this setting, a common approach is to prescribe the measurement noise covariance by exploiting the available physical sensors specifications. An optimization procedure regarding the process noise term is then put in place in a rather heuristic manner, i.e., either by trial and error or by means of regularization schemes, such as the L-curve [85]. Besides its offline nature, this method often generates a plot which exhibits a non-perfect L-shape, thus hindering the interpretation of the regularization results for several Kalman-type filters, e.g. the AKF [49] and the DKF [52]. This limitation is mainly caused by the formulation of the norms adopted within the L-curve, which is often unsuitable for representing the actual estimation inaccuracies. Additionally, the relationship between these norms is non-trivial for real-life experiments due to external sources of uncertainty which may act on the analyzed system. The employment of regularization schemes is also limited to the use cases in which only one parameter is to be calibrated. The working principle behind the L-curve has been adapted and used for simultaneously tuning more than one term in [86, 41]. An online alternative to the previously mentioned methods for identifying the disturbances consists in using adaptive filtering techniques for both the process and measurement noise terms [43]. These approaches can be classified into four main categories [87]: Bayesian [88], maximum-likelihood estimation [89], correlation [90, 91, 92, 93] and covariance matching [94] methods. These methods comprise generic adaptive filtering strategies, which are typically characterized by excessive computational times. Additionally, the majority of these techniques are based on seeking the most suitable process and measurement noise covariance matrices steady-state estimates, rather then their current optimal values.

The present chapter describes the effect of the selected noise terms on Kalman-based filters accuracy. As most of the attention in this dissertation is placed on the input-state estimation problem for structural dynamics applications, this chapter further treats the use of conventional methods for process noise covariance tuning in an input-state estimation framework. In this view, a more intuitive approach is then proposed in this chapter for adaptive process noise covariance matrix tuning using the AKF. In this context, both the terms modeling the states and the unknown input uncertainties are taken into consideration for optimization. Moreover, the covariance matrix of the "augmented" process noise is considered to be time-variant, since the modeling uncertainty and the dynamic characteristics of the unknown load may vary in time. The developed method, addressed as A-AKF, is based on reference response estimates built using the CMS-ME approach presented in Chapters 3.

4.1 Effect of noise covariance matrix selection on the Kalman filter performance

In Section 2.2, the BDM of Eq. 2.18 has been derived from a conventional SSM via integration of the process and measurement noise terms, i.e., mutually uncorrelated zero-mean white noises used to respectively represent modeling uncertainties and noise affecting the measurements. These two noise terms are defined by the values of their respective covariance matrices $\mathbf{Q}$ and $\mathbf{R}$. When dealing with input-state estimation, the process noise covariance matrix can be distinguished into the actual $\mathbf{Q}$ associated to the original system state vector $\mathbf{x}$ and $\mathbf{Q}^u$, which instead embeds the unknown input uncertainty. In specific situations in which the AKF is employed for simultaneous prediction of the states and the unknown loads, the process noise covariance matrices associated to the two vectors $\mathbf{x}$ and $\mathbf{u}$ are concatenated into the "augmented" process noise covariance matrix $\mathbf{Q}^a \in \mathbb{R}^{n_{aug} \times n_{aug}} = \mathbb{E}\{\mathbf{w}_k^a \mathbf{w}_l^{a^T}\} = \begin{bmatrix} \mathbf{Q} & \mathbf{0} \\ \mathbf{0} & \mathbf{Q}^u \end{bmatrix} \geq 0$. Algorithms 3, 12 and 13 show that each of the mentioned covariance matrices appear in the analyzed Kalman-based algorithms, therefore implying that their values can significantly drive the achievable estimation results [137].
To provide a clear explanation about the role of these noise terms in the estimation, the KF update equations for a uni-variate distribution example are hereby postulated:

$$Kg = \frac{c\sigma_Q^2}{\sigma_R^2 + c^2\sigma_Q^2} \tag{4.1}$$

$$\mu = \mu_m + Kg(y - c\mu_m - gu) \tag{4.2}$$

$$\sigma^2 = \sigma_Q^2 - cKg\sigma_Q^2. \tag{4.3}$$

In Eq. 4.1, σ_Q^2 and σ_R^2 are respectively the process and measurement noise variances. Assuming that c, a transformation scalar value, is equal to one, two extreme cases can be analyzed. In the first scenario, the process noise variance σ_Q^2 is assigned a high value and the measurement noise variance σ_R^2 is close to zero such that $\sigma_Q^2 \gg \sigma_R^2$. The Kalman gain would then be close to 1. Re-evaluating Eq. 4.1, the following expressions are obtained:

$$\begin{aligned} Kg &\sim \frac{\sigma_Q^2}{\sigma_Q^2 + 0} \Leftrightarrow Kg \sim 1 \\ \mu &\sim \mu_m + (y - \mu_m - gu) \Leftrightarrow \mu \sim y - gu \\ \sigma^2 &\sim \sigma_Q^2 - \sigma_Q^2 \Leftrightarrow \sigma^2 \sim 0 \end{aligned} \tag{4.4}$$

This implies that a process noise variance higher than the measurement noise variance generates a high Kalman gain, and hence induces the KF to correct more the mean and covariance predictions through the measurements. To the contrary, if the measurement noise variance has a high value and the process noise variance is close to zero such that $\sigma_R^2 \gg \sigma_Q^2$, the Kalman gain results in a very contained value (close to 0). Substituting in Eq. 4.1 yields:

$$\begin{aligned} Kg &\sim \frac{0}{0 + \sigma_R^2} \Leftrightarrow Kg \sim 0 \\ \mu &\sim \mu_m + (0)(y - \mu_m - gu) \Leftrightarrow \mu \sim \mu_m \\ \sigma^2 &\sim \sigma_Q^2 - (0)\sigma_Q^2 \Leftrightarrow \sigma^2 \sim \sigma_Q^2. \end{aligned} \tag{4.5}$$

The equations in Eq. 4.5 imply that a measurement noise covariance higher than the process noise covariance generate a lower Kalman gain value, introducing a lower correction of the mean and covariance predictions through the measurements. The validity of the extrapolated logic, which is depicted in Fig. 4.1, can be expanded to the multivariate case.

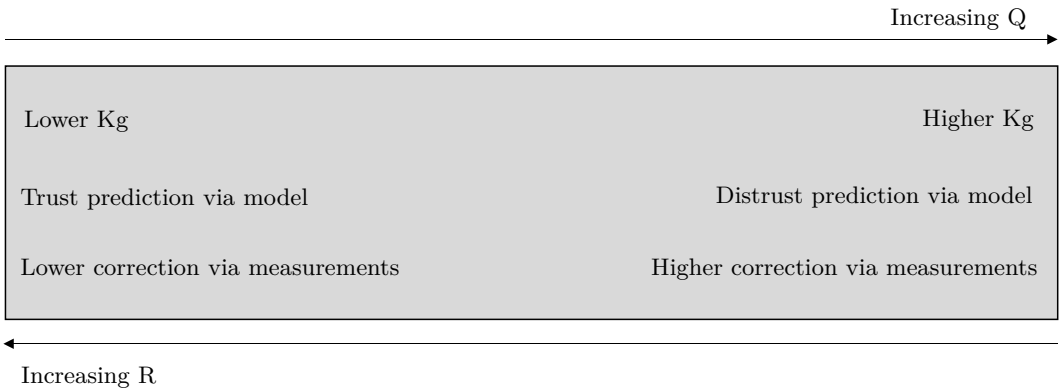

Figure 4.1: Effect of the selected noise covariance matrices on the KF working principle

Figure 4.1 visually describes the KF functioning with respect to the noise covariance matrices selection, which defines how the information carried by the model and the measurements is weighted, thus determining the adjustment of their effect on the estimation results. The reported logic is essential for the correct functioning of the KF and must be therefore taken into account in every situation in which a Kalman-based estimator is employed for recursive prediction of QoI. This results into a necessary tuning step, which must always be put into place prior to online employment of the estimator. The most common approach for tuning of the noise covariance matrices consists in setting $\mathbf{R}$ via the available physical sensors specifications and installing a trial and error scheme for selecting $\mathbf{Q}$. The latter relies on the generic guidelines expressed in Fig. 4.1, according to which a balance is sought after basing on the trust posed by the user in the model/measurements. It is worth noting that this process is not always straightforward and several runs might be needed to find the noise covariance matrices optimal values, i.e., values which minimize the estimation error in the specific analyzed circumstances. This renders the estimation via Bayesian filtering strongly user-dependent and not easily applicable for real-time inference, especially when no reference is available to evaluate the accuracy of the achieved predictions. An online alternative consists in using techniques based on adaptive filtering schemes [87] developed for generic use of Kalman-type filters. These approaches imply high computational effort and require adaptation to the specific estimator and application domain. Moreover, they are often limited to the identification of steady-state estimates of both the process and the measurement noise covariance matrices.

4.2 Process noise covariance selection for input-state estimation via Kalman-based estimators

When joint input-state estimation is pursued, the augmented process noise covariance matrix can be written as a block diagonal matrix $\mathbf{Q}^a = \begin{bmatrix} \mathbf{Q} & \mathbf{0} \\ \mathbf{0} & \mathbf{Q}^u \end{bmatrix} \geq 0$ with diagonal $\mathbf{Q}$ and $\mathbf{Q}^u$ under the assumption of uncorrelated noise sources. While the diagonal elements of $\mathbf{Q}$ are typically assigned a constant value that is very low when compared against the order of magnitude of the state vector, the process noise covariance matrix $\mathbf{Q}^u$ associated to the unknown input is treated as a regularization matrix, especially when joint input-state estimation is performed through the AKF. This common practice derives from the dependence of the smoothness of the estimation on $\mathbf{Q}^u$, which can be therefore tuned to tackle the ill-conditioning of the problem [49, 50, 138]. In doing so, the resulting diagonal elements of $\mathbf{Q}^u$, i.e., the uncertainty related to the unknown inputs, are typically higher than the ones associated to the regular states (reflecting mostly modeling errors). The diagonal elements of $\mathbf{Q}^u$ are commonly assigned by either setting a standard regularization parameter estimation, e.g. the L-curve [85], or via trial and error. The latter depends on the user expertise and does not provide a unique solution to the problem. On the other hand, the L-curve does not exhibit its standard L-shape when used for input-state estimation via use of the AKF with experimental data [49, 52, 139], which renders the estimation of the regularization parameter

user-dependent. This behavior is commonly not encountered for fully simulated data sets in absence of process noise [140, 141]. It is also worth noting that regularization parameter values obtained through the L-curve are related to the optimal estimates of the measured responses, which do not necessarily imply optimized predictions for the unmeasured quantities. Moreover, both the L-curve and the trial and error schemes may only be applied in an offline fashion, preventing real-time applicability. The applicability of the L-curve will be tested for some of the case studies analyzed within this dissertation, for which it will be adopted as reference covariance tuning method.

4.2.1 Adaptive-noise Augmented Kalman filter

In this work, an automated procedure for estimating the optimal $\mathbf{Q}^a$ matrix for joint input-state estimation in a near-online fashion is presented. Specifically, the simultaneous tuning of both $\mathbf{Q}$ and $\mathbf{Q}^u$ is proposed. The matrix optimality expression is based on the minimization of an overall error estimate which takes into account the prediction inaccuracy of the quantities of interest, i.e., unknown input vector and measured and unmeasured responses. The process relies on the following assumptions:

- The process noise covariance $\mathbf{Q}$ is assumed to be fully determined by two parameters, i.e., two distinct covariance values respectively assigned across all the displacement and all the velocity components of the state vector. This assumption allows to adopt different noise levels for displacement and velocity components in order to account for their amplitude discrepancy. On the other hand, a different input process noise covariance component is assigned to each unknown load entry. Matrices $\mathbf{Q}$ and $\mathbf{Q}^u$ can be expressed as $\mathbf{Q} = \begin{bmatrix} q^{n_d}\mathbf{I} & \mathbf{0} \\ \mathbf{0} & q^{n_v}\mathbf{I} \end{bmatrix}$ with $\mathbf{I} \in \mathbb{R}^{n_r \times n_r}$ and $\mathbf{Q}^u = \mathbf{q}^u\mathbf{I}$ with $\mathbf{I} \in \mathbb{R}^{n_i \times n_i}$ and $\mathbf{q}^u = \begin{bmatrix} q_1^u \dots q_{n_i}^u \end{bmatrix}^T$. For the sake of simplicity, the situation in which the structure is subjected to a single excitation source is considered in what follows. While the reported methodology will thus address three scalar quantities q^{n_d}, q^{n_v} and q^u, it should be stated that it is straightforward to generalize for more excitation sources. The procedure can be easily extended for the case of multiple loads by including all the elements of $\mathbf{q}^u$ in the set of scalar quantities to be optimally selected.

- The standard $\mathbf{Q}^a$ matrix estimation procedure treats this matrix as time-invariant, implying that the same expression is adopted for the AKF at each k^{th} iteration [85, 52, 86, 44]. To the contrary, the hereby proposed methodology assumes a time-variant $\mathbf{Q}^a$ matrix, which is updated every N time-steps. This hypothesis allows to select the optimal augmented process noise covariance matrix in near real-time, allowing to perform input-state prediction while measurements acquisition is running.

- The proposed approach does not require user intervention, except for an a priori assumption regarding the ranges within which q^{n_d}, q^{n_v} and q^u can vary: $q_{min}^{n_d} \leq q^{n_d} \leq q_{max}^{n_d}$, $q_{min}^{n_v} \leq q^{n_v} \leq q_{max}^{n_v}$ and $q_{min}^u \leq q^u \leq q_{max}^u$. As will be demonstrated in Chapter 7, the correct functioning of the algorithm is guaranteed for large ranges, thus rendering the method user-independent.

The herein presented methodology can be applied starting from the a priori selected bounds for q^{n_d}, q^{n_v} and q^u. Suitable values for each variable are sampled in the assigned range on a logarithmic uniformly distributed scale. In order to ensure that the displacement and velocity components are differentiated, the ranges associated to q^{n_d} and q^{n_v} are set to be equivalent and a constraint between the corresponding sampled values within these ranges is imposed. M combinations of q^{n_d}, q^{n_v} and q^u, i.e., M distinct $\mathbf{Q}^a$ matrices, can be derived from the sampled values. Figure 4.2 shows a block diagram scheme for the developed A-AKF. The algorithm operates by running a bank of filters (AKF) in parallel, one for each of the generated M $\mathbf{Q}^a$ samples, for N time-steps. For the N-steps window, an overall error estimate $\bar{E}$ is computed for each candidate AKF and minimized to select the optimal $\mathbf{Q}^a$. The latter is adopted to derive the best estimates for the state vector, error covariance matrix and responses throughout the N-steps window. The estimated $\hat{\mathbf{x}}_{k+N}^{a+}$ and $\mathbf{P}_{k+N}^{+}$ are used

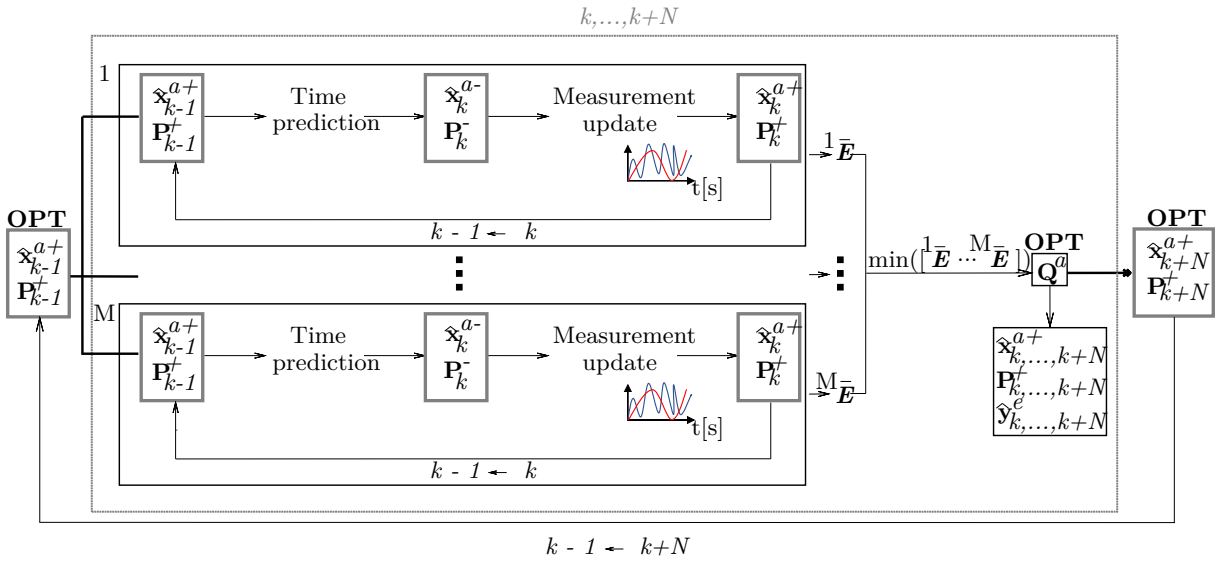

Figure 4.2: A-AKF scheme

as input for the estimation at step $k+N+1$. The employed error quantification for each of the parallely run filters needs to account for imprecision in both the input and measured/unmeasured response estimates during the N-steps batch. To do so, the overall error estimate is formulated as:

$$\bar{E} = \|\mathbf{E}\|_2, \quad \mathbf{E} = \begin{bmatrix} E^o & E^p & E^u \end{bmatrix}^T \tag{4.6}$$

where E^u represents the unknown input prediction error, while E^o and E^p respectively quantify the prediction error for the measured and unmeasured responses. Equation 4.6 postulates that the estimated quantities for both the measured and unmeasured responses must be taken into account in the error quantification equation, offering global insights into the AKF response prediction accuracy during the analyzed time window. The measured and unmeasured responses can be calculated via evaluation of Eq. 3.20 for both $\hat{\mathbf{y}}^o_{k,\dots,k+N}$ and $\hat{\mathbf{y}}_{k,\dots,k+N}{}^e$ by selecting the appropriate output matrix. The error estimates for the unknown input, re-estimated observations and the predicted responses have been formulated after practical implementation of the A-AKF on different structures and for different type of excitation signals. Indeed, the outcome observed from the use of this approach for the case studies presented in this dissertation led to the identification of prediction inaccuracy indicators to be used in the algorithm in order to cover several hypothetical scenarios. The adopted error estimate for the unknown input, the re-estimated observations and the predicted responses for each N-steps window are reported next for two common excitation scenarios in structural testing.

4.2.1.1 Pull and release excitation

Pull and release tests are typically performed on WT blades in a laboratory environment to easily determine their modal parameters from output-only measurements. During this type of tests, the blade is clamped at the root and pulled downward by making use of a bungee applied at a certain distance from the clamping. Once the blade tip reaches the desired displacement, it is released and the free vibration response, i.e., a free decay type of response, recorded. In this scenario, the prediction inaccuracy regarding the measured (observed) quantities can be straightforwardly quantified by means of the following estimate:

$$E^o = \frac{1}{n_o}\sqrt{\sum_{l=1}^{n_o}\left(\text{argmin}_\theta \|\theta \mathbf{y}^o_l - (\mathbf{y}^o_l - \hat{\mathbf{y}}^o_l)\|_2\right)^2} \tag{4.7}$$

where $\mathbf{y}^o_l = \begin{bmatrix} y^o_{l_1} \dots y^o_{l_j} \dots y^o_{l_N} \end{bmatrix}$ is the response acquired at the l^{th} measured DOF, i.e., $1 \leq l \leq n_o$, during the current window ($1 \leq j \leq N$). Similarly, $\hat{\mathbf{y}}^o_l = \begin{bmatrix} \hat{y}^o_{l_1} \dots \hat{y}^o_{l_j} \dots \hat{y}^o_{l_N} \end{bmatrix}$ is the response re-

estimated by the AKF at the l^{th} measured DOF at the N time-steps within the current time batch. The term θ in Eq. 4.7 is the scalar result of the least-squares solution of a system of linear equations $\theta \mathbf{y}_l^o = (\mathbf{y}_l^o - \hat{\mathbf{y}}_l^o)$ for the l^{th} measured response, where $\mathbf{y}_l^o \in \mathbb{R}^N$ and $(\mathbf{y}_l^o - \hat{\mathbf{y}}_l^o) \in \mathbb{R}^N$. The latter vector quantifies the deviation between the re-estimated and the measured signals at each time-step, while the vector $\mathbf{y}_l^o$ is used to normalize this deviation in order to get a dimensionless estimate. For the pull and release excitation scenario, the least-squares formulation in Eq. 4.7 has been preferred to other types of estimates, e.g. mean value of N instantaneous errors, since it allows for a smoothed error estimate over the N time-steps which guarantees stable input and response predictions for large q^{n_d}, q^{n_v} and q^u range bounds. This exempts the A-AKF user from the need of selecting ad hoc bounds for the variables to be tuned.
In order to quantify the prediction error for the unmeasured (predicted) response quantities, the formulation in Eq. 4.7 can be reformulated as follows:

$$E^p = \frac{1}{n_e} \sqrt{\sum_{l=1}^{n_e} \left(\text{argmin}_\beta \| \beta \mathbf{y}_l^e - (\mathbf{y}_l^e - \hat{\mathbf{y}}_l^e) \|_2 \right)^2} \tag{4.8}$$

where $\hat{\mathbf{y}}_l^e = \left[\hat{y}_{l_1}^e \dots \hat{y}_{l_j}^e \dots \hat{y}_{l_N}^e \right]$ is the response estimated by the AKF during the current window at the l^{th} unmeasured DOF, i.e., $1 \leq l \leq n_e$, and $\mathbf{y}_l^e$ is its actual value. Being the latter quantity not available, the A-AKF adopts a reference estimate $\hat{\mathbf{z}}_k^p$ computed via the CMS-ME method, yielding:

$$E^p = \frac{1}{n_e} \sqrt{\sum_{l=1}^{n_e} \left(\text{argmin}_\beta \| \beta \hat{\mathbf{z}}_l^p - (\hat{\mathbf{z}}_l^p - \hat{\mathbf{y}}_l^e) \|_2 \right)^2} \tag{4.9}$$

where $\hat{\mathbf{z}}_l^p = \left[\hat{z}_{l_1}^p \dots \hat{z}_{l_j}^p \dots \hat{z}_{l_N}^p \right]$ and $\hat{\mathbf{y}}_l^e$ are the responses respectively estimated by the CMS-ME approach and the AKF at the l^{th} unmeasured DOF, i.e., $1 \leq l \leq n_e$, during the current time batch $(1 \leq j \leq N)$.
To what concerns the input prediction error, when the AKF is generally adopted for input-state estimation, this is intrinsically contained in the error covariance matrix $\mathbf{P}$. The latter is indeed defined as:

$$\mathbf{P} = \begin{bmatrix} \mathbf{P}^{nn} & \mathbf{P}^{nu} \\ \mathbf{P}^{un} & \mathbf{P}^{uu} \end{bmatrix} \tag{4.10}$$

where $\mathbf{P}^{uu} = \mathbb{E}\{ (\mathbf{u} - \hat{\mathbf{u}}) (\mathbf{u} - \hat{\mathbf{u}})^T \} \in \mathbb{R}^{n_i \times n_i}$ expresses the covariance of the unknown input error. For the sake of clarity, the explicit time dependency in Eq. 4.10 has been omitted. The diagonal elements of this matrix represent the variance of each unknown input estimation error. The error term for a single input prediction $\hat{u}$, during the current N-steps window, is therefore expressed as follows:

$$E^u = \sqrt{\frac{1}{N} \sum_{j=k}^{k+N} \frac{P_j^{uu}}{\hat{u}_j^2}} \tag{4.11}$$

where the squared amplitude of the corresponding estimated input at each j^{th} time-step within the window $\hat{u}_j^2$ has been used for normalization. By considering zero cross-correlation of noise sources, or in other words zero diagonal entries for $\mathbf{P}^{uu}$, the hereby presented approach works under the assumption that negligible cross-correlation terms (both between the various inputs and between the states and the inputs) are encountered. It is worth noting that adjustments of the method may be needed in case large off-diagonal terms are expected in the $\mathbf{P}$ matrix. In case of multiple excitation sources, the error E^u computed for each input can be included in the vector $\mathbf{E}$.

4.2.1.2 Random excitation

Random signals are commonly adopted for testing of structures as they reproduce everyday life excitation scenarios thanks to their non-predictable nature. Indeed, a random vibration test is to be considered realistic as it allows to excite all the frequencies within a selected spectrum at any

time. In this specific circumstances, the prediction inaccuracy related to the measured (observed) quantities has been quantified by means of the following estimate:

$$E^o = \frac{1}{n_o}\sqrt{\sum_{l=1}^{n_o}\left(\frac{RMSE_{\hat{\mathbf{y}}_l^o}}{std(\mathbf{y}_l^o)}\right)^2}, \quad RMSE = \sqrt{\sum_{j=k}^{k+N}\frac{(\hat{\mathbf{y}}_{l_j}^o - \mathbf{y}_{l_j}^o)^2}{N}} \tag{4.12}$$

where $\mathbf{y}_l^o = \left[y_{l_1}^o \dots y_{l_j}^o \dots y_{l_N}^o\right]$ is the response acquired at the l^{th} measured DOF, i.e., $1 \leq l \leq n_o$, during the current window ($1 \leq j \leq N$). Similarly, $\hat{\mathbf{y}}_l^o = \left[\hat{y}_{l_1}^o \dots \hat{y}_{l_j}^o \dots \hat{y}_{l_N}^o\right]$ is the response re-estimated by the AKF at the l^{th} measured DOF at the N time-steps within the current time batch. This formulation differs from the one proposed in Eq. 4.7 since the least-squares solution employed for the pull and release excitation would have averaged the error quantification, thus smoothing the resulting response estimates. To the contrary, the expression postulated in Eq. 4.12 guarantees a limited averaging effect as it relies on i) the Root Mean Square Error (RMSE) between the measured and the re-estimated quantities and ii) on the standard deviation, i.e., the variability, of the measured responses.
The prediction error for the unmeasured (predicted) response quantities can be postulated adapting the expression in Eq. 4.12 for the vector $\hat{\mathbf{y}}_l^e$ by exploiting the CMS-ME predictions $\hat{\mathbf{z}}_l^p$ as references:

$$E^p = \frac{1}{n_e}\sqrt{\sum_{l=1}^{n_e}\left(\frac{RMSE_{\hat{\mathbf{y}}_l^e}}{std(\hat{\mathbf{z}}_l^p)}\right)^2}, \quad RMSE = \sqrt{\sum_{j=k}^{k+N}\frac{(\hat{\mathbf{y}}_{l_j}^o - \hat{\mathbf{z}}_{l_j}^p)^2}{N}} \tag{4.13}$$

where $\hat{\mathbf{z}}_l^p = \left[\hat{z}_{l_1}^p \dots \hat{z}_{l_j}^p \dots \hat{z}_{l_N}^p\right]$. Following what reported in Subsubsection 4.2.1.1, the input prediction error can be expressed in function of the unknown input error covariance $\mathbf{P}^{uu}$ for the random excitation scenario as well. Specifically, the following formula can be employed to compute the input inaccuracy indicator:

$$E^u = \frac{\sqrt{\frac{1}{N}\sum_{j=k}^{k+N} P_j^{uu}}}{|std(\hat{\mathbf{u}})|} \tag{4.14}$$

where $\mathbf{u} = \left[\hat{u}_1 \dots \hat{u}_j \dots \hat{u}_N\right]$. The standard deviation of $\mathbf{y}_l^o$, $\hat{\mathbf{z}}_l^p$ and $\hat{\mathbf{u}}$ in the current time-batch are used in Eqs. 4.12, 4.13 and 4.14 to normalize, for a signal with random nature, the deviation quantified by the numerators in order to obtain a dimensionless estimate. In Eqs. 4.7, 4.9 and 4.11, as well as Eqs. 4.12, 4.13 and 4.14, the square root has been introduced in order to respect the dimensionality of the absolute quantity to which the error is referring, i.e., uE for the strain responses and N for the input.

4.3 Summary

The problem of uncertainties modeling in Bayesian filtering is treated in this chapter. A description of the effect of the selected noise terms on Kalman-based filters accuracy is proposed. Indeed, Bayesian estimators rely on two noise terms, i.e., the process and measurement noise, to respectively account for uncertainties arising from modeling errors and measurement noise. This chapter demonstrates how these terms robustly control the accuracy of Kalman-based filters. The use of conventional methods for process noise covariance tuning in an input-state estimation framework are presented. A newly developed approach is then proposed in this chapter for adaptive tuning of the time-variant process noise covariance matrix using the AKF. The method, addressed as A-AKF, is based on reference response estimates computed via the CMS-ME approach.

5

LATENT FORCE MODELING FOR BAYESIAN INPUT-STATE ESTIMATION

Chapter 3 has dealt with the joint input-state estimation problem by proposing the AKF and DKF schemes. Both the algorithms rely on a prior assumption regarding the dynamic model of the unknown input, which is constructed via a RW model. Although the RW is a widely adopted solution, it is sometimes not representative of the actual loading conditions a structure is subject to. This results in the need of a user-dependent dedicated offline tuning procedure for the unknown input covariance, which strongly controls the force prediction accuracy. In Chapter 4, a method for adaptively tuning the process noise covariance matrix for joint input-state estimation using the AKF has been proposed. However, for loads featuring complex dynamics, thus strongly deviating from the assumption of BM to which the RW belongs, the prediction accuracy may not reach satisfactory values even adopting automated tuning methods. For this reason, this chapter proposes a prior transition equation for the unknown input shaped by a LFM derived from regression via stochastic processes using training data. The RW model is presented and investigated in Section 5.1 and the alternative input prior representation constructed using the basic regression concepts of Subsection 2.3.1 is presented in Section 5.2.

5.1 The Random Walk model

RWs represent one of the most basic processes studied in probability theory and can be defined as a sequence of discrete, fixed-length steps in random directions. As they easily represent random movements, RWs are commonly adopted to mathematically model BM, i.e., the random motion of particles suspended in a medium, by discretizing time and space, which are instead continuous in BM as they describe movements in nature. Examples of the use of RWs in practical problems are the modeling of a gambler financial status or the changes in stock prices in finance, which are assumed to take a random and unpredictable path such that past movements of a stock price cannot be used to predict its future movement.

To introduce the RW formulation, this section offers a simple one-dimensional example of a marker on the integer number line moving via unitary steps left or right with a symmetrical probability (50% of going left and 50% of going right). The problem is presented in Fig. 5.1, where the marker is placed at zero, and a fair coin is flipped to determine the next position. If it lands on heads, the marker is moved one unit to the right. If it lands on tails, the marker is moved one unit to the left.

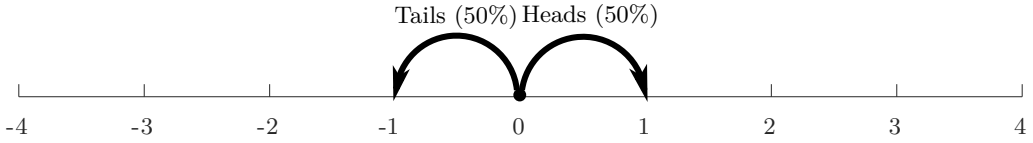

Figure 5.1: Marker 1^{st} movement

After the 1^{st} coin flip, the marker position can be -1 or 1. After a 2^{nd} coin flip, the marker can be located at three possible positions:-2, 0, 2. A 3^{rd} coin flip would place the marker at -3, -1, 1

or 3. Figures 5.2-5.5, indicate the possible positions and the corresponding probability value for the 4 coin flips.

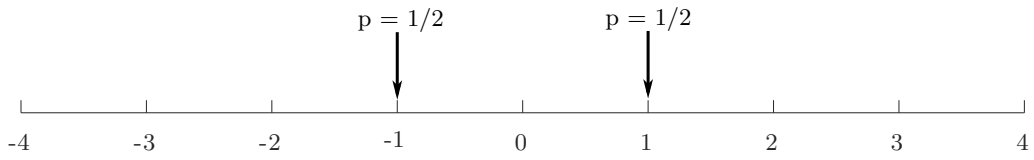

Figure 5.2: 1^{st} coin flip: possible positions and probabilities

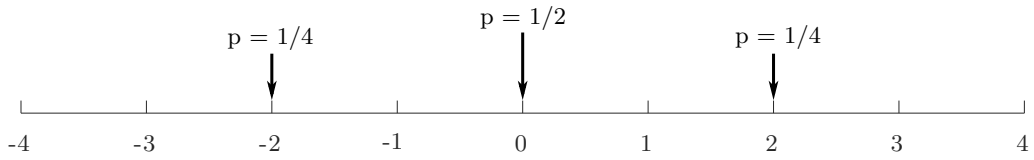

Figure 5.3: 2^{nd} coin flip: possible positions and probabilities

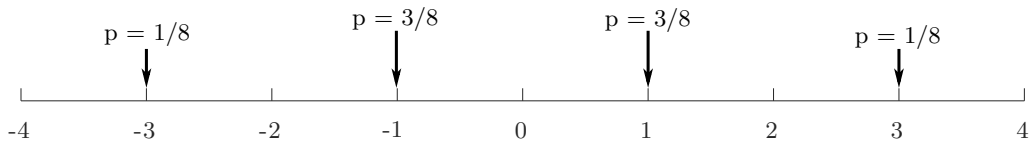

Figure 5.4: 3^{nd} coin flip: possible positions and probabilities

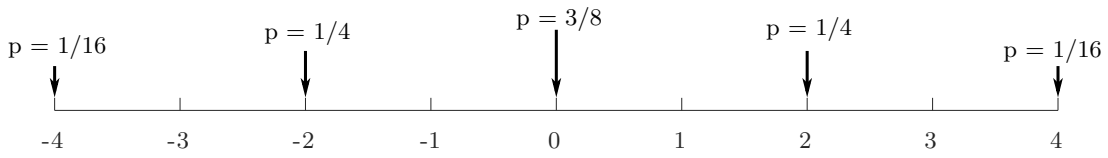

Figure 5.5: 4^{th} coin flip: possible positions and probabilities

For an odd number of coin flips, the marker can be placed at odd positions. On the other hand, for an even number of coin flips, the marker can only be at even locations. The resulting distribution is spread around the central value and it approaches a normal distribution as the number of coin flips increases. Hence, being X_i a random variable that indicates the outcome of the i^{th} coin flip, the X_i distribution is defined in mathematical terms as $X_i \sim \mathcal{N}(0,1)$. Additionally, a random variable S_n can be introduced to define the location of the RW after n flips. S_n corresponds to the sum of the coin flips outcome:

$$S_n = X_1 + X_2 + \cdots + X_n. \tag{5.1}$$

As a result, S_n is also a Gaussian distribution $S_n \sim \mathcal{N}(0,n)$ with mean and variance defined by:

$$\begin{aligned} \mu_{S_n} &= \mu_{X_1} + \mu_{X_2} + \cdots + \mu_{X_n} = 0 + 0 + \cdots + 0 = 0 \\ \sigma^2_{S_n} &= \sigma^2_{X_1} + \sigma^2_{X_2} + \cdots + \sigma^2_{X_n} = 1 + 1 + \cdots + 1 = n. \end{aligned} \tag{5.2}$$

Generalizing for a d dimensional symmetrical problem, for a RW initialized at $S_0 \in \mathbb{R}^d$, the sequence S_n can be written as:

$$S_n = S_{n-1} + \varepsilon_n, \quad n \geq 1 \tag{5.3}$$

where $\varepsilon_n \sim \mathcal{N}(0, \sigma^2_{X_n})$ is a sequence of independent and equivalently distributed random variables. In other terms, Eq. 5.3 postulates that the current RW value is obtained via a random step, determined by $\sigma^2_{X_n}$, from the previous value. As a result, the RW is to be considered a non-stationary process by nature. In fact, one can treat a RW as a special first order Autoregressive (AR) model. AR models are used to represent stochastic processes by specifying that a variable depends linearly on its own previous values and on a stochastic term. An AR model of order p is denoted as:

$$S_n = \sum_{i=1}^{p} \phi_i S_{n-i} + \varepsilon_n \tag{5.4}$$

where $\phi_1, \cdots, \phi_n$ are the model parameters and ε_n is white noise. For each AR model, the corresponding characteristic equation can be solved to compute the roots of the characteristic polynomial, which determine the dynamic behavior of the model. An AR(p) model is a model of order p, i.e., with p roots. Having all the roots lying outside the unit circle is a necessary condition for the model to be considered wide-sense stationary. The comparison of Eqs. 5.3 and 5.4 confirms that a RW model belongs to a specific AR(1) model class featuring a unity parameter $\phi_1 = 1$, which does not satisfy the weak stationarity condition of AR models. A RW series is, therefore, often referred to as a unit-root non-stationary time series.

As reported in Chapters 3, RWs are employed for establishing the necessary fictitious equation dictating the unknown input dynamics within Kalman-based input-state estimators. The resulting prior assumption on the input evolution assumes that its current value is obtained from its previous value via a random step, which depends on the selected process noise. Hence, the chosen input process noise covariance $\mathbf{Q}^u$ plays an important role in the definition of the prior assumption on the input evolution. In this sense, the selection of this value drives the achievable flexibility of the model to adapt to the loading conditions of the specific application case, thus determining the prediction accuracy obtained by the Bayesian estimator. This approach is typically successful for excitation scenarios with a strong random component. However, the RW assumption is commonly used in any case in which information regarding the loading conditions a system is subject to is lacking, including situations that lie beyond the common identification scheme on which the RW assumption has typically been tested on and excels in, e.g. when abrupt load changes in time are experienced or a periodic exciting component is present. In this challenging estimation cases, conventionally adopted settings and tuning methods do not always bring to satisfactory results. This chapter introduces and analyzes alternative input modeling schemes which, by relying on data-driven methods, have the ability to more easily and flexibly adapt to several articulated excitation conditions.

5.2 Latent Force Models

A more flexible and comprehensive alternative to the conventional RW for establishing a prior model for the unkwown input in a Kalman filtering setting consists in employing LFMs [70, 69], i.e., hybrid schemes that incorporate data-driven paradigms in a relatively simple mechanistic model. This approach rises from the need of compensating for the lack of knowledge that physics-based models may feature due to the high degree of simplification they embed with respect to the complexity of systems they are designed for. Despite this, physics-based models still retain the advantage over data-driven models of allowing for predictions in regions of the system where no training data is available. The key idea behind LFMs construction is to make use of a mechanistic model of the system which is augmented via data-driven techniques in order to provide enough flexibility to allow for the resulting model to fit the actual system even when mechanistic assumptions are not precisely met. According to this approach, any model in which the system is forced by latent functions can be referred as LFM. Hence, the continuous-time SSM in Eq. 2.8 describing the motion of a linear structural system can be interpreted as a LFM if the components of the forcing vector $\mathbf{u}(t)$ are modeled as zero-mean independent stochastic processes. GPs represent a valuable class of stochastic process for modeling the so-called latent forces as they can be easily incorporated

into the inference process following the procedure described in Subsubsection 2.3.1.1. In a GPLFM framework, the components of the forcing vector of the system in Eq. 2.8 are postulated by:

$$f^{(j)}(t) \sim \mathcal{GP}\left(0, k_j(t,t')\right) \tag{5.5}$$

where f^j is the jth component of the forcing vector $\mathbf{u}$, i.e., $j = 1, ..., n_i$.
The approach proposed in [70, 69] stems from the assumption that the system state vector in Eq. 2.8 can be modeled as a multi-dimensional GP:

$$\mathbf{x}(t) \sim \mathcal{GP}(\mathbf{0}, \mathbf{K}_{xx}(t,t')). \tag{5.6}$$

By re-writing the output equation in Eq. 2.8 in the form:

$$\mathbf{g}(t) = \begin{bmatrix}\mathbf{C} & \mathbf{G}\end{bmatrix} \begin{bmatrix}\mathbf{x}(t) \\ \mathbf{u}(t)\end{bmatrix} = \mathbf{C}_g \boldsymbol{\eta}(t) \tag{5.7}$$

it appears that $\mathbf{g}(t)$ is a linear combination of two GPs. Hence, a new GP can be introduced:

$$\mathbf{g}(t) \sim \mathcal{GP}(\mathbf{0}, \mathbf{K}_{gg}(t,t')). \tag{5.8}$$

where $\mathbf{K}_{gg}(t,t') = \mathbf{C}_g \mathbf{K}_{\eta\eta} \mathbf{C}_g^T$ and the covariance matrix $\mathbf{K}_{\eta\eta}$ has the form:

$$\mathbf{K}_{\eta\eta}(t,t') = \begin{bmatrix}\mathbf{K}_{xx}(t,t') & \mathbf{K}_{xu}(t,t') \\ \mathbf{K}_{ux}(t,t') & \mathbf{K}_{uu}(t,t')\end{bmatrix} \tag{5.9}$$

where $\mathbf{K}_{uu} = \mathbb{E}\left[\mathbf{u}(t)\mathbf{u}^T(t')\right] = diag[k_1(t,t'), ..., k_j(t,t'), ..., k_{n_i}(t,t')]$ is the joint covariance matrix of all the latent forces within the forcing vector $\mathbf{u}(t)$, which is diagonal according to the independence assumption of the forcing terms. In absence of this assumption, the forcing vector would admit correlated terms, which would thus need to be modeled by related GPs, i.e., $\mathbf{K}_{uu}$ off-diagonal terms would be non-zero. GP regression for full covariance matrices is addressed in literature via use of instantaneous mixing [142, 143, 144] or convolution [145, 146, 147] of a series of independent processes to construct correlated processes. These approaches require more advanced calculations and, consequently, additional computational effort. The independent forcing terms hypothesis is thus adopted in this dissertation to simplify the construction of LFMs. This assumption does not introduce a too strict simplification within the context of Kalman-based input-state estimation algorithms, where prior information regarding the location and the direction of the unknown forcing terms is assumed to be available. This allows to easily differentiate the several excitation sources acting on the system, thus allowing to treat them independently. Despite this simplification, the resulting LFM turns into a GP regression problem that still requires complex numerical integration for computing $\mathbf{K}_{xx}$, which may not always have a closed-form. A workaround to this problem consists in adopting the temporal state-space GP formulation presented in Subsection 2.3.2 to model the latent forcing terms, which are then used to augment the system mechanistic model resulting in a practical joint state-space form.

5.2.1 Latent Force Models for joint input-state estimation

The GPLFM approach has been originally adopted for input-state estimation in a Kalman filtering framework in [71] and further exploited in [72] for offline input-state-parameter estimation. The basic principle consists in adopting the GP state-space representation derived in Subsection 2.3.2 to model the (unknown) latent forces acting on the system under the assumption of conventional covariance functions, i.e., squared exponential, exponential or Matérn type. The corresponding SSM is then used in combination with the system state-space (mechanistic) model in Eq. 2.8 by

augmenting the state vector $\mathbf{x}$ with the input state vector $\mathbf{z}$ defined in Eq. 2.73, yielding the final augmented model:

$$\begin{bmatrix} \dot{\mathbf{x}}(t) \\ \dot{\mathbf{z}}^{(1)}(t) \\ \dot{\mathbf{z}}^{(2)}(t) \\ \vdots \\ \dot{\mathbf{z}}^{(n_i)}(t) \end{bmatrix} = \begin{bmatrix} \mathbf{A} & \mathbf{b}_1\mathbf{H}^{(1)} & \mathbf{b}_2\mathbf{H}^{(2)} & \dots & \mathbf{b}_{n_i}\mathbf{H}^{(n_i)} \\ 0 & \mathbf{F}^{(1)} & 0 & \dots & 0 \\ 0 & 0 & \mathbf{F}^{(2)} & \dots & 0 \\ \vdots & \vdots & \vdots & \ddots & \vdots \\ 0 & 0 & 0 & \dots & \mathbf{F}^{(n_i)} \end{bmatrix} \begin{bmatrix} \mathbf{x}(t) \\ \mathbf{z}^{(1)}(t) \\ \mathbf{z}^{(2)}(t) \\ \vdots \\ \mathbf{z}^{(n_i)}(t) \end{bmatrix} + \begin{bmatrix} \mathbf{w}(t) \\ \widetilde{\mathbf{w}}^{(1)}(t) \\ \widetilde{\mathbf{w}}^{(2)}(t) \\ \vdots \\ \widetilde{\mathbf{w}}^{(n_i)}(t) \end{bmatrix} \tag{5.10}$$

$$\mathbf{y}(t) = \begin{bmatrix} \mathbf{C} & \mathbf{g}_1\mathbf{H}^{(1)} & \mathbf{g}_2\mathbf{H}^{(2)} & \dots & \mathbf{g}_{n_i}\mathbf{H}^{(n_i)} \end{bmatrix} \begin{bmatrix} \mathbf{x}(t) \\ \mathbf{z}^{(1)}(t) \\ \mathbf{z}^{(2)}(t) \\ \vdots \\ \mathbf{z}^{(n_i)}(t) \end{bmatrix} + \mathbf{v}(t) \tag{5.11}$$

where $\mathbf{b}_1, \mathbf{b}_2, \cdots, \mathbf{b}_{n_i}$ are the columns of the $\mathbf{B}$ matrix and $\mathbf{g}_1, \mathbf{g}_2, \cdots, \mathbf{g}_{n_i}$ are the columns of the $\mathbf{G}$ matrix in Eq. 2.8. $\widetilde{\mathbf{w}}^{(j)}(t) \in \mathbb{R}^m$ is a vector-valued GP given by $\widetilde{\mathbf{w}}^{(j)}(t) = \mathbf{L}^{(j)}w^{(j)}(t)$, with spectral density $\mathbf{Q}_c^{(j)} \in \mathbb{R}^{m\times m}$ expressed as $\mathbf{Q}_c^{(j)} = \mathbf{L}^{(j)}q_c(\mathbf{L}^{(j)})^T$. In shorthand notation, the augmented SSM shown in Eqs. 5.10 and 5.11 can be expressed as follows:

$$\begin{cases} \dot{\mathbf{x}}^a(t) &= \mathbf{A}^a\mathbf{x}^a(t) + \mathbf{w}^a(t) \\ \mathbf{y}\,(t) &= \mathbf{C}^a\mathbf{x}^a\,(t) + \mathbf{v}(t) \end{cases} \tag{5.12}$$

where $\mathbf{x}^a(t) \in \mathbb{R}^{n_{aug}}$ is the augmented state vector and matrices $\mathbf{A}^a \in \mathbb{R}^{n_{aug}\times n_{aug}}$, $\mathbf{L}^a \in \mathbb{R}^{n_{aug}\times n_i}$, $\mathbf{w}^a(t) \in \mathbb{R}^{n_{aug}}$ is the augmented process noise vector, and $\mathbf{C}^a \in \mathbb{R}^{n_o\times n_{aug}}$, where $n_aug = 2n_r + m \times n_i$ if the LTI SDE in Eq. 2.71 is of the same order m for all the latent forces.
Given the continuous nature of the equations in Eq. 5.12, a discretization process needs to be put in place to allow employment of the augmented system within a Kalman filtering scheme for recursively estimating the augmented state vector, i.e., to reconstruct the unmeasured structural response of the system along with the unknown loads it is subject to and the respective derivatives up to order m. For this purpose, an exponential time discretization scheme can be applied, yielding:

$$\begin{cases} \mathbf{x}^a_{k+1} &= \mathbf{A}^a_d\mathbf{x}^a_{k-1} + \mathbf{w}^a_{k-1} \\ \mathbf{y}_k &= \mathbf{C}^a\mathbf{x}^a_k + \mathbf{v}_k \end{cases} \tag{5.13}$$

where $\mathbf{A}^a_d = e^{(\mathbf{A}^a\,\Delta t)}$, while the output matrix $\mathbf{C}^a$ remains unchanged because of its inner discrete nature. $\mathbf{w}^a_{k-1}$ is a discretized version of the augmented process noise vector, which is associated to the covariance matrix $\mathbf{Q}^a = blkdiag\,[\mathbf{Q}, \mathbf{Q}_c]$. In the last expression, $\mathbf{Q}$ is the discretized version of the process noise covariance matrix associated with the state vector $\mathbf{x}$, while $\mathbf{Q}_c = blkdiag\,[\mathbf{Q}^1_c, ..., \mathbf{Q}^{n_i}_c]$. The discretization step for matrix $\mathbf{Q}_c$, which now contains information regarding the process noise associated with all the modeled latent forces, is performed by exploiting Eq. 2.75:

$$\mathbf{Q}_{d_{k-1}} = \int_0^{\Delta t} exp(\mathbf{A}^a(\Delta t - \tau))\mathbf{Q}_c exp(\mathbf{A}^{a^T}(\Delta t - \tau))d\tau. \tag{5.14}$$

As a result of the independence assumption made on the latent inputs, the error covariance matrix $\mathbf{P}^a_k$ associated with the augmented state vector $\mathbf{x}^a_k$ has a block diagonal form of the type:

$$\mathbf{P}^a_k = blkdiag\left[\mathbf{P}_k, \mathbf{P}^1_k, ..., \mathbf{P}^{(j)}_k, ...\mathbf{P}^{n_i}_k\right] \tag{5.15}$$

where $\mathbf{P}_k$ is the covariance matrix for the non-augmented state vector $\mathbf{x}_k$ and $\mathbf{P}^{(j)}_k$ is the covariance matrix for the j-th latent force, whose initial condition is set according to what reported in Eq. 2.77.

Joint recursive inference of states and inputs can be performed by employing the augmented system in Eq. 5.13 in a sequential scheme made up of a KF and a RTS smoother (see Algs. 7 and 8).

The main steps necessary for the estimation are summarized in Alg. 14, while a schematic representation is provided in Fig. 5.6.

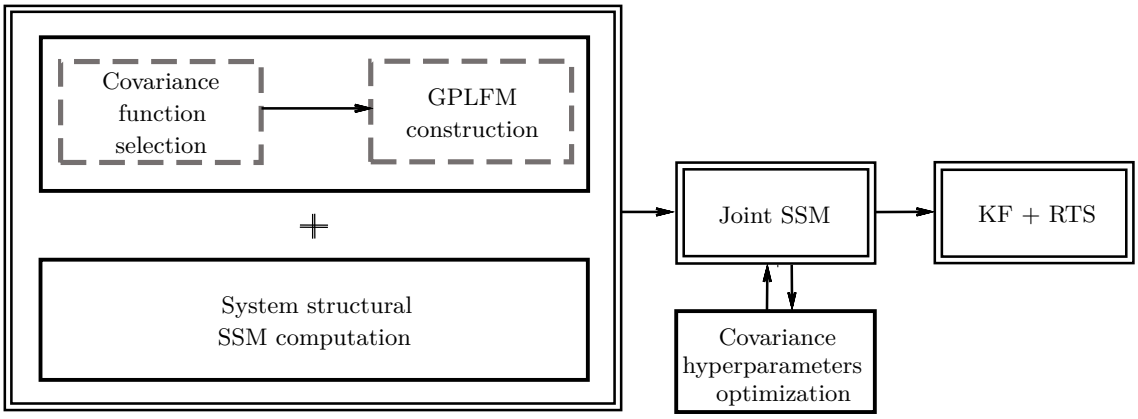

Figure 5.6: GPLFM for joint input-state estimation scheme

Algorithm 14 Joint input-state estimation via the GPLFM

1: Calculate the continuous-time state-space matrices $\mathbf{A}, \mathbf{B}, \mathbf{C}$ and $\mathbf{G}$ of the structural model and collect training data $\mathcal{D} = \{\mathbf{y}_1, \cdots, \mathbf{y}_n\}$
2: **for** $j = 1, ..., n_i$ **do**
3: Choose the covariance function depending on the application (section 2.3.1.3) and initialize the hyperparameters $\grave{}$
4: Convert the GP covariance functions into an equivalent continuous-time state space matrices and obtain $\mathbf{F}^{(j)}$, $\mathbf{H}^{(j)}$, $\mathbf{L}^{(j)}$, $\mathbf{P}_{\infty}^{(j)}$ and $\mathbf{Q}_c$
5: **end for**
6: Construct the discrete-time augmented SSM matrices, $\mathbf{A}_d^a$, $\mathbf{C}^a$, $\mathbf{Q}^a$
7: Initialize the covariance matrices $\mathbf{Q}$, $\mathbf{R}$, $\mathbf{P}_{0|0}^x$ and mean vector $\hat{\mathbf{x}}_{0|0}^a$. Calculate the augmented state vector covariance matrix $\mathbf{P}_{0|0}^a = \mathit{blkdiag}\left[\mathbf{P}_{0|0}, \mathbf{P}_{\infty}\right]$.
8: Compute the optimal hyperparameters, $\grave{}$, by maximizing the log marginal likelihood of the observed data $\mathcal{D}$
9: With the optimal hyperparameters $\grave{}$, compute the optimal discrete time augmented SSM matrices, $\hat{\mathbf{A}}_d^a$, $\hat{\mathbf{C}}^a$, $\hat{\mathbf{Q}}^a$ and $\hat{\mathbf{P}}_{0|0}^a$.
10: Using the matrices constructed in the previous step, estimate the unknown inputs and states using the KF and RTS in Algs. 7 and 8.

It is worth noting that the GPLFM can be considered as a generalization of the augmented SSM in Eq. 3.17 used in the AKF. Indeed, the system in Eq. 5.12 reduces to Eq. 3.17 if $\mathbf{z}(t) = \mathbf{u}(t)$, i.e., $\mathbf{F}^{(j)} = \mathbf{0}_{m \times m}$ since $\dot{\mathbf{z}} = \mathbf{0}$. In discrete-time, this translates in observing that Eq. 2.74 is a general expression for Eq. 3.18, where $\mathbf{F}_{d_{k-1}} = \mathbf{I}$. Following this logic, properties of the augmented system in Eq. 3.17 such as detectability and observability can be also evaluated for the GPLFM. Specifically, it has been found that if the pair $(\mathbf{A}, \mathbf{C})$ (from the system structural SSM in Eq. 2.8) is observable and each latent force has an exponentially stable state-space representation, the augmented system $(\mathbf{A}^a, \mathbf{C}^a)$ is detectable [71]. The proof for this statement can be easily derived by observing the Popov-Belevitch-Hautus (PBH) matrix for the SSM in Eq. 5.12:

$$PBH = \begin{bmatrix} s\mathbf{I} - \mathbf{A} & -\mathbf{B}^* \\ \mathbf{0} & s\mathbf{I} - \mathbf{F}^* \\ \mathbf{C} & \mathbf{G}^* \end{bmatrix} \tag{5.16}$$

where matrices $\mathbf{B}^*$, $\mathbf{F}^*$ and $\mathbf{G}^*$ are respectively defined as:

$$\mathbf{B}^* = \begin{bmatrix} \mathbf{b}_1\mathbf{H}^{(1)} & \mathbf{b}_2\mathbf{H}^{(2)} & \dots & \mathbf{b}_{n_i}\mathbf{H}^{(n_i)} \end{bmatrix}, \quad \mathbf{F}^* = \begin{bmatrix} \mathbf{F}^{(1)} & 0 & \dots & 0 \\ 0 & \mathbf{F}^{(2)} & \dots & 0 \\ \vdots & \vdots & \ddots & \vdots \\ 0 & 0 & \dots & \mathbf{F}^{(n_i)} \end{bmatrix}, \tag{5.17}$$
$$\mathbf{G}^* = \begin{bmatrix} \mathbf{g}_1\mathbf{H}^{(1)} & \mathbf{g}_2\mathbf{H}^{(2)} & \dots & \mathbf{g}_{n_i}\mathbf{H}^{(n_i)} \end{bmatrix}.$$

Under the assumption of observability of $(\mathbf{A}, \mathbf{C})$ and stability of each $\left(\mathbf{F}^{(j)}, \mathbf{H}^{(j)}\right)$ for $j = 1, ..., n_i$, the PBH matrix in Eq. 5.16 has full column-rank $\forall s \in \mathbb{C}$, which proves that the GPLFM is detectable for all types of measurements. This property adds further flexibility to the use of the GPLFM for joint input-state estimation in real-life problem for any type of data set. In particular, the method is applicable to measurements sets containing only acceleration sensors, which is instead a well-known limitation to the AKF due to un-observability issues arising under this condition [50]. In this dissertation, this GPLFM peculiarity will be proven via the proposed case studies, for which it will be demonstrated that, in contrast to what provided by the AKF, the method allows accurate estimations also in absence of displacement-level sensors.

Although the validity of using GPLFMs as postulated in Fig. 5.6 and Alg. 14 has been demonstrated in [71, 72] and will also be proved in this dissertation via the proposed experimental case studies, the following considerations must be made.

- The GPLFM approach has been proposed in literature for specific and rather conventional classes of covariance functions, i.e., Matérn, squared exponential, exponential. In Subsubsection 2.3.2.3, the equivalent state-space representation of a GP featuring such covariance functions has been found to always have real and coincident roots with multiplicity dependent on the adopted Matérn smoothness parameter. The achieved state-space representation hence corresponds to a "critically damped" dynamic system whose response, i.e., the model imposed for the unknown input in the joint input-state estimation framework, has a time waveform dominated by the term $w(t)$ in Eq. 2.90 and modulated by an exponentially decaying trend. As a result, conventional covariance functions represent a generic and easy-to-derive modeling choice which, however, does not account for specific content that the input may feature, e.g. harmonics, biases, sudden changes. For this reason, additional covariance functions have been introduced in Subsubsection 2.3.1.3 and the associated SSMs have been derived in Subsection 2.3.2. Among the proposed functions, periodic covariance functions allow for a dynamic model including undamped harmonics, thus representing the most suitable choice for regression of sinusoidal signals. However, real-life signals too often deviate from pure sinusoidals as they are noise-contaminated, affected by disturbances or rather obtained as compositions of signals of different nature, i.e., random multisines. To take these aspects into account, quasiperiodic covariance functions can be employed for regression. Additionally, linear and constant covariance functions can be adopted in combination with other covariance functions (to obtain, e.g. the biased quasiperiodic covariance function) to respectively model linear trends and biases in data. Finally, the Wiener covariance function can be exploited to construct an alternative and more flexible SSM for the unknown input satisfying the RW assumption, thus finding its best application in regression of ambient noise signals. The hereby reported considerations will be extensively proved in Subsubsection 5.2.1.1, where the mentioned covariance functions will be employed for joint input-state estimation of a 3DOFs system subject to inputs of different nature. Additionally, an experimental validation will be provided in Section 8.3 via the case study explored in Chapters 8.

- In Subsection 2.3.2, a sequence of a KF and a RTS smoother has been reported as a solution for recursive regression via stochastic processes. Including smoothing in the algorithm allows to obtain estimations at the current instant of time on the basis of past and future observations.

The combination of a KF and a RTS smoother thus allows to exactly transfer stochastic process regression from its batch to its recursive form. Nevertheless, this operation is in contrast with the more practical need of deploying real-time estimators for operational and experimental data since it foresees a certain lag to be taken into account before acquiring estimations at a given instant of time. Additionally, Subsubsection 5.2.1.1 will prove that including the smoothing step in the algorithm renders the resulting predictions more prone to accumulation errors. This dissertation therefore proposes to exclude the RTS from the algorithm in Fig. 5.6 and Alg. 14, thus running a forward KF only.

- The approach in Fig. 5.6 and Alg. 14 foresees the use of the entire set of measurements used for the joint input-state estimation for selecting the covariance function hyperparameters. This implies that a substantially large set of observations needs to be acquired prior to the operational employment of the estimator. Additionally, the use of multiple signals for Bayesian model selection drastically increases the required computational time. To remedy these problems, the use of a single pre-recorded measurement will be proposed in this dissertation for both the simulated and the experimental case studies. It is worth noting that the most convenient choice for the pre-recorded signal corresponds to an acceleration signal at the unknown input location. Indeed, a collocated acceleration features a direct link to the unknown input via the feedthrough matrix. In absence of a collocated measurement, any other acceleration on the structure may be used to select the covariance function hyperparameters. Acceleration signals are instead not suitable in presence of biased inputs, e.g. a pull and release load, as they do not provide static information. In this situations, a displacement-level signal should be adopted.

- The use of LFMs for joint input-state estimation in structural dynamics relies on the use of GP regression. However, other type of stochastic process may also find application in the analyzed framework. When dealing with real-life data, which often contains outliers, Student-t processes may represent a valid alternative. According to the considerations reported in Subsection 2.3.2, a LFM can indeed be constructed by exploiting STPs instead of GPs. The formulation of a STPLFM follows what postulated by Eq. 5.10 with the sole difference that spectral density $\mathbf{Q}_c^{(j)}$ associated to the process noise vector $\tilde{\mathbf{w}}^{(j)}$ of the j-th latent force, is controlled by an inverse gamma random variable γ: $\mathbf{Q}_c^{(j)} = \mathbf{L}^{(j)}\gamma q_c(\mathbf{L}^{(j)})^T$. Similarly, the initial state vector covariance for the j-th latent force must be set such as $p(\mathbf{z}_0^{(j)}) = \mathcal{N}(\mathbf{0}, \gamma\mathbf{P}_\infty^{(j)})$. Within the sequential inference scheme adopted for STP regression, the DOF parameter ν introduced by the STP assumption gets updated as $\nu_k = \nu_{k-1} + n_k$ where $n_k = 1$ for observations and $n_k = 0$ for predictions of test points. Besides the mentioned modifications, the joint input-state estimation via a STPLFM can be constructed following the steps reported in this section for the GPLFM, with the only difference of running the Student-t filter and smoother reported in Algs. 9 and 10 instead of the KF-RTS coupling adopted within the GPLFM scheme.

5.2.1.1 Joint input-state estimation using Latent Force Models: a 3DOFs example

This subsection makes use of the GPLFM approach for input-state estimation of the 3 DOFs system in Fig. 5.7, excited by a force applied at the 3^{rd} mass. The system masses m_1, m_2 and m_3 are assumed to be 100, 80 and 80 kg, respectively. The springs stiffness values have been selected as follows: $k_1 = 2 \times 10^5$, $k_2 = 1.5 \times 10^5$, $k_3 = 1.5 \times 10^5$ N/m. Damping has been defined assuming a proportional behavior such that $\mathbf{C} = 2 \times 10^{-2}\mathbf{M} + 3 \times 10^{-4}\mathbf{K}$. The system natural frequencies and damping ratios are provided in Tab. 5.1. The proposed simulated example is hereby exploited to implement and prove the comments listed in the previous subsection. To explore the spectrum of covariance functions proposed in Subsubsection 2.3.1.3, the input-state prediction problem has been implemented for the 3 DOFs system under the assumption of several types of inputs acting on the 3^{rd} mass, i.e., random, sine, random multisine, impulse, step. Every loading scenario has been addressed adopting the corresponding most suitable covariance function and the achieved input and response predictions have been compared with the results obtained via a conventional

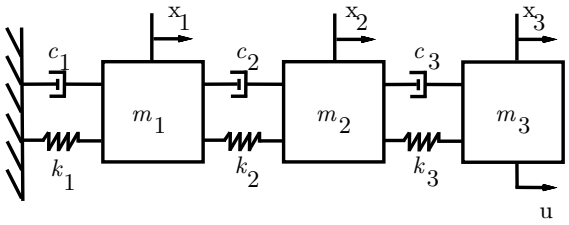

Figure 5.7: 3 DOFs system

Table 5.1: Natural frequencies and damping ratios of the 3 DOFs system

Modes	1	2	3
Natural frequency [Hz]	3.26	8.52	12.16
Damping ratio [%]	0.36	0.82	1.16

Matérn covariance function. Moreover, the hereby applied estimator is constructed using a KF only in order to guarantee real-time applicability. To validate this choice, predictions are compared to the ones achieved via sequential KF and RTS as in Fig. 5.6, for every loading case. The state process noise covariance matrix $\mathbf{Q}$ and the measurement noise covariance matrix $\mathbf{R}$, necessary for the implementation of the adopted filtering and smoothing algorithms, have been set by trial and error and kept unchanged across all the loading scenarios for consistency. The trial and error process conducted to select these matrices has been based on differentiating the covariance order of magnitude according to the associated quantity, e.g. displacements and velocities for $\mathbf{Q}$ and displacements and accelerations for $\mathbf{R}$, to ensure a realistic quantification of the modeled errors. A single collocated "measurement", i.e., a response simulated at the 3^{rd} mass and contaminated by noise, is adopted as observation for input-state estimation. When the input has a step profile, the 3^{rd} mass displacement is used as measurement to ensure that a static information is acquired. Otherwise, a collocated acceleration measurement is preferred in order to guarantee a feedthrough term with the unknown input. The same observed response time signal is also used for Bayesian model selection, i.e., for determining the covariance function hyperparamenters prior to online estimation. For implementing the marginal likelihood optimization step, the initial hyperparameters values are chosen so as to avoid the method to incur in erroneous local minima.

Sine load

This paragraph reports on the input-state estimation results for the analyzed system excited by a sinusoidal input (1 Hz) applied at the 3^{rd} mass. In this loading scenario, the use of a periodic covariance function for constructing the GPLFM is strongly preferable to the conventional Matérn function since it allows to account for harmonic features within the adopted GP rather than relying on the "critically damped" Matérn model. Table 5.2 summarizes the selected initialization values of the parameters necessary for the algorithm. Figure 5.8 compares the actual input and 1^{st} mass displacement against the predictions achieved using the GPLFM approach with filtering only. Both the predictions obtained via the proposed periodic covariance function and a Matérn covariance function ($\nu = 1.5$) are displayed in Fig. 5.8. A visual inspection of the results confirms that the periodic covariance function is more suitable for estimating signals featuring pure harmonic components. This is specifically applicable for simulated systems such as the one hereby analyzed, where external noise sources are limited and damping follows a precise model. To the contrary, when dealing with physical systems, selecting a periodic covariance function may correspond to a too strict assumption on the content of the analyzed signals. Indeed, noise can perturb the signal periodicity and damping may not follow the model used when defining the system state-space equations. To mitigate these effects, a quasiperiodic covariance function is to be preferred when

treating real-life problems.

Table 5.2: 3 DOFs system, sine load: estimators initialization values

Initial state mean	Initial error cov. matrix	Initial hyperparameters periodic	Initial hyperparameters Matérn	Process noise cov. matrix ($\mathbf{Q}$)	Measurement noise cov. matrix ($\mathbf{R}$)
$\hat{\mathbf{x}}^a_{0\|0} = \mathbf{0}$	$\hat{\mathbf{P}}^x_{0\|0} = \mathbf{0}$	$\sigma^2 = 1 \times 10^{-1}$ $l = 5 \times 10^{-1}$ $t_{period} = 1$	$\sigma^2 = 5$ $l = 1 \times 10^{-2}$	$\mathbf{Q}_{\text{displ}} = 10^{-20} \times \mathbf{I}_{\text{displ}}$ $\mathbf{Q}_{\text{vel}} = 10^{-10} \times \mathbf{I}_{\text{vel}}$	$\mathbf{R}_{\text{displ}} = 10^{-15} \times \mathbf{I}_{\text{displ}}$ $\mathbf{R}_{\text{acc}} = 10^{-12} \times \mathbf{I}_{\text{acc}}$

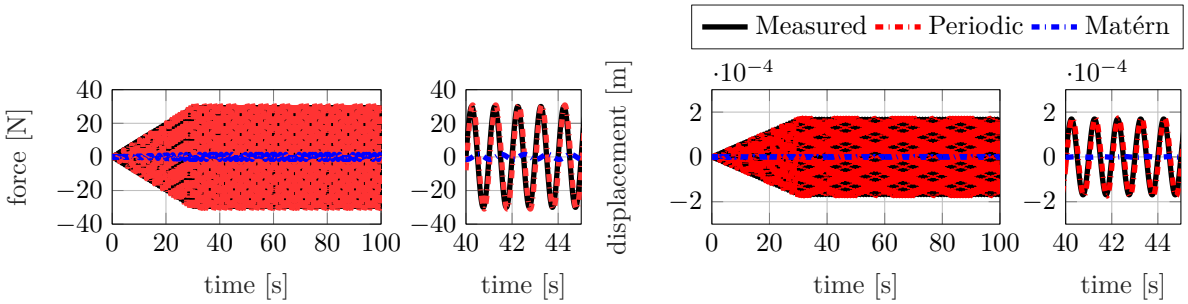

Figure 5.8: 3 DOFs system: time and detailed time histories of the sine input and the resulting 1^{st} DOF displacement. "Measured" signals are shown by a solid black line, while those estimated (via filtering only) by making use of a periodic and a Matérn covariance function ($\nu = 1.5$) are respectively denoted via a dashed red and blue line.

A time-domain comparison between the results obtained via filtering only and the ones achieved via sequential KF and RTS smoother is offered in Fig. 5.9. The displayed signals confirm that combining filtering and smoothing generates accumulation errors which result in low frequency components affecting the estimated time histories.

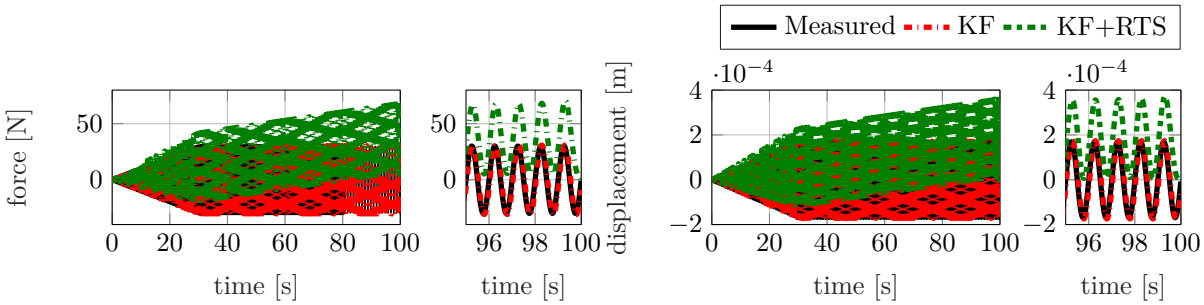

Figure 5.9: 3 DOFs system: time and detailed time histories of the sine input and the resulting 1^{st} DOF displacement. "Measured" signals are shown by a solid black line, while those estimated by filtering only and a sequence of filtering and smoothing (periodic covariance function) are respectively denoted via a dashed red and green line.

A quantification of the estimation errors obtained by the analyzed estimators is reported in Tab. 5.3 for both the unknown force and the estimated responses by means of the Normalized Root Mean Square Error (NRMSE), i.e., the RMSE between the estimated and the corresponding "measured" signal, normalized with respect to the "measured" signal Root Mean Square (RMS) value. Table 5.3 demonstrates that the employment of a periodic covariance function within a GPLFM solved with filtering only allows for the optimal performance of both input and response estimation in a sinusoidal loading scenario.

Table 5.3: 3 DOFs system, sine load: NRMSE values between "measured" and estimated signals (responses and force).

	NRMSE_{displ}			NRMSE_{vel}			NRMSE_{acc}			NRMSE	NRMSE
	DOF1	DOF2	DOF3	DOF1	DOF2	DOF3	DOF1	DOF2	DOF3	mean resp.	force
Periodic (KF)	0.245	0.245	0.245	0.247	0.247	0.247	0.248	0.248	0.003	0.220	0.261
Matérn (KF)	1.001	1.001	1.000	0.999	1.001	0.994	0.963	1.042	0.982	0.998	1.001
Periodic (KF+RTS)	1.048	1.059	1.076	0.257	0.257	0.257	0.253	0.251	0.003	0.496	1.177

Random load

This paragraph reports on the input-state estimation results for the analyzed system excited by a pure random (white noise) input applied at the 3^{rd} mass. In this loading scenario, the use of a Wiener covariance function for constructing the GPLFM is proposed as an alternative to the conventional Matérn function. As mentioned in Subsubsection 2.3.1.3, a GP with a Wiener covariance function is a RW model. Implementing a GPLFM approach for input-state prediction with a Wiener covariance function thus represents a non-conventional method for adopting a RW model for the unknown input. Unlike traditional Kalman-based estimators, where the RW assumption implies the need of a challenging tuning exercise, the GP-based formulation offers a flexible way for employing the RW model for input-state prediction. Indeed, in this framework the tuning effort is substituted with the preliminary training phase aimed at determining the hyperparameters. Following what stated in Section 5.1, it is evident that a Wiener covariance function represents the best choice for regression of purely randomic signals. Table 5.4 summarizes the selected initialization values of the necessary parameters for the algorithm. Figures 5.10 and 5.11 respectively compare the actual input and 1^{st} mass displacement in time and frequency domains obtained via the proposed Wiener covariance function and the Matérn covariance function. The analysis of Figs. 5.10 and 5.11 confirms that a Wiener covariance function allows to better capture the stochastic nature of the input.

Table 5.4: 3 DOFs system, random load: estimators initialization values

Initial state mean	Initial error cov. matrix	Initial hyperparameters Wiener	Initial hyperparameters Matérn	Process noise cov. matrix ($\mathbf{Q}$)	Measurement noise cov. matrix ($\mathbf{R}$)
$\hat{\mathbf{x}}^a_{0\|0} = \mathbf{0}$	$\hat{\mathbf{P}}^x_{0\|0} = \mathbf{0}$	$\sigma^2 = 1 \times 10^{-4}$	$\sigma^2 = 5$ $l = 1 \times 10^{-2}$	$\mathbf{Q}_{\text{displ}} = 10^{-20} \times \mathbf{I}_{\text{displ}}$ $\mathbf{Q}_{\text{vel}} = 10^{-10} \times \mathbf{I}_{\text{vel}}$	$\mathbf{R}_{\text{displ}} = 10^{-15} \times \mathbf{I}_{\text{displ}}$ $\mathbf{R}_{\text{acc}} = 10^{-12} \times \mathbf{I}_{\text{acc}}$

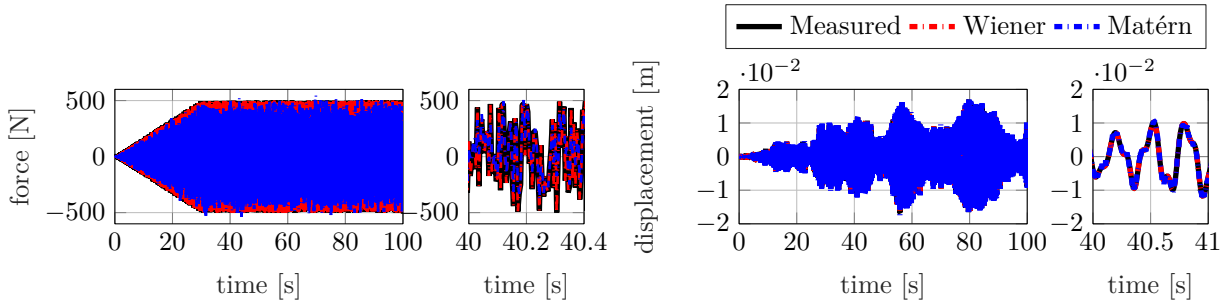

Figure 5.10: 3 DOFs system: time and detailed time histories of the random input and the resulting 1^{st} DOF displacement. "Measured" signals are shown by a solid black line, while those estimated (via filtering only) by making use of a Wiener and a Matérn covariance function ($\nu = 1.5$) are respectively denoted via a dashed red and blue line.

Figure 5.12 offers a time-domain comparison between the results obtained via filtering only and the ones achieved via sequential KF and RTS smoother. The input and response time histories estimated by combining filtering and smoothing show low frequency errors which are not generated when using Kalman filtering only.

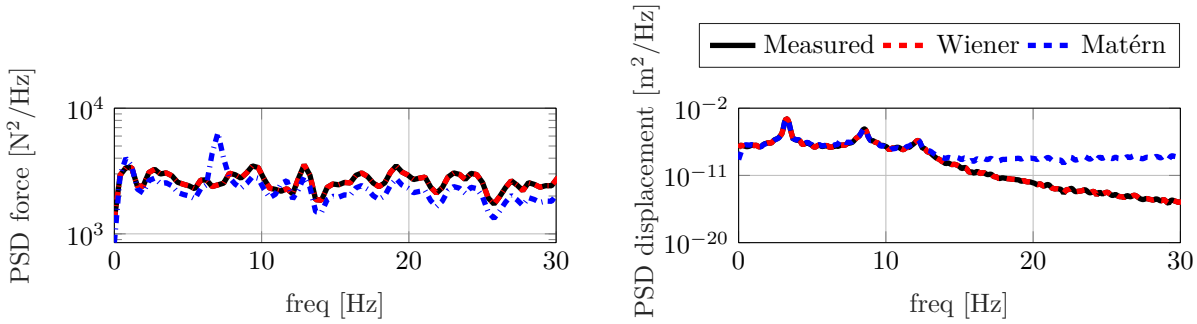

Figure 5.11: 3 DOFs system: PSDs of the random input and the resulting 1^{st} DOF displacement. "Measured" signals are shown by a solid black line, while those estimated (via filtering only) by making use of a Wiener and a Matérn covariance function ($\nu = 1.5$) are respectively denoted via a dashed red and blue line.

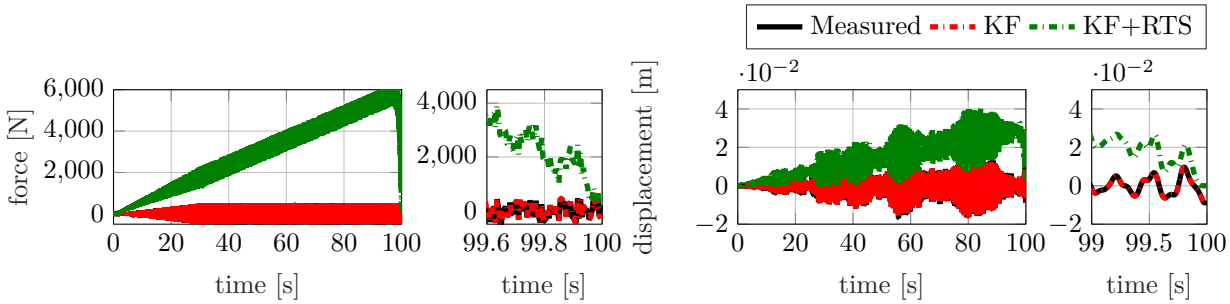

Figure 5.12: 3 DOFs system: time and detailed time histories of the random input and the resulting 1^{st} DOF displacement. "Measured" signals are shown by a solid black line, while those estimated by filtering only and a sequence of filtering and smoothing (Wiener covariance function) are respectively denoted via a dashed red and green line.

Table 5.5 quantifies the estimation inaccuracy for the analyzed estimators by offering the NRMSE values computed between the estimated and the "measured" signals for both the unknown force and the predicted responses. Table 5.5 confirms that adopting a Wiener covariance function within a GPLFM solved with filtering only guarantees the highest performance for both input and response estimation in a random loading setting.

Table 5.5: 3 DOFs system, random load: NRMSE values between "measured" and estimated signals (responses and force).

	$\text{NRMSE}_{displ} \times 10^5$			$\text{NRMSE}_{vel} \times 10^5$			$\text{NRMSE}_{acc} \times 10^5$			$\text{NRMSE} \times 10^5$	NRMSE
	DOF1	DOF2	DOF3	DOF1	DOF2	DOF3	DOF1	DOF2	DOF3	mean resp.	force
Wiener (KF)	0.078	0.091	0.111	0.003	0.002	0.001	0.005	0.005	0.010	0.034	0.014
Matérn (KF)	10178.163	11413.813	13798.689	5949.576	3661.975	1992.402	8319.623	7659.016	3143.413	734.630	0.459
Wiener (KF+RTS)	32660.282	38181.965	46559.658	635.706	445.016	318.899	829.560	742.271	158.739	13392.455	13.077

Random multisine load

In this paragraph, the input-state predictions obtained for the 3 DOFs system subjected to a random multisine input at the 3^{rd} mass are summarized. A random multisine signal is constructed as a superposition of sines with random phase within a selected frequency range (0-20 Hz). The use of a quasiperiodic covariance function is hereby proposed for representing this type of load and performing the hyperparameters training by regression of the 3^{rd} mass acceleration. Indeed, adopting a quasiperiodic covariance function rather than a periodic one allows to simultaneously account for periodic and damping effects, which result from the damped nature of the analyzed dynamical system. Figures 5.13 and 5.14 compare the predictions obtained via the quasiperiodic and the Matérn covariance functions for the actual input and the 1^{st} mass displacement in time and frequency domains respectively. The initialization values for the algorithm under the different covariance

assumptions are summarized in Tab. 5.6. Figures 5.13 and 5.14 show that a quasiperiodic covariance function allows to better match the amplitude and the frequency content of the unknown input. The same conclusion can be drawn for the response estimate which, however, exhibits a slight mismatch between 15 and 20 Hz. This error can be explained by the use of only one acceleration observation, which reflects the input frequency content because of their direct feedthrough. Part of this content is then erroneously transferred to the response estimates of different type, i.e., displacement as the one in Figs. 5.13 and 5.14. This issue is normally solved in practically applications by including different types of responses within the observations set.

Table 5.6: 3 DOFs system, random multisine load: estimators initialization values

Initial state mean	Initial error cov. matrix	Initial hyperparameters quasiperiodic	Initial hyperparameters Matérn	Process noise cov. matrix ($\mathbf{Q}$)	Measurement noise cov. matrix ($\mathbf{R}$)
$\hat{\mathbf{x}}^a_{0\|0} = \mathbf{0}$	$\hat{\mathbf{P}}^x_{0\|0} = \mathbf{0}$	$\sigma^2 = 2 \times 10^{-2}$ $l = 3 \times 10^{-1}$ $t_{period} = 1$ $l_{matern} = 1.3$	$\sigma^2 = 5$ $l = 1 \times 10^{-2}$	$\mathbf{Q}_{\text{displ}} = 10^{-20} \times \mathbf{I}_{\text{displ}}$ $\mathbf{Q}_{\text{vel}} = 10^{-10} \times \mathbf{I}_{\text{vel}}$	$\mathbf{R}_{\text{displ}} = 10^{-15} \times \mathbf{I}_{\text{displ}}$ $\mathbf{R}_{\text{acc}} = 10^{-12} \times \mathbf{I}_{\text{acc}}$

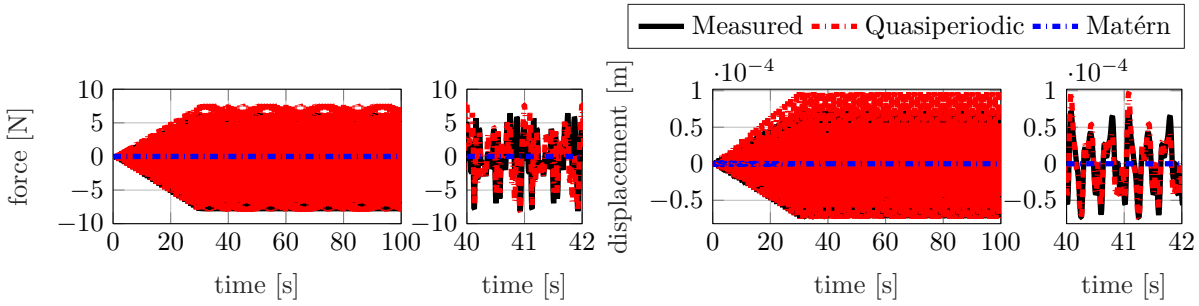

Figure 5.13: 3 DOFs system: time and detailed time histories of the multisine input and the resulting 1^{st} DOF displacement. "Measured" signals are shown by a solid black line, while those estimated (via filtering only) by making use of a quasiperiodic and a Matérn covariance function ($\nu = 1.5$) are respectively denoted via a dashed red and blue line.

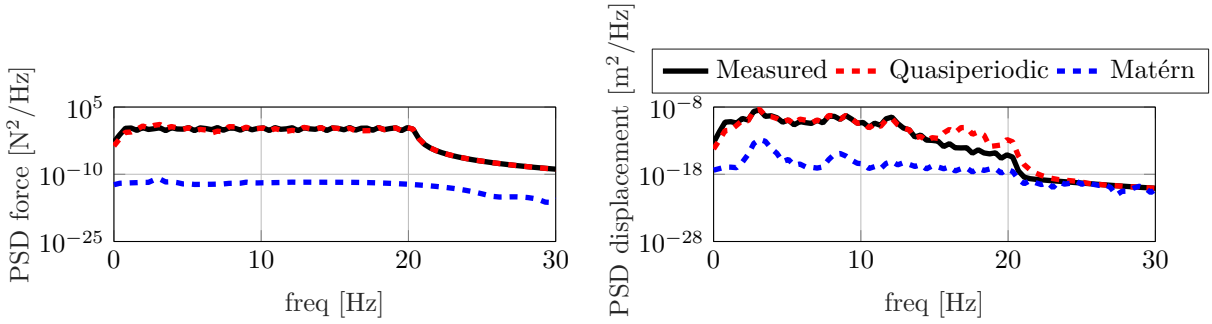

Figure 5.14: 3 DOFs system: PSDs of the multisine input and the resulting 1^{st} DOF displacement. "Measured" signals are shown by a solid black line, while those estimated (via filtering only) by making use of a quasiperiodic and a Matérn covariance function ($\nu = 1.5$) are respectively denoted via a dashed red and blue line.

Figure 5.15 shows a time-domain comparison between the estimations obtained via filtering only and the ones achieved via sequential KF and RTS smoother. The input and response time histories estimated by combining filtering and smoothing exhibit a deviation error in the last two seconds of the analyzed time window. This effect only appears when smoothing is combined with filtering.

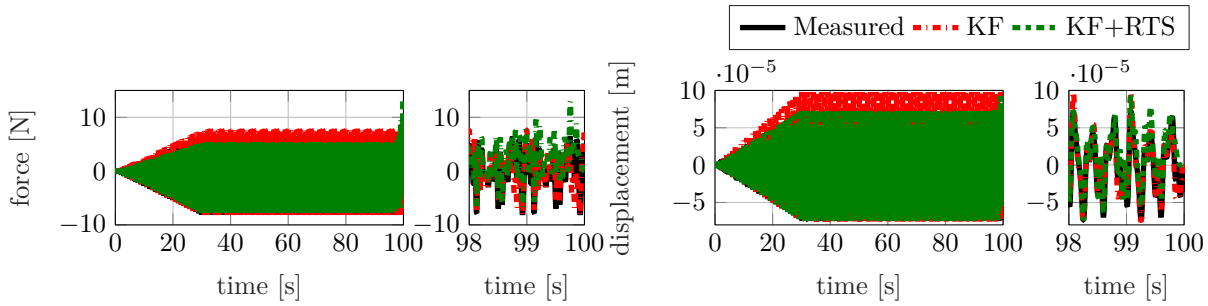

Figure 5.15: 3 DOFs system: time and detailed time histories of the multisine input and the resulting 1^{st} DOF displacement. "Measured" signals are shown by a solid black line, while those estimated by filtering only and a sequence of filtering and smoothing (quasiperiodic covariance function) are respectively denoted via a dashed red and green line.

The overall highest prediction performance achieved under the assumption of a quasiperiodic covariance function (with filtering only) for a random multisine excitation is confirmed by Tab. 5.7, which reports on the NRMSE values computed between the estimated and the "measured" signals for both the unknown force and the estimated responses.

Table 5.7: 3 DOFs system, random multisine load: NRMSE values between "measured" and estimated signals (responses and force).

	NRMSE_{displ}			NRMSE_{vel}			NRMSE_{acc}			NRMSE	NRMSE
	DOF1	DOF2	DOF3	DOF1	DOF2	DOF3	DOF1	DOF2	DOF3	mean resp.	force
Quasiperiodic (KF)	0.352	0.447	0.538	0.097	0.094	0.104	0.089	0.076	0.039	0.204	0.800
Matérn (KF)	1.000	1.000	1.000	1.000	1.000	1.000	1.000	1.000	1.000	1.000	1.000
Quasiperiodic (KF+RTS)	0.253	0.174	2.666	0.187	0.156	0.069	0.177	0.173	0.046	0.434	1.039

Impulse load

This paragraph treats the input-state predictions obtained for the 3 DOFs system when an impulse load is applied at the 3^{rd} mass. A quasiperiodic covariance function is hereby compared with an exponential covariance function (Matérn with ν=0.5) for regression of the 3^{rd} mass acceleration and subsequent construction of the unknown input model. Indeed, a quasiperiodic covariance function is optimal for regression of damped dynamical systems free responses since these are expected to exhibit an oscillatory response with damped frequency content linked to the system modal properties. The exponential covariance function, i.e., a Matérn covariance function with $\nu = 0.5$, has been chosen as reference since this class of functions appear to be the most suitable for detecting large discontinuities in time due to the linked GPs being non-smooth, i.e., mean square non-differentiable. A summary of the initialization values selected for the algorithm parameters is reported in Tab. 5.8. Figure 5.16 (left) compares the actual input time history against the predictions achieved using the GPLFM approach with filtering only (both for a quasiperiodic and an exponential covariance function). Figure 5.16 (right) offers the time-domain estimation results for the 1^{st} DOF displacement when a quasiperiodic or an exponential covariance function is adopted. Additionally, the corresponding Power Spectral Densitys (PSDs) are presented in Fig. 5.17. From the analysis of Figs. 5.16 and 5.17 it can be concluded that the quasiperiodic covariance function generates larger estimation errors for both input and response estimations. This may be due to the quasiperiodic covariance function being centered on a specific frequency, e.g. the first natural frequency of the system, and only including its harmonics. This assumption excludes the possibility to include higher natural frequencies (2^{nd} and 3^{rd} for this application) in the GP representation and renders the hereby adopted quasiperiodic covariance function too strict for such application. A workaround for this limitation consists in constructing a covariance function as a product of quasiperiodic covariance functions centered at the 3 natural frequencies of the system.

Table 5.8: 3 DOFs system, impulse load: estimators initialization values

Initial state mean	Initial error cov. matrix	Initial hyperparameters quasiperiodic	Initial hyperparameters exponential	Process noise cov. matrix ($\mathbf{Q}$)	Measurement noise cov. matrix ($\mathbf{R}$)
$\hat{\mathbf{x}}^a_{0\|0} = \mathbf{0}$	$\hat{\mathbf{P}}^x_{0\|0} = \mathbf{0}$	$\sigma^2 = 6 \times 10^{-1}$ $l = 2.5 \times 10^{-1}$ $t_{period} = 0.3$ $l_{matern} = 1$	$\sigma^2 = 5$ $l = 1 \times 10^{-2}$	$\mathbf{Q}_{\text{displ}} = 10^{-20} \times \mathbf{I}_{\text{displ}}$ $\mathbf{Q}_{\text{vel}} = 10^{-10} \times \mathbf{I}_{\text{vel}}$	$\mathbf{R}_{\text{displ}} = 10^{-15} \times \mathbf{I}_{\text{displ}}$ $\mathbf{R}_{\text{acc}} = 10^{-12} \times \mathbf{I}_{\text{acc}}$

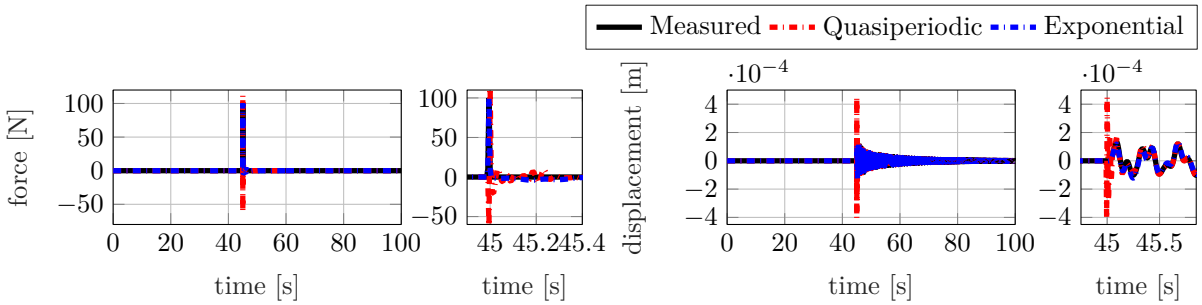

Figure 5.16: 3 DOFs system: time and detailed time histories of the impulse input and the resulting 1^{st} DOF displacement. "Measured" signals are shown by a solid black line, while those estimated (via filtering only) by making use of a quasiperiodic and an exponential covariance function are respectively denoted via a dashed red and blue line.

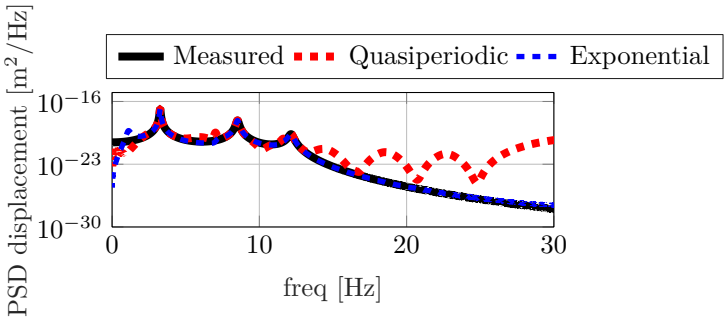

Figure 5.17: 3 DOFs system: PSDs of the 1^{st} DOF displacement resulting from the impulse excitation. "Measured" signals are shown by a solid black line, while those estimated (via filtering only) by making use of a quasiperiodic and an exponential covariance function are respectively denoted via a dashed red and blue line.

Figure 5.18 shows a time-domain comparison between the estimations obtained via filtering only and the ones achieved via sequential KF and RTS smoother under the assumption of an exponential covariance function. The input and response time histories estimated by combining filtering and smoothing exhibit a deviation error in the last two seconds of the analyzed time window. These deviations are limited with respect to the ones experienced in the previously considered scenarios. This may be ascribed to the low signals amplitude at the end of the analyzed time frame for impulse response, which therefore generates lower accumulation errors.
A quantification of the estimation errors obtained by the analyzed estimators is reported in Tab. 5.9 by means of the NRMSE values computed between the estimated and the "measured" signals for both the unknown force and the estimated responses. Table 5.9 confirms that the use of a quasiperiodic covariance function centered at a specific frequency within a GPLFM generates large prediction inaccuracy for both the input and response estimations under an impulse excitation.

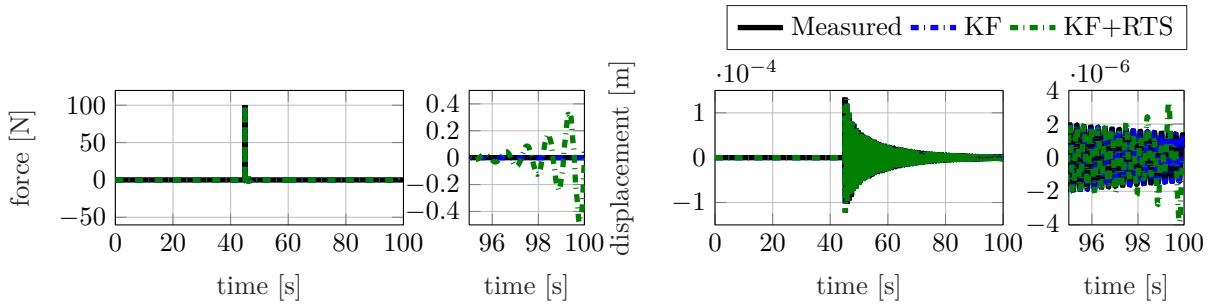

Figure 5.18: 3 DOFs system: time and detailed time histories of the impulse input and the resulting 1^{st} DOF displacement. "Measured" signals are shown by a solid black line, while those estimated by filtering only and a sequence of filtering and smoothing (exponential covariance function) are respectively denoted via a dashed blue and green line.

Table 5.9: 3 DOFs system, impulse load: NRMSE values between "measured" and estimated signals (responses and force).

	$\text{NRMSE}_{displ} \times 10^2$			$\text{NRMSE}_{vel} \times 10^2$			$\text{NRMSE}_{acc} \times 10^2$			$\text{NRMSE} \times 10^2$	NRMSE
	DOF1	DOF2	DOF3	DOF1	DOF2	DOF3	DOF1	DOF2	DOF3	mean resp.	force
Quasiperiodic (KF)	37.570	44.491	54.658	7.738	5.337	2.895	10.131	10.102	9.753	20.297	1.792
Exponential (KF)	8.541	9.800	11.660	3.756	3.688	3.836	3.851	3.776	0.023	5.437	0.332
Exponential (KF+RTS)	8.605	9.876	11.751	3.768	3.708	3.864	3.854	3.780	0.074	5.475	0.334

Step load

In this paragraph, the input-state estimation results for the 3 DOFs system subject to a step load are investigated. A quasiperiodic and an exponential covariance function have been selected for this problem following the same reasons standing for the impulse response. However, a step type of input features a static component which is normally difficult to identify via Bayesian estimators since these tools exploit a dynamical model of the system under study and a non-stationary model such as the RW for the unknown input. The GPLFM approach can remedy to this problem if: i) displacement-level sensors are included in the observations set; ii) a constant offset is included in the covariance function used for regression of a displacement-level response. A biased quasiperiodic covariance function, as explained in Subsubsection 2.3.1.3, embeds a static component in the prior when performing regression. This allows to fit the bias present in a displacement response caused by a step input, thus guaranteeing its representation within the resulting unknown input model employed in the input-state estimation. The same approach has been used to build a biased exponential covariance function as a summation of a constant and an exponential (Matérn with $\nu = 0.5$) covariance function. The resulting covariance function has been adopted for estimation and results have been compared with the predictions obtained via the biased quasiperiodic covariance function. Table 5.10 presents an overview of the initialization values selected for the algorithm necessary parameters. Figure 5.19 (left) proposes a time-domain comparison between the actual input and the estimations achieved using the GPLFM approach with filtering only (both via the biased quasiperiodic covariance function and the biased exponential covariance function). The load time histories comparison shows that both the covariance functions allow to easily detect the step profile, but the biased exponential covariance function generates a large error at the last time instants of the analyzed time frame. Moreover, oscillations around the mean value are larger when adopting a biased exponential covariance function. Figure 5.19 (right) offers the actual 1^{st} DOF displacement and the corresponding predictions achieved via the GPLFM approach in time domain. The presented comparison shows that a good response prediction can be obtained via both the analyzed covariance functions. However, by analyzing the PSDs comparison in Fig. 5.20, it can be concluded that the response estimate produced by the biased quasiperiodic covariance function better matches the "measured" response frequency content. These results are in contrast to the impulse response case, where the exponential covariance function provides more accurate estimations. This can be due to a different effect introduced by the constant covariance function when used in combination with a quasiperiodic or an exponential covariance function. While in both cases it allows to capture the bias, it may influence differently the hyperparameters values

of the "dynamic" (quasiperiodic or exponential) covariance function selected during the training phase. As a generic conclusion, it can be stated that both the proposed covariance functions can be adopted for the analyzed loading scenario as the results deviation is limited.

Table 5.10: 3 DOFs system, step load: estimators initialization values

Initial state mean	Initial error cov. matrix	Initial hyperparameters biased quasiper.	Initial hyperparameters biased exp.	Process noise cov. matrix ($\mathbf{Q}$)	Measurement noise cov. matrix ($\mathbf{R}$)
$\hat{\mathbf{x}}^a_{0\|0} = \mathbf{0}$	$\hat{\mathbf{P}}^x_{0\|0} = \mathbf{0}$	$\sigma^2 = 2 \times 10^{-1}$ $\sigma^2_{constant} = 2 \times 10^{-1}$ $l = 3 \times 10^{-1}$ $t_{period} = 0.3$ $l_{matern} = 1.3$	$\sigma^2 = 2 \times 10^{-1}$ $\sigma^2_{constant} = 2 \times 10^{-1}$ $l = 3 \times 10^{-1}$	$\mathbf{Q}_{\text{displ}} = 10^{-20} \times \mathbf{I}_{\text{displ}}$ $\mathbf{Q}_{\text{vel}} = 10^{-10} \times \mathbf{I}_{\text{vel}}$	$\mathbf{R}_{\text{displ}} = 10^{-15} \times \mathbf{I}_{\text{displ}}$ $\mathbf{R}_{\text{acc}} = 10^{-12} \times \mathbf{I}_{\text{acc}}$

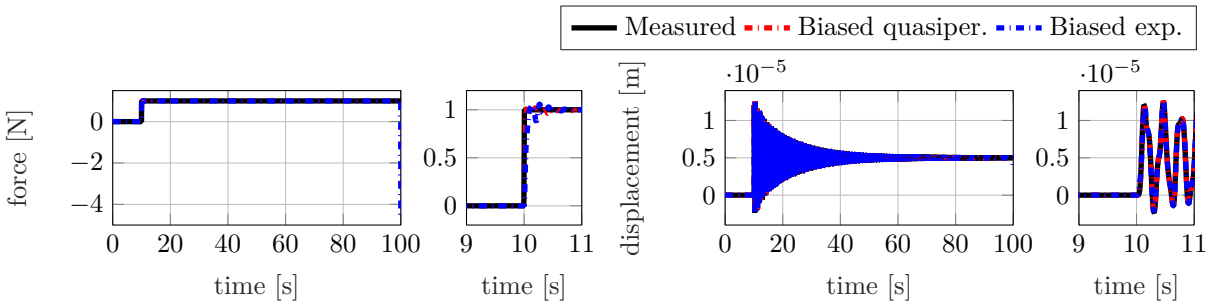

Figure 5.19: 3 DOFs system: time and detailed time histories of the step input and the resulting 1^{st} DOF displacement. "Measured" signals are shown by a solid black line, while those estimated (via filtering only) by making use of a biased quasiperiodic and a biased exponential covariance function are respectively denoted via a dashed red and blue line.

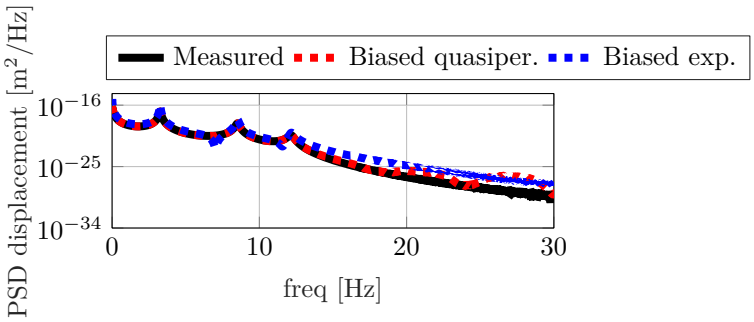

Figure 5.20: 3 DOFs system: PSDs of the 1^{st} DOF displacement resulting from the step excitation. "Measured" signals are shown by a solid black line, while those estimated (via filtering only) by making use of a biased quasiperiodic and a biased exponential covariance function are respectively denoted via a dashed red and blue line.

Figure 5.21 offers a time-domain comparison between the results obtained via filtering only and the ones achieved via sequential KF and RTS smoother in the step loading scenario. The input and response time histories estimated by combining filtering and smoothing show large deviations at the end of the analyzed time window.
Table 5.11 quantifies the estimation inaccuracy for the analyzed estimators by offering the NRMSE values computed between the estimated and the "measured" signals for both the unknown force and the predicted responses. Table 5.11 proves that adopting a biased quasiperiodic covariance function within a GPLFM solved with filtering only allows for the optimal prediction performance for both input and responses under a step type of load.

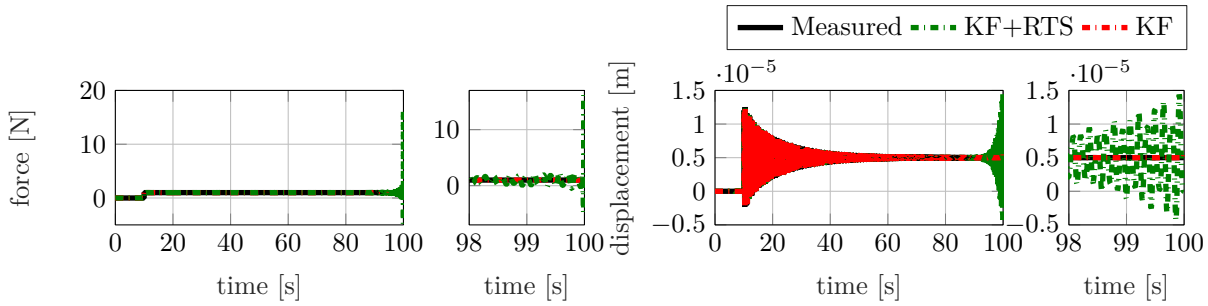

Figure 5.21: 3 DOFs system: time and detailed time histories of the step input and the resulting 1^{st} DOF displacement. "Measured" signals are shown by a solid black line, while those estimated by filtering only and a sequence of filtering and smoothing (biased quasiperiodic covariance function) are respectively denoted via a dashed red and green line.

Table 5.11: 3 DOFs system, step load: NRMSE values between "measured" and estimated signals (responses and force).

	NRMSE_{displ}			NRMSE_{vel}			NRMSE_{acc}			NRMSE	NRMSE
	DOF1	DOF2	DOF3	DOF1	DOF2	DOF3	DOF1	DOF2	DOF3	mean resp.	force
Biased quasiperiodic (KF)	0.016	0.017	0.005	0.173	0.251	0.180	0.287	0.428	0.513	0.208	0.055
Biased exponential (KF)	0.238	0.251	0.007	0.900	1.968	2.136	0.534	8.246	5.271	2.172	0.148
Biased quasiperiodic (KF+RTS)	0.040	0.023	0.009	0.328	0.205	0.212	0.765	0.611	0.488	0.298	0.066

5.3 Summary

This chapter focuses on the input modeling task within the context of input-state estimation via Bayesian filtering. The conventional RW transition model is described, along with a detailed analysis of the limitations derived from its employment. The use of structured LFMs is then proposed as a more comprehensive and flexible alternative to the RW transition model. A structured LFM can be constructed by exploiting the SDE representation for stochastic process regression derived in Chapter 2, which exhibits different features according to the chosen kernel. The analysis conducted in Chapter 2 has highlighted the tendency of certain classes of kernels towards a better regression performance in specific loading conditions. This result is hereby tested by means of a simulated example.

6

ENVIRONMENTAL TESTING: THE BOX ASSEMBLY WITH REMOVABLE COMPONENT

Environmental testing is a standard procedure in spacecraft engineering used for qualification of spacecrafts mechanical design. These tests, performed for verifying the resistance of the system and all its components to the random excitation to which they are subjected, are particularly crucial for ensuring and demonstrating the spacecraft integrity against the dynamical launch environment. Environmental testing therefore represents an essential specification procedure during which the spacecraft is placed on a big electrodynamic or hydraulic shaker testing facility, which provides a controlled excitation with the purpose of replicating the in-service structural response of the tested structure. Besides the difficulties in the execution of these tests due to the structure dimensions, the most critical aspect is related to the poor operational environment representation which may be achieved while testing. Indeed, limitations in the adopted vibration control strategies and the interaction between the structure under test and the testing facility, can give rise to undesired issues, e.g. over- or under testing, errors in time to failure estimation or even damage. In this framework, a collaboration between Kansas City National Security Campus (managed by Honeywell Federal Manufacturing & Tecnology) and Sandia National Laboratories introduced the BCC. The goal of this project is to improve the in-service environment replication at a component level, leading to the establishment of component failure mechanisms closer to the ones that may arise during its operational life. The challenge focuses on the BARC setup, a simple mock-up that can yet represent the relevant challenges from the BCC point of view. Several BARC specimens have been distributed among the large number of research institutes that have accepted the BCC and that are now investigating the BARC with the purpose of providing new solutions [99, 100, 102]. To address the BCC, VS techniques can be employed in environmental testing applications to retrieve the complete strain field on the tested component both in operation and during tests, allowing for a more complete comparison of the two conditions. Entire stress fields can be derived from strain information, based on which component failure can be more easily predicted. Moreover, forces are usually not measured during this type of tests. Therefore, a simultaneous estimation of states and inputs can be used to retrieve such relevant quantities. To this end, this chapter proposes the use of data assimilation via Kalman-type filters for calculating an estimate of the QoI, e.g. excitation or responses of the system at locations that may not be easily instrumented via physical sensors.
The first section of this chapter presents the BARC specimen and the FE model, along with the validation and update results achieved using experimental modal parameters extrapolated from a free-free test campaign. Secondly, the environmental testing campaign carried out on the BARC is described. The last part of this chapter documents the VS results obtained from the use of Kalman-type filters during environmental tests on the BARC. To this end, the adopted ROM of the system is derived by employing RIRA modes in order to take into account the test BCs. During the environmental tests under study, the AKF is first evaluated for a strains-only and a mixed (strains and accelerations) observation set. The resulting predictions are then compared to the ones obtained by employing a conventional GPLFM for input-state estimation with a Matérn covariance function. Section 6.4 reports the conclusions for this chapter.

6.1 The Box Assembly with Removable Component

The BCC addresses the development of a methodology for assessing the design of environmental testing procedures, leading to more realistic response reconstruction for systems in operation. When looking at environment replication at the component level, differences in BCs between single component testing and full assembly testing must be taken into account. Removing the component from its original subassembly and testing it on a shaker, rather than directly testing the entire assembly, obviously gives rise to shifts in BCs, thereby impacting the structural dynamics. Common practice consists in overtesting the structure, which typically results in undesired oversizing of the component and an erroneous environmental vibration replication. The ultimate goal of the BCC is to propose an alternative to overtesting, looking for new solutions able to improve the in-service environment replication, e.g. studying the influence of different excitation mechanisms and BCs. The BCC makes use of a test bed comprising a relatively simple aluminum structure, the BARC shown in Figure 6.1. It consists of a "component", made from the assembly of two C-channels connected by a beam, and a "subassembly", hereby referred as box, consisting of a cut box-beam, on which the component rides. The component plays the role of the unit under testing, while the subassembly represents a generic operational support. In the BARC specimen provided to Siemens Industry Software (SISW), four M5 holes have been drilled at the box base to directly connect the BARC to a commonly used 75 lbf shaker and an M8 hole has been added, in order to permit connection to a larger shaker.

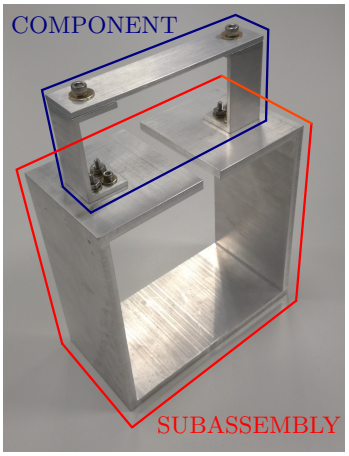

Figure 6.1: The Box Assembly with Removable Component

6.1.1 Finite Element model: validation and update

Figure 6.2 illustrates the FE model developed in Simcenter^{TM} 3D (NX^{TM} Nastran) for the BARC specimen. The model has been generated from the available Computer Aided Design (CAD) model using a 2D shell mesh of a total of around 2400 CQUAD4 elements, whose dimensions have been differentiated according to the specific component. The model is indeed made up of four distinct parts: the box, the beam and two C-channels. Bolted connections have been introduced at the interface between the several components to model the bolts connecting the physical parts. These bolted connections are constructed using Rigid Body Element (RBE) connections at the holes and a BAR element to model the screws. This solution allowed to account for the screws presence, which, given the limited dimensions of the specimen, have a non-negligible influence on the numerical modal properties. Additionally, face contact has been modeled between the coupled surfaces to avoid bodies interpenetration. Following the specifications provided by the BCC, the following materials have been adopted to model the different components: 6063 aluminum alloy for the C-channels, 6061 aluminum alloy for the beam and the box, AISI 316 stainless steal for the screws.

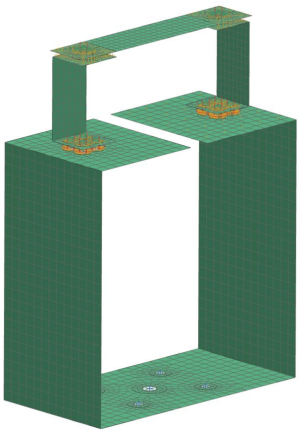

Figure 6.2: BARC FE model

The model has been validated with test data acquired during impact testing of the BARC in free-free conditions (in Fig. 6.3), processed with Simcenter^{TM} Testlab PolyMAX. To guarantee consistency between the model and the test configuration, four masses at the four installed triaxial accelerometers locations have been included in the FE model. The initial correlation between experimental and numerical modal parameters has been improved through a model update procedure via the Simcenter^{TM} 3D Model Update tool, which makes use of NX Nastran SOL 200. By spanning the pre-selected ranges for the design variables, the model updating process seeks for the minimal frequency error and the maximal Modal Assurance Criterion (MAC) value between the first ten numerical and experimental mode pairs via a genetic algorithm. The adopted design variables are reported in Tab. 6.1, along with the corresponding initial and updated values. To improve the correlation between FE model and test data, both material and geometrical properties have been accounted for in the design variables set. The latter thus included: the densities and the Young's moduli of all the involved materials, the CQUAD4 elements thickness for each substructure, the screws section radius.

Figure 6.3: Free-free impact testing on the BARC

Table 6.2 reports on the model update results by comparing the initial and updated numerical frequencies with the reference test frequencies for the first 10 modes. Additionally, Tab. 6.2 offers the initial and updated frequency errors as well as a comparison between the initial and updated MAC values for the diagonal mode pairs. From the analysis of Tab. 6.2 it can be concluded that the implemented update strategy allowed to achieve frequency errors below the 3% threshold and improved MAC values for the first seven modes, with a large improvement on mode 4 and 5. These

benefits came with the cost of reducing the correlation for modes from 8 to 10. However, the accuracy decrease for these three modes is contained enough to justify the selection of the optimal update results hereby reported.

Table 6.1: BARC FE model update: design variables initial and updated values

Design variables	Initial value	Updated value
$E_{screws}[Mpa]$	190000.000	187287.778
$E_{box,beam}[Mpa]$	68980.000	68855.944
$E_{channels}[Mpa]$	68900.000	68169.447
$\rho_{screws}[g/cm^3]$	8.020	8.420
$\rho_{box,beam}[g/cm^3]$	2.711	2.613
$\rho_{channels}[g/cm^3]$	2.700	2.827
$r_{screws_{box}}[mm]$	2.153	2.153
$r_{screws_{beam}}[mm]$	2.807	2.867
$T_{beam}[mm]$	3.300	3.135
$T_{box}[mm]$	6.040	6.094
$T_{channels}[mm]$	3.140	3.112

Table 6.2: BARC FE model initial and updated frequencies, frequency errors and MAC pairs

Modes	f_i^{test} [Hz]	f_i^{initial}[Hz]	f_i^{updated}[Hz]	$err_{f_i}^{\text{initial}}$ [%]	$err_{f_i}^{\text{updated}}$[%]	$\text{MAC}_{ii}^{\text{initial}}$	$\text{MAC}_{ii}^{\text{updated}}$
1	182.844	185.425	186.181	1.412	1.825	0.983	0.994
2	201.223	197.716	200.019	-1.743	-0.598	0.937	0.959
3	256.399	254.382	252.967	-0.787	-1.338	0.991	0.991
4	417.736	440.075	429.883	5.348	2.908	0.594	0.933
5	460.104	477.089	462.946	3.691	0.618	0.623	0.965
6	545.446	553.83	551.001	1.537	1.019	0.983	0.986
7	572.081	563.784	568.916	-1.45	-0.553	0.806	0.815
8	648.572	650.843	651.205	0.35	0.406	0.981	0.976
9	1069.990	1030.891	1012.083	-3.654	-5.412	0.942	0.941
10	1125.120	1109.906	1101.535	-1.352	-2.096	0.937	0.875

6.2 Environmental testing

The test setup adopted during environmental tests on the BARC foresees the clamping of the BARC base on a commonly used shaker of comparable size. Figure 6.4 (left) shows the complete test setup of the measurement campaign conducted on the BARC, while detailed focus on the sensors and BARC connection to the shaker is provided in Fig. 6.4 (right). The four M5 holes on the BARC base have been used to create a 4-points bolted connection with the "The Modal Shop" 2025E electro-dynamic modal shaker. In addition, four PCB monoaxial force cells have been placed between the BARC and the shaker in order to measure the applied forces in the vertical direction (Z). Simcenter^{TM} SCADAS Mobile hardware and Simcenter^{TM} Testlab software have been used to control the shaker and acquire data during the hereby described tests. Several excitation signals with different amplitude levels have been used during tests: continuous random (maximum level: 0.3, 0.4 and 0.5 V), pseudo random (RMS level: 0.1,0.15,0.2,0.25,0.3 V), sine (3.2, 20, 300, 650 Hz), linear sine sweep (sweep rate: 2, 3 Hz; voltage level: 0.1, 0.2 V), logarithmic sine sweep (sweep rate: 1, 2 oct/min; voltage level: 0.1, 0.2 V). Sixteen strain gauges and four triaxial accelerometers have been attached to the system to both measure strain and acceleration data. The sensors locations have been selected via an existing OSP strategy [44, 57] which aims at selecting the optimal sensors set to guarantee system observability for input-state estimation using Kalman-based data assimilation strategies. Figure 6.5 shows the test sensors locations and the modeled excitation scheme, i.e., four vertical forces transmitted at the four bolted connections between the BARC base and the shaker head.

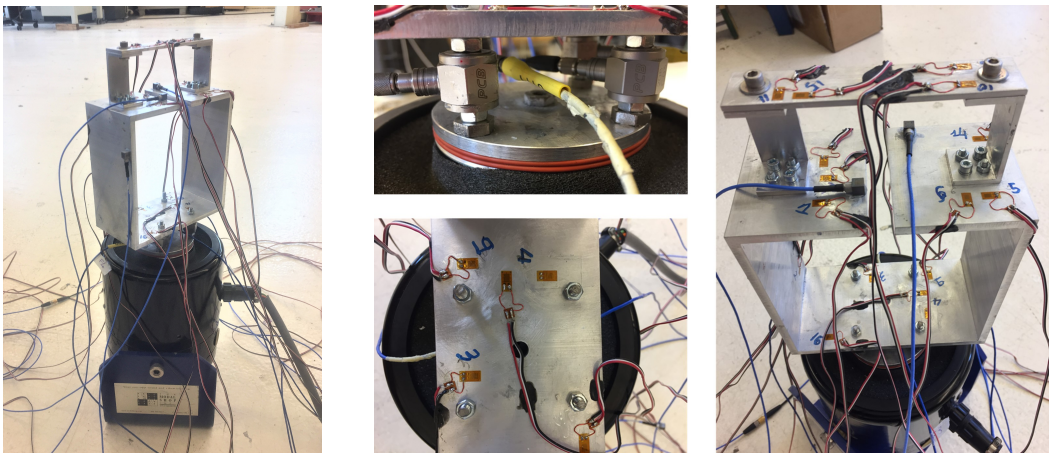

Figure 6.4: BARC environmental testing: BARC mounted on a monoaxial shaker (left); detailed view of BARC attachment to the shaker (middle); detailed view of sensors (right).

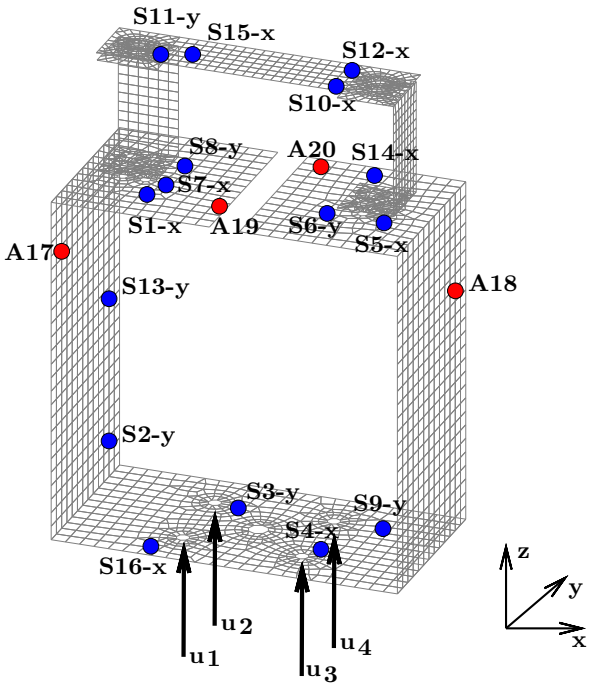

Figure 6.5: Sensing configuration during environmental testing on the BARC: accelerometers (red), strain gauges (blue)

6.3 Joint input-state estimation

This section proposes the use of VS techniques for the estimation of the quantities of interest during the environmental tests performed on the BARC using a pseudo random signal (0.3 V RMS level). In order to build the required BARC SSM, the updated FE model described in Subsection 6.1.1 has been employed and complemented with the necessary assumptions regarding the BCs to which the system is subjected during tests. In the analyzed configuration, the applied constraint demands the BARC base connection points to move together with the shaker. Therefore, no fixed constraint is provided for the vertical translation in the global frame. This layout has been replicated in a numerical environment by fixing all the DOFs, except the vertical translation, of the RBE2 connections central nodes at the BARC base in the free-free FE model. To reduce the

computational effort and enable online applicability of the proposed input-state estimation methods, the resulting model has undergone the MOR process postulated in Subsubsection 2.1.1.1. The use of RIRA modes instead of more conventional residual attachment modes deals with the presence of rigid body motion introduced by unconstrained DOFs such as the BARC vertical translation enabled during environmental tests. Indeed, rigid body motion prevents the computation of the static solution, and hence of the residual attachment modes.
In order to test the potential of the adopted estimators, the two different observations sets in Tab. 6.3 have been constructed by selecting two subsets of sensors among the physically instrumented locations reported in Fig. 6.5. The remaining ones have been used as reference quantities to check the validity of the achieved response estimation. For the first set, only strain responses have been considered. The measured locations have been chosen in order to focus on response estimation at the component level and to guarantee that measurements collocated with the applied forces could be included. Indeed, collocated measurements allow for a more accurate reconstruction of the inputs [148]. The observability requirements for the reduced sensor set have been checked by ensuring that the condition number of the observability matrix [149] for the reduced set is of the same order of magnitude as the one obtained for the full sensor set, which is guaranteed by the employed OSP adopted strategy. The second observations set has been defined as an extension of the first, to which also the four acceleration sensors (three directions) have been added.

Table 6.3: BARC environmental tests: observations sets used for VS validation

Strains only	S12,S1,S8,S13,S2,S16,S3,S4,S9
Strains and accelerations	S12,S1,S8,S13,S2,S16,S3,S4,S9,A17,A18,A19,A20

6.3.1 *Input-response estimation through the Augmented Kalman Filter*

This section reports on the results obtained by applying the AKF for jointly estimating inputs and responses during the BARC environmental tests illustrated in Section 6.2. A comparison will be offered between the estimation results obtained using the two observations sets in Tab. 6.3. In order to launch the estimation, the necessary AKF parameters have been selected a priori as described next. The system initial displacement and velocity have been assumed to be equal to zero, as well as the the initial error covariance matrix $\mathbf{P}_0$. The coviarance matrix $\mathbf{R}$ associated to the measurement noise is a diagonal matrix, the elements of which are equal to the covariance of the noise associated to each of the measurements. These values have been retrieved by recording the background noise measured by each channel on the test day. To what concerns the process noise covariance matrix $\mathbf{Q}^a$, the diagonal elements of $\mathbf{Q}$ have been set to very low values with respect to the state vector components. For the strains-only case, the $\mathbf{Q}^u$ matrix diagonal elements have resulted from a calibration procedure based on the use of the L-curve method [150], which involves the use of the smoothing and error norms postulated in Section 11.2. In Fig. 6.6, the L-curve for each input targeted in the estimation problem treated in this work is reported.
The minimum of the error norm and a stable value of the smoothing norm are achieved when the diagonal elements of $\mathbf{Q}^u$ are all equal to $10^7 N^2$, which is the value that has been set for the estimation. The adopted values of $\mathbf{R}$ and $\mathbf{Q}^u$ are such that $\mathbf{Q} \gg \mathbf{R}$, i.e., the assumption that the model is less reliable than the measured data has been made. For the mixed observations set instead, the $\mathbf{Q}^u$ matrix diagonal elements have been selected by trial and error as the L-curve plots resulted to be of difficult interpretation.
Figure 6.7 illustrates the response estimation of strain sensors S10 and S11 when the strains-only data set is used, compared against the corresponding physically measured signals. A comparison with the results obtained adopting the mixed observations set is also offered. Moreover, Fig. 6.8 offers the RMSE values of the entire set of estimated responses with respect to their measured time histories, including the adopted strain observations, for both the analyzed sensors sets. From Fig. 6.7 and Fig. 6.8, it can be concluded that a good global agreement with the reference measured signals is obtained for the AKF estimations achieved with both the sensors sets in Tab. 6.3.

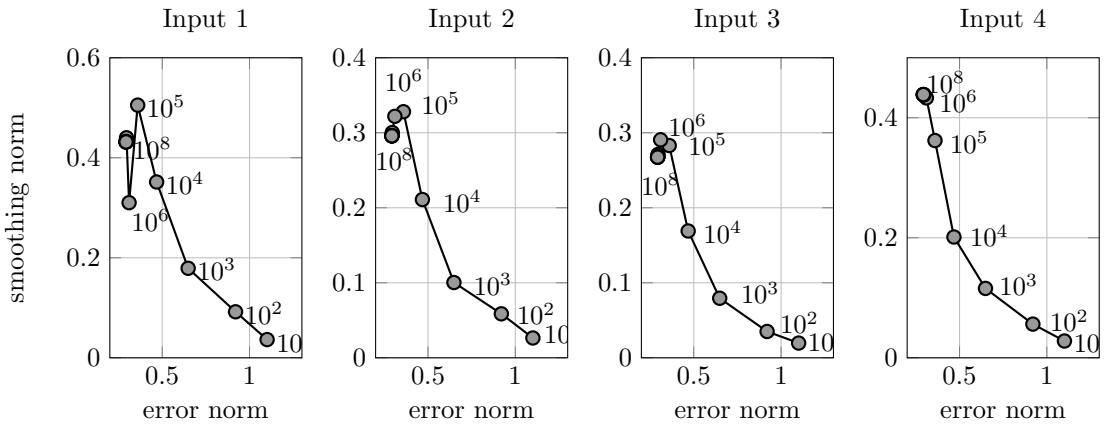

Figure 6.6: BARC environmental tests: L-curve for the four unknown inputs estimation via the AKF and a strain-based observations set

The poor reconstruction of high frequency components magnitude on the sensor measuring in Y direction can be ascribed to possible model inaccuracies. This model gap is well compensated for measured signals in X direction, such as S10, because the X axis resulted to be more excited during the performed measurement campaign, i.e., lower measured response levels appeared for all the sensors in Y direction.

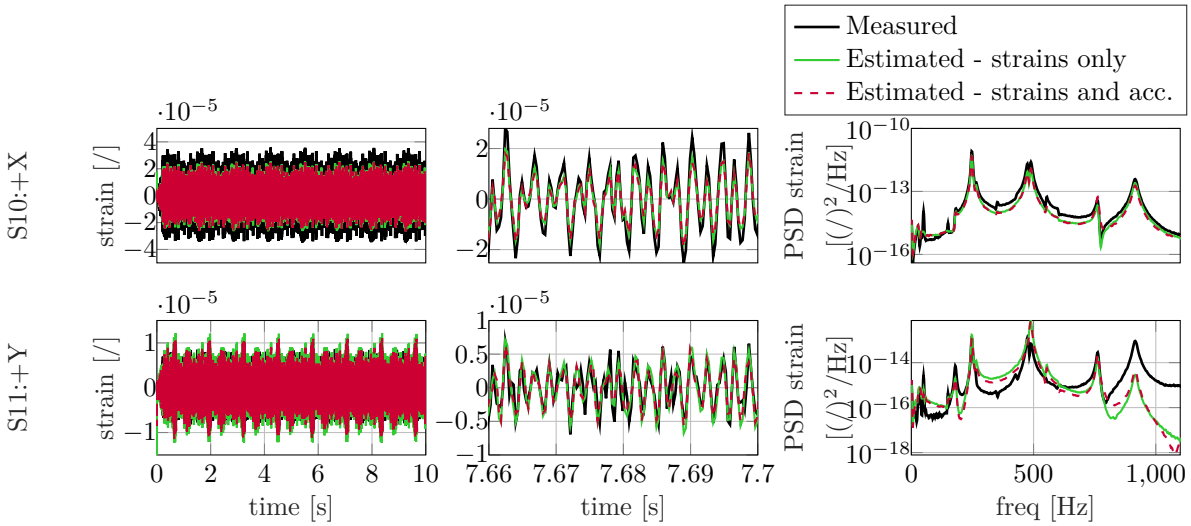

Figure 6.7: BARC environmental tests: time history (left), detailed time history (middle) and PSD (right) of strain responses S10 and S11. Measured signals are shown by a solid black line, while those estimated by the AKF via the strain-based and the mixed observations set are respectively denoted via a solid green line and a dashed red line. dashed green line.

Figure 6.9 proposes the input estimation results obtained in the strains-only case and compares them with both the experimentally measured ones and the estimations achieved in case the combined set of strains and accelerations is used. The AKF fails in providing a precise estimation of the inputs when a strains-only data set is adopted, except for input 4. The inaccurate estimation can be explained by the evident differences in the measured forces PSDs in Fig. 6.9 (right), which should theoretically be equivalent. These differences are introduced by the presence of strong BCs uncertainties that can be summarized by the following aspects:

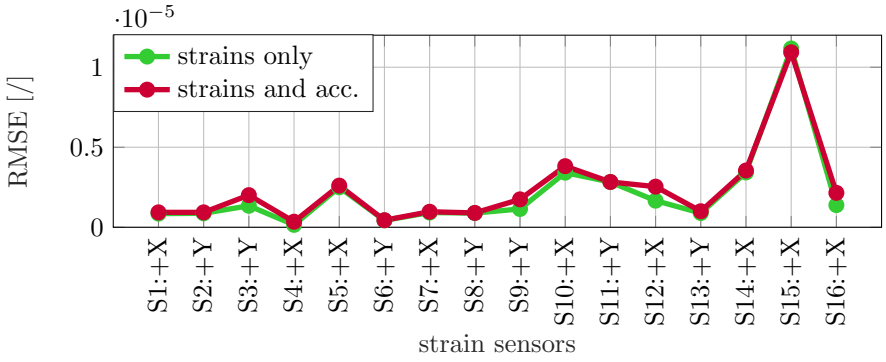

Figure 6.8: BARC environmental tests: RMSE values of the strain responses estimated by the AKF (strain-based observations set - green, mixed observations set - red) with respect to their measured time histories.

- Errors in reproducing the same connection conditions for all the four bolts during tests are present;
- Reaction forces at the connection between the BARC and the shaker arise during tests;
- The BCs used in the model introduce a strong approximation of the test configuration.

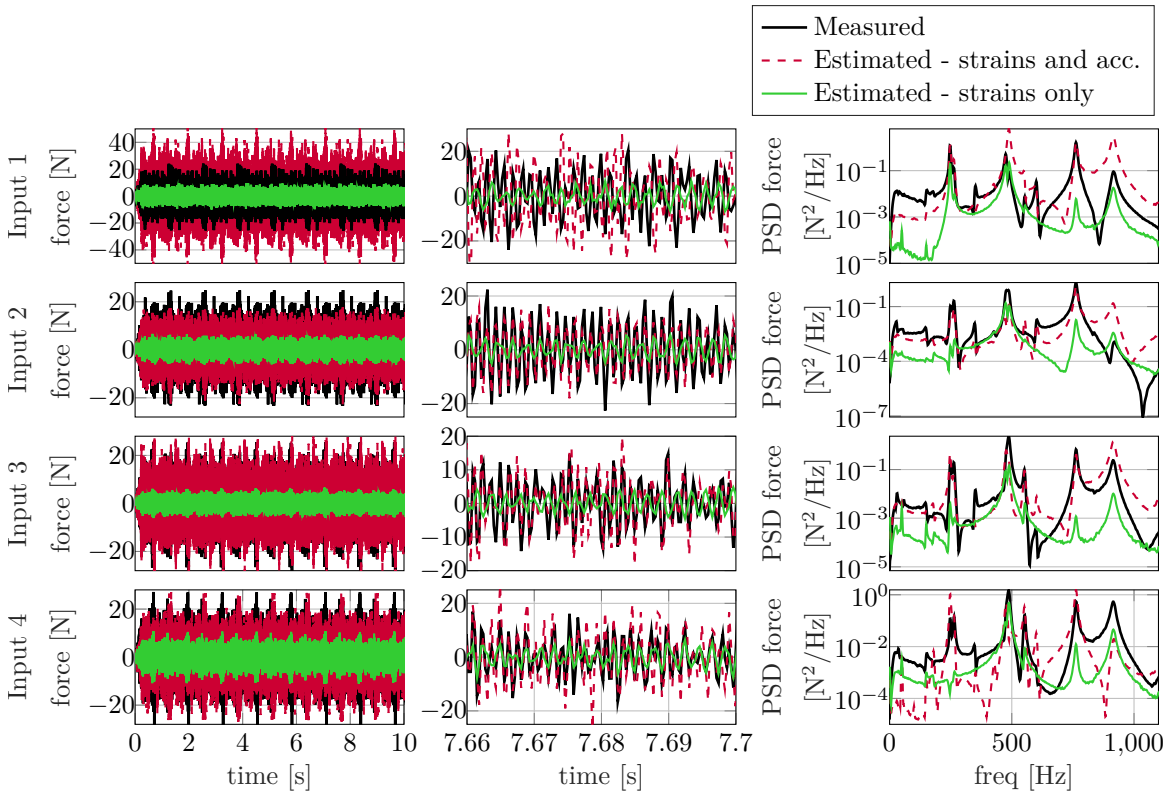

Figure 6.9: BARC environmental tests: time history (left), detailed time history (middle) and PSD (right) of input 1, input 2, input 3 and input 4. Measured signals are shown by a solid black line, while those estimated by the AKF via the strain-based and the mixed observations set are respectively denoted via a solid green line and a dashed red line.

Figure 6.9 further indicates that the introduction of the accelerometers direct feedthrough, i.e., a non-zero output-input matrix in the observation equation of the SSM, allows for an overall improvement in force estimation. In particular, Fig. 6.9 (right) shows that including accelerations allows to detect PSDs peaks, e.g. at around 250, 550 and 760 Hz, that are not identified when using only strains. Moreover, from Fig. 6.9 (left) it can be concluded that the force amplitude better

matches the actually measured one, with the exception of input 1, which is overestimated.
Table 6.4 compares, for the four loads, the RMS values of the estimated signals with the RMS values of the reference measured signals. The quantitative comparison proposed in Tab. 6.4 confirms the results reported in Fig. 6.9: the introduction of acceleration measurements allows for more accurate detection of the actual loads amplitude. Additionally, the RMSE values of the four estimated inputs with respect to their measured time histories are offered in Tab. 6.5. The RMSEs comparison for input 2 reflects the enhancement achieved by introducing acceleration observations. To the contrary, the RMSE values associated with inputs 1,3 and 4 show an increase with respect to the corresponding quantities in the strains-only case. These poor RMSE values can be explained by the poor reproduction of the test BCs in the model. This can negatively influence the terms relating the loads and the acceleration observations in the output-input matrix of the system SSM.

Table 6.4: BARC environmental tests: RMS values of the inputs measured and estimated by the AKF (strain-based and mixed observations sets)

	Input 1	Input 2	Input 3	Input 4
Measured	6.9	7.1	7.3	6.9
Strains only	2.9	2.0	1.9	3.1
Strains and accelerations	14.3	6.0	7.9	7.3

Table 6.5: BARC environmental tests: RMSE values of the inputs estimated by the AKF (strain-based and mixed observations sets) with respect to their measured time histories

	Input 1	Input 2	Input 3	Input 4
Strains only	8.1	7.1	8.7	4.8
Strains and accelerations	17.7	6.9	11.6	8.9

6.3.1.1 Augmented Kalman Filter estimation improvement via modeling alternatives

The join-input estimation results reported in Subsection 6.3.1 have demonstrated the negative effect that BCs modeling mismatches may have on the predictions achieved via Kalman-based strategies during environmental tests, even when a mixed observation set is adopted. In this respect, a potential improvement consists in providing modeling solutions which would reduce the discrepancy between the adopted SSM and the experimental setup. In an environmental testing setup, modeling the shaker and its interaction with the specimen under test represents the best option. However, this would possibly introduce the necessity of more complex substructuring approaches and increase the computational load, which is not beneficial for real-time applications. For this reason, a more straightforward alternative modeling scheme is proposed in this section. The investigated modeling alternative consists in adopting four vertical springs, one for each connection point on the BARC base. The springs have been defined in the FE model as CBUSH1D elements with one end corresponding to the central independent nodes of the holes on the BARC base. All the DOFs, except the vertical translation, of the four central RBE2 holes are fixed. The free-end of each spring is instead fixed, i.e., all the DOFs are constrained. The springs stiffness has been determined via a MATLAB-based optimization procedure aimed at minimizing the RMSE between the measured responses in the mixed observations set in Tab. 6.3 and the responses reconstructed at the same location via a forward simulation of the model. The resulting value, equivalent for the four springs, is 5000 N/m.
Figure 6.10 displays the signals at S10 and S11 estimated via the AKF using the mixed observations set in Tab. 6.3 and the hereby proposed alternative model. The strain response predictions are compared against the reference measured signals and the estimations presented in Subsection 6.3.1,

i.e., achieved via the AKF when the mixed observations set is adopted in conjunction with the original model. Figure 6.11 offers global insights regarding the response estimation accuracy delivered by the AKF with the two analyzed models by comparing the RMSE values for the set of estimated and re-estimated strain responses. From the analysis of Figs. 6.10 and 6.11 it can be inferred that the employment of the alternative model does not introduce any improvement in terms of response estimation.

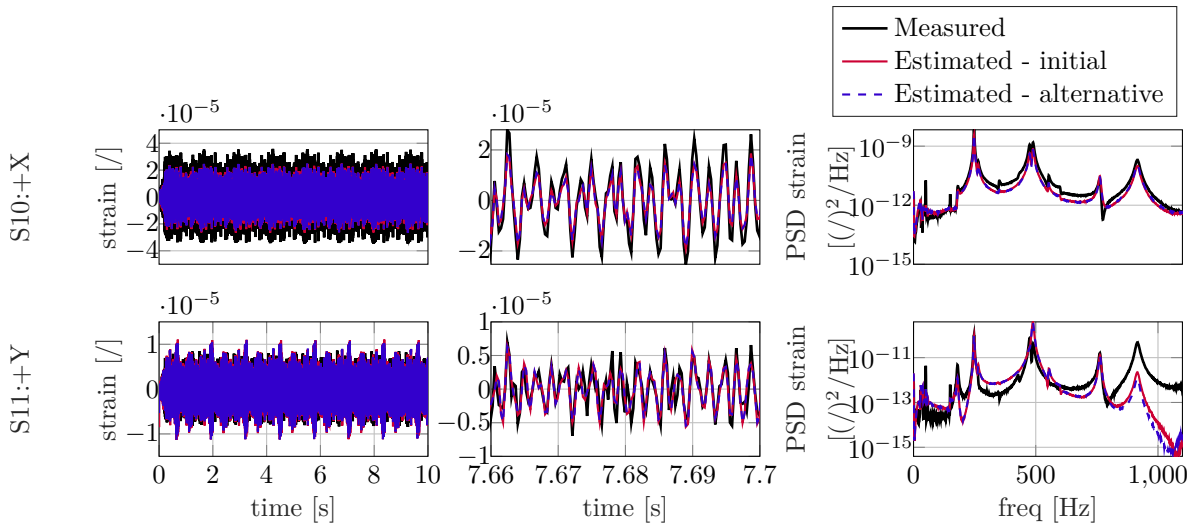

Figure 6.10: BARC environmental tests: time history (left), detailed time history (middle) and PSD (right) of strain responses S10 and S11. Measured signals are shown by a solid black line, while those estimated by the AKF via the original and the alternative model are respectively denoted via a solid red line and a dashed blue line.

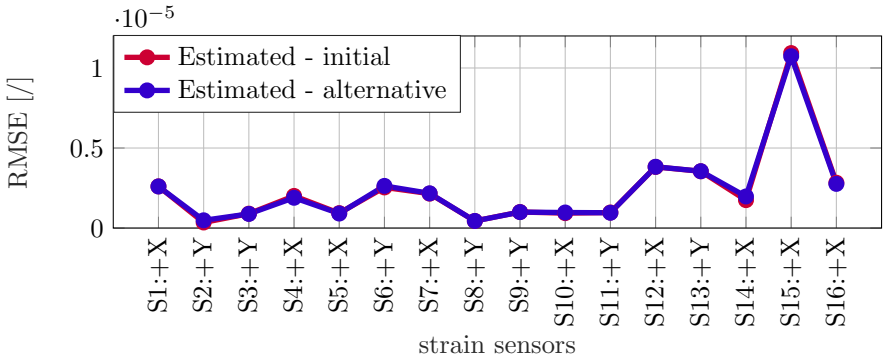

Figure 6.11: BARC environmental tests: RMSE values of the strain responses estimated by the AKF (initial model - red, alternative model - blue) with respect to their measured time histories

The load estimations are reported in Fig. 6.12 and a quantitative comparison is proposed in Tabs. 6.6 and 6.7, where the RMS and RMSE values of the estimated force signals under the two modeling assumptions are respectively compared.

Table 6.6: BARC environmental tests: RMS values of the inputs measured and estimated by the AKF (initial and alternative model) compared to their measured time histories

	Input 1	Input 2	Input 3	Input 4
Measured	6.9	7.1	7.3	6.9
Initial model	14.3	6.0	7.9	7.3
Alternative model	7.9	4.4	7.2	7.9

Table 6.7: BARC environmental tests: RMSE values of the inputs estimated by the AKF (initial and alternative model) with respect to their measured time histories

	Input 1	Input 2	Input 3	Input 4
Initial model	17.7	6.9	11.6	8.9
Alternative model	12.6	7.7	8.2	9.7

Table 6.6 and Fig. 6.12 (input 1, left) highlight that the overestimation affecting input 1 can be substantially reduced if the BCs uncertainties are contained by making use of the hereby presented alternative modeling strategy. A further improvement concerns the reduction of the RMSE for input 1 and 3, which reflects the enhanced estimation of inputs 1 and 3 PSD peaks at 915 Hz. The PSD plot for input 4 also shows a prediction improvement for the 915 Hz peak through the alternative model. However, the use of spring elements generates imprecise estimation at low frequency, hence providing a slightly higher RMSE.

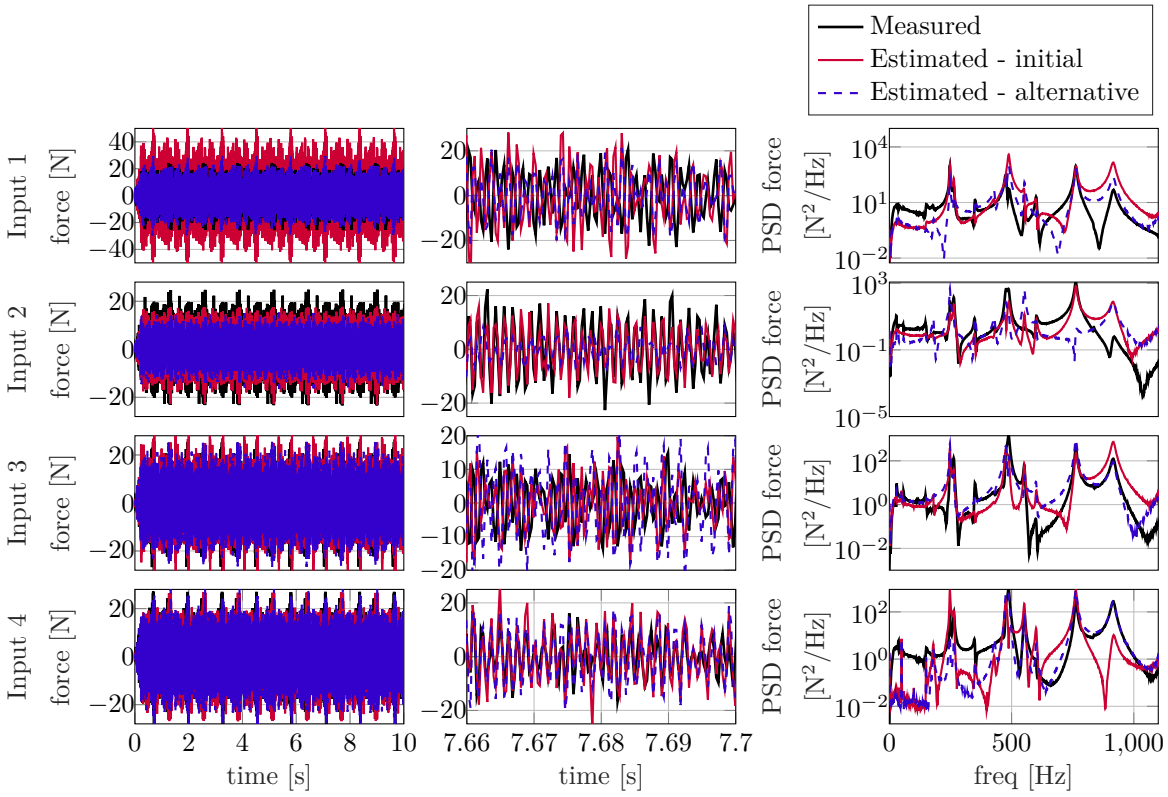

Figure 6.12: BARC environmental tests: time history (left), detailed time history (middle) and PSD (right) of input 1, input 2, input 3 and input 4. Measured signals are shown by a solid black line, while those estimated by the AKF via the original and the alternative model are respectively denoted via a solid red line and a dashed blue line.

The results offered in this section demonstrate that the hereby proposed modeling solution allows for a substantial enhancement of the high frequency content of the loads predictions via the AKF. To the contrary, the input estimations at low frequency are not improved, as well as the response estimates, whose accuracy is left unchanged. For this reasons and to provide a fair comparison between the adopted algorithms, the remainder of the chapter will present the use of data assimilation methods during the BARC environmental tests when the original model is employed.

6.3.2 Gaussian Process Latent Force Model for joint input-state estimation

In this subsection, the use of GPLFMs for input-state estimation during environmental testing on the BARC is proposed. For this purpose, the original FE model presented in Subsection 6.1.1 has been adopted to construct the BARC SSM. Following Fig. 5.6 and Alg. 14, once the system structural SSM is computed, a covariance function must be chosen according to the specific application. Indeed, while the use of state-of-the-art Kalman-based recursive estimators finds its most common application for random excitation sources such as the one shown in Figs. 6.9 and 6.12, the GP-based approach proposed in Section 5.2 features higher flexibility regarding the nature of the unknown input targeted by the prediction. However, thanks to their stochastic nature, environmental testing loading sources represent a primary benchmark for the GPLFM as well. It follows that this section will deal with the use of the most common covariance function for building the GPLFM which will serve for the estimation, i.e., the Matérn covariance function in Eq. 2.61 with smoothness parameter $\nu = 1.5$ (Fig. 2.7). As described in Alg. 14, the covariance function hyperparameters must be initialized before computing the SSM for the input. For this application, the following values have been used as initial hyperparameters: $l = 2 \times 10^{-4}$, $\sigma^2 = 2 \times 10^{-4}$. For what concerns instead the quantities associated to the BARC SSM, i.e., $\mathbf{Q}$, $\mathbf{R}$, $\mathbf{P}^x_{0|0}$, and the mean vector $\hat{\mathbf{x}}^a_{0|0}$, they have been selected following the logic reported in Subsection 6.3.1. The GP-based data-assimilation technique is hereby tested by making use of two measurements sets constructed as a subset of the sensors shown in Fig. 6.5: the mixed observations set presented in Tab. 6.3 and a pure acceleration-based set. In both scenarios, the entire set of observations is used for the hyperparameters training phase within the GP-based approach. The latter is constructed by maximizing the log marginal likelihood of data via the minimization function available in MATLAB^{TM}.

6.3.2.1 Predictions via a mixed observations set

This subsection reports on the joint input-state estimation results obtained via the GPLFM approach during the environmental tests described in Section 6.2 when the mix measurements set in Tab. 6.3 is adopted. The achieved results are compared against the reference AKF predictions presented in Subsection 6.3.1. In order to provide a consistent reference for the following subsection, which will deal with the use of pure acceleration-based measurements, response predictions for both strains and accelerations are hereby reported. Therefore, Figs. 6.13 and 6.14 respectively compare two strain responses and an acceleration response predicted by the GP-based method against the corresponding AKF estimations. Figures 6.15 and 6.16 provide instead a global information regarding the strain and acceleration predictions accuracy achieved by the joint estimation via the GPLFM. The offered results highlight that the GPLFM allows for higher prediction accuracy for both "unobserved" and "observed" locations, e.g. all the available acceleration sensors. This proves that the adopted input modeling in a joint input-state estimation logic, not only drives the input estimation but also influences response prediction accuracy. It is indeed proved that, even if the adopted measurements and the associated noise covariance matrix $\mathbf{R}$ are equivalent, their effect on the estimation still depends on how the system and the input uncertainties are modeled, i.e., via a time-invariant and manually selected process noise covariance matrix $\mathbf{Q}^a$ as for the AKF or using a more articulated strategy such as the GPLFM.
Figure 6.17 reports on the input estimation results obtained via the GP-based approach and compares them to the reference AKF predictions. Figure 6.17 is complemented by Tab. 6.8, which provides a comparison between the RMSE values of the signals estimated respectively by the AKF and the GP-based method with respect to their measured counterpart. The resulting load predictions show slightly higher accuracy with respect to the AKF ones, confirming that the proposed approach allows for accurate load reconstruction without the need of particular user-dependent tuning effort.

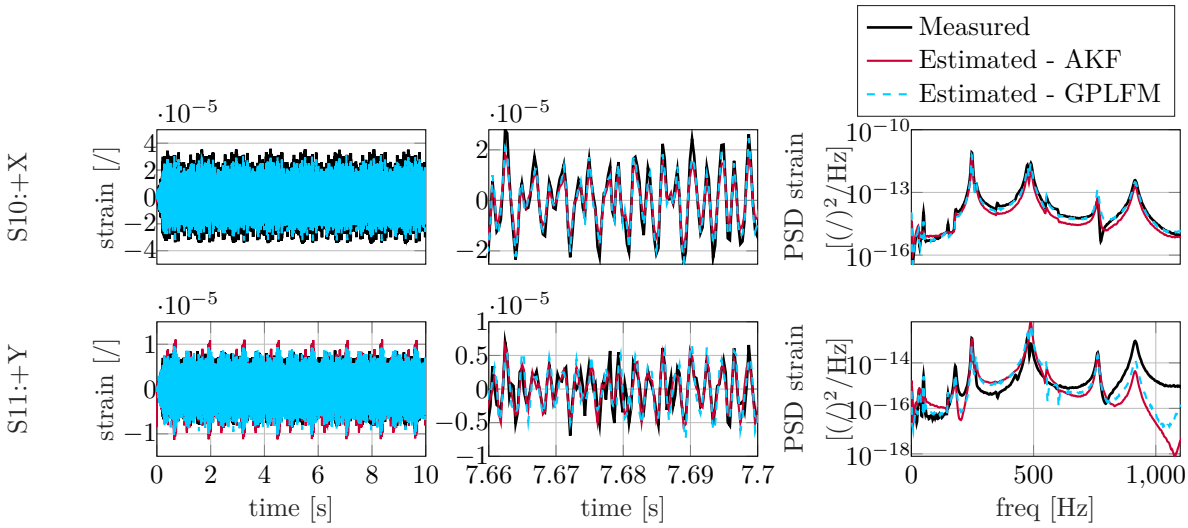

Figure 6.13: BARC environmental tests: time history (left), detailed time history (middle) and PSD (right) of strain responses S10 and S11. Measured signals are shown by a solid black line, while those estimated via the AKF and the GPLFM are denoted via a solid red line and a dashed cyan line.

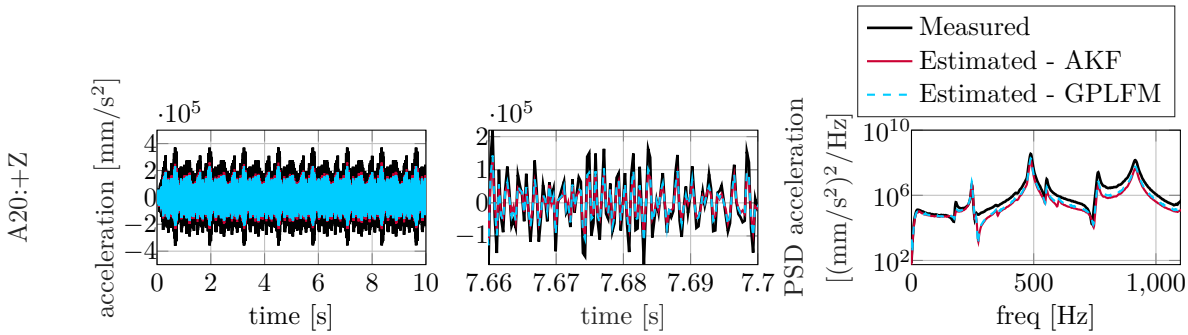

Figure 6.14: BARC environmental tests: time history (left), detailed time history (middle) and PSD (right) of acceleration response A20 (+Z). Measured signals are shown by a solid black line, while those estimated via the AKF and the GPLFM are respectively denoted via a solid red line and a dashed cyan line.

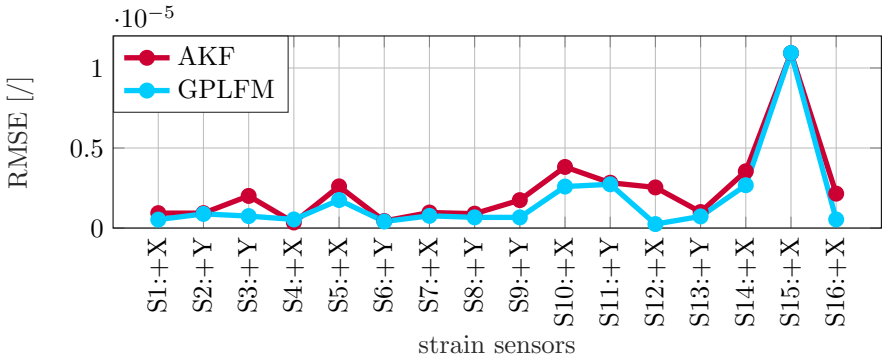

Figure 6.15: BARC environmental tests: RMSE values of the estimated strain responses (AKF - red, GPLFM - cyan) with respect to their measured time histories

6.3.2.2 Predictions via acceleration-only measurements

This subsection finally reports on the joint input-state estimation results obtained via the GPLFM approach during the environmental tests described in Section 6.2 when a pure acceleration-based measurements set is adopted. The latter contains all the DOFs measured by the four accelerometers in Fig. 6.5. The initial estimator settings described in the previous subsection have been replicated for this application. As with the previous analyses, the estimation results are being compared

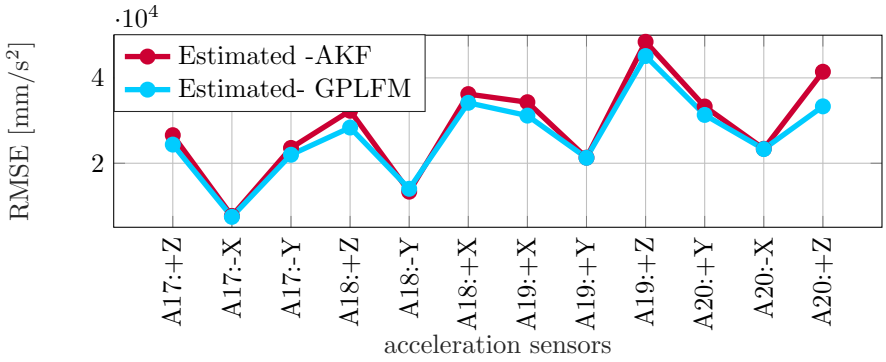

Figure 6.16: BARC environmental tests: RMSE values of the estimated acceleration responses (AKF - red, GPLFM - cyan) with respect to their measured time histories

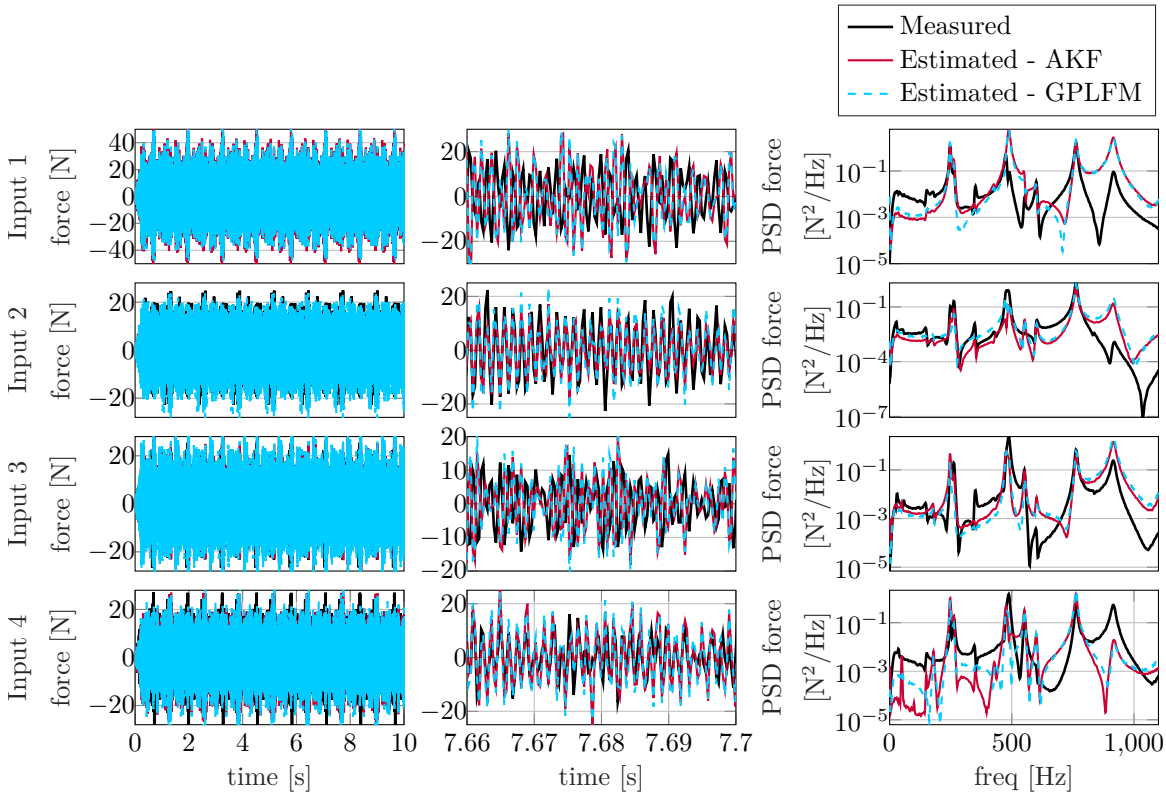

Figure 6.17: BARC environmental tests: time history (left), detailed time history (middle) and PSD (right) of input 1, input 2, input 3 and input 4. Measured signals are shown by a solid black line, while those estimated via the AKF and the GPLFM are respectively denoted via a solid red line and a dashed cyan line.

Table 6.8: BARC environmental tests: RMSE values of the inputs estimated by the AKF and the GPLFM with respect to their measured time histories

	Input 1	Input 2	Input 3	Input 4
AKF	17.7	6.9	11.6	8.9
GPLFM	17.3	8.5	12.7	9.9

with reference AKF estimations obtained with the same observations set. It is worth noting that the AKF is known to suffer from unobservability issues when only acceleration measurements are adopted. This section aimes at experimentally proving that this limitation is overcome by the GP-based approach, as mathematically demonstrated in Section 5.2. Figures 6.18 and 6.19 show the estimations obtained via the two compared techniques for S10, S11 and A20 (vertical direction).

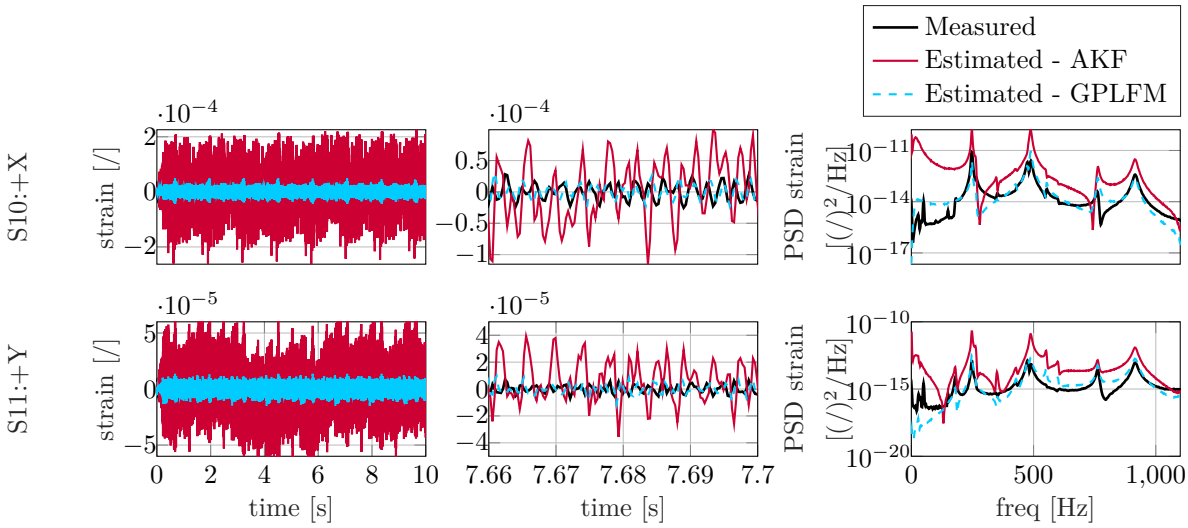

Figure 6.18: BARC environmental tests: time history (left), detailed time history (middle) and PSD (right) of strain responses S10 and S11. Measured signals are shown by a solid black line, while those estimated via the AKF and the GPLFM are denoted via a solid red line and a dashed cyan line.

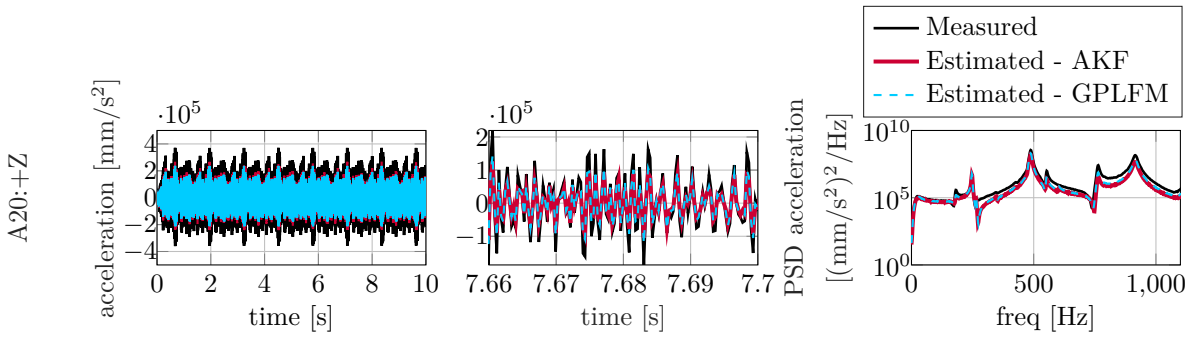

Figure 6.19: BARC environmental tests: time history (left), detailed time history (middle) and PSD (right) of acceleration response A20 (+Z). Measured signals are shown by a solid black line, while those estimated via the AKF and the GPLFM are respectively denoted via a solid red line and a dashed cyan line.

A global comparison is instead offered in Figs. 6.20 and 6.21 via the RMSE values for both the strain and acceleration responses.

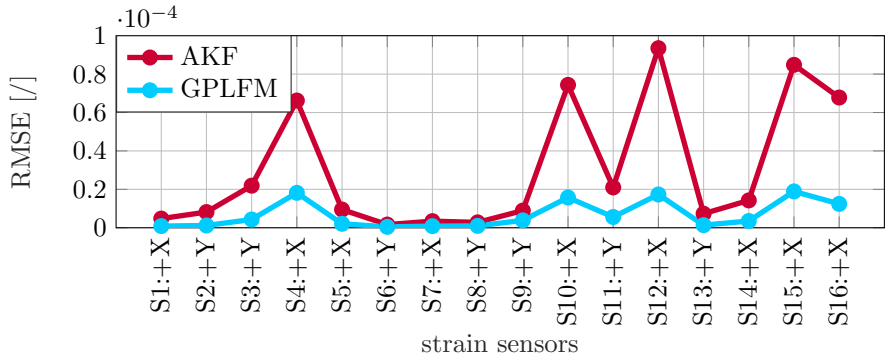

Figure 6.20: BARC environmental tests: RMSE values of the estimated strain responses (AKF - red, GPLFM - cyan) with respect to their measured time histories

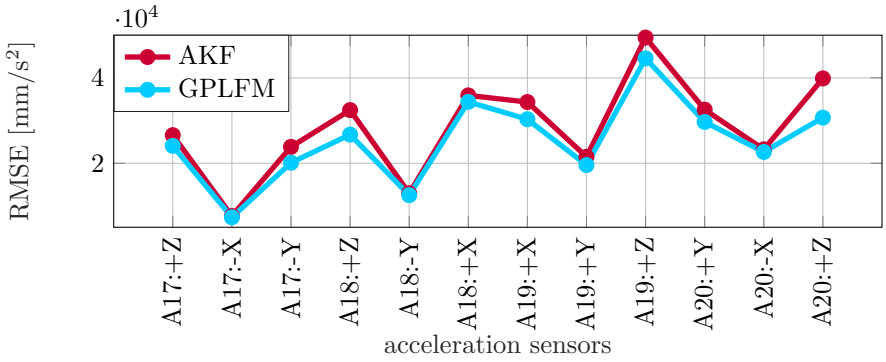

Figure 6.21: BARC environmental tests: RMSE values of the estimated acceleration responses (AKF - red, GPLFM - cyan) with respect to their measured time histories

The presented results indicate that even though the accelerations can be accurately re-predicted by both the estimators, the AKF inaccuracy level is still higher due to the unobservability condition which affects the proper functioning of the algorithm. For what concerns strain responses instead, both the time and frequency signals reported in Fig. 6.18 and the RMSE values in Fig. 6.20 demonstrate that the GP-based approach enables accurate predictions. To the contrary, the AKF estimations are affected by high RMSE due to amplitude mismatches and low frequency drifts generated by the unobservability condition.
To what concerns loads estimations, the same conclusions drawn for strain responses can be inferred by analyzing Fig. 6.22 and Tab. 6.9. It is indeed clear that while the AKF generates signals featuring low frequency drifts and higher RMSE values, the GP-based method provides predictions with accuracy comparable to the case study presented in the previous subsection, i.e., when also strain responses are measured.

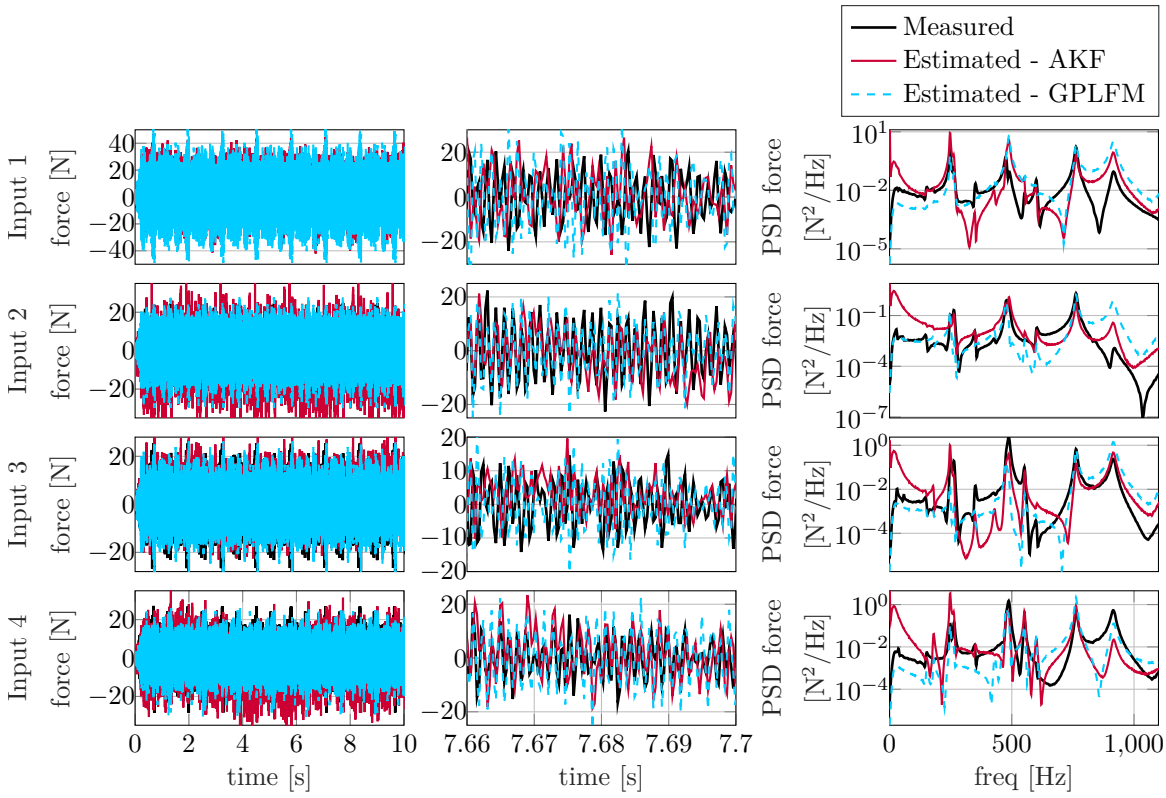

Figure 6.22: BARC environmental tests: time history (left), detailed time history (middle) and PSD (right) of input 1, input 2, input 3 and input 4. Measured signals are shown by a solid black line, while those estimated via the AKF and the GPLFM are respectively denoted via a solid red line and a dashed cyan line.

Table 6.9: BARC environmental tests: RMSE values of the inputs estimated by the AKF and the GPLFM with respect to their measured time histories.

	Input 1	Input 2	Input 3	Input 4
AKF	17.7	6.9	11.6	8.9
GPLFM	17.0	6.4	11.9	7.2

6.4 Summary

The operational environment replication comprises one of the main challenges in the context of spacecraft environmental testing. To facilitate this need, full-field response of components under test can be evaluated in conjunction with additional QoI, e.g. unknown loads, via data assimilation strategies relying on Bayesian recursive estimators. This chapter has investigated the use of two alternative estimators during environmental tests on the BARC specimen for simultaneously predicting responses and unknown excitation sources. The proposed approaches are based on the employment of a validated model which accurately represents the system during tests, with a focus on utilizing realistic BCs assumptions. To this end, a CMS method relying on the use of RIRA modes has been used to construct the BARC ROM.

As first step, the AKF has been tested and the variation of the achieved predictions with the type of adopted measurements has been explored. It has been found that the use of a mixed observations set, including both strain and acceleration sensors, substantially improves the input estimation accuracy, Additionally, an enhanced model containing springs to represent the shaker-structure interaction has been proposed. The comparison between the AKF results obtained by employing the original and the alternative model has demonstrated that unknown loads predictions could be improved via a model refinement.

This chapter has further examined the use of the GP-based input modeling for input-state estimation of the BARC. The accurate results obtained when a mixed observations set is employed, confirm that the method comprises a valid alternative to the more conventional AKF. This is particularly true when a pure acceleration-based observation set is adopted since in this situation, the AKF has been proven to suffer from unobservability issues. To the contrary, it has been demonstrated that the GP-based approach, whose observability in presence of acceleration-only measurements has been mathematically proven in Section 5.2, provides accurate estimations also in absence of displacement-level sensors.

7

WIND TURBINE BLADES TESTING: LARGE SCALE COMPOSITE BLADE

The situation in which loads acting on an engineering structure cannot be measured arises in many areas of engineering; one key example is wind energy industry. The cyclic loading acting on WTs may lead to high strain values at critical locations and finally to structural failure. It is therefore important to continuously monitor the strain response time histories at these locations. Laboratory measurements on WT blades can be exploited with the purpose of establishing a dynamic virtualization process, which could be considered to evolve in real-time, provided that the employed algorithms can be applied online or near-online. During this type of test campaigns, structural response is acquired at a finite (limited) number of locations. In this context, Bayesian filtering i) allows to extend the information from a few sensed locations to the entire full-field blade response and ii) delivers an estimate of the unmeasured loads acting on the blade. Bayesian VS thus offers a tool with the potential to operate in real-time, employing fusion of the measured data with a numerical (FE-based) model of the system, thus delivering a hybrid model, suited for virtualization. This process can be installed throughout the life cycle of WT blades (including operational conditions) for enabling a continuous performance evaluation with the purpose of lifetime prediction and predictive maintenance. In this chapter, a dynamic virtualization process is installed for a 14.3 m long research WT blade during pull and release tests.
The large scale blade is presented in Section 7.1, where the output-only measurements perfomed during laboratory testing are reported, along with its FE model validation results. Next, Subsection 7.1.3 validates the CMS-ME approach proposed in Subsection 3.1.1 by offering the response predictions for the analyzed case study and comparing them with the standard ME results. Subsection 7.1.3 continues reporting a parametric analysis of the input-response predictions achieved by the conventional AKF for several choices of the time-invariant process noise covariance associated to the unknown input. The outcome of this analysis serves as reference for the input-response predictions produced by the A-AKF, which are then presented in Subsubsection 7.1.3.3, along with a parametric assessment of the method and a comparison with the results achieved via the conventional AKF and the CMS-ME approach. Finally, conclusions for this chapter are drawn in Section 7.2.

7.1 Large scale composite wind turbine blade

The experimental case study presented in this section includes pull and release tests on a 14.3 m long research blade made of GFRPs. The WT blade was entirely designed by DTU Wind Energy and manufactured by Olsen Wings in the framework of the "BLATIGUE" project. The DTU Wind Energy department has kindly provided the FE model of the blade required for the present work, along with the experimental data this work refers to.

7.1.1 Wind turbine blade output-only measurements

As shown in Fig. 7.1 (left), during the hereby considered pull and release tests, the blade was clamped to a rigid steel-reinforced concrete block through the circular interface plate in a flapwise configuration. The test consisted in pulling the blade downward by making use of a bungee applied at a distance of 13.1 m from the clamping. Once the blade tip had reached the desired displacement, the blade was released and the free vibration response recorded. The load time history has not been acquired. Nevertheless, the scalar value of the static load applied right before the release instant

is available. The blade was instrumented via 76 strain gauges distributed on 12 sections along its length, all measuring along the axial direction of the blade (z-axis in Fig. 7.1). Each instrumented section includes 4 or 8 strain gauges. The sensors configuration is reported in Fig. 7.1 (right), while Fig. 7.2 (left) shows the strain gauges located on section 4.0 of the blade (at 4.0m distance from the clamping). Figure 7.2 (right) shows the strain time histories measured by 2 of the 8 sensors placed on section 4.0.

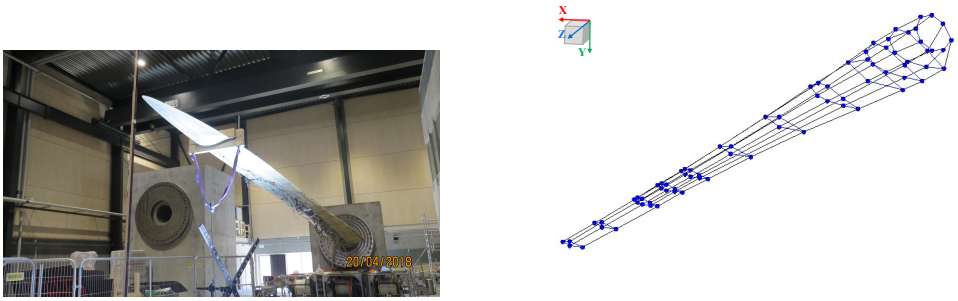

Figure 7.1: Large scale WT blade setup during the pull and release test (left). Test geometry (right).

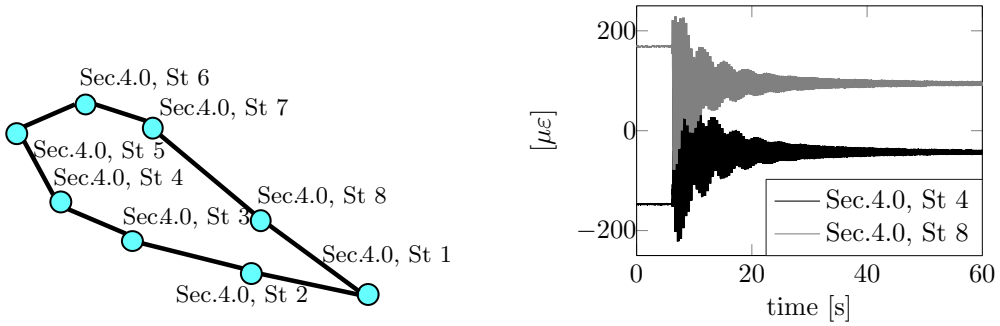

Figure 7.2: Large scale WT blade sensor locations on section 4.0 (left). Strain responses measured by strain gauges 4 and 8 on section 4.0 during the pull and release test.

7.1.2 Numerical model: Finite Element model validation and Reduced Order Model

The WT blade FE model shown in Fig. 7.3 has been developed by DTU Wind Energy using the commercial software MSC^{TM} Nastran and afterwards exported to Simcenter^{TM} 3D for model validation. It consists in a 3D model made up of around 130000 six-sided layered composite (8 or 20 nodes) elements. At the blade root, a spider connection links the nodes belonging to the circular interface plate to the central node of the root section, which is clamped. The model

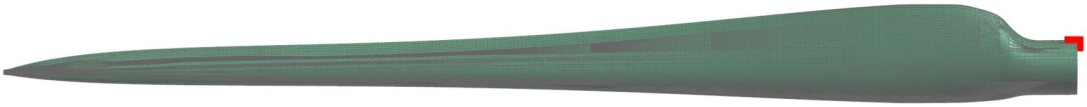

Figure 7.3: Large scale WT blade FE model in Simcenter^{TM} 3D

has been validated using modal parameters estimated via Simcenter^{TM} Testlab PolyMAX from hammer and shaker tests performed on the blade in free-free conditions [113, 151]. Afterwards, the model materials characteristics have been tuned to the specific application by referencing to modal

properties determined via Simcenter^{TM} Testlab PolyMAX using data acquired during hammer tests with the blade in clamped-free conditions, i.e., the same BCs adopted during the pull and release tests. During the considered hammer test, the blade was excited either in the flapwise or edgewise direction and it was instrumented via 64 accelerometers measuring both X and Y directions (including the driving point one). Sensors were distributed along the blade on 14 sections as shown in Fig. 7.4 and only half of the blade surface was covered. Figure 7.4 (left) shows the MAC diagram resulting from the correlation of the FE model mode shapes (computed using NX^{TM} Nastran SOL103 Real Eigenvalues) and the experimental mode shapes obtained from the described hammer test. Although a good matching between the numerical and experimental mode shapes is globally achieved for the first ten normal modes, i.e., up to 43 Hz, the switching of modes 8 and 9 in the MAC diagram must be highlighted. Modes 8 and 9 comprise a combination of torsion and high-order flap-wise bending. Therefore, the 20% and 13% relative frequency errors, respectively associated to mode 8 and 9, could be ascribed to the blade being instrumented only on the top surface during tests. In Bayesian filtering, this type of modeling errors are compensated via the process noise term, which allows for reliable predictions even in presence of model mismatches. A ROM of the blade has been built following the procedure outlined in Subsection 2.1.1 in order to reduce the computational effort derived from the high dimensionality of the original FE model. The ROM reduction basis has been built taking into account the first ten modes (frequency range of interest: 0-43 Hz) and one residual attachment mode related to the unknown force to be estimated via the chosen Bayesian estimators. The considered application point and direction for the unknown input $\mathbf{u}$ are highlighted in Fig. 7.4 (right). A visual information regarding the accuracy of the resulting ROM is displayed in Fig. 7.5 via the comparison between the experimental and the simulated responses in frequency domain for strain gauges 4 and 8 on section 4.0. The simulated responses have been computed by performing a forward simulation of the model, pre-loaded by the blade weight, with a load time history reconstructed using the available static load scalar value.

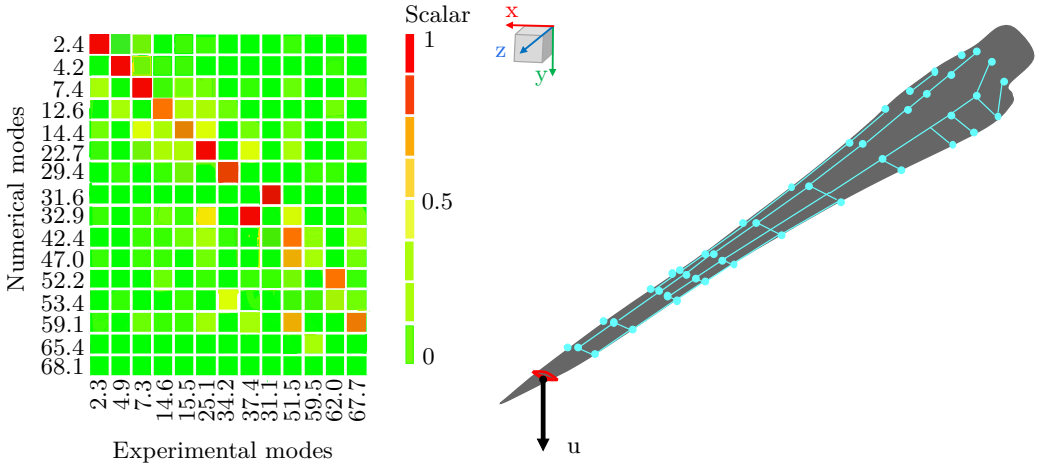

Figure 7.4: Large scale WT blade: MAC between numerical and experimental mode shapes from hammer test (left). WT blade test and FE model geometries alignment (right).

7.1.3 Joint input-state estimation

The target of this subsubsection lies in input and strain response estimation during the pull and release tests of the large scale blade in clamped-free BCs. In order to validate the efficacy of the proposed algorithms on the task of input-response prediction, it is common practice to compare estimated signals to the corresponding measured reference. We follow such a procedure here by splitting the set of recorded dynamic response data into a measured and an unmeasured subset. The unmeasured subset refers to the quantities that are to be estimated via use of the proposed scheme. The "virtually sensed" signals are then compared to the reference (measured) time histories

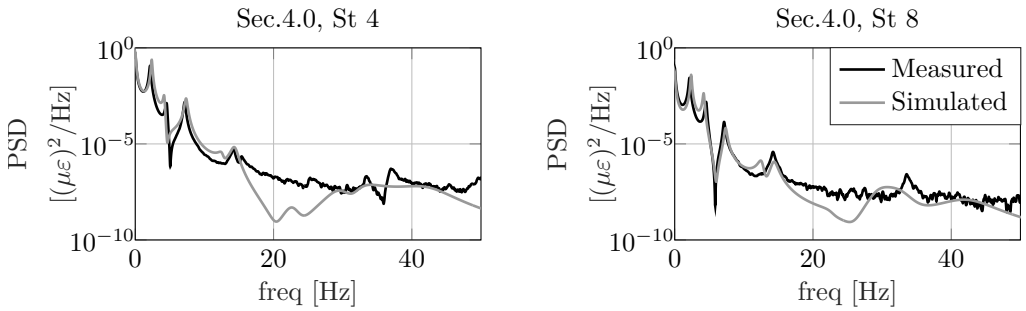

Figure 7.5: Large scale WT blade pull and release test: PSD of responses measured (solid black line) and simulated (solid gray line) at locations St.4 (Sec4.0), St.8 (Sec4.0).

in order to evaluate the prediction performance. For the hereby analyzed pull and release tests on the research WT blade, the "measured" and "unmeasured" locations were defined by assuming that the blade could only be instrumented at certain sections, due to time constraints and limited sensor availability. The resulting sensing configuration, according to which strain response is acquired at only 28 locations out of the original 76 positions, is reported in Fig. 7.6.

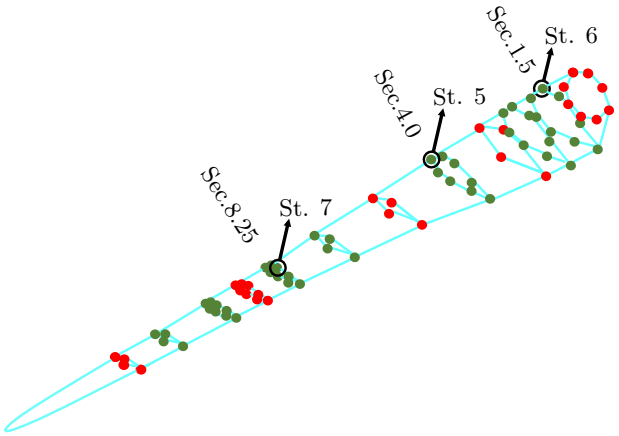

Figure 7.6: Large scale WT blade sensing configuration during pull and release tests: "measured" (red) and "unmeasured" (green) locations

It is worth recalling that the A-AKF relies on CMS-ME for response estimation. As a consequence, the number of sensors selected for the A-AKF must satisfy the CMS-ME requirement of having at least $n_o = n_r = 11$ measured signals. The fulfillment of this requisite guarantees robust response predictions for the CMS-ME approach and, as a result, for the A-AKF as well. However, a higher amount of sensors such as the one adopted for this case study, can be a benefit in terms of noise suppression and possibility to capture local deformations and high frequency dynamics. In this sense, OSP procedures constructed for the AKF, e.g. the one proposed in [57, 58], could be exploited for determining the optimal number of measurements for the A-AKF starting from the CMS-ME minimum threshold. The employment of such methodologies would help in guaranteeing both accurate load and response predictions.

7.1.3.1 Response prediction through the Component Mode Synthesis - Modal Expansion approach

This subsubsection discusses the prediction results achieved by exploiting the CMS-ME approach proposed in Subsection 3.1.1. Figure 7.7 illustrates the strain response estimation results achieved using the CMS-ME approach (in green) at three "unmeasured" locations according to the sensing configuration reported in Fig. 7.6. The curves estimated via the CMS-ME approach are compared

in Fig. 7.7 to the experimentally measured time histories (in black) and those estimated using the standard ME technique (in orange). Moreover, Fig. 7.7 reports in gray the simulated time histories, i.e., the response signals obtained by performing a forward simulation of the model (pre-loaded by the blade weight) for the given loading history. During the analyzed pull and release tests, only the scalar value of the static force applied right before the blade release instant was acquired. Therefore, an artificial input time history has been reconstructed using this information for obtaining the simulated free-vibrations shown in gray in Fig. 7.7.

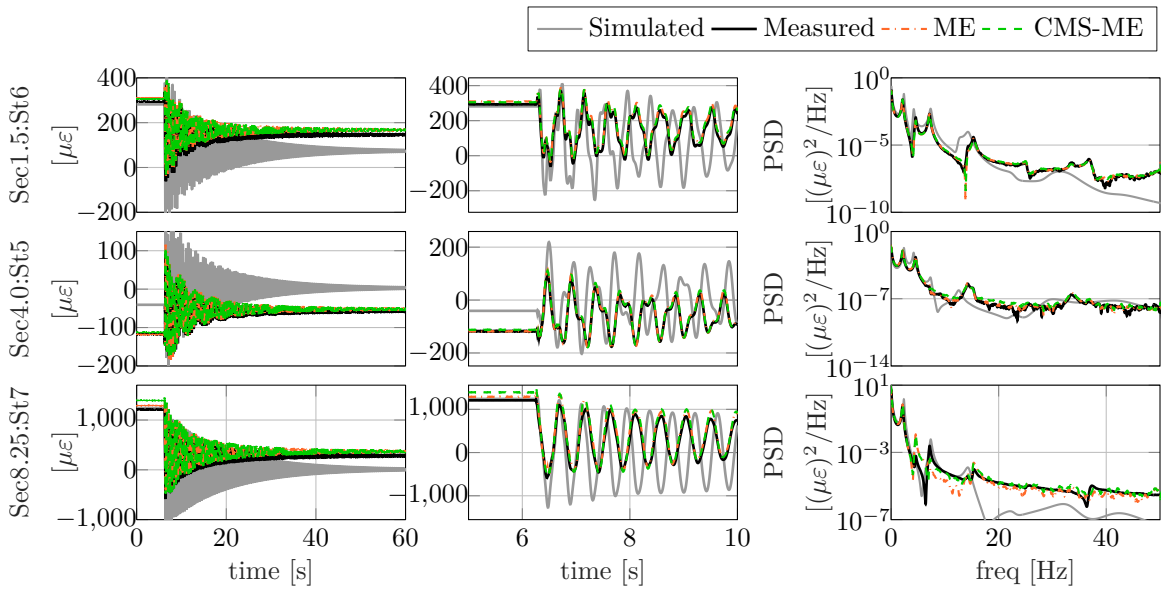

Figure 7.7: Large scale WT blade pull and release tests: time history (left), detailed time history (middle) and PSD (right) of responses of strain sensors St.6 (Sec1.5), St.5 (Sec4.0) and St. 7 (Sec. 8.25). Measured and simulated signals are respectively shown by a solid black line and a solid gray line, while those estimated via ME and CMS-ME are respectively denoted via a dashed orange line and a dashed green line.

Figure 7.7 reports a good agreement between the experimentally measured time histories (in black) and those estimated using ME (in orange) and CMS-ME (in green) at the corresponding locations. Moreover, the results confirm that the process of expanding measured quantities to unmeasured locations through a modal basis allows to correct modeling errors, as indicated by the discrepancy delivered purely via use of the simulation model. From the time histories and PSDs comparison, quite a high mismatch can be observed between the measured and the simulated signals due to approximations in modeling damping. To the contrary, the curves estimated via standard ME technique and our CMS-ME approach are not affected by this error, since the methods exploits ME from sparse measurements; a step which delivers a correction of the response in the unmeasured locations. The analysis of the strain response time histories highlights the slightly better performance of the CMS-ME method with respect to the standard ME approach. Indeed, the strain response PSDs reveal that the CMS-ME estimates have a better agreement with the experimental strain responses in frequency domain, e.g., PSD at location Sec8.25:St7 between 7 and 15 Hz.
For extending the validity of the characteristic results reported in Fig. 7.7 to all the "unmeasured" locations along the blade, an overview of the strain estimation results obtained through the ME and CMS-ME approaches is offered in Figs. 7.8 and 7.9. The plots in Figs. 7.8 and 7.9 quantify the global prediction accuracy, respectively, in time and frequency domain by making use of the Time Response Assurance Criterion (TRAC) and Frequency Response Assurance Criterion (FRAC) indicators postulated in Section 11.1. For the analyzed case study, the entire time length of the recorded signals has been used for the TRAC computation.

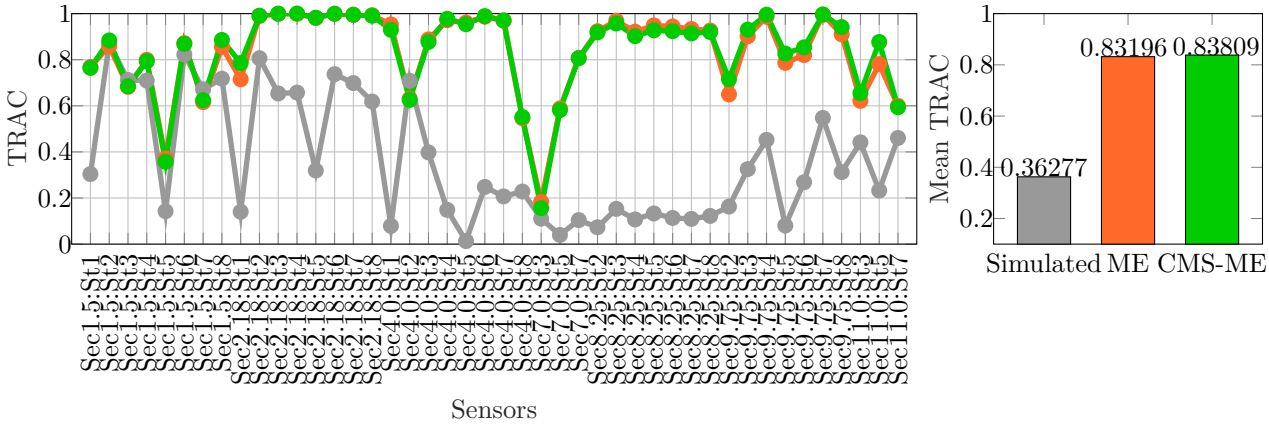

Figure 7.8: Large scale WT blade pull and release tests: TRAC values for the simulated strain responses (gray line), the ME (orange line) and CMS-ME (green line) strain response predictions at "unmeasured" locations according to the adopted sensing configuration (left). Mean TRAC values for the simulated strain responses (gray), the ME (orange) and CMS-ME (green) strain response predictions at "unmeasured" locations (right).

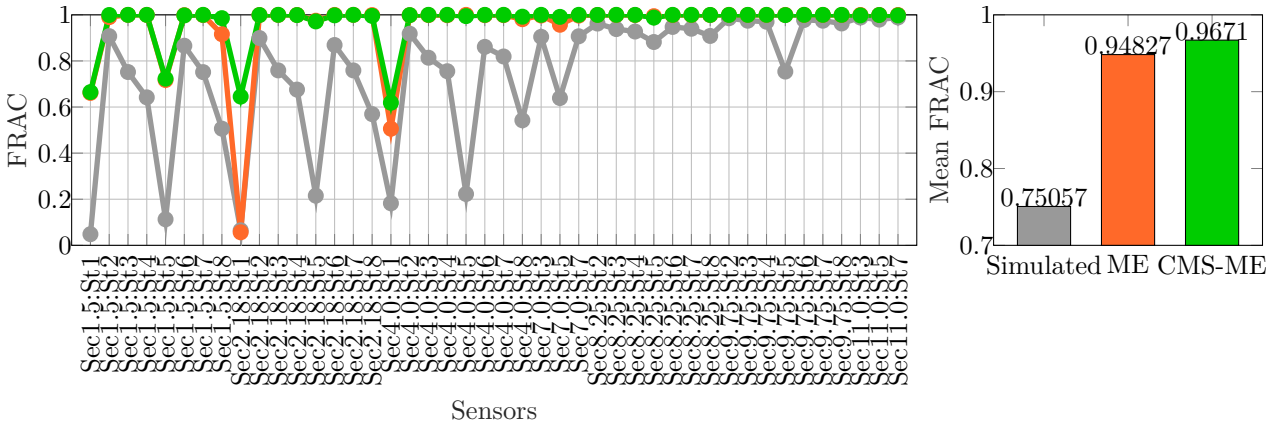

Figure 7.9: Large scale WT blade pull and release tests: FRAC values for the simulated strain responses (gray line), the ME (orange line) and CMS-ME (green line) strain response predictions at "unmeasured" locations according to the adopted sensing configuration (left). Mean FRAC values for the simulated strain responses (gray), the ME (orange) and CMS-ME (green) strain response predictions at "unmeasured" locations (right).

Figure 7.8 (left) compares the TRAC values for the simulated strain responses (in gray) and the ME (in orange) and CMS-ME (in green) predictions at the "unmeasured" locations ordered from the blade root (left) to the blade tip (right). Figure 7.8 (right) reports the TRAC value averaged over the entire set of predicted strain signals for the three cases hereby taken into account. Both the TRAC trend and the low averaged TRAC value for the simulated responses confirm the inaccuracy delivered via the simulation model. Figure 7.8 (left) shows that a TRAC value higher than 0.6 is achieved via both the ME and the CMS-ME approach for the 88% of the estimated quantities and higher than 0.8 for the 70%. The low TRAC appearing for sensors close to the blade root, i.e., section 1.5, can be due to possible errors in the ME and CMS-ME bases due to BC uncertainties. The mean FRAC (Fig. 7.9 (right)) and the FRAC trend along the blade (Fig. 7.9 (left)) confirm the potential of both the ME-based approaches to deliver accurate frequency domain predictions in the chosen bandwidth (0-50 Hz). Moreover, the discrepancy between the simulated and measured frequency domain signals encountered in the PSDs plots in Fig. 7.7 is clearly highlighted in Fig. 7.9. From the global comparison provided in Fig. 7.8 (right) and Fig. 7.9 (right), it can be concluded that the CMS-ME approach outperforms - on average - the standard ME method. Despite the valuable response predictions achieved via the CMS-ME approach, the focus of this chapter lies

in the Bayesian filtering context with the intent to exploit the ability of Bayesian estimators to better account for model and measurement errors. Additionally, specific filters, e.g. the AKF, can be adopted for joint input-state estimation, thus allowing to simultaneously address response prediction and inverse load identification from sparse response measurements. Nevertheless, the presented results suggest that the CMS-ME estimations can be adopted as reference for prediction inaccuracy computation within the framework proposed in Subsection 4.2.1.

7.1.3.2 Input-response estimation through the Augmented Kalman Filter

This subsection treats the use of the AKF for input-state estimation during the pull and release tests described in Subsection 7.1.1. The results presented in this subsection will serve as a reference for evaluating the A-AKF performance. The AKF time-invariant $\mathbf{Q}^a$ matrix is conventionally chosen by setting q^{n_d} and q^{n_v} to very low numbers respectively compared to the order of magnitude of the displacements and velocities within the state vector and selecting q^u by means of the L-curve metric. The diagonal entries of $\mathbf{R}$ can be instead set basing on the noise recorded by the relative measurement channels. For this application, an order of magnitude of $10^{-2}uE^2$ has been computed and used for all the $\mathbf{R}$ matrix diagonal entries. The initial condition, $\hat{\mathbf{x}}_0^a$, of the augmented state vector contains the information regarding the pre-deformation of the blade under its weight. In Fig. 7.10 the L-curve is presented, where the smoothing and error norms trend, whose formulation is provided in Section 11.2, is shown for several values of q^u. It is observed that the plot shown in Fig. 7.10 does not appear like a perfect L-shape. However, the curve trend for the analyzed experimental case study can be easily interpreted by the user and q^u can be selected at 10^9N^2 for the joint input-state estimation via the AKF. For the sake of conciseness, the measurement unit for the covariance matrices will be omitted in the remainder of the thesis.

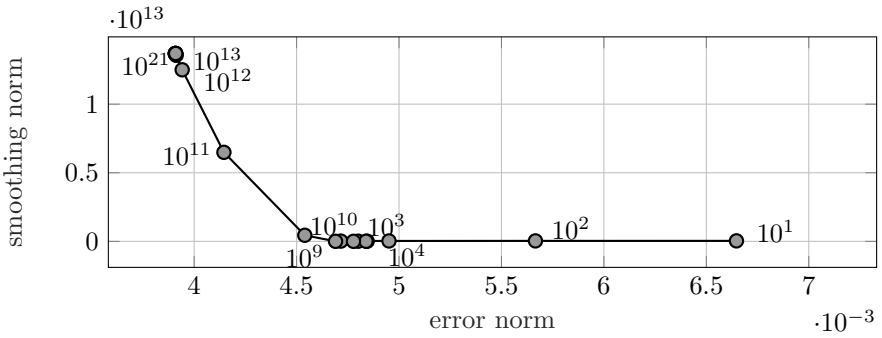

Figure 7.10: The L-curve for the joint input-state estimation of the large scale WT blade during pull and release tests using the AKF. Values for q^u are reported on the figure.

A parametric study regarding the AKF prediction accuracy variation with the selected input process noise covariance is hereby presented. The study has been conducted by analyzing the evolution of response and input estimates quality indicators when q^u varies on a logarithmic uniformly distributed scale. For simplicity, a variable Q can be defined as $q^u = 10^Q$. The TRAC and FRAC indicators have been adopted for response estimation, while the Static Error (SE) and the Standard Deviation (SD) have been used for input prediction evaluation. SE is formulated as the difference between the actual static input ($3.17kN$ before the blade release and $0N$ afterwards) and the mean value of the estimated input profile. SD, instead, quantifies the oscillations that affect the estimated time history after the blade release. Fig. 7.11 displays the evolution of the AKF response estimation accuracy for Q varying from 2 to 21 with a 1-step increase. In particular, the evolution with Q of the TRAC and FRAC trends along the blade, i.e., their values at "unmeasured" locations ordered from the blade root (left) to the blade tip (right), is reported in Fig. 7.11 (left). Fig. 7.11 (right) displays instead the values, for the several Q choices, of the TRAC and FRAC indicators averaged over the entire set of predicted responses. The entire time length of the recorded signals has been adopted for the TRAC computation, while the frequency range 0-50 Hz has been used for calculating

the FRAC values. The analysis of the TRAC and FRAC trends with Q highlights that the most reliable response predictions are achieved for $Q \geq 10$.

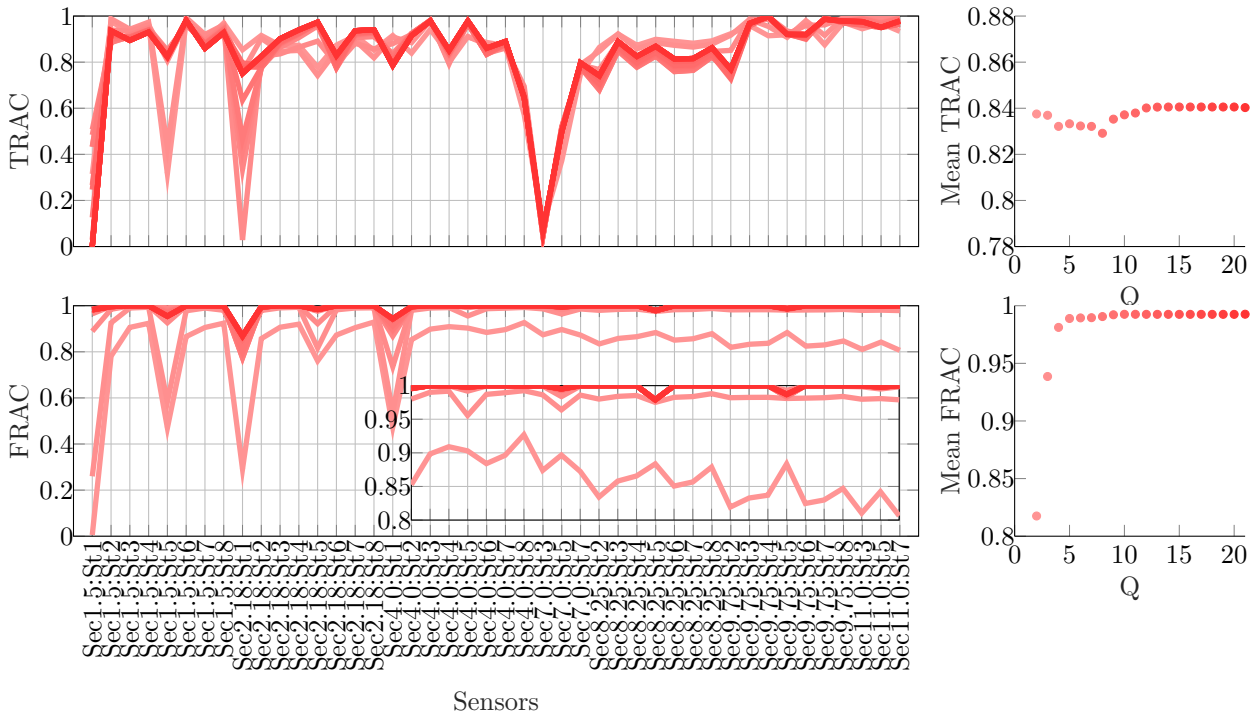

Figure 7.11: Large scale WT blade pull and release tests: AKF TRAC trend (top, left) and mean TRAC (top, right) values with increasing Q. AKF FRAC trend and detailed AKF FRAC trend from location Sec4.0:St2 to Sec11.0:St7 (bottom, left). Mean FRAC values with increasing Q (bottom, right).

While response estimates are not strongly affected by the variation of Q above $Q = 10$, the input prediction accuracy is instead highly dependent on Q, as depicted in Fig. 7.12 via the SE and SD trends. According to the latter, values of Q that optimize response estimation ($Q \geq 10$) generate high input prediction inaccuracy. Moreover, the minimization of SE is achieved for $Q = 4$, while the value which minimizes SD is $Q = 7$. This behavior demonstrates that there is no level of Q able to provide both the lowest amount of oscillations and the minimal static error. Fig. 7.12 also shows that the Q value identified via the L-curve ($Q = 9$) produces SE and SD levels which are higher than the achievable minima. Therefore, the SD and SE evolution reported in Fig. 7.12 proves that the L-curve approach is not optimal for pull and release type of data sets.

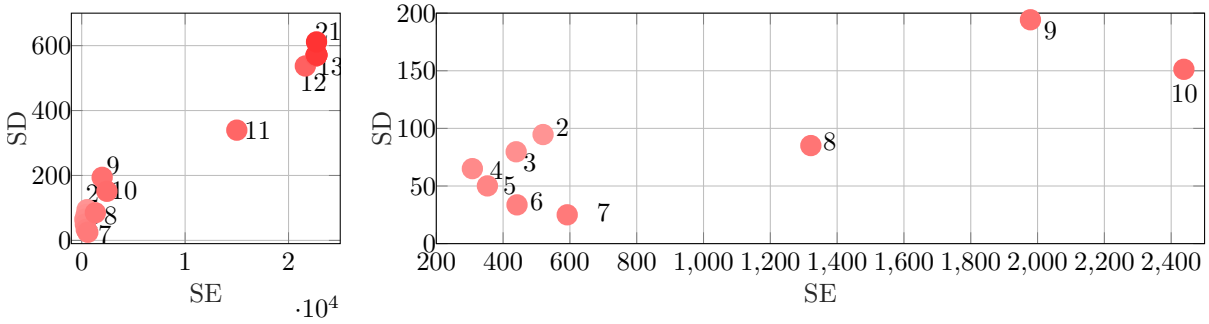

Figure 7.12: Large scale WT blade pull and release tests: AKF SE and SD evolution with increasing Q: full (left) and detailed (right) view. Values for Q are reported on the figure.

Figure 7.13 shows a comparison between the input time histories estimated via the AKF with $Q = 4$ (value which allows for SE minimization), $Q = 7$ (value which allows for SD minimization), $Q = 9$ (value identified via the L-curve) and the typical step-type load adopted during pull and release tests. As these tests are taken in an output-only fashion, only the scalar value of the static force

applied right before the blade release is available from test data. The "measured" curve proposed in Fig. 7.13 has been artificially reconstructed using this information, with the purpose of validating the achieved load predictions. Therefore, it is worth noting that the actual load applied during the test may be slightly deviating from the black curve reported in Fig. 7.13.

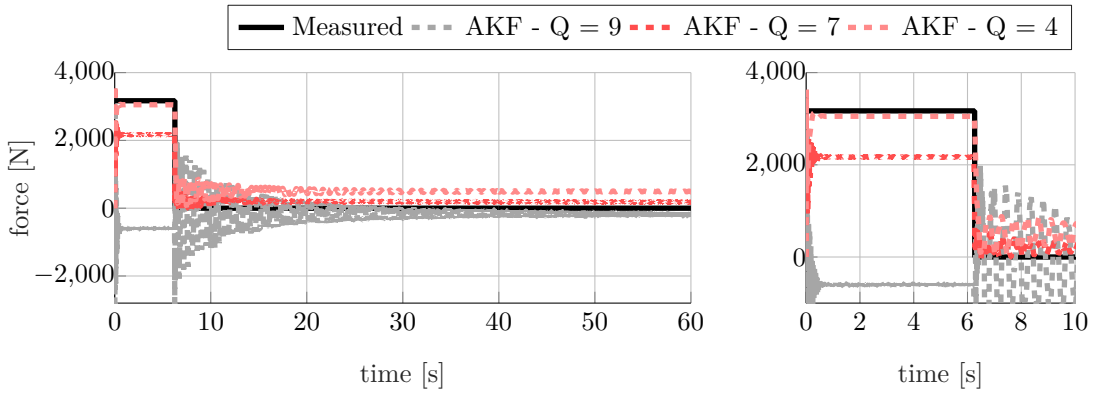

Figure 7.13: Large scale WT blade pull and release tests: input "measured" (black) and estimated (AKF) time histories (left) and detailed time histories (right) at different levels of Q.

The input time histories reported in Fig. 7.13 reflect the SE and SD trends: oscillations are minimal for $Q = 7$, while the static load is better captured by the AKF when $Q = 4$. Moreover, the input process noise covariance identified via the L-curve ($Q = 9$) generates large mismatches between the estimated and the actual load profiles. This result confirms that the L-curve is not suitable for tuning the AKF when applied for input-state estimation during tests with a pull and release type of loading. The latter comprise a constant input which is then abruptly removed and, therefore, deviates from the common random noise loading scenario in which the AKF normally excels. The pull and release load, i.e., a stationary load before and after the release instant, is difficult to be captured by the AKF, which adopts a RW model, i.e., a non-stationary model, to represent the unknown input evolution in time. In fact, the RW model can be treated as a first order AR process that has a root on the unit circle, which does not satisfy the stationarity condition [39]. As a result, the oscillations and the biased error appearing in the estimated input time history can be reduced by manual tuning but not completely removed, as displayed in Figs. 7.12 and 7.13. Despite the inability of the L-curve to provide satisfactory input estimations, the AKF predictions obtained for $Q = 9$ will be adopted as reference for evaluating the performance of the hereby proposed algorithm. Indeed, the Q values which minimize the input errors ($Q = 4$ and $Q = 7$) would generate lower TRAC and FRAC values, i.e., lower response prediction accuracy. Additionally, since the A-AKF approach aims to be a user-independent procedure, reference results should also be obtained with limited manual intervention.

7.1.3.3 Input-response estimation through the Adaptive-noise Augmented Kalman Filter

This subsection reports on the results obtained by applying the A-AKF described in Subsection 4.2.1 for joint input-state estimation during the pull and release tests on the large scale WT blade. For assessing the algorithm validity, the sensing configuration shown in Fig. 7.6 has been adopted. In order to apply the newly proposed algorithm for the pull and release data set, broad ranges for q^{n_d}, q^{n_v} and q^u have been selected as follows: $q^{n_d}_{min} = q^{n_v}_{min} = q^u_{min} = 10^{-20}$, $q^{n_d}_{max} = q^{n_v}_{max} = q^u_{max} = 10^{20}$. The prediction results described in this subsection have been obtained via the A-AKF with a $N = 100$ time-steps time window. Two parametric studies regarding the variability of the estimation accuracy with, respectively, the dimension of the window length and the selected ranges bounds adopted for the A-AKF will be presented later in this subsection. This subsection also proposes a comparison between the prediction results achieved adopting the A-AKF and those obtained via the AKF when q^u is selected by means of the L-curve metric. Similarly to the AKF settings, the diagonal entries of $\mathbf{R}$ have been set to 10^{-2} for the A-AKF. To the contrary, the

A-AKF initialization is performed differently from the AKF: while the AKF initial condition only contains the pre-deformation due to the gravity load, the A-AKF adopts the CMS-ME estimates to define the initial condition. The latter is therefore more accurate since it already contains information about the static response of the blade under the applied unknown load.

Response Estimation

Figure 7.14 shows the time histories and the related frequency content of the blade response at the three locations pointed out in Fig. 7.6. A comparison between the signals estimated via CMS-ME, the conventional AKF and the ones obtained by using the proposed A-AKF scheme is offered. Moreover, the estimated curves are compared to the experimentally measured responses at the corresponding locations to prove the algorithm validity.

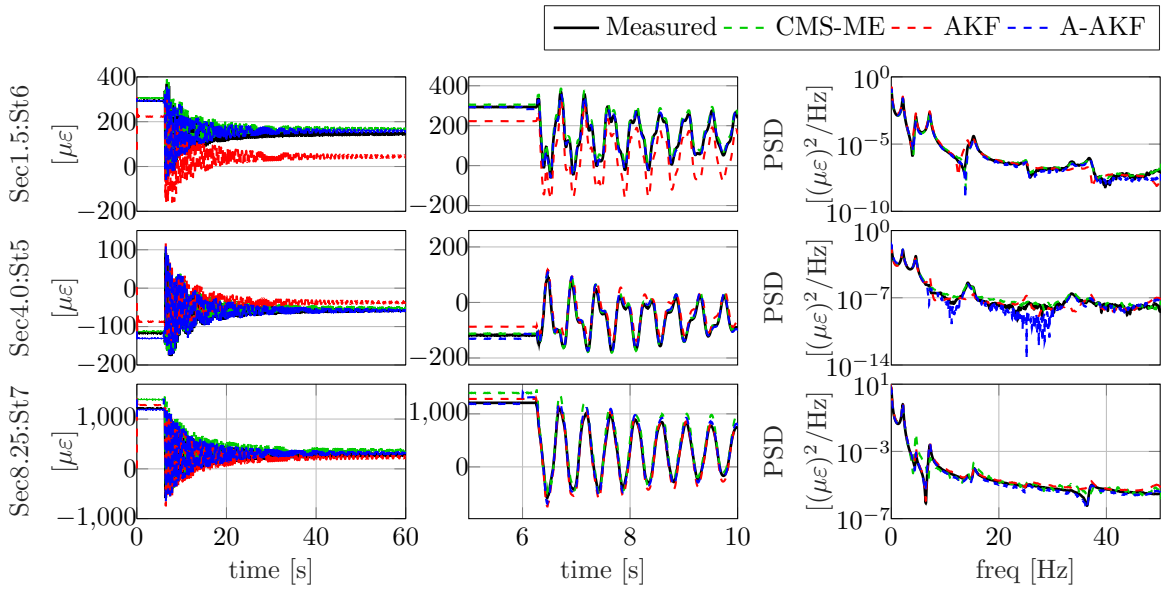

Figure 7.14: Large scale WT blade pull and release tests: time history (left), detailed time history (middle) and PSD (right) of strain response for sensors St.6 (Sec1.5), St.5 (Sec4.0) and St. 7 (Sec. 8.25). Measured signals are indicated via a solid black line. Signals estimated via CMS-ME are indicated in a dashed green line, signals obtained via the conventional AKF in a dashed red line, while those predicted via the A-AKF are denoted via a dashed blue line.

A global comparison between the conventional approach and the herein proposed procedure, in terms of response estimation accuracy, is shown in Figs. 7.15 and 7.16, where, respectively, the TRAC and FRAC values at "unmeasured" locations are displayed for the conventional AKF, the A-AKF and the CMS-ME approach. In particular, Figs. 7.15 and 7.16 (left) show, respectively, the TRAC and FRAC trends along the blade, i.e., their values at "unmeasured" locations ordered from the blade root (left) to the blade tip (right). Figures 7.15 and 7.16 (right) display the TRAC and FRAC values averaged over the entire set of predicted responses. The entire time length of the recorded signals has been adopted for the TRAC computation, while the frequency range 0-50 Hz has been used for calculating the FRAC values. Figures 7.14, 7.15 and 7.16 demonstrate good predictive capabilities for the A-AKF.

The time histories reported in Fig. 7.14 indicate that the A-AKF estimation captures the physical blade response both in the static and the dynamic time frames, while the conventional AKF predictions are affected by higher inaccuracy. Indeed, the AKF response predictions report on average a 25% deviation from the measured value in the static time frame, which is clearly visible in Fig. 7.14. To the contrary, the A-AKF matches the measured static responses thanks to the more realistic initial conditions determined from the CMS-ME estimates. Figure 7.15 confirms the comparison results in time domain: the mean TRAC achieved through the A-AKF overcomes the AKF mean TRAC by providing a TRAC value higher than 0.6 for the 93% of the estimated

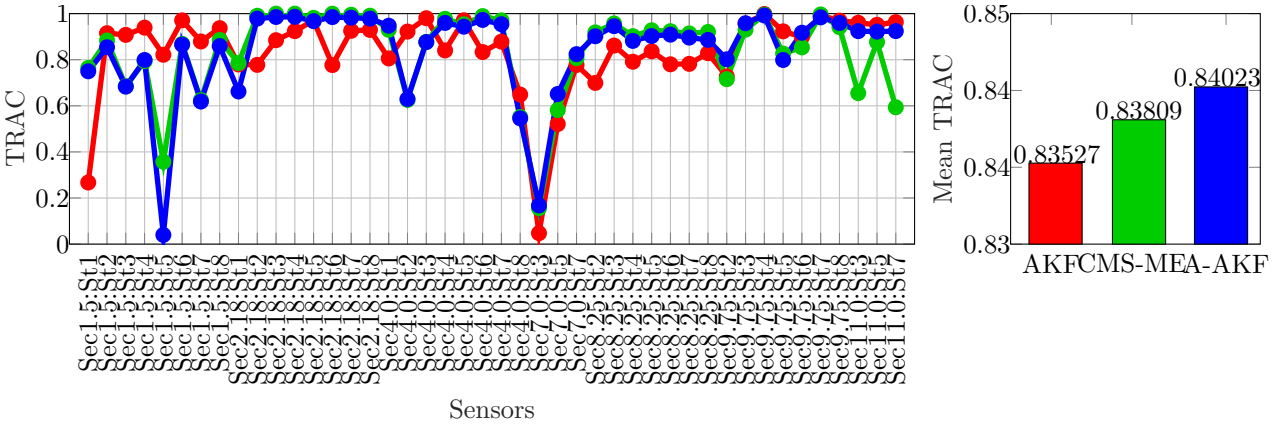

Figure 7.15: Large scale WT blade pull and release tests: TRAC values for the CMS-ME (green line), conventional AKF (red line) and A-AKF (blue line) strain response predictions at "unmeasured" locations according to the adopted sensing configuration (left). Mean TRAC values for the CMS-ME (green), conventional AKF (red) and A-AKF (blue) strain response predictions at "unmeasured" locations (right).

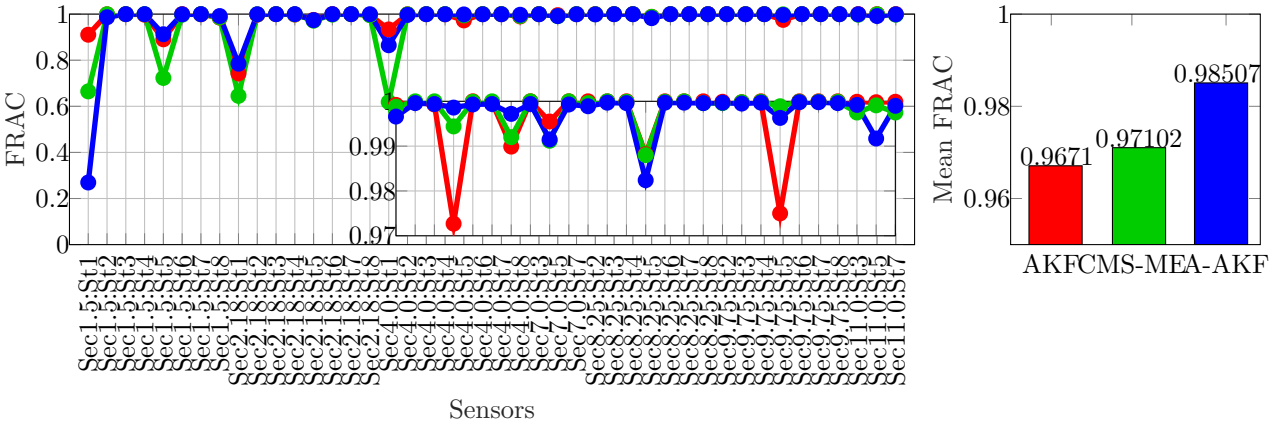

Figure 7.16: Large scale WT blade pull and release tests: FRAC values for the CMS-ME (green line), conventional AKF (red line) and A-AKF (blue line) strain response predictions at "unmeasured" locations according to the adopted sensing configuration (left). A detailed view from location Sec4.0:St2 to Sec11:St7 is shown on the plot. Mean FRAC values for the CMS-ME (green), conventional AKF (red) and A-AKF (blue) strain response predictions at "unmeasured" locations (right).

quantities and higher than 0.8 for the 80%. Fig. 7.14 (right) shows that the proposed approach allows to capture the blade response in frequency domain. Moreover, the proposed PSD plots show that the A-AKF estimations follow the frequency content of the physically acquired responses throughout the analyzed frequency bandwidth with good accuracy. However, Fig. 7.16 (right) reports a 1.43% lower mean FRAC value for the A-AKF with respect to the mean FRAC delivered by the conventional AKF. This trend can be ascribed to the instabilities that the near-online adaptation of the process noise covariance may cause when adopting the A-AKF. Due to this behavior, non-smooth frequency response can appear in certain bandwidths, e.g. PSD at location Sec4.0:St5 between 20 and 30 Hz. Nonetheless, Fig. 7.14 (right) clearly demonstrates that, outside the limited frequency ranges in which the described effect occurs, the A-AKF predicted spectra match the measured ones with higher accuracy than the signals generated via the conventional AKF regime. Figures 7.15 and 7.16 further show a good agreement between the predictions furnished via the proposed A-AKF algorithm and the reference CMS-ME method both in time and frequency domains. More specifically, a slightly higher mean TRAC value can be obtained when the A-AKF is adopted with $N = 100$. The superior performance of the proposed algorithm in the frequency domain, i.e., the higher FRAC value reported in Fig. 7.16 (right), can be visualized by comparing the response PSDs at location Sec8.25:St7 reported in Fig. 7.14. While the A-AKF predicted signal

correctly matches the frequency content of the measured signal in the entire frequency bandwidth, the CMS-ME method overestimates the PSD amplitude around the 4.5 Hz and 15.5 Hz peaks and underestimates it around the 7.2 Hz peak. Moreover, the CMS-ME estimated signal appears highly contaminated by noise at higher frequencies. This behavior confirms that the proposed approach, which draws from the CMS-ME method, simultaneously outperforms it thanks to the higher ability of Bayesian filtering to track measurement and modeling errors by including the noise terms in the system representation.

Input Estimation

Figure 7.17 shows the input estimation results for the unknown force applied to the blade when the AKF (process noise covariance matrix via the L-curve) and the proposed methodology are adopted.

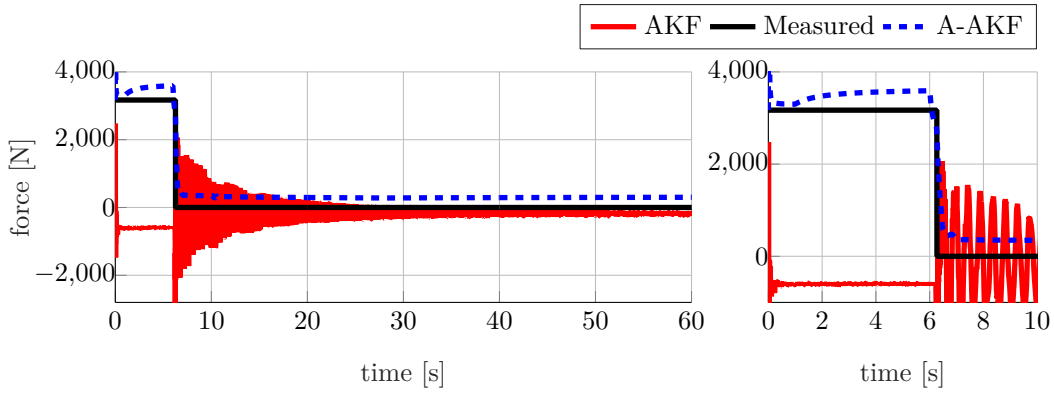

Figure 7.17: Large scale WT blade pull and release tests: input "measured" (black) and estimated (red – AKF, blue – A-AKF) time histories (left) and detailed time histories (right).

The two predicted time signals are compared with the reconstructed step-profile followed by the input during the pull and release tests. From the analysis of the time histories reported in Fig. 7.17, it can be inferred that a good matching between the input predicted via the A-AKF and the actual input profile can be achieved. In particular, both the time instant when the blade is released and the previous static value are identified. To the contrary, when the AKF is used in conjunction with a conventionally selected augmented process noise matrix, the typical pull and release step profile is not detected, i.e., the prediction does not capture the actual input static value and it is affected by high-amplitude oscillations after the blade release. For quantitative comparison purposes, the SE and SD indicators are reported in Tab. 7.1 for both the AKF and the A-AKF. The major contribution to the A-AKF SE is given by the constant offset that affects the A-AKF input profile. Although the blade pre-deformation under its weight is already taken into account, biased errors may be introduced by the assumptions made to model the gravity load, e.g. approximation of the center of gravity position. Hence, part of the gravity load may be estimated together with the external unknown force by the estimators. Moreover, it should be reminded that the unknown input is modeled as a punctual load for VS purposes. This condition only approximates the actual system used to apply the force during tests, i.e., a bungee applied at a certain section. Indeed, the latter generates a distributed load over the section, which could further be affected by fluctuations due to the bungee elasticity. The results listed in Tab. 7.1 show that a lower prediction error can be achieved if an automated process noise covariance selection is put in place via the A-AKF. It is important to notice that improved SE and SD indicators can be achieved via the conventional AKF, as presented in Subsubsection 7.1.3.2 via the parametric study. However, these results would require a substantial manual tuning effort, also implying deterioration of response estimation accuracy.

Table 7.1: Large scale WT blade pull and release tests: input prediction errors for the conventional AKF and the A-AKF

	Conventional AKF	A-AKF
SE	$1978N$	$303N$
SD	$194.25N$	$58N$

Parametric study: influence of the time window length

The newly proposed approach for joint input-state estimation relies on the use of a N-steps time window for computing the global prediction error to be minimized within the algorithm. This paragraph analyzes the influence of the time window length on the estimation accuracy when ranges for q^{n_d}, q^{n_v} and q^u are selected as follows: $q^{n_d}_{min} = q^{n_v}_{min} = q^u_{min} = 10^{-20}$, $q^{n_d}_{max} = q^{n_v}_{max} = q^u_{max} = 10^{20}$. Figure 7.18 shows the evolution of the A-AKF response prediction accuracy for N varying from 10 to 500 with a 10-steps increase. From the analysis of the TRAC trend plot (Fig. 7.18 (top, left)) it can be inferred that the influence of the chosen time window length is bounded within a narrow range of variation. This behavior is confirmed by Fig. 7.18 (top, right), which shows that the mean TRAC maintains a value bounded between and 0.80 and 0.86 with increasing N. It can be further noticed that an increasing trend is exhibited for low N values. After this first adaptation phase, the algorithm yields mean TRAC values which exhibit low variability. The evolution of the A-AKF response estimation accuracy in the frequency domain is reported in Fig. 7.18 by means of the FRAC trend and mean FRAC evolution with increasing N. Similarly to the mean TRAC trend, the mean FRAC shows an initial phase affected by higher variability after which it stabilizes around a value approximately equal to 0.97. From Fig. 7.18, it can be inferred that the mean FRAC spans an even narrower range $(0.965 - 0.975)$ with respect to the mean TRAC.

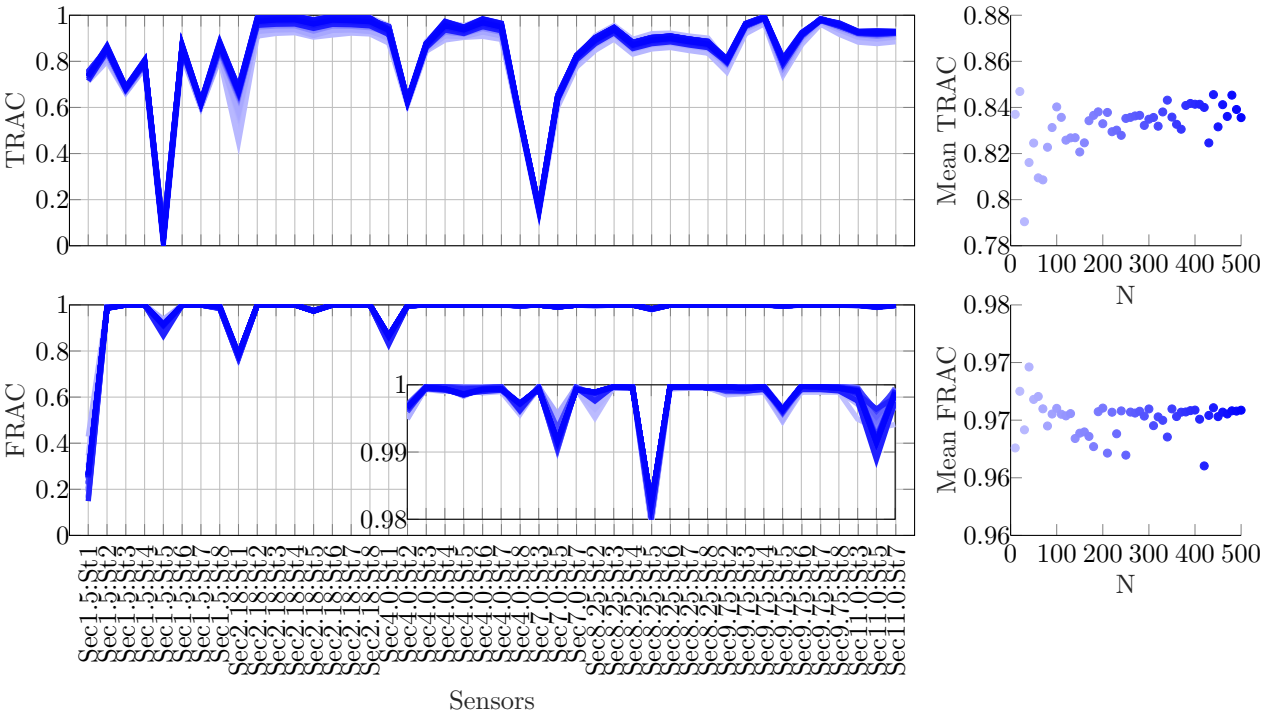

Figure 7.18: Large scale WT blade pull and release tests: A-AKF TRAC trend (top, left) and mean TRAC (top, right) values with increasing N. A-AKF FRAC trend and detailed A-AKF FRAC trend from location Sec4.0:St2 to Sec11.0:St7 (bottom, left). Mean FRAC values with increasing N (bottom, right).

Figure 7.19 displays the variation of the SE and SD input estimation inaccuracy indicator for increasing values of N. The conclusions drawn for the response estimation accuracy can be extended to the input prediction based on Fig. 7.19; both SE and SD reach their maximum for low N, while

stable minimum values for both variables are obtained from a certain N value (between 100 and 150). The last assumption is particularly valid for what concerns the SD indicator. For values higher than $N = 100$, the selection of a broader time window for the A-AKF algorithm does not improve the oscillatory behavior, which results as an artifact in the estimated input profile. It is important to emphasize that the values for which the SE and SD minima are found lie close to the optimal values for which both the mean TRAC and mean FRAC become stable.

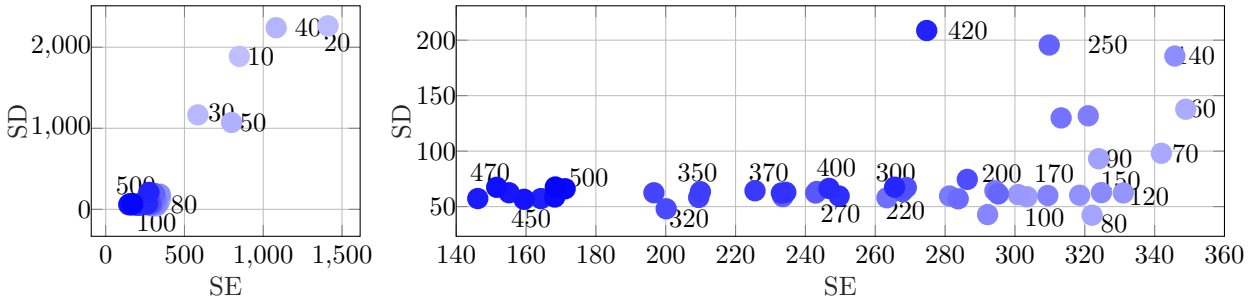

Figure 7.19: Large scale WT blade pull and release tests: A-AKF SE and SD evolution with increasing N: full (left) and detailed (right) view. Values for N are reported on the figure.

The conducted parametric study thus demonstrates that a unique choice for N will generate the same effect on the input and response estimation accuracy delivered via the A-AKF. The optimal choice for N should be high enough to surpass regions of algorithmic instability. On the other hand, an exaggerated increase in N would cause the A-AKF to deviate from the near real-time assumption and would not bring any benefit in terms of estimation accuracy. For this reason, N values between 100 and 150 can be considered as optimal. It should be noted that, although a default choice for N in the suggested range would already make the algorithm user-independent, a random N selection could still be put in place. The latter would be justified by the generally limited fluctuations in the prediction accuracy for $10 \leq N \leq 500$. However, such a random selection should still employ a limited time window length in order to ensure near real-time applicability.

Parametric study: influence of q^{n_d}, q^{n_v} and q^u range bounds

The A-AKF requires a priori selection of the ranges within which q^{n_d}, q^{n_v} and q^u can vary. This paragraph studies the influence of the covariances range on the overall input and response estimation accuracy when a $N = 100$ time-steps window is adopted. In order to simplify the analysis, the following assumptions are made:

- The ranges are symmetrical, i.e, $q^{n_d}_{min} = -q^{n_d}_{max}$, $q^{n_v}_{min} = -q^{n_v}_{max}$ and $q^u_{min} = -q^u_{max}$;
- The same range is adopted for the three variables q^{n_d}, q^{n_v}, q^u.

Therefore, a variable Q can be defined such that: $q^{n_d}_{min} = q^{n_v}_{min} = q^u_{min} = 10^{-Q}$ and $q^{n_d}_{max} = q^{n_v}_{max} = q^u_{max} = 10^Q$.
Figure 7.20 displays the evolution of the A-AKF response estimation accuracy for Q varying from 2 to 23 with a 1-step increase. The TRAC trend and mean TRAC plots reported in Fig. 7.20 show that approximately up to a 3% higher response estimation accuracy could be achieved by adopting a very low Q, i.e., by heavily bounding the range of values that q^{n_d}, q^{n_v} and q^u could span. For $Q \geq 5$, the TRAC seems to stabilize around a certain value. However, the FRAC and mean FRAC evolution reported in Fig. 7.20 show a different behavior: the response estimation accuracy in frequency domain reaches the highest value for $Q = 5$ and remains stable for higher Q.
Figure 7.21 displays the variation of the SE and SD input estimation inaccuracy indicators for increasing values of Q. For $2 \leq Q \leq 4$, the SE indicator reaches the lowest values while SD is maximized. This result highlights that for very narrow ranges, the best match between the predicted input mean value and the measured one could be achieved but the estimated time history would be affected by large oscillations, i.e., the predicted input would not be static. For $Q \geq 5$, both SD and

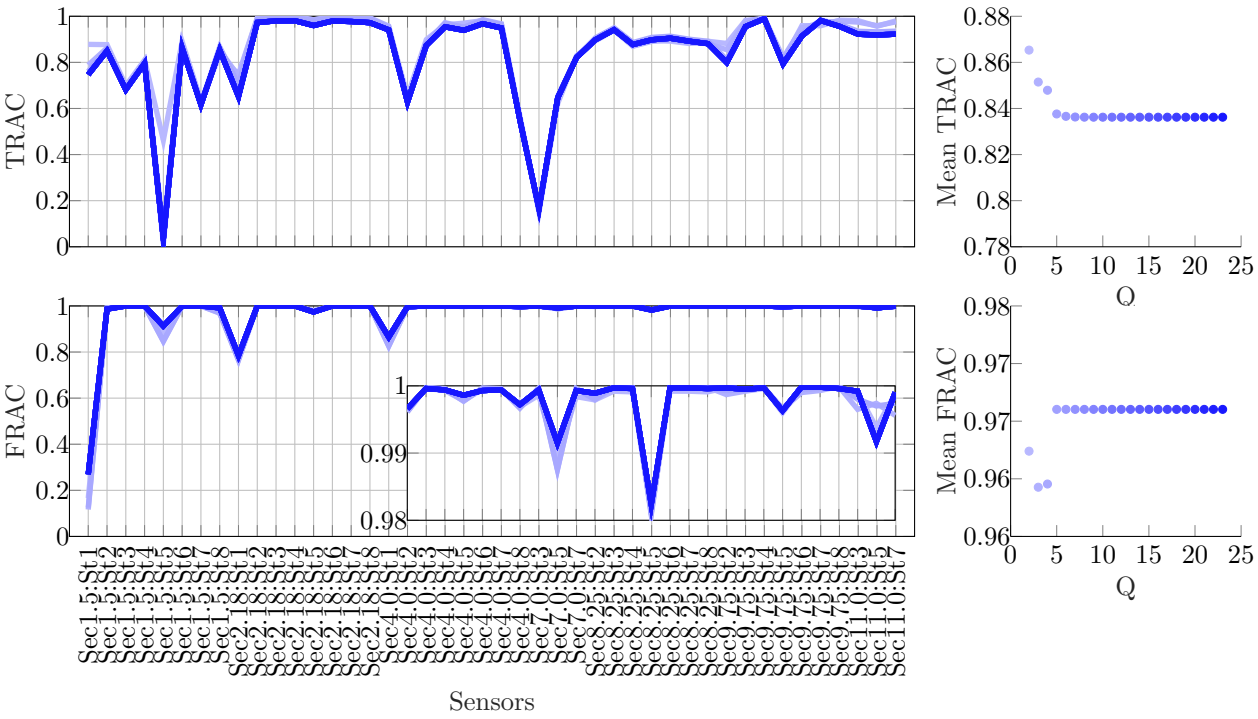

Figure 7.20: Large scale WT blade pull and release tests: A-AKF TRAC trend (top, left) and mean TRAC (top, right) values with increasing Q. A-AKF FRAC trend and detailed A-AKF FRAC trend from location Sec4.0:St2 to Sec11.0:St7 (bottom, left). Mean FRAC values with increasing Q (bottom, right).

SE stabilize, i.e., varying the ranges width would not cause any variation in the input prediction accuracy.

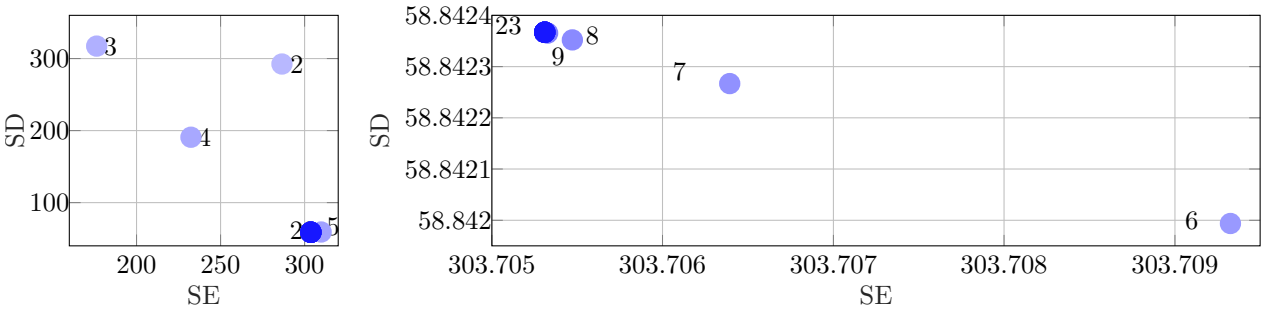

Figure 7.21: A-AKF SE and SD evolution with increasing Q: full (left) and detailed (right) view. Values for Q are reported on the figure.

According to Figures 7.20 and 7.21, the same overall estimation accuracy can be achieved for $Q \geq 5$. Although selecting narrow ranges, i.e., $Q \leq 5$, would improve the TRAC and SE estimators, the resulting response error in frequency domain would increase and the predicted input would be affected by large oscillations. The parametric study reported in this paragraph demonstrates that broad ranges can be set by the user for q^{n_d}, q^{n_v} and q^u without affecting the estimation results. Therefore, no particular prior belief on the most suitable ranges for q^{n_d}, q^{n_v} and q^u is required for obtaining optimal results via the A-AKF.

7.2 Summary

The case study analyzed in this chapter, i.e., a large scale composite blade, has been exploited for validation of the A-AKF, a novel approach to tackle the problem of adaptive noise calibration for the task of joint input-state estimation via Kalman-type filters. This task is the driving process

during VS applications, where typically few sparse response measurements are available and recovery of response and inputs in unmeasured locations is sought after. The proposed methodology has been tested for loads (input) and full-field response prediction during the so-called pull and release experimental tests on a full-scale research WT blade. In order to reduce the computational effort due to the high dimensionality of the blade numerical model, a ROM has been derived from an experimentally validated FE model using a CMS technique. The results indicate that the A-AKF provides accurate response predictions without the need for offline user-dependent selection of the covariance matrix associated to model uncertainties, which forms a well-known limitation of the conventional AKF. A parametric study has demonstrated that the A-AKF response prediction accuracy outperforms both the conventional AKF and the CMS-ME methods, provided that a sufficiently large time window is adopted for the algorithm. To what concerns the input, large errors are encountered when a conventional augmented process noise covariance matrix is adopted, with the input-related covariance term assigned via the classical L-curve approach. As demonstrated via the presented parametric study, these errors could be minimized via a substantial manual tuning. Besides the need of user intervention, the tuning procedure has proven not to be able to simultaneously minimize both the oscillations and the static error. Additionally, minimized AKF input errors would lead to deterioration of response estimation accuracy. When the process noise covariance matrix is tuned via the L-curve, the AKF is not able to capture the actual input profile (corresponding to a step) and large oscillations are affecting the estimated signal following blade release. To the contrary, by adopting the A-AKF, the predicted input profile matches the actual experimental load and both the static error, as well as the standard deviation of the oscillations following release, are minimized. The same behavior for different adopted time window lengths can be observed for the input. Moreover, the input inaccuracy indicators are minimized for the same time window dimension which maximizes the response performance both in time and frequency domains. It should be noted that the variability in performance as a result of the chosen window length is sufficiently limited to justify a random selection of the latter, which should though comprise narrow ranges in order to guarantee a near-online procedure. Under these latter assumptions, the A-AKF can be considered as a user-independent method for joint input-state estimation in near real-time. The latter statement is confirmed by the proved independence of the overall A-AKF estimation accuracy from the selected covariance ranges. The parametric study with respect to the ranges bounds has proven that no prior knowledge regarding the most suitable ranges width is needed in order to guarantee the A-AKF optimal performance.

8

WIND TURBINE BLADES TESTING: 3D-PRINTED SCALED BLADE

This chapter reports on the use of the proposed data assimilation strategies during a test campaign on a 3D-printed scaled titanium WT blade owned by SISW and manufactured by 3D Systems (Leuven, Belgium) [104]. The 3D printing process of metals introduces many additional technological challenges, e.g. limitations to 3D-printed specimens dimensions. For this reason, it is common practice to print the several subparts of the final product individually and then weld them together. Weld beads create areas of structural properties discontinuity which are difficult to be modeled. Moreover, intrinsic manufacturing process defects and thickness variations due to surface post-processing often arise. Canonical virtualization techniques produce realistic estimates under static conditions. Within the dynamic domain, the punctual stiffness variation caused by the mentioned limitations leads to large discrepancies between the DT and the physical structure. To overcome these limitations, a model updating process based on experimental data has been combined with conventional and newly developed Bayesian estimators for virtualization of the 3D-printed scaled blade.
The blade of study is presented in Section 8.1, along with a description of the measurement campaign, the FE model and its validation and update results. Next, Section 8.2 explores the use of several estimators for Bayesian VS of the 3D-printed scaled WT blade. Specifically, a validation of the A-AKF for a random load scenario is provided via its employment for input-state estimation during random tests of the 3D-printed scaled blade. For the same random tests, the AKF and the GP-based approach with conventional Matérn covariance function have been compared i) under the assumption of available strain and acceleration measurements and ii) in presence of acceleration-only measurements. Next, Subsection 8.2.2 makes use of the pull and release test data to validate the use of the GP-based approach with conventional Matérn covariance function for an uncommon load type. The resulting predictions are verified through a comparison with the more conventional AKF and DKF estimators. As a final investigation, Section 8.3 explores the use of ad hoc covariance functions for input-state prediction via GPLFMs on the 3D-printed WT blade under different loading conditions. Lastly, Section 8.4 reports on the conclusions for this chapter.

8.1 3D-printed scaled wind turbine blade

The case study analyzed in this chapter concerns a 3D-printed scaled titanium WT blade. The entire 3D-printed specimen, manufactured by 3D Systems, comprises the scaled blade and a flange which was designed to allow the blade clamping to a concrete block. The CAD model employed for printing has been retrieved scaling down an existing larger CAD model shared by DTU Wind Energy in the framework of the "ReliaBlade" research project. Figure 8.1 shows the manufacturing process, consisting of the following steps:

- 3D-printing of four subparts of the entire structure
- stress relief heat treatment of the four subparts
- welding of the four subparts
- plate removal via wire through Electrical Discharge Machining (EDM)
- polishing of the structure.

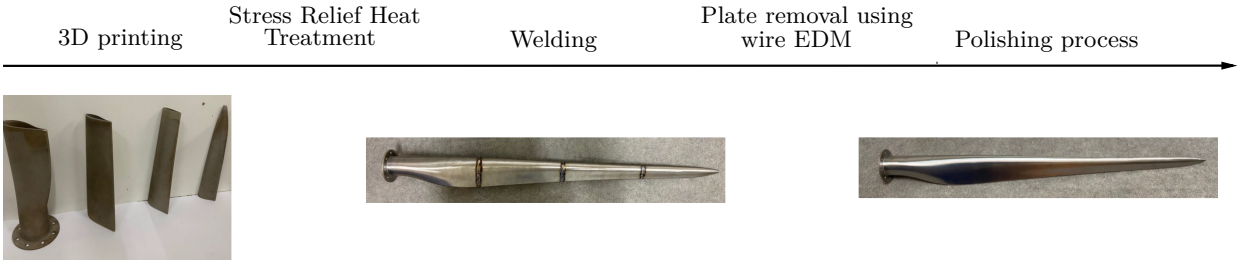

Figure 8.1: 3D-printed scaled titanium WT blade manufacturing process

8.1.1 Measurement campaign

This section describes the setup adopted during the test campaign carried out at SISW on the scaled blade, along with the series of tests performed with different types of excitation. Figure 8.2 shows the setup adopted during the measurements on the scaled WT blade. During all the hereby described tests, the WT blade was clamped to a concrete block as depicted in details in Fig. 8.6.

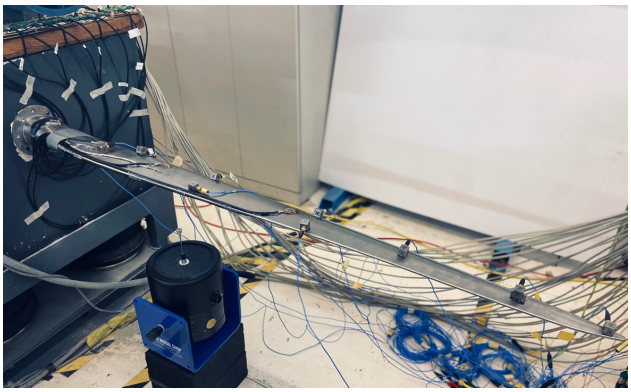

Figure 8.2: 3D-printed scaled titanium WT blade experimental setup

The entire setup includes 3 types of sensors: 4 uniaxial strain gauges, 8 rosettes and 10 triaxial accelerometers. Figure 8.3 shows the sensors locations. Strain sensors are arranged in sections along the blade on both the top and bottom surfaces, while accelerometers have been positioned only on the top surface. It is worth noting that during the described tests, the main component of the recorded acceleration and strain are respectively oriented along the vertical (Y) and axial (Z) directions. Therefore, the remainder of the chapter will only consider accelerations along Y and strains along Z. During the test campaign, a Simcenter^{TM} SCADAS system and Simcenter^{TM} Testlab software have been used for data acquisition. Three types of tests have been performed according to the adopted excitation method: impact testing using a modal hammer, shaker testing and the so-called pull and release tests. Figure 8.3 shows the shaker and the impact locations. Data acquired during the impact test has been used to determine the scaled WT blade modal properties, which have been extracted using Simcenter^{TM} PolyMAX. Table 8.1 reports the resulting experimental frequencies and damping ratios in the frequency range of interest 0-500 Hz.
During shaker testing, constant frequency sine tests and continuous random tests up to 450 Hz were carried out. Finally, pull and release tests were performed by applying an initial static load via a mass (known weight equal to 1.5 kg) at the blade tip. As displayed in Fig. 8.4, during this test the blade is then released by cutting the plastic tie used to hang the mass. This leads to free vibrations of the blade, which are recorded via the installed sensors.

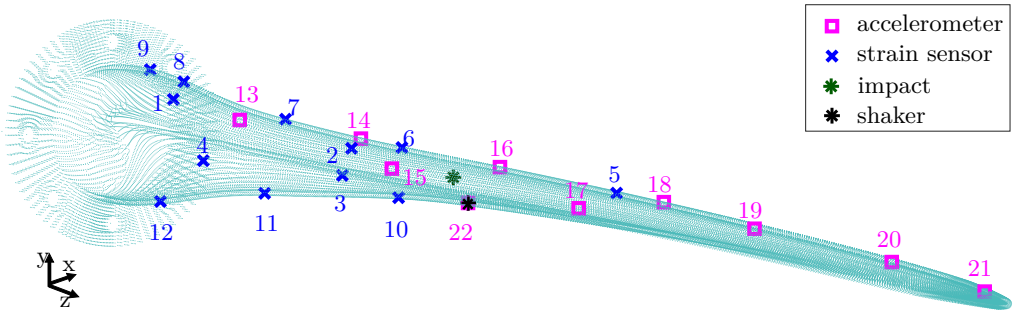

Figure 8.3: 3D-printed scaled WT blade sensing configuration: strain sensors (blue), accelerometers (magenta)

Table 8.1: Experimental modal frequencies and damping ratios for the 3D-printed scaled titanium WT blade in clamped-free conditions

Modes	Frequency [Hz]	Damping [%]
1	25.0	1.27
2	55.0	0.91
3	90.4	0.56
4	193.2	0.56
5	236.4	0.32
6	343.2	1.78

Figure 8.4: Pull and release tests on the 3D-printed scaled WT blade

8.1.2 *Numerical model: Finite Element model udpdate and Reduced Order Model*

The scaled WT blade FE model shown in Fig. 8.5, has been developed in Simcenter^{TM} 3D starting from the CAD model used for 3D printing. The mesh is made up of around 65000 nodes and 33804 six-sided solid elements. The initial isotropic material (Ti6Al4V) properties have been defined according to the data sheet provided by the manufacturer. Figure 8.6 (left) shows the physical BCs obtained by means of 2 bolts used to clamp the flange to the concrete block and a layer of glue. The described BCs have been reproduced in the FE model by means of two RBE2 connections at the holes where the bolts were placed and four springs. More specifically, the flange has been divided into four parts, each connected to a spring via a RBE2 connection. As shown in Fig. 8.6 (right), the free ends of the springs have been fixed. An initial stiffness value of 30000 N/mm has been adopted

for each spring. Concentrated masses have been added to the FE model at the accelerometers locations to account for their presence and increase the correlation with experimental data.

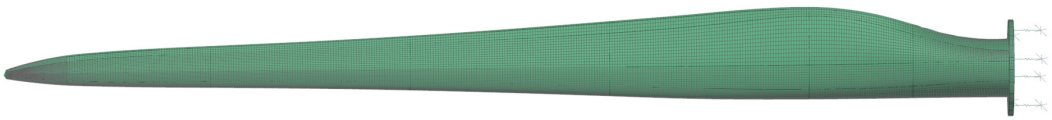

Figure 8.5: 3D-printed scaled titanium WT blade FE model

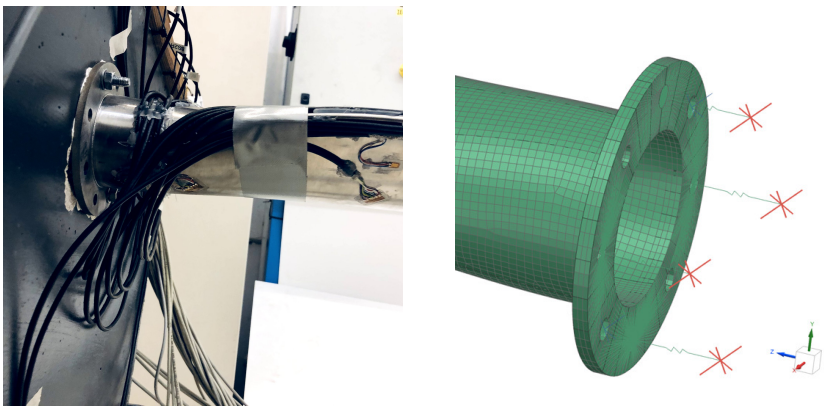

Figure 8.6: 3D-printed scaled WT blade clamping system (left). 3D-printed scaled WT blade FE model BCs (right).

Numerical modes in the frequency range 0-450 Hz have been computed using NX^{TM} Nastran SOL 103. NX^{TM} Nastran SOL 200 has been adopted in Simcenter^{TM} 3D for updating the FE model using the experimental modal parameters in Tab. 8.1 as reference and a genetic algorithm for optimization. The following parameters have been set as design variables for the optimization process: springs stiffness, isotropic material Young's modulus, Poisson's ratio and density. Some of the adopted ranges for the design variables have been selected from the processing data sheet provided by the manufacturer of the WT blade, others were kept below a 10% deviation. Table 8.2 shows the initial and optimized values for the selected design variables. Table 8.3 reports on the model update results

Table 8.2: 3D-printed scaled WT blade FE model update: design variables initial and updated values

Design variables	Initial value	Updated value
$K_{springs}[N/mm]$	30000	33167.2
$E[Gpa]$	121	116.039
$\rho[kg/mm^3]$	4.430×10^{-6}	4.873×10^{-6}
$\nu[/]$	0.34	0.34208

by comparing the initial and updated numerical frequencies with the reference test frequencies for the first six modes. Additionally, Tab. 8.3 offers the initial and updated frequency errors as well as a comparison between the initial and updated MAC values for the diagonal mode pairs. Figure 8.7 shows a visual representation of the MAC matrix between the reference experimental modes and the updated numerical modes. From the analysis of Tab. 8.3 it can be concluded that the implemented update strategy allowed to substantially decrease the frequency errors, as well as to improve MAC values for the first six modes.
A ROM of the scaled blade has been built following the procedure outlined in Subsection 2.1.1 taking into account the first six modes (frequency range of interest: 0-450 Hz) and one residual attachment mode related to the unknown force to be estimated via the chosen Bayesian estimators. For shaker tests, the residual attachment mode has been computed by applying a unitary force at

Table 8.3: 3D-printed scaled WT blade FE model initial and updated frequencies, frequency errors and MAC pairs

	f_i^{test} [Hz]	f_i^{initial}[Hz]	f_i^{updated}[Hz]	$err_{f_i}^{\text{initial}}$ [%]	$err_{f_i}^{\text{updated}}$[%]	$\text{MAC}_{ii}^{\text{initial}}$	$\text{MAC}_{ii}^{\text{updated}}$
1	25.020	26.313	24.758	5.165	-1.047	0.985	0.985
2	55.004	57.548	54.512	4.626	-0.894	0.976	0.977
3	90.426	99.557	93.405	10.098	3.294	0.947	0.949
4	193.201	199.369	187.902	3.192	-2.743	0.904	0.909
5	236.416	258.387	242.358	9.293	2.513	0.875	0.881
6	343.176	372.511	349.807	8.548	1.932	0.914	0.916

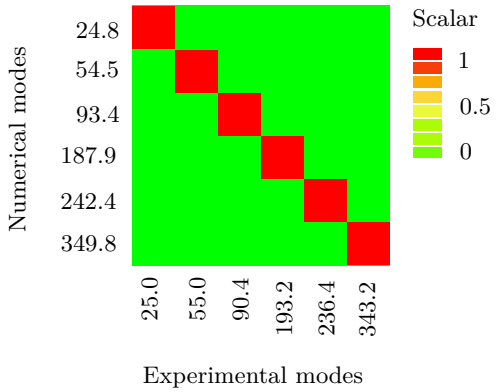

Figure 8.7: 3D-printed scaled WT blade: MAC between numerical and experimental mode shapes from hammer test

the shaker location pointed out in Fig. 8.3 along the positive Y direction. For pull and release tests, the unitary force for residual attachment mode computation has been applied at a tip node along the negative Y axis.

8.2 Joint input-state estimation

In this section, the joint input-state predictions achieved via several state-of-the-art and newly developed estimators during tests on the 3D-printed scaled WT blade are explored. Initially, the 3D-printed blade random tests are exploited to validate the ability of the A-AKF to provide a practical solution to the challenges derived from the necessary tuning process of Kalman-based filters for joint input-state estimation in a random load condition. Next, to complement Subsection 6.3.2 with a WT application, the GP-based approach presented in Subsection 5.2.1 will be adopted and compared to the standard AKF for simultaneous load and response prediction during random tests on the 3D-printed scaled blade. The comparison is provided for both a mixed observations set and an acceleration-only measurements set. It is worth noting that the GP-based approach analyzed in this section follows the steps in Alg. 14 and Fig. 5.6, except for the missing RTS step. Indeed, this section aims at experimentally proving the filtering-only algorithm adaptation proposed in Subsection 5.2.1, which is introduced and preferred due to its real-time applicability. Except to this latter aspect, the hereby adopted algorithm follows what reported in Alg. 14, i.e., it employs a conventional Matérn covariance function whose hyperparameters are selected in the training phase by exploiting the entire set of observations used within the online estimation step. The hyperparameters selection step is perfomed by setting the log marginal likelihood maximization via the SHERPA ("Simultaneous Hybrid Exploration that is Robust, Progressive and Adaptive") algorithm available in Simcenter^{TM} HEEDS. The SHERPA algorithm searches for the global maximum/minimum with the least amount of evaluations by using a simultaneous combination of local and global search methods for fast "learning" from the design space. The use of data assimilation techniques during pull and release tests on the 3D-printed scaled WT blade is also treated in this chapter. The same

GP-based approach tested for the random load is validated for pull and release tests and compared against the conventional AKF and DKF on the task of joint input-state estimation.

8.2.1 Random test

The VS approaches compared within this subsection have been tested for joint input-state estimation during shaker tests on the 3D-printed scaled titanium WT blade. During the measurements hereby taken into account, the blade was excited using a white noise excitation applied via the shaker at the location pointed out in Fig. 8.3. This test configuration is first adopted to validate the applicability of the A-AKF for adaptively tuning the process noise covariance matrix during input-state estimation under a random load condition. Next, the use of the GP-based approach with conventional Matérn covariance function is proposed for WT blades testing by comparing it against the state-of-the-art AKF on the task of input-state estimation under the assumption of both a mixed observations set and an acceleration-only measurements set.

8.2.1.1 Input-response estimation through the Adaptive-noise Augmented Kalman Filter

The target of what follows lies in input and strain response prediction during shaker testing (random excitation) of the 3D-printed scaled WT blade by means of the A-AKF algorithm presented in Subsection 4.2.1. Specifically, the inaccuracy metric proposed in Subsubsection 4.2.1.2 is hereby exploited to set up the A-AKF. In order to validate the efficacy of the proposed algorithm on the task of input-response prediction, the state-of-the-art AKF is hereby proposed as reference. Moreover, the CMS-ME response estimations are offered for demonstrating their validity and proving that they can be employed within the A-AKF algorithm as described in Subsection 4.2.1. For evaluating the performance of Bayesian estimators, it is common practice to compare estimated signals to the corresponding measured reference. The set of recorded dynamic response data is thus split into a measured and an unmeasured subset. The "unmeasured" subset refers to the quantities that are to be estimated via use of the proposed scheme. The "virtually sensed" signals are then compared to the reference (measured) time histories in order to evaluate the prediction performance. The "measured" and "unmeasured" locations for the A-AKF algorithm during random tests on the 3D-printed scaled blade are reported in Tab. 8.4, where the sensors numbers refer to the layout in Fig. 8.3. For the hereby treated case study, the observed locations have been selected to be equally distributed over the sensed area on the scaled WT blade. Strain responses only are adopted for the A-AKF in order to guarantee the real-time applicability of the method. Additionally, the minimum required amount of sensors, i.e., 7 strain responses, is employed for this case study in order to prove the efficacy of the method. Table 8.4 also offers a summary of the initialization values adopted for the necessary estimators (AKF and A-AKF) parameters. For the AKF, the chosen time-invariant $\mathbf{Q}$ and $\mathbf{Q}^u$ matrices are reported. The latters have been conventionally chosen by setting $q^{n_d} = q^{n_v}$ to very low numbers compared to the order of magnitude of the state vector and selecting q^u by means of the L-curve metric presented in Fig. 8.8, where the smoothing and error norms refer to the formulation available in Section 11.2. It is observed that the plot in Fig. 8.8 does not exhibit a perfect L-shape. However, the curve trend for the analyzed experimental case study can be interpreted by the user and the q^u value shown in Tab. 8.4 can be selected. The diagonal entries of $\mathbf{R}$ have been instead set basing on the noise recorded by the relative measurement channels. Since the hereby investigated tests do not foresee a static load component, the initial condition, $\hat{\mathbf{x}}_0^a$, of the augmented state vector has been set to $\mathbf{0}$ for both the estimators. For the A-AKF, the chosen time-window length (N = time steps within each analyzed batch) and the selected ranges for q^{n_d}, q^{n_v} and q^u are offered in Tab. 8.4.

Figure 8.9 shows the time histories and the related frequency content for sensors 6 and 7, i.e., an "unmeasured" and a "measured" strain response. A comparison between the signals estimated via CMS-ME, the conventional AKF and the ones obtained by using the proposed A-AKF scheme is offered. The estimated curves are compared against the experimentally measured responses at the corresponding locations to prove the algorithm validity.

Table 8.4: 3D-printed scaled WT blade random test: AKF and A-AKF observations sets and initialization values

Estimator	Observations	Initial state mean	Initial error cov. matrix	Input noise cov./ input noise cov. range and N	Process noise cov. / process noise cov. ranges	Measurement noise cov. matrix ($\mathbf{R}$)
AKF	1, 3, 5, 7, 8, 10, 12	$\hat{\mathbf{x}}^a_{0\|0} = \mathbf{0}$	$\hat{\mathbf{P}}^a_{0\|0} = 10^{-10} \times \mathbf{I}$	$\mathbf{Q}^u = 10^{-3} \times \mathbf{I}$	$\mathbf{Q} = 10^{-10} \times \mathbf{I}$	$\mathbf{R}_{\text{strain}} = 10^{-14} \times \mathbf{I}$
A-AKF	1, 3, 5, 7, 8, 10, 12	$\hat{\mathbf{x}}^a_{0\|0} = \mathbf{0}$	$\hat{\mathbf{P}}^x_{0\|0} = 10^{-10} \times \mathbf{I}$	$10^{-20} \leq q^u \leq 10^{20}$ $N = 15$	$10^{-20} \leq q^{n_d} \leq 10^{20}$ $10^{-20} \leq q^{n_v} \leq 10^{20}$	$\mathbf{R}_{\text{strain}} = 10^{-14} \times \mathbf{I}$

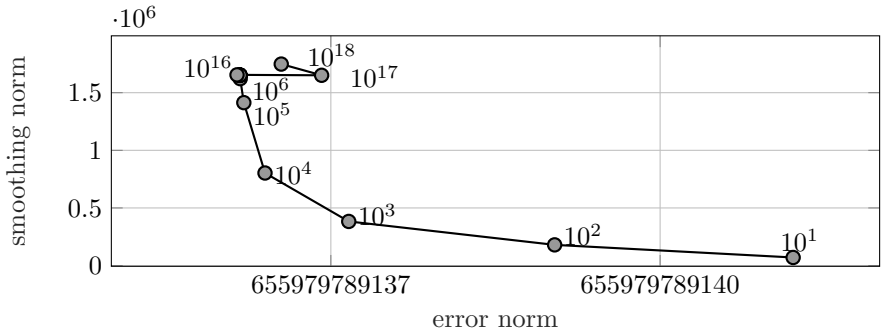

Figure 8.8: The L-curve for joint input-state estimation of the 3D-printed scaled WT blade during random tests using the AKF. Values for q^u are reported on the figure.

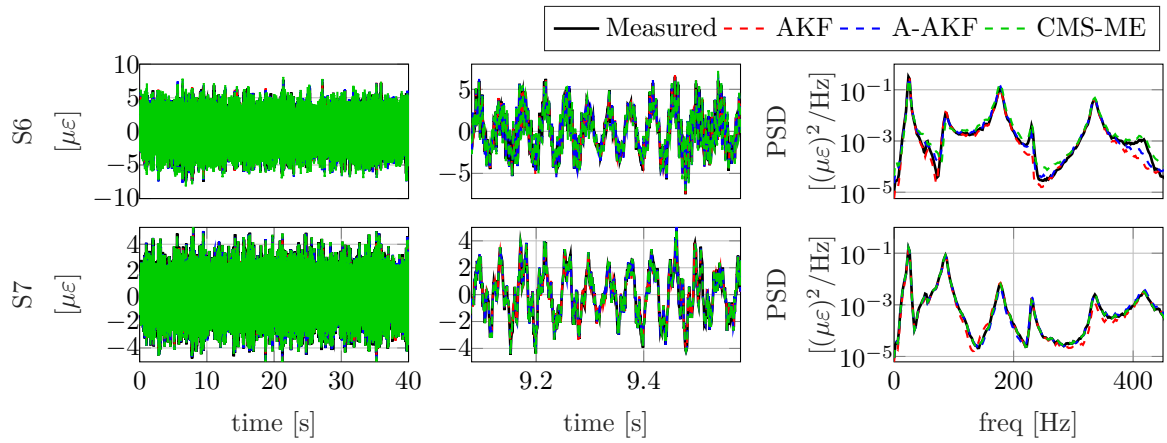

Figure 8.9: 3D-printed scaled WT blade random test: time history (left), detailed time history (middle) and PSD (right) of strain response for sensor 6 and 7. Measured signals are indicated via a solid black line. Signals estimated via CMS-ME are indicated in a dashed green line, signals obtained via the conventional AKF in a dashed red line, while those predicted via the A-AKF are denoted via a dashed blue line.

A global response estimation accuracy comparison between the conventional AKF, the CMS-ME and the A-AKF is shown in Figs. 8.10 and 8.11, where the TRAC and FRAC values (formulated in Section 11.1) achieved via the three methods are respectively displayed. In particular, Figs. 8.10 and 8.11 (left) show, respectively, the TRAC and FRAC trends along the blade, while Figs. 8.10 and 8.11 (right) display the TRAC and FRAC values averaged over the complete set of responses. The entire time length of the recorded signals has been adopted for the TRAC computation and the frequency range 0-450 Hz has been used for calculating the FRAC values.
Figures 8.9, 8.10 and 8.11 demonstrate that the A-AKF can provide a high level of accuracy in terms of response estimation for tests featuring a random type of load. The time histories reported in Fig. 8.9 indicate that the A-AKF predictions are comparable to the ones achieved via the AKF and the CMS-ME methods. This is confirmed by Fig. 8.10, which shows that the three compared approaches all provide high response prediction accuracy in time domain (high mean TRAC value). However, from the presented comparison it can be concluded that the AKF tuned

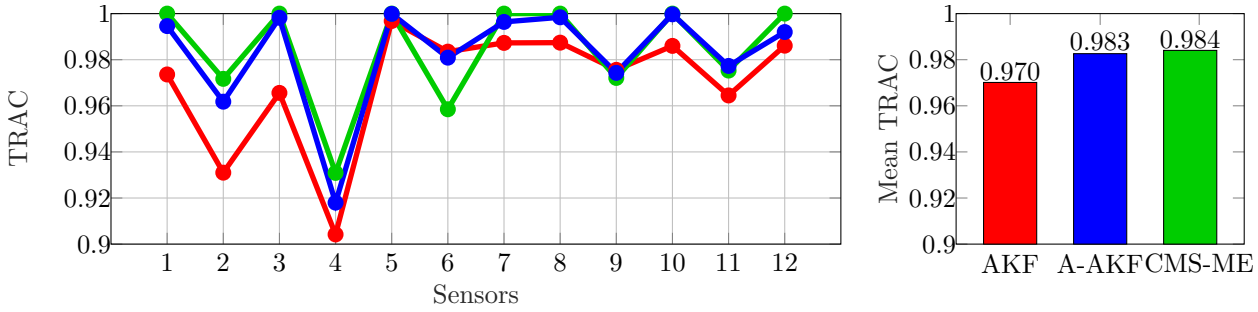

Figure 8.10: 3D-printed scaled WT blade random test: TRAC values for the CMS-ME (green line), conventional AKF (red line) and A-AKF (blue line) strain response predictions (left). Mean TRAC values for the CMS-ME (green), conventional AKF (red) and A-AKF (blue) strain response predictions (right).

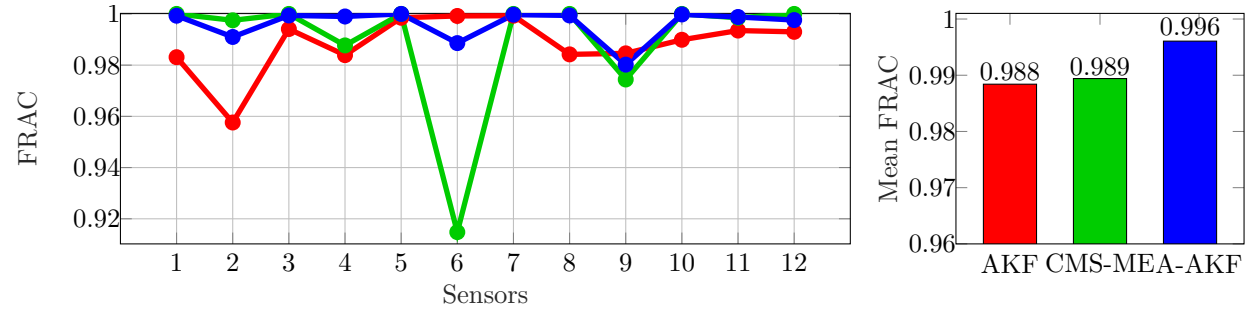

Figure 8.11: 3D-printed scaled WT blade random test: FRAC values for the CMS-ME (green line), conventional AKF (red line) and A-AKF (blue line) strain response predictions (left). Mean FRAC values for the CMS-ME (green), conventional AKF (red) and A-AKF (blue) strain response predictions (right).

via the L-curve metric provides the lowest mean TRAC value. Indeed, while the A-AKF and the CMS-ME approaches exhibit approximately the same response prediction performance, the AKF produces the lowest TRAC for almost the totality of the strain sensors, as depicted in Fig. 8.10 (left). Figure 8.9 (right) shows that the A-AKF estimations, similarly to the ones generated by the CMS-ME and the AKF, follow the frequency content of the physically acquired responses throughout the analyzed frequency bandwidth with good accuracy. Moreover, Fig. 8.11 (right) reports the highest mean FRAC value for the A-AKF and the lowest value for the CMS-ME approach. The latter is indeed negatively influenced by sensor 6, for which, according to the FRAC trend shown in Fig. 8.11, the CMS-ME method provides the lowest FRAC. The level of accuracy reached by the A-AKF in frequency domain instead mediates between the one achievable via the CMS-ME and the AKF. This an indicative example confirming that the A-AKF draws from the CMS-ME but is also able to outperform it by exploiting the stochastic framework in which it lies. Figure 8.11 (right) also confirms the analogous response estimation performance of the three estimators for sensor 7 shown in Fig. 8.9.

Figure 8.12 shows the input estimation results for the unknown force applied to the 3D-printed scaled blade when the AKF and the A-AKF are adopted. The predicted time signals and their relative PSDs are compared with the measured force, which has been acquired by a force cell placed between the shaker and the structure. From the analysis of the time histories reported in Fig. 8.12, it can be inferred that an adequate amplitude matching between the input predicted via the A-AKF and the actual input is achieved. To the contrary, the AKF tuned via the L-curve underestimates the force amplitude. However, the detailed time history and PSD comparisons highlight that the A-AKF produces artificial low frequency components which reduce the load estimation precision. These are due to the batch nature of the algorithm, which seeks for the optimal process noise covariance matrix within subsequent time windows. An “averaged” estimation is therefore produced within each analyzed time window. This is contrast with the prominent dynamic nature of the examined random input, which would be more suitable for a step-by-step error minimization rather

than a batch computation. The resulting poor input reconstruction is also validated by Tab. 8.5, which offers an overview of the input TRAC and FRAC produced by the A-AKF and the standard AKF. Indeed, according to Tab. 8.5, both the data assimilation approaches provide extremely low TRAC and FRAC values. The poor input estimation performance can be also explained by the complete absence of acceleration measurements within the set of observations employed for prediction. As it will be demonstrated in the remainder of this chapter, introducing acceleration measurements within the observations set allows to better capture the dynamics of the system under test thanks to the presence of a direct feedthrough with the unknown input, thus allowing for a more accurate prediction of the latter.

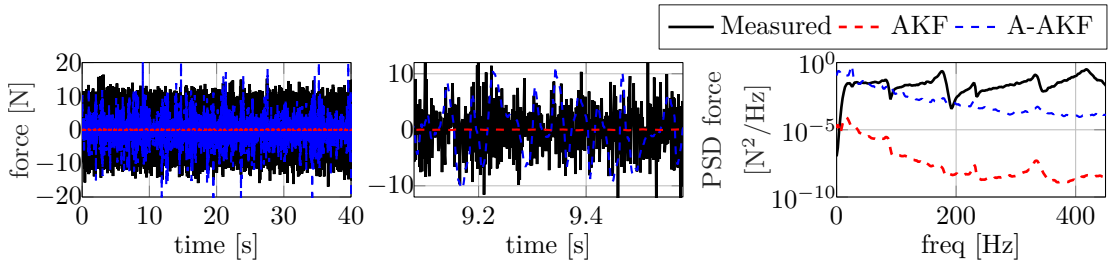

Figure 8.12: 3D-printed scaled WT blade random test: measured (black) and estimated (AKF - red, A-AKF - blue) input time histories (left), detailed time histories (center), PSDs (right).

Table 8.5: 3D-printed scaled WT blade random test: AKF and the A-AKF input prediction errors

	Conventional AKF	A-AKF
TRAC	0.004	0.001
FRAC	0.005	0.002

This case study leaves ample room for future developments as it demonstrates that the A-AKF i) allows for extremely accurate response estimation and ii) provides a good input amplitude prediction but iii) fails to accurately estimate the frequency content of the actual load. Improvements could be introduced by extending the applicability of the A-AKF for mixed observations sets, i.e., including both strains and accelerations. Additionally, alternative error estimates could be explored to be employed within the A-AKF algorithm with the purpose of avoiding the low frequency distortions arising from the averaging effect of the current error metric.

8.2.1.2 Input-response estimation through the Augmented Kalman Filter and the Gaussian Process Latent Force Model

This subsection treats the use of the GP-based approach in Alg. 14 for input-state estimation during random tests of the 3D-printed scaled WT blade. To check the effectiveness of the method, results are compared with predictions produced by the more conventional AKF in the same working conditions. A first comparison between the AKF and the GPLFM is provided under the assumption of availability of both strain and acceleration measurements. Next, focus is placed on the use of the GPLFM for response and load prediction in presence of acceleration-only measurements. An acceleration measurement collocated with the unknown force has been included in the observations set for both the studies presented in this paper since it allows for more accurate load predictions. This is justified by the force directly contributing to the acceleration at the same location via the direct feedthrough term.

GPLFM and AKF predictions via a mixed observations set

This subsection compares the GPLFM and the AKF input-state estimation results obtained using the mixed observations set (strain and acceleration) reported in Tab. 8.6. The chosen values for the necessary initial conditions and the process and measurement noise covariance matrices are also shown. The latter has been retrieved from the background noise recorded by sensors during

tests, while the first has been instead tuned by trial and error. For the AKF, the process noise covariance values associated to the states and the input are highlighted. To the contrary, the states process noise covariance and the GP covariance function initial hyperparameters are presented for the GPLFM.

Table 8.6: 3D-printed scaled WT blade random test: AKF and GPLFM observations sets and initialization values for a mixed observations set

Estimator	Observations	Initial state mean	Initial error cov. matrix	Input noise cov./ initial hyperparameters	Process noise cov. matrix ($\mathbf{Q}$)	Measurement noise cov. matrix ($\mathbf{R}$)
AKF	1, 3, 8,12, 15, 18, 21, 22	$\hat{\mathbf{x}}^a_{0\|0} = \mathbf{0}$	$\hat{\mathbf{P}}^a_{0\|0} = 10^{-10} \times \mathbf{I}$	$\mathbf{Q}^u = 10^{13} \times \mathbf{I}$	$\mathbf{Q} = 10^{-10} \times \mathbf{I}$	$\mathbf{R}_{\text{strain}} = 10^{-14} \times \mathbf{I}$ $\mathbf{R}_{\text{acc}} = 10^{-7} \times \mathbf{I}$
GPLFM	1, 3, 8, 12, 15, 18, 21, 22	$\hat{\mathbf{x}}^a_{0\|0} = \mathbf{0}$	$\hat{\mathbf{P}}^x_{0\|0} = 10^{-10} \times \mathbf{I}$	$\sigma^2 = 3 \times 10^1$ $l = 1 \times 10^{-4}$	$\mathbf{Q} = 10^{-10} \times \mathbf{I}$	$\mathbf{R}_{\text{strain}} = 10^{-14} \times \mathbf{I}$ $\mathbf{R}_{\text{acc}} = 10^{-7} \times \mathbf{I}$

Figure 8.13 shows a comparison in both time and frequency domains between the actual force and the input predictions obtained via the AKF and the GPLFM. A quantification of the input estimations accuracy in time and frequency domains is respectively reported in Tabs. 8.8 and 8.10 (last column) by means of the TRAC and FRAC estimators. From the results reported in Figs. 8.13, 8.8 and 8.10, it can be concluded that both the hereby analyzed estimators provide an accurate input estimation when a mix of strain and acceleration sensors are adopted as measurements. The slightly lower TRAC and FRAC values for the GPLFM input prediction are caused by the discrepancy between the measured and the GPLFM estimated PSD below 100 Hz.

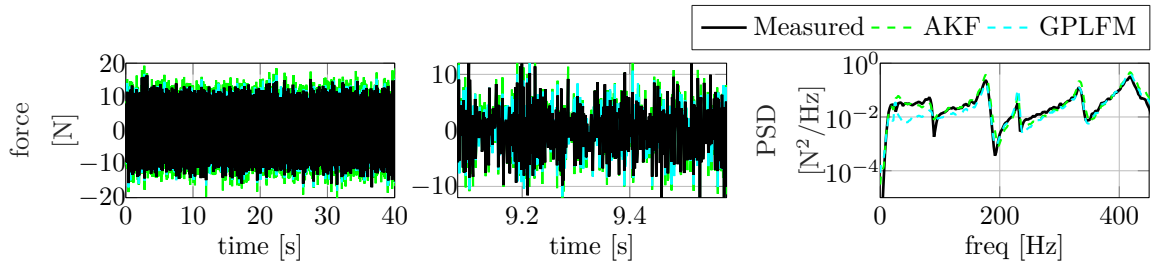

Figure 8.13: 3D-printed scaled WT blade random test: measured (black) and estimated (AKF - green, GPLFM - cyan via a mixed observations set) force signals

Figures 8.14 and 8.15 present the comparison between measured and estimated signals respectively for a strain and an accelerometer that are not included in the observations set. These results demonstrate that a good and comparable prediction accuracy can be achieved by the AKF and the GPLFM for both strain and acceleration predictions. An overall information regarding the response estimation precision is reported in Tables 8.7-8.10 respectively by means of the TRAC and FRAC values. The presented indicators show high values for both strain and acceleration response, confirming the results proposed in Figs. 8.14 and 8.15. Additionally, Fig. 8.16 reports a comparison of the measured RMS trend for the entire set of responses (strain gauges-left, accelerometers-right) with the RMS trends of the signals estimated at the same locations by means of the AKF and the GPLFM. From the visual information provided in Fig. 8.16 it can be concluded that the response estimation obtained via the two estimators are also comparable in terms of amplitude, with a slightly lower AKF accuracy detectable for some of the strain responses (e.g. strain sensors 5,7,8,9).

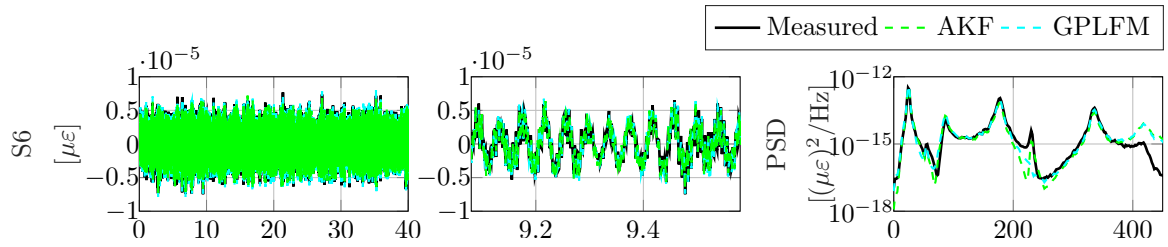

Figure 8.14: 3D-printed scaled WT blade random test: measured (black) and estimated (AKF - green, GPLFM - cyan via a mixed observations set) strain at location 6

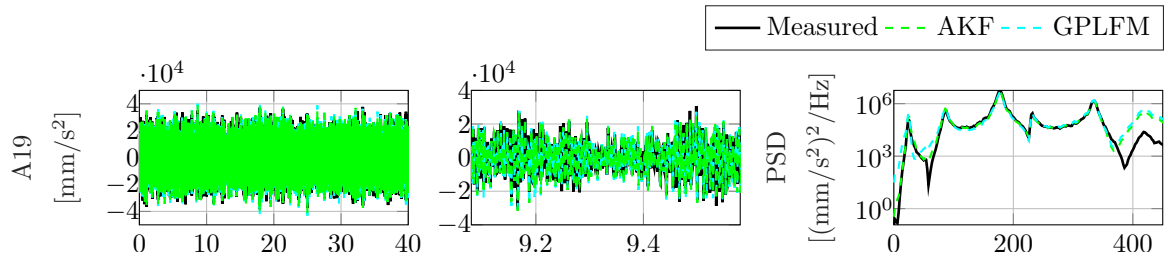

Figure 8.15: 3D-printed scaled WT blade random test: measured (black) and estimated (AKF - green, GPLFM - cyan via a mixed observations set) acceleration at location 19

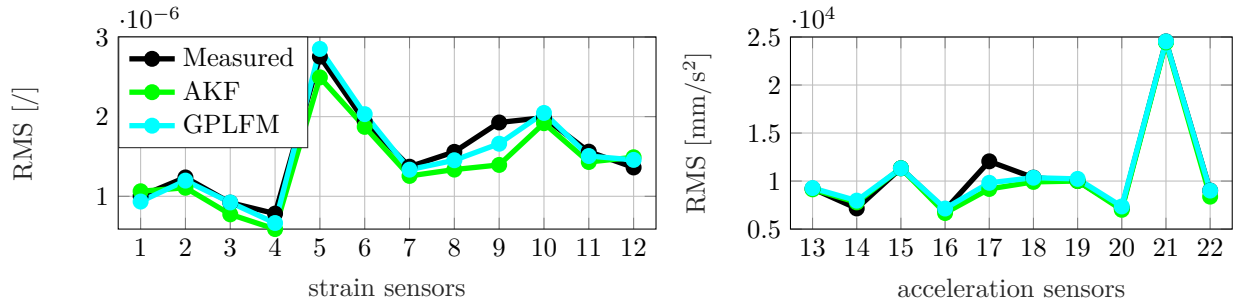

Figure 8.16: 3D-printed scaled WT blade random test: measured (black) and estimated (AKF - green, GPLFM - cyan via a mixed observations set) strain (left) and acceleration (right) responses RMS values

Table 8.7: 3D-printed scaled WT blade random test: TRAC values between measured and estimated (AKF and GPLFM via a mixed observations set) strain responses. Observations are underlined.

Estimator	1	2	3	4	5	6	7	8	9	10	11	12
AKF	0.948	0.828	0.897	0.834	0.903	0.898	0.959	0.969	0.969	0.834	0.984	0.949
GPLFM	0.985	0.691	0.995	0.880	0.746	0.938	0.965	0.997	0.969	0.745	0.960	0.983

Table 8.8: 3D-printed scaled WT blade random test: TRAC values between measured and estimated (AKF and GPLFM via a mixed observations set) force and acceleration responses. Observations are underlined.

Estimator	13	14	15	16	17	18	19	20	21	22	**force**
AKF	0.916	0.517	1.000	0.300	0.125	0.995	0.913	0.635	0.999	0.993	0.910
GPLFM	0.919	0.563	1.000	0.314	0.048	1.000	0.865	0.578	1.000	1.000	0.870

Table 8.9: 3D-printed scaled WT blade random test: FRAC values between measured and estimated (AKF and GPLFM via a mixed observations set) strain responses. Observations are underlined.

Estimator	1	2	3	4	5	6	7	8	9	10	11	12
AKF	0.943	0.885	0.974	0.934	0.869	0.962	0.969	0.977	0.986	0.928	0.991	0.996
GPLFM	0.995	0.840	0.999	0.996	0.788	0.974	0.987	0.999	0.972	0.899	0.989	0.996

Table 8.10: 3D-printed scaled WT blade random test: FRAC values between measured and estimated (AKF and GPLFM via a mixed observations set) force and acceleration responses. Observations are underlined.

Estimator	13	14	15	16	17	18	19	20	21	22	**force**
AKF	0.986	0.259	1.000	0.105	0.698	0.991	0.986	0.887	1.000	0.979	0.967
GPLFM	0.971	0.304	1.000	0.107	0.703	1.000	0.956	0.827	1.000	1.000	0.931

GPLFM and AKF predictions via acceleration-only measurements

This subsection presents the GPLFM and the AKF input-state estimation results obtained using the acceleration-only measurements set shown in Tab. 8.11. Table 8.11 also reports the adopted values for the estimators initial conditions, the process and measurement noise covariance matrices and the tuned GP covariance hyperparameters.

Table 8.11: 3D-printed scaled WT blade random test: AKF and GPLFM observations sets and initialization values for an acceleration-based observations set

Estimator	Observations	Initial state mean	Initial error cov. matrix	Input noise cov./ initial hyperparameters	Process noise cov. matrix ($\mathbf{Q}$)	Measurement noise cov. matrix ($\mathbf{R}$)
AKF	15, 18, 21, 22	$\hat{\mathbf{x}}^a_{0\|0} = \mathbf{0}$	$\hat{\mathbf{P}}^a_{0\|0} = 10^{-10} \times \mathbf{I}$	$\mathbf{Q}^u = 10^{13} \times \mathbf{I}$	$\mathbf{Q} = 10^{-10} \times \mathbf{I}$	$\mathbf{R}_{\text{acc}} = 10^{-7} \times \mathbf{I}$
GPLFM	15, 18, 21, 22	$\hat{\mathbf{x}}^a_{0\|0} = \mathbf{0}$	$\hat{\mathbf{P}}^x_{0\|0} = 10^{-10} \times \mathbf{I}$	$\sigma^2 = 6 \times 10^1$ $l = 1 \times 10^{-4}$	$\mathbf{Q} = 10^{-10} \times \mathbf{I}$	$\mathbf{R}_{\text{acc}} = 10^{-7} \times \mathbf{I}$

Figure 8.17 shows a comparison in both time and frequency domains between the actual force and the input predictions obtained via the AKF and the GPLFM. From both the time histories and the PSD plots, it can be concluded that the GPLFM provides a good load prediction for the analyzed data set. To the contrary, the AKF estimation suffers from the low frequency drift caused by the unobservability condition in absence of displacement-level sensors. The previous statement is confirmed by the TRAC and FRAC values associated to the AKF and GPLFM input estimations, respectively reported in Tabs. 8.13 and 8.15 (last column).

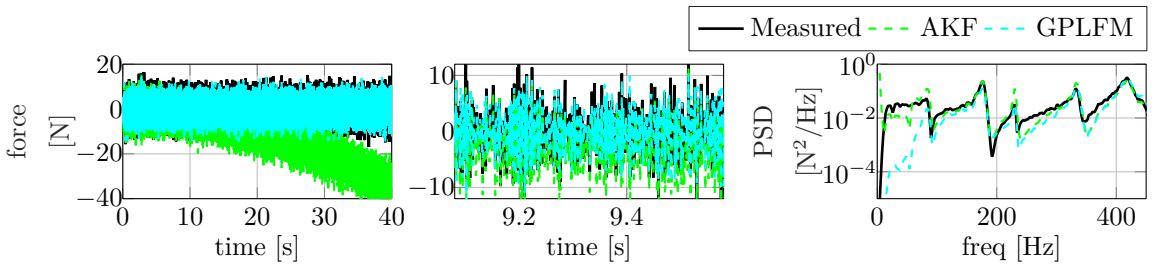

Figure 8.17: 3D-printed scaled WT blade random test: measured (black) and estimated (AKF - green, GPLFM - cyan via an acceleration-based observations set) force signals

Figures 8.18 and 8.19 show the comparison between measured and estimated signals (AKF - green, GPLFM - cyan) respectively for a strain and an accelerometer that are not included in

the observations set. From the presented results, it can be concluded that the GPLFM provides a good prediction accuracy for both the strain and the acceleration response even in presence of accelerations-only measurements. The AKF instead, generates a sufficiently good estimation for the acceleration response while the strain response is affected by a large low frequency drift. This behavior is confirmed by the overall information regarding the response estimation precision reported in Tabs. 8.12-8.15 in both time and frequency domains. High values are manifested for both strain and acceleration response in the GPLFM case, while the AKF produces sufficiently large values for accelerations but very low values for strain signals.

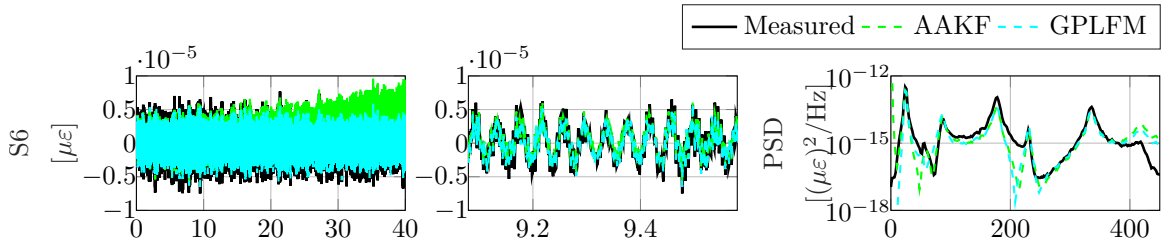

Figure 8.18: 3D-printed scaled WT blade random test: measured (black) and estimated (AKF - green, GPLFM - cyan via an acceleration-based observations set) strain at location 6

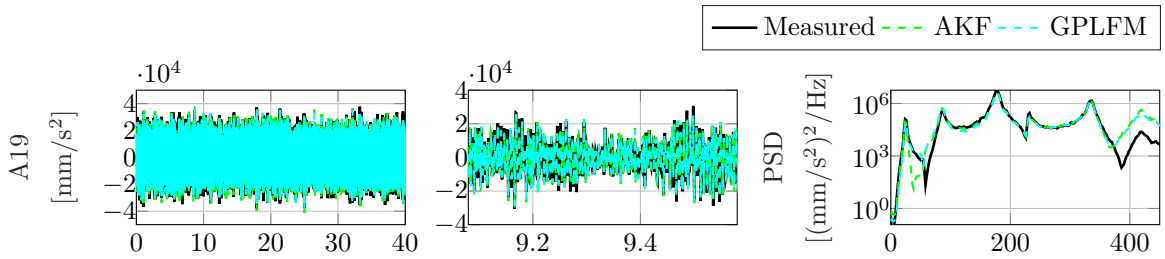

Figure 8.19: 3D-printed scaled WT blade random test: measured (black) and estimated (AKF - green, GPLFM - cyan via an acceleration-based observations set) acceleration at location 19

The RMS trend comparison for the acceleration-only case is shown in Fig. 8.20 for strains (left) and accelerations (right). Figure 8.20 demonstrates that the response estimation obtained via the two estimators is comparable in terms of accelerations RMS but not for the strains, for which the AKF provides a large RMS overestimation.

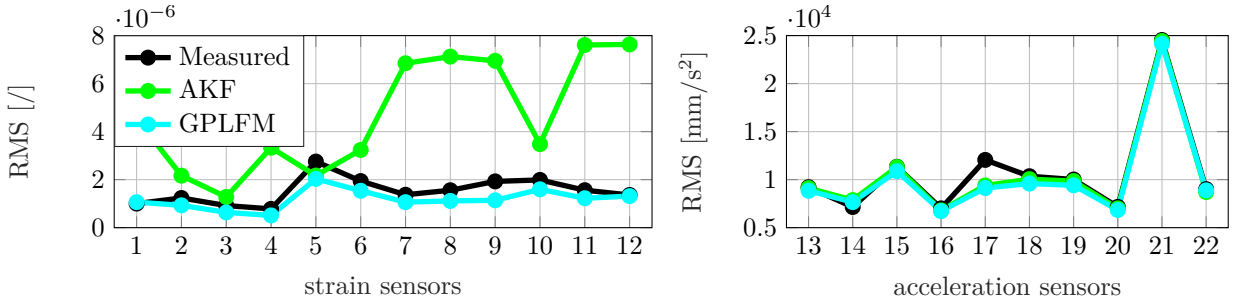

Figure 8.20: 3D-printed scaled WT blade random test: measured (black) and estimated (AKF - green, GPLFM - cyan via an acceleration-based observations set) strain (left) and acceleration (right) responses RMS values

The comparison provided in this paragraph between the GP-based approach and the AKF shows that the GPLFM allows for load and response estimations which are comparable to those delivered by the AKF under the mixed measurements assumption. This confirms that the GP-based approach represents an accurate, more flexible and user-independent alternative to standard VS methods. The GPLFM proves good estimation capabilities also for the acceleration-only measurements scenario.

Table 8.12: 3D-printed scaled WT blade random test: TRAC values between measured and estimated (AKF and GPLFM via an acceleration-based observations set) strain responses. Observations are underlined.

Estimator	1	2	3	4	5	6	7	8	9	10	11	12
AKF	0.069	0.159	0.172	0.017	0.926	0.190	0.026	0.029	0.032	0.183	0.033	0.036
GPLFM	0.739	0.729	0.703	0.529	0.773	0.802	0.714	0.643	0.676	0.775	0.747	0.613

Table 8.13: 3D-printed scaled WT blade random test: TRAC values between measured and estimated (AKF and GPLFM via an acceleration-based observations set) force and acceleration responses. Observations are underlined.

Estimator	13	14	15	16	17	18	19	20	21	22	**force**
AKF	0.913	0.494	1.000	0.303	0.092	0.998	0.902	0.594	1.000	0.997	0.040
GPLFM	0.913	0.510	0.998	0.306	0.081	0.993	0.920	0.567	0.997	1.000	0.635

Table 8.14: 3D-printed scaled WT blade random test: FRAC values between measured and estimated (AKF and GPLFM via an acceleration-based observations set) strain responses. Observations are underlined.

Estimator	1	2	3	4	5	6	7	8	9	10	11	12
AKF	6.67e-04	6.99e-03	0.013	1.30e-04	0.991	0.011	1.44e-04	9.89e-05	8.57e-05	9.66e-03	1.89e-04	1.95e-04
GPLFM	0.887	0.821	0.970	0.835	0.920	0.953	0.895	0.799	0.780	0.890	0.942	0.905

Table 8.15: 3D-printed scaled WT blade random test: FRAC values between measured and estimated (AKF and GPLFM via an acceleration-based observations set) force and acceleration responses. Observations are underlined.

Estimator	13	14	15	16	17	18	19	20	21	22	**force**
AKF	0.984	0.239	1.000	0.105	0.710	0.997	0.982	0.851	1.000	0.990	4.85e-05
GPLFM	0.987	0.261	0.996	0.103	0.706	0.992	0.986	0.840	1.000	0.999	0.906

In the latter, the GP-based algorithm is superior to the AKF, which normally generates predictions affected by a low frequency drift due to unobservability.

8.2.2 Pull and release test

This subsection proposes the use of VS techniques for the estimation of the quantities of interest during the pull and release tests performed on the 3D-printed scaled WT blade. Specifically, the use of the GP-based approach formulated in Alg. 14 is hereby validated for WT blades pull and release testing by comparing it against two state-of-the-art estimators, i.e., the AKF and DKF, on the task of input-state estimation. The hereby adopted estimators have been employed for input-state prediction using the mixed observations set (strain and acceleration) reported in Tab. 8.16, where the sensors numbers refer to the layout in Fig. 8.3. The measurements acquired at the remaining locations have been used to validate the estimations provided by the investigated methods. The chosen values for the necessary initial conditions and the process and measurement noise covariance matrices are also shown in Tab. 8.16. During pull and release tests, the applied static load (blade weight + external mass) determines initial deformation of the blade, thus causing a non-zero initial condition for the states. However, being the applied mass "unknown" for the estimators, no information can be retrieved regarding the initial state vector. Hence, the latter is set to be equal to a vector $\boldsymbol{\eta}$ containing only the blade deformation under its own weight. The initial condition related to the unknown load is instead set to zero for all the three analyzed estimators. The measurement noise has been retrieved from the background noise recorded by sensors during tests, while the

process noise covariance matrix has been tuned by trial and error. For the AKF and the DKF, the process noise covariance values associated to the states and the input are highlighted. To the contrary, the states process noise covariance and the GP covariance function initial hyperparameters are presented for the GP-based approach. For this application, a common Matérn covariance function with smoothness parameter $\nu = 2.5$ (Fig. 2.7) has been adopted for building the GPLFM which will serve for the estimation.

Table 8.16: 3D-printed scaled WT blade pull and release test: AKF, DKF and GPLFM observations sets and initialization values

Algorithm	Observations	Initial state mean	Initial error cov. matrix	Input noise cov./ initial hyperparameters	Process noise cov. matrix ($\mathbf{Q}$)	Measurement noise cov. matrix ($\mathbf{R}$)
AKF	1, 3, 8, 15, 17, 21	$\hat{\mathbf{x}}^a_{0\|0} = \begin{bmatrix} \boldsymbol{\eta} \\ \mathbf{0} \end{bmatrix}$	$\hat{\mathbf{P}}^a_{0\|0} = 10^{-10} \times \mathbf{I}$	$\mathbf{Q}^u = 10^{15} \times \mathbf{I}$	$\mathbf{Q} = 10^{-20} \times \mathbf{I}$	$\mathbf{R}_{\text{strain}} = 10^{-14} \times \mathbf{I}$ $\mathbf{R}_{\text{acc}} = 10^{-7} \times \mathbf{I}$
DKF	1, 3, 8, 15, 17, 21	$\hat{\mathbf{x}}_{0\|0} = \boldsymbol{\eta}$ $\hat{\mathbf{u}}_{0\|0} = \mathbf{0}$	$\hat{\mathbf{P}}^x_{0\|0} = 10^{-10} \times \mathbf{I}$ $\hat{\mathbf{P}}^u_{0\|0} = 10^{-10} \times \mathbf{I}$	$\mathbf{Q}^u = 10^{11} \times \mathbf{I}$	$\mathbf{Q} = 10^{-11} \times \mathbf{I}$	$\mathbf{R}_{\text{strain}} = 10^{-14} \times \mathbf{I}$ $\mathbf{R}_{\text{acc}} = 10^{-7} \times \mathbf{I}$
GPLFM	1, 3, 8, 15, 17, 21	$\hat{\mathbf{x}}^a_{0\|0} = \begin{bmatrix} \boldsymbol{\eta} \\ \mathbf{0} \end{bmatrix}$	$\hat{\mathbf{P}}^x_{0\|0} = 10^{-10} \times \mathbf{I}$	$\sigma^2 = 2.2 \times 10^3$ $l = 9 \times 10^{-2}$	$\mathbf{Q} = 10^{-8} \times \mathbf{I}$	$\mathbf{R}_{\text{strain}} = 10^{-14} \times \mathbf{I}$ $\mathbf{R}_{\text{acc}} = 10^{-7} \times \mathbf{I}$

Figure 8.21 offers the predicted input signals provided by each estimator and compares them against the "measured" force, i.e., the step-type of input reconstructed on the basis of the known weight of the mass in Fig. 8.4. Table 8.17 presents the SE and the SD inaccuracy indicators, already adopted in Chapter 7, for the three analyzed algorithms.
Figure 8.21 and Tab. 8.17 highlight that the the three analyzed estimators can easily detect the release instant. However, the AKF provides higher SE and SD. The latter indicator quantitatively expresses the oscillations around the zero mean value that affect the estimated time history after the blade release. While both the AKF and DKF provide larger oscillations, the GP-based approach, conventionally implemented via a Matérn covariance function, damps them more efficiently. It is therefore concluded that the GP-based method outperforms the hereby analyzed conventional approaches on the input estimation task during pull and release tests.

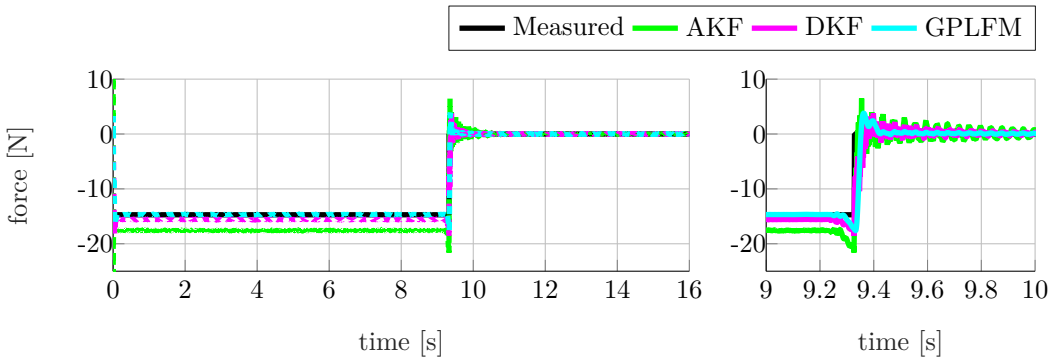

Figure 8.21: 3D-printed scaled WT blade pull and release test: input "measured" (black) and estimated (AKF - green, DKF - magenta, GPLFM - cyan) time histories (left) and detailed time histories (right)

Table 8.17: 3D-printed scaled WT blade pull and release test: input prediction errors for the AKF, the DKF and the GPLFM

	AKF	DKF	GPLFM
SE	$1.44N$	$0.44N$	$0.026N$
SD	$0.24N$	$0.15N$	$0.10N$

Figures 8.22 and 8.23 show the responses estimated by the algorithms of study for strain gauge 10 and accelerometer 14 in time and frequency domain. The predictive capabilities of the three estimators are proved by comparing their predictions against the corresponding measured signals. However, the produced time signals are affected by i) high frequency mismatches for the AKF predictions and ii) incorrect static contribution for the DKF and the GP-based approach.

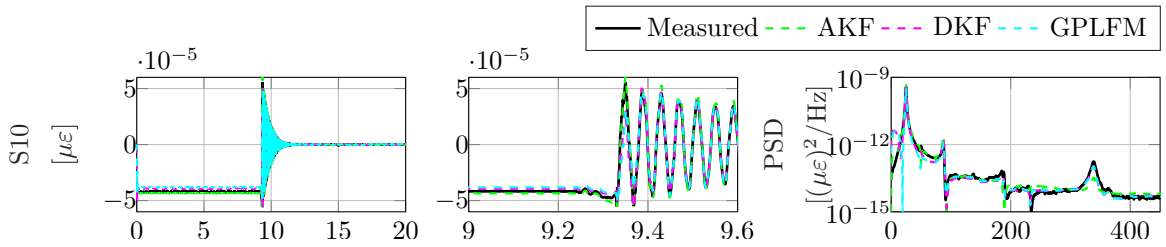

Figure 8.22: 3D-printed scaled WT blade pull and release test: measured (black) and estimated (AKF - green, DKF - magenta, GPLFM - cyan) strain at location 10

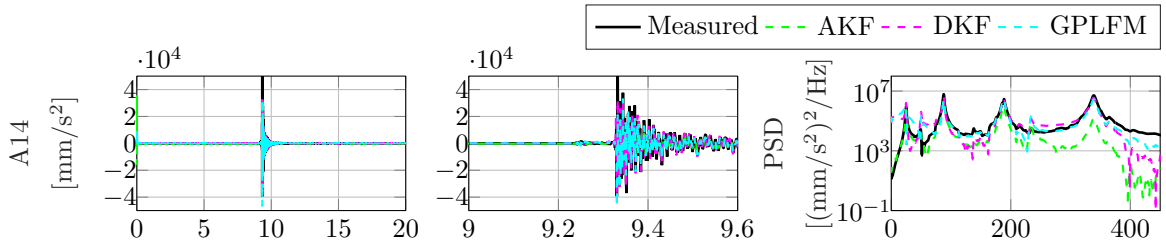

Figure 8.23: 3D-printed scaled WT blade pull and release test: measured (black) and estimated (AKF - green, DKF - magenta, GPLFM - cyan) acceleration at location 14

The TRAC and FRAC quality indicators described in Section 11.1 are hereby adopted to provide a complete evaluation of the global response estimation accuracy achieved by the studied estimators, respectively in time and frequency domain. For the analyzed case study, the entire time length of the recorded signals has been used for the TRAC computation and the frequency range 0-450 Hz has been adopted for the FRAC computation. Tables 8.18 and 8.19 provide the TRAC values for the entire set of estimated responses (respectively strain and acceleration) produced by the three algorithms. The FRAC values for the strain and acceleration responses are instead offered in Tabs. 8.20 and 8.21. The analysis of the TRAC and FRAC indicators confirms that the three hereby analyzed approaches allow for accurate strain and acceleration prediction and does not highlight any particular difference between the results achieved via the different approaches.

Table 8.18: 3D-printed scaled WT blade pull and release test: TRAC values between measured and estimated (AKF, DKF and GPLFM) strain responses. Observations are underlined.

Estimator	1	2	3	4	5	6	7	8	9	10	11	12
AKF	1.000	1.000	1.000	0.999	1.000	1.000	1.000	0.999	0.996	1.000	1.000	0.999
DKF	0.997	0.997	0.997	0.997	0.997	0.997	0.997	0.997	0.993	0.997	0.997	0.997
GPLFM	0.998	0.997	0.997	0.997	0.997	0.997	0.997	0.997	0.994	0.997	0.998	0.997

Table 8.19: 3D-printed scaled WT blade pull and release test: TRAC values between measured and estimated (AKF, DKF and GPLFM) acceleration responses. Observations are underlined.

Estimator	13	14	15	16	17	18	19	20	21
AKF	0.201	0.423	0.900	0.897	0.891	0.864	0.680	0.786	0.997
DKF	0.506	0.677	1.000	0.960	1.000	0.967	0.624	0.823	1.000
GPLFM	0.558	0.711	0.962	0.936	0.981	0.933	0.643	0.837	1.000

Table 8.20: 3D-printed scaled WT blade pull and release test: FRAC values between measured and estimated (AKF, DKF and GPLFM) strain responses. Observations are underlined.

Estimator	1	2	3	4	5	6	7	8	9	10	11	12
AKF	0.998	1.000	1.000	1.000	0.999	1.000	1.000	1.000	0.999	1.000	1.000	1.000
DKF	0.996	0.998	0.999	0.999	0.994	0.999	0.999	0.999	0.999	0.998	0.999	0.999
GPLFM	0.993	0.990	0.994	0.997	0.970	0.992	0.996	0.997	0.996	0.990	0.995	0.997

Table 8.21: 3D-printed scaled WT blade pull and release test: FRAC values between measured and estimated (AKF, DKF and GPLFM) acceleration responses. Observations are underlined.

Estimator	13	14	15	16	17	18	19	20	21
AKF	0.190	0.446	0.989	0.979	0.969	0.938	0.991	0.993	0.998
DKF	0.929	0.963	1.000	0.991	1.000	0.985	0.978	0.993	1.000
GPLFM	0.835	0.905	0.996	0.991	0.999	0.986	0.847	0.811	1.000

An overall information regarding the amplitude estimation accuracy is instead provided by Fig. 8.24, where the measured RMS trend for the entire set of responses (strain gauges - left, accelerations - right) is plotted as reference for validating the RMS trends of the signals estimated at the same locations by means of the investigated algorithms. These plots demonstrate that an analogous response amplitude estimation performance is globally achieved by the three estimators.

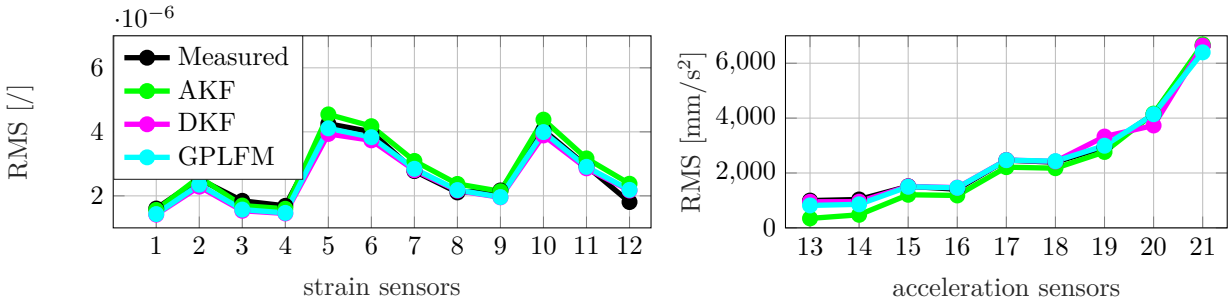

Figure 8.24: 3D-printed scaled WT blade pull and release test: measured (black) and estimated (AKF - green, DKF - magenta, GPLFM - cyan) strain (left) and acceleration (right) responses RMS values.

8.3 Covariance functions for joint input-state estimation via Gaussian Process Latent Force Models

This section offers an experimental validation of the ad hoc covariance function selection proposed in this dissertation for input-state estimation via GPLFMs. By proposing a 3DOFs exampled, Subsubsection 5.2.1.1 has proved that a proper covariance function selection plays an important role

within the use of GPLFMs for estimating unknown loads and unmeasured structural responses in a Bayesian setting. In this section, three different loading conditions adopted during the 3D-printed scaled WT blade tests are treated: pull and release, random and sinusoidal load. For each loading condition, the most suitable covariance function is proposed in contrast to a conventional Matérn covariance function for construction of the LFM to be coupled with the scaled WT blade SSM. It is worth noting that i) the filtering-only version is hereby adopted for the GPLFM and ii) a single measurement is used for the training phase instead of the entire observations set. As mentioned in Subsection 5.2.1, the most convenient choice for the time signal to be used for training consists in adopting a pre-recorded measurement collocated with the unknown input. Specifically, an acceleration signal is ideal for the random and sinusoidal load cases, while a displacement-level sensor, i.e., a strain signal, is preferred for the pull and release loading condition.

8.3.1 Pull and release test

This subsection proposes the use of a biased quasiperiodic covariance function for the GP adopted to construct the LFM for input-state estimation during the pull and release test performed on the 3D-printed scaled WT blade. The ad hoc covariance function selection is validated by comparing the estimation results against the ones achieved by making use of a biased exponential (equivalent to a Matérn function with $\nu = 0.5$) covariance function. It is worth noting that biased covariance functions are hereby adopted to include a prior assumption on the static nature of the applied load. This is in contrast with Subsection 8.2.2, where the same pull and release test is treated from a joint input-state estimation perspective via a conventional Matérn covariance function. This discrepancy is justified by the nature of the signals involved in the covariance function hyperparameters training: while in Subsection 8.2.2 the entire set of observations, i.e., strain and acceleration signals, has been used for training, a single strain measurement is hereby adopted for the same purpose. The use of an unbiased Matérn covariance function thus provides a reasonable input prediction in Subsection 8.2.2 thanks to the presence of acceleration responses within the training data, which reduce the need of a biased covariance function for regression. To the contrary, the latter is necessary when a unique response featuring a static component is employed for training. Specifically, sensor 1 has been hereby selected for training since no strain response collocated with the unknown load (applied at the tip) was available for this loading scenario. The hereby adopted estimators have been employed for input-state prediction using the mixed observations set (strain and acceleration) reported in Tab. 8.22. The measurements acquired at the remaining locations have been used to validate the estimations provided by the investigated methods. The chosen values for the necessary initial conditions, the states process noise covariance and the measurement noise covariance matrices are also shown in Tab. 8.22. Additionally, the analyzed GP covariance functions initial hyperparameters are presented in Tab. 8.22.

Table 8.22: 3D-printed scaled WT blade pull and release test: GPLFMs observations sets and initialization values for a biased exponential and a biased quasiperiodic covariance function

Algorithm	Observations	Initial state mean	Initial error cov. matrix	Initial hyperparameters	Process noise cov. matrix ($\mathbf{Q}$)	Measurement noise cov. matrix ($\mathbf{R}$)
Biased exponential	1, 3, 8, 15, 17, 21	$\hat{\mathbf{x}}^a_{0\|0} = \begin{bmatrix} \boldsymbol{\eta} \\ \mathbf{0} \end{bmatrix}$	$\hat{\mathbf{P}}^x_{0\|0} = 10^{-10} \times \mathbf{I}$	$\sigma^2 = 1.5$ $\sigma^2_{constant} = 1.1 \times 10^{-1}$ $l = 1 \times 10^{-1}$	$\mathbf{Q}_{displ} = 10^{-15} \times \mathbf{I}$ $\mathbf{Q}_{vel} = 10^{-7} \times \mathbf{I}$	$\mathbf{R}_{\text{strain}} = 10^{-14} \times \mathbf{I}$ $\mathbf{R}_{\text{acc}} = 10^{-7} \times \mathbf{I}$
Biased quasiperiodic	1, 3, 8, 15, 17, 21	$\hat{\mathbf{x}}^a_{0\|0} = \begin{bmatrix} \boldsymbol{\eta} \\ \mathbf{0} \end{bmatrix}$	$\hat{\mathbf{P}}^x_{0\|0} = 10^{-10} \times \mathbf{I}$	$\sigma^2 = 2 \times 10^{-1}$ $\sigma^2_{constant} = 2 \times 10^{-1}$ $l = 3 \times 10^{-1}$ $t_{period} = 4 \times 10^{-2}$ $l_{matern} = 10^{-1}$	$\mathbf{Q}_{displ} = 10^{-15} \times \mathbf{I}$ $\mathbf{Q}_{vel} = 10^{-7} \times \mathbf{I}$	$\mathbf{R}_{\text{strain}} = 10^{-14} \times \mathbf{I}$ $\mathbf{R}_{\text{acc}} = 10^{-7} \times \mathbf{I}$

Figure 8.25 offers the predicted input signals provided by the GP-based approach when the two investigated covariance functions are adopted. Predictions are compared against the “measured”

force, i.e., the step-type of input reconstructed on the basis of the known weight of the mass in Fig. 8.4. Table 8.23 presents the SE and the SD inaccuracy indicators for the two analyzed cases. Figure 8.25 highlights that the GPLFM with both the proposed covariance functions can easily detect the initial static load with limited inaccuracy. However, while the biased quasiperiodic covariance function allows for a correct detection of the release instant, the biased exponential covariance function produces a time history which does not follow the instantaneous release. Indeed, the estimated signal features a slow decay to zero which is reflected in both high SE and SD. It is therefore concluded that the use of a biased quasiperiodic covariance function to construct the GPLFM outperforms the biased exponential covariance function on the input estimation task during pull and release tests on the scaled WT blade.

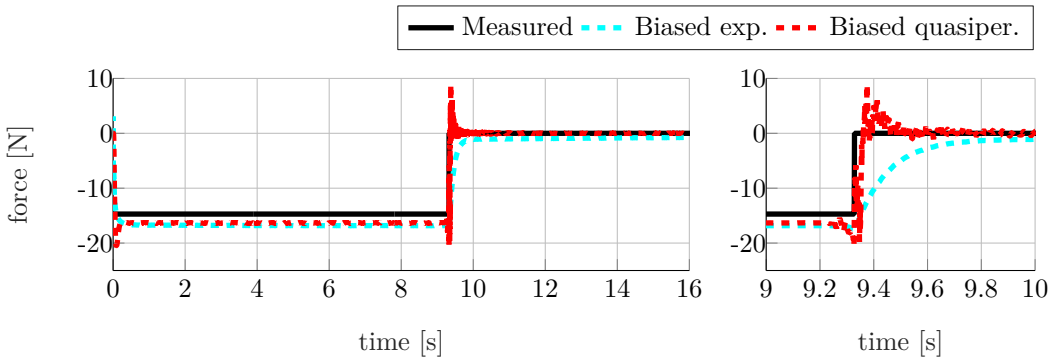

Figure 8.25: 3D-printed scaled WT blade pull and release test: input "measured" (black) and estimated (GPLFM with biased exponential cov. - cyan, GPLFM with biased quasiperiodic cov. - red) time histories (left) and detailed time histories (right)

Table 8.23: 3D-printed scaled WT blade pull and release test: input prediction errors for the GPLFM with biased exponential and biased quasiperiodic covariance functions

	Biased exponential	Biased quasiperiodic
SE	$11.23N$	$1.06N$
SD	$1.91N$	$0.20N$

Figures 8.26 and 8.27 show the time and frequency content of the responses estimated by the GPLFM algorithm for strain gauge 10 and accelerometer 14 when the analyzed covariance functions are used. In both cases, the estimated signals match their measured counterparts with relatively high accuracy. This conclusion is confirmed by Fig. 8.28 which compares the amplitude (RMS) of the entire set of responses predicted when the two covariance functions are used, against the measured signals RMS values. Indeed, Fig. 8.28 highlights a comparable behavior between the two analyzed scenarios in terms of amplitude estimation. A more detailed time domain analysis of

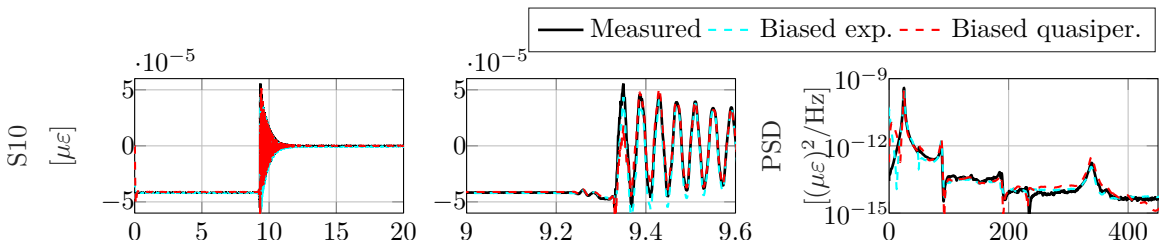

Figure 8.26: 3D-printed scaled WT blade pull and release test: measured (black) and estimated (GPLFM with biased exponential cov. - cyan, GPLFM with biased quasiperiodic cov. - red) strain at location 10

the prediction results is offered in Tabs. 8.24 and 8.25 via the TRAC values for the entire set of estimated responses (respectively strain and acceleration). The FRAC values for the strain and acceleration responses are instead offered in Tabs. 8.26 and 8.27 respectively. The analysis of the

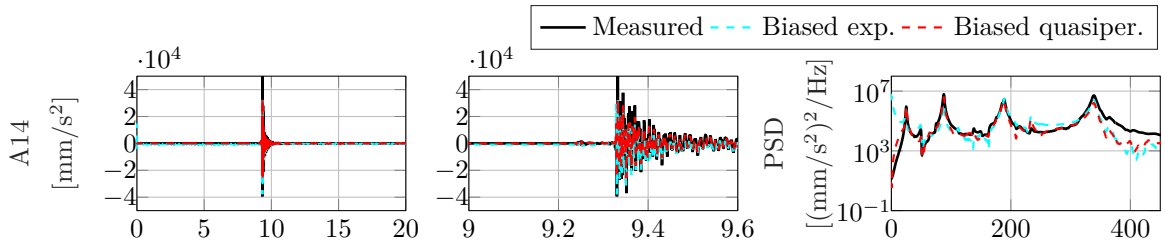

Figure 8.27: 3D-printed scaled WT blade pull and release test: measured (black) and estimated (GPLFM with biased exponential cov. - cyan, GPLFM with biased quasiperiodic cov. - red) acceleration at location 14

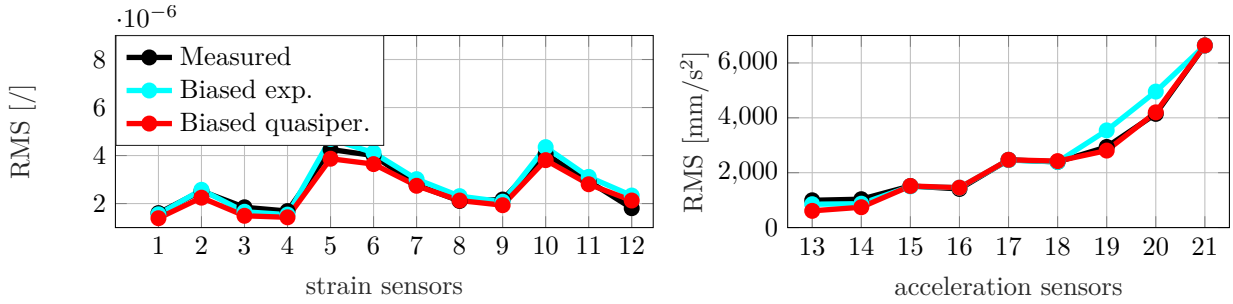

Figure 8.28: 3D-printed scaled WT blade pull and release test: measured (black) and estimated (GPLFM with biased exponential cov. - cyan, GPLFM with biased quasiperiodic cov. - red) strain (left) and acceleration (right) responses RMS values.

TRAC and FRAC indicators shows that, while a similar result is achieved in terms of strain response estimation, the accuracy of acceleration response prediction is substantially higher when adopting a biased quasiperiodic covariance function. This is also demonstrated by the frequency content provided in Fig. 8.27, where a low frequency component erroneously affects the signal estimated by the biased exponential covariance function. To the contrary, the biased quasiperiodic covariance function produces a PSD which matches the measured signal in the entire reported frequency range (including low frequency).

Table 8.24: 3D-printed scaled WT blade pull and release test: TRAC values between measured and estimated (GPLFM with biased exponential and biased quasiperiodic covariance functions) strain responses. Observations are underlined.

Estimator	1	2	3	4	5	6	7	8	9	10	11	12
Biased exponential	0.997	0.997	0.998	0.998	0.996	0.998	0.998	0.998	0.995	0.997	0.998	0.998
Biased quasiperiodic	0.994	0.995	0.995	0.994	0.995	0.995	0.995	0.993	0.989	0.995	0.995	0.995

Table 8.25: 3D-printed scaled WT blade pull and release test: TRAC values between measured and estimated (GPLFM with biased exponential and biased quasiperiodic covariance functions) acceleration responses. Observations are underlined.

Estimator	13	14	15	16	17	18	19	20	21
Biased exponential	0.282	0.459	0.997	0.961	1.000	0.971	0.408	0.729	1.000
Biased quasiperiodic	0.762	0.866	1.000	0.961	1.000	0.973	0.904	0.931	1.000

8.3.2 Random test

This subsection proposes the use of a Wiener covariance function for the GP adopted within the LFM constructed for input-state estimation during random tests performed on the 3D-printed scaled WT blade. The ad hoc covariance function selection is validated by comparing the estimation results

Table 8.26: 3D-printed scaled WT blade pull and release test: FRAC values between measured and estimated (GPLFM with biased exponential and biased quasiperiodic covariance functions) strain responses. Observations are underlined.

Estimator	1	2	3	4	5	6	7	8	9	10	11	12
Biased exponential	0.992	0.988	0.996	0.999	0.919	0.993	0.998	0.999	0.999	0.990	0.997	0.998
Biased quasiperiodic	0.982	0.991	0.994	0.997	0.972	0.993	0.996	0.997	0.997	0.992	0.995	0.996

Table 8.27: 3D-printed scaled WT blade pull and release test: FRAC values between measured and estimated (GPLFM with biased exponential and biased quasiperiodic covariance functions) acceleration responses. Observations are underlined.

Estimator	13	14	15	16	17	18	19	20	21
Biased exponential	0.445	0.604	1.000	0.991	1.000	0.984	0.481	0.954	1.000
Biased quasiperiodic	0.837	0.864	1.000	0.992	1.000	0.981	0.994	0.985	1.000

obtained using the mixed observations set (strain and acceleration) reported in Tab. 8.28 against the ones achieved by making use of a conventional Matérn covariance function ($\nu = 1.5$). The chosen values for the necessary initial conditions and the process and measurement noise covariance matrices are also summarized in Tab. 8.28. Additionally, the analyzed GP covariance functions initial hyperparameters are presented in Tab. 8.28. The hyperparameters have been tuned during the training phase by maximizing the log marginal likelihood of the acceleration collocated with the unknown input, i.e., at the shaker location indicated in Fig. 8.3. It is thus worth noting that the results presented in this section differ from the ones proposed for the mixed observations set in Subsubsection 8.2.1.2, where the entire set of observations has been used within the training step and a smoothness $\nu = 2.5$ has been chosen for the Matérn covariance function.

Table 8.28: 3D-printed scaled WT blade random test: GPLFMs observations sets and initialization values for a Matérn (ν=1.5) and a Wiener covariance function

Estimator	Observations	Initial state mean	Initial error cov. matrix	Initial hyperparameters	Process noise cov. matrix ($\mathbf{Q}$)	Measurement noise cov. matrix ($\mathbf{R}$)
Matérn	1, 3, 8,12, 15, 18, 21, 22	$\hat{\mathbf{x}}^a_{0\|0} = \mathbf{0}$	$\hat{\mathbf{P}}^a_{0\|0} = 10^{-10} \times \mathbf{I}$	$\sigma^2 = 3 \times 10^3$ $l = 2 \times 10^{-4}$	$\mathbf{Q}_{displ} = 10^{-20} \times \mathbf{I}$ $\mathbf{Q}_{vel} = 10^{-10} \times \mathbf{I}$	$\mathbf{R}_{\text{strain}} = 10^{-14} \times \mathbf{I}$ $\mathbf{R}_{\text{acc}} = 10^{-7} \times \mathbf{I}$
Wiener	1, 3, 8, 12, 15, 18, 21, 22	$\hat{\mathbf{x}}^a_{0\|0} = \mathbf{0}$	$\hat{\mathbf{P}}^x_{0\|0} = 10^{-10} \times \mathbf{I}$	$\sigma^2 = 3 \times 10^3$	$\mathbf{Q}_{displ} = 10^{-20} \times \mathbf{I}$ $\mathbf{Q}_{vel} = 10^{-10}$	$\mathbf{R}_{\text{strain}} = 10^{-14} \times \mathbf{I}$ $\mathbf{R}_{\text{acc}} = 10^{-7} \times \mathbf{I}$

Figure 8.29 offers a comparison in both time and frequency domains between the actual force and the input predictions obtained by adopting the GPLFM in combination with a Wiener and a Matérn covariance function ($\nu = 1.5$). A quantification of the input estimations accuracy in time and frequency domains is respectively reported in Tabs. 8.30 and 8.32 (last column) by means of the TRAC and FRAC estimators. From the results reported in Tabs. 8.30 and 8.32, it can be concluded that a Wiener covariance function allows for higher input estimation accuracy. Figure 8.29 indeed highlights that the Matérn covariance function generates a distorted frequency content between 0 and 100 Hz.

Figures 8.30 and 8.31 present the comparison between measured and estimated signals respectively for a strain and an accelerometer that are not included in the observations set. These results demonstrate that a good prediction accuracy can be achieved by the GPLFM for both strain and acceleration predictions when each of the two analyzed covariance functions is adopted. However, the Matérn covariance function seems to produce a mismatch between 0 and 90 Hz in both the strain and the acceleration response. An overall information regarding the response estimation precision is

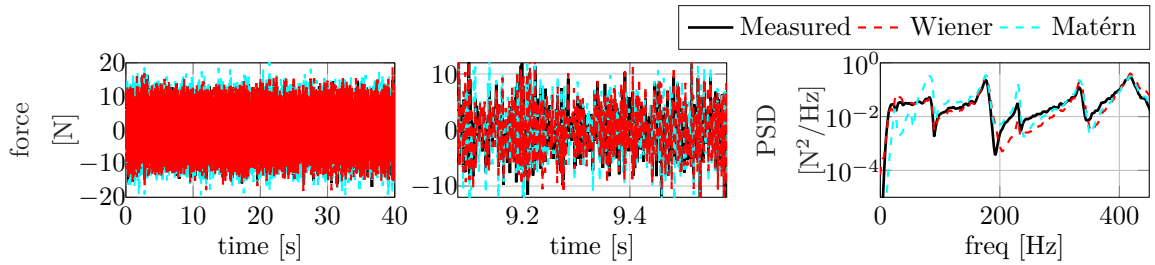

Figure 8.29: 3D-printed scaled WT blade random test: input measured (black) and estimated (GPLFM with Matérn cov. - cyan, GPLFM with Wiener cov. - red) force signals

reported in Tabs. 8.29-8.32 by means of the TRAC and FRAC indicators. The presented indicators show higher values (especially for strains) when the Wiener covariance function is adopted, confirming the conclusion drawn from Figs. 8.30 and 8.31. Additionally, Fig. 8.32 reports a comparison of the measured RMS trend for the entire set of responses (strain gauges-left, accelerometers-right) with the RMS trends of the signals estimated at the same locations by means of the GPLFM with a Wiener and a Matérn covariance function. From the visual information provided in Fig. 8.32 it can be concluded that the response estimation obtained via the two investigated covariance functions are almost comparable in terms of amplitude, with a slightly higher accuracy of the Wiener covariance function for the strain responses. The latter is linked to the prediction error (visible in Fig. 8.30) provided by the Matérn covariance function at low frequency.

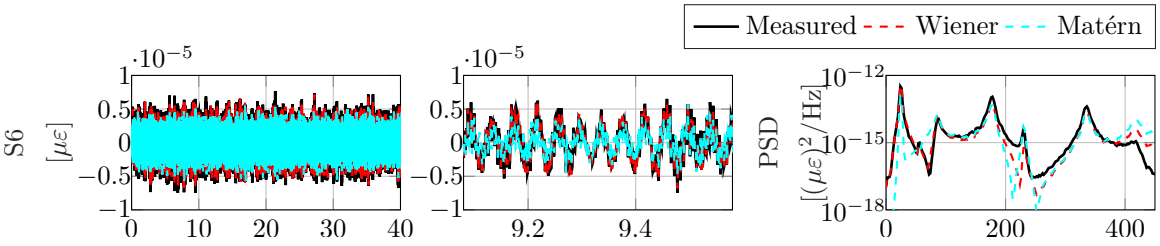

Figure 8.30: 3D-printed scaled WT blade random test: measured (black) and estimated (GPLFM with Matérn cov. - cyan, GPLFM with Wiener cov. - red) strain at location 6

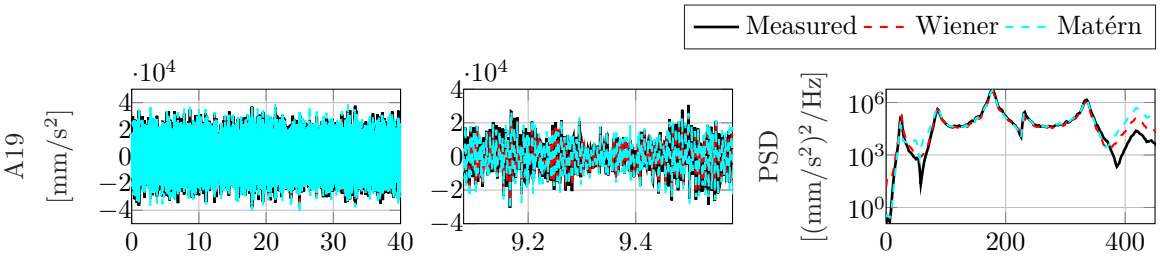

Figure 8.31: 3D-printed scaled WT blade random test: measured (black) and estimated (GPLFM with Matérn cov. - cyan, GPLFM with Wiener cov. - red) acceleration at location 19

Table 8.29: 3D-printed scaled WT blade random test: TRAC values between measured and estimated (GPLFM with Matérn and Wiener covariance functions) strain responses. Observations are underlined.

Estimator	1	2	3	4	5	6	7	8	9	10	11	12
Matérn	0.595	0.584	0.513	0.510	0.743	0.601	0.652	0.654	0.693	0.581	0.630	0.607
Wiener	0.938	0.848	0.825	0.889	0.828	0.903	0.889	0.959	0.951	0.853	0.943	0.942

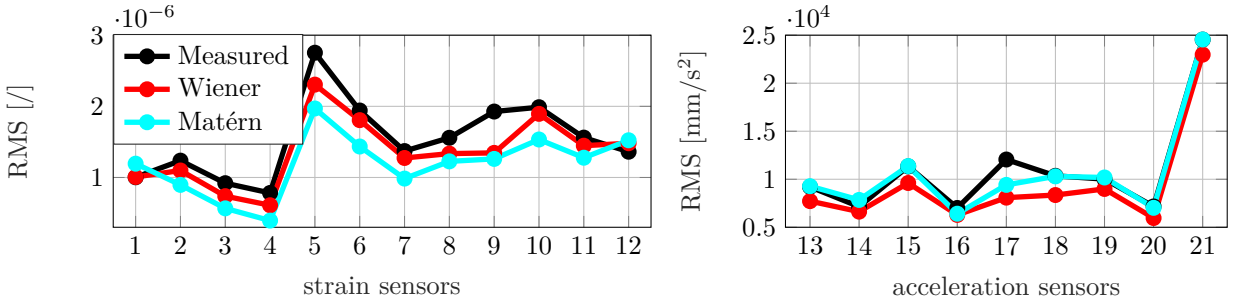

Figure 8.32: 3D-printed scaled WT blade random test: measured (black) and estimated (GPLFM with Matérn cov. - cyan, GPLFM with Wiener cov. - red) strain (left) and acceleration (right) responses RMS values.

Table 8.30: 3D-printed scaled WT blade random test: TRAC values between measured and estimated (GPLFM with Matérn and Wiener covariance functions) force and acceleration responses. Observations are underlined.

Estimator	13	14	15	16	17	18	19	20	21	22	**force**
Matérn	0.914	0.494	1.000	0.305	0.095	1.000	0.882	0.558	1.000	0.977	0.642
Wiener	0.913	0.532	0.988	0.329	0.109	0.964	0.960	0.628	0.989	0.999	0.863

Table 8.31: 3D-printed scaled WT blade random test: FRAC values between measured and estimated (GPLFM with Matérn and Wiener covariance functions) strain responses. Observations are underlined.

Estimator	1	2	3	4	5	6	7	8	9	10	11	12
Matérn	0.730	0.673	0.937	0.943	0.907	0.912	0.855	0.851	0.899	0.794	0.756	0.878
Wiener	0.961	0.890	0.931	0.974	0.786	0.936	0.9867	0.968	0.977	0.920	0.993	0.997

Table 8.32: 3D-printed scaled WT blade random test: FRAC values between measured and estimated (GPLFM with Matérn and Wiener covariance functions) force and acceleration responses. Observations are underlined.

Estimator	13	14	15	16	17	18	19	20	21	22	**force**
Matérn	0.981	0.239	1.000	0.107	0.702	1.000	0.979	0.842	1.000	0.943	0.781
Wiener	0.969	0.280	0.973	0.109	0.594	0.966	0.997	0.831	1.000	0.997	0.937

8.3.3 Sine test

The use of a quasiperiodic covariance function for constructing a GPLFM is hereby explored for input-state estimation during sinusoidal tests performed on the 3D-printed scaled WT blade. As anticipated in Subsection 5.2.1, experimentally recorded data are often affected by external sources of disturbance. For this reason, even when a sinusoidal signal is selected to drive the shaker, the actual load acting on the structure and recorded by the load cell may deviate from the pure sine assumption. To take this effect into account when constructing the GPLFM, a quasiperiodic covariance function is preferred to a periodic covariance function. The ad hoc covariance function selection is hereby adopted for prediction during sine tests using the mixed observations set (strain and acceleration) reported in Tab. 8.33. The estimation results are compared against the ones achieved by making use of the same measurements set in combination with a conventional Matérn covariance function ($\nu = 1.5$). Moreover, the predictions achieved via the state-of-the-art AKF are hereby introduced and compared with the GPLFM predictions. The chosen values for the necessary initial conditions and the process and measurement noise covariance matrices are also shown. The latter has been retrieved from the background noise recorded by sensors during tests, while the first has been instead tuned by trial and error. For the AKF, the process noise covariance values

associated to the states and the input are highlighted. To the contrary, for the GPLFM the states process noise covariance and the GP covariance functions initial hyperparameters are presented. The hypeparameters have been selected by maximizing the log marginal likelihood of the acceleration collocated with the unknown input, i.e., at the shaker location indicated in Fig. 8.3.

Table 8.33: 3D-printed scaled WT blade sine test: AKF and GPLFMs observations sets and initialization values for a Matérn (ν=1.5) and a quasiperiodic covariance function

Estimator	Observations	Initial state mean	Initial error cov. matrix	Input noise cov. Initial hyperparameters	Process noise cov. matrix ($\mathbf{Q}$)	Measurement noise cov. matrix ($\mathbf{R}$)
AKF	1, 3, 8,12, 15, 18, 21, 22	$\hat{\mathbf{x}}^a_{0\|0} = \mathbf{0}$	$\hat{\mathbf{P}}^a_{0\|0} = 10^{-10} \times \mathbf{I}$	$\mathbf{Q}_u = 10^{15} \times \mathbf{I}$	$\mathbf{Q}_{displ} = 10^{-20} \times \mathbf{I}$ $\mathbf{Q}_{vel} = 10^{-10} \times \mathbf{I}$	$\mathbf{R}_{\text{strain}} = 10^{-14} \times \mathbf{I}$ $\mathbf{R}_{\text{acc}} = 10^{-7} \times \mathbf{I}$
Matérn	1, 3, 8,12, 15, 18, 21, 22	$\hat{\mathbf{x}}^a_{0\|0} = \mathbf{0}$	$\hat{\mathbf{P}}^a_{0\|0} = 10^{-10} \times \mathbf{I}$	$\sigma^2 = 3 \times 10^3$ $l = 2 \times 10^{-4}$	$\mathbf{Q}_{displ} = 10^{-20} \times \mathbf{I}$ $\mathbf{Q}_{vel} = 10^{-10} \times \mathbf{I}$	$\mathbf{R}_{\text{strain}} = 10^{-14} \times \mathbf{I}$ $\mathbf{R}_{\text{acc}} = 10^{-7} \times \mathbf{I}$
Quasiperiodic	1, 3, 8, 12, 15, 18, 21, 22	$\hat{\mathbf{x}}^a_{0\|0} = \mathbf{0}$	$\hat{\mathbf{P}}^x_{0\|0} = 10^{-10} \times \mathbf{I}$	$\sigma^2 = 5 \times 10^{-1}$ $l = 5 \times 10^{-1}$ $t_{period} = 1.2 \times 10^{-2}$ $l_{matern} = 8 \times 10^{-1}$	$\mathbf{Q}_{displ} = 10^{-20} \times \mathbf{I}$ $\mathbf{Q}_{vel} = 10^{-10}$	$\mathbf{R}_{\text{strain}} = 10^{-14} \times \mathbf{I}$ $\mathbf{R}_{\text{acc}} = 10^{-7} \times \mathbf{I}$

Figure 8.33 offers a time domain comparison between the actual force and the input predictions obtained via the AKF and the GPLFM with a quasiperiodic and a Matérn covariance function. During the tests, the force applied by the shaker has been recorded by a force cell placed between the shaker and the structure. A quantification of the input estimations accuracy is reported in Tab. 8.35 (last column) by means of the TRAC estimator. From the results reported in Fig. 8.33, it can be concluded that while the AKF and the GPLFM with a Matérn covariance function both overestimate the load amplitude, a more accurate estimation is obtained via the GPLFM with a quasiperiodic covariance function. This result is confirmed by the TRAC values offered in Tab. 8.35.

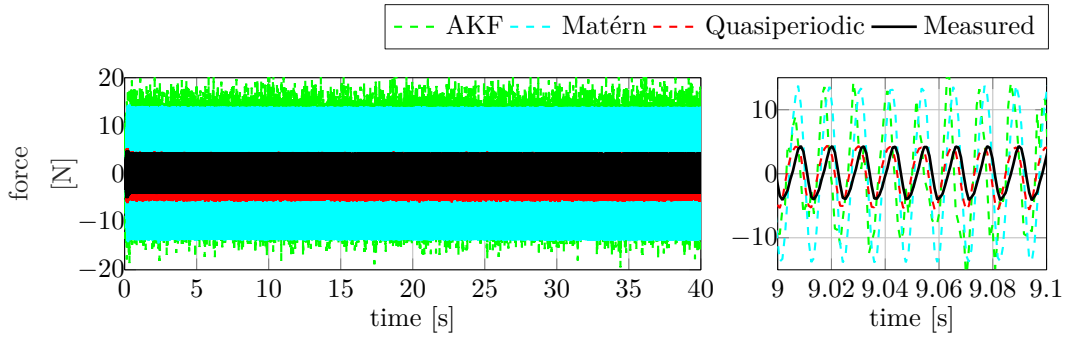

Figure 8.33: 3D-printed scaled WT blade sine test: input measured (black) and estimated (AKF - green, GPLFM with Matérn cov. - cyan, GPLFM with quasiperiodic cov. - red) force signals

Figures 8.34 and 8.35 present the comparison between measured and estimated signals respectively for a strain and an accelerometer that are not included in the observations set. These results demonstrate that a good and comparable prediction accuracy can be achieved by the GPLFM with a quasiperiodic or a Matérn covariance function for both strain and acceleration predictions. To the contrary, the AKF produces an accurate response prediction for the strain response, while it underestimates the acceleration response amplitude. An overall information regarding the response estimation precision is reported in Tabs. 8.34 and 8.35 by means of the TRAC values. The presented indicators show comparable values for both strain and acceleration responses when the GPLFM is adopted with one of the two analyzed covariance functions. However, lower TRAC values are generated by the AKF for the acceleration responses. Additionally, Fig. 8.36 reports a comparison of the measured RMS trend for the entire set of responses (strain gauges-left, accelerometers-right)

with the RMS trends of the signals estimated at the same locations by means of the AKF and the GPLFM (quasiperiodic or Matérn covariance function). Figure 8.36 confirms that the three compared approaches produce a comparable strain estimation accuracy, while for the acceleration responses an overall higher amplitude error is provided by the AKF.

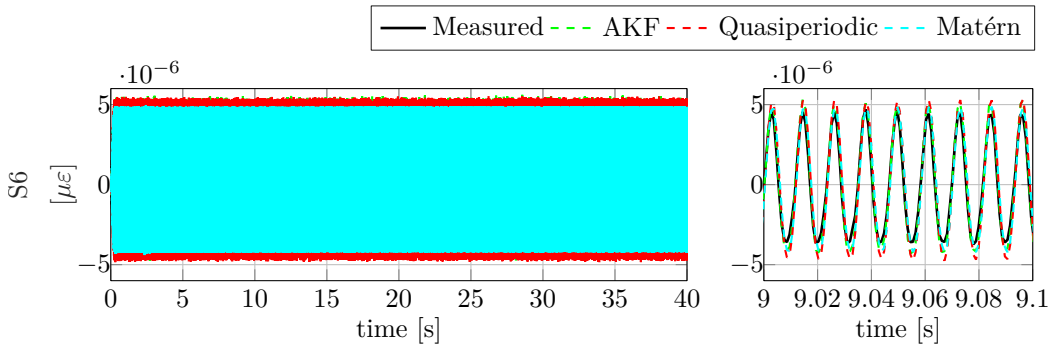

Figure 8.34: 3D-printed scaled WT blade sine test: measured (black) and estimated (AKF - green, GPLFM with Matérn cov. - cyan, GPLFM with quasiperiodic cov. - red) strain at location 6

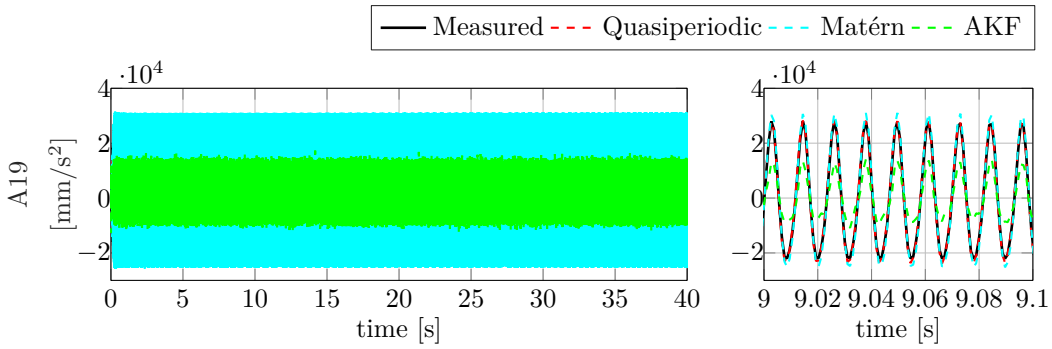

Figure 8.35: 3D-printed scaled WT blade sine test: measured (black) and estimated (AKF - green, GPLFM with Matérn cov. - cyan, GPLFM with quasiperiodic cov. - red) acceleration at location 19

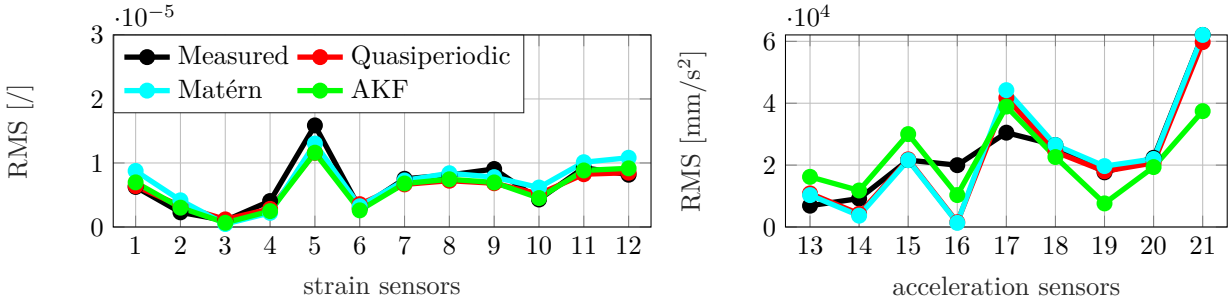

Figure 8.36: 3D-printed scaled WT blade sine test: measured (black) and estimated (AKF - green, GPLFM with Matérn cov. - cyan, GPLFM with quasiperiodic cov. - red) strain (left) and acceleration (right) responses RMS values.

The content offered in this section provides an experimental validation of the concepts elaborated in Subsection 5.2.1 and proved numerically in Subsubsection 5.2.1.1. The ad hoc covariance function selection for GPLFMs construction in the framework of joint input-state estimation is hereby evaluated during tests on the 3D-printed scaled blade under different loading conditions. The produced results prove that a proper a priori selection of the covariance function allows to considerably enhance the achievable load estimation accuracy.

Table 8.34: 3D-printed scaled WT blade sine test: TRAC values between measured and estimated (AKF, GPLFM with Matérn and quasiperiodic covariance functions) strain responses. Observations are underlined.

Estimator	1	2	3	4	5	6	7	8	9	10	11	12
AKF	0.993	0.974	0.537	0.915	0.994	0.992	0.998	0.992	0.979	0.984	0.998	0.999
Matérn	0.994	0.988	0.221	0.999	1.000	0.946	0.997	0.994	0.992	0.987	0.995	0.992
Quasiperiodic	0.981	0.985	0.685	0.889	0.997	0.968	0.988	0.994	0.985	0.996	1.000	0.999

Table 8.35: 3D-printed scaled WT blade sine test: TRAC values between measured and estimated (AKF, GPLFM with Matérn and quasiperiodic covariance functions) force and acceleration responses. Observations are underlined.

Estimator	13	14	15	16	17	18	19	20	21	22	**force**
AKF	0.754	0.547	0.911	0.672	0.971	0.908	0.967	0.916	0.926	0.730	0.057
Matérn	0.986	0.976	1.000	0.923	0.998	1.000	0.997	0.998	1.000	1.000	0.767
Quasiperiodic	0.989	0.986	1.000	0.947	0.998	0.999	0.995	0.999	1.000	1.000	0.812

8.4 Summary

An extensive test campaign conducted on a 3D-printed scaled WT blade has been described in this chapter and exploited to validate the methodological tools developed in this thesis. After a first description of the scaled WT blade, details on the experiments and on the ROM employed for VS are reported. Data collected during shaker tests on the blade under study is then adopted to validate the A-AKF estimator for random loads. The algorithm response predictions are compared against the ones produced by the CMS-ME and the state-of-the-art AKF tuned via the conventional L-curve metric. The provided comparison highlights that the A-AKF provides a global accuracy comparable to the referenced CMS-ME method, with improvements at specific locations dictated by the enhanced stochastic setting. The conventional AKF instead features the lowest prediction performance. Both the AKF and the A-AKF fail in the task of input estimation due to absence of acceleration responses in the observations set. However, the A-AKF allows to better capture the unknown load amplitude. On the other hand, low frequency components contaminate the A-AKF input prediction due to the batch nature of the error estimates employed within this algorithm. The investigated case study has thus demonstrated that the A-AKF can be used for automated process noise selection in joint input-state estimation for random tests. Despite accurate response predictions are achieved, further research must be carried out concerning the error estimates adopted within the algorithm and the applicability of the method for observations sets containing both displacement-level and acceleration measurements.

The use of a GP-based approach for joint input-state estimation has been then evaluated for random tests on the scaled blade. The conventionally constructed GPLFM has been used for VS purposes in two different scenarios: in presence of a mixed observations set composed by strain gauges and accelerometers and under the assumption of accelerations-only availability. It is worth noting that the hereby employed GP-based approach i) is built using a Matérn covariance function and ii) adopts the entire set of measurements for training the covariance function hyperparameters. The comparison of the GPLFM predictions against the ones achieved via the more conventional AKF shows a comparable accuracy under the mixed measurements assumption. This confirms that the GP-based approach represents an accurate, more flexible and user-independent alternative to standard VS methods. The GPLFM proves good estimation capabilities also for the acceleration-only measurements scenario, where the AKF instead generates predictions affected by a low frequency drift due to unobservability. Next, the GP-based approach has been also successfully tested for pull and release tests and compared against the state-of-the-art AKF and DKF for a mixed observations

set. Finally, the proposed ad hoc GPLFM covariance function selection, previously validated numerically in Subsubsection 5.2.1.1, is verified for an array of different loading scenarios (random, pull and release, sine) reproduced during the experimental campaign on the 3D-printed scaled blade. All three case studies confirm that i) the unknown input features are better captured if the GP covariance function is selected ad hoc for the specific test, ii) a good prediction performance can be achieved even adopting a single measurement for training the covariance function hyperparameters. The hereby presented study focuses on VS for WT blades applications when observations sets including a collocated acceleration measurement are adopted. Future investigations should focus on addressing the same problem when collocated measurements are not available.

9

WIND TURBINE BLADES TESTING: COMPOSITE SCALED BLADE

In this thesis, light is shed on dynamic virtualization of WT blades as they comprise WT components of elevated importance and complexity. Extensive testing campaigns are usually conducted on blades prior to installation. The establishment and validation of a DT for each blade at this stage of its life cycle represents an essential resource for future monitoring and maintenance of these structures in the field. In this sense, experimentally acquired modal properties can be used within optimization algorithms to reduce uncertainties in the available models. Bayesian VS [122] can be then exploited to extend the information from a few sensed locations to the entire full-field blade response and estimate the unmeasured loads acting on the blade during tests. The proposed virtualization process has been extensively validated in Chapter 7 and 8, respectively for a large scale composite blade and a 3D-printed scaled titanium WT blade. In this chapter instead, a novel Kalman-based strategy is tested for joint input-state-response estimation of a SISW-owned small scale composite blade. By proposing the implementation of a virtualization process for a small scale WT blade made of GFRPs, this chapter introduces additional challenges for state-of-the-art and newly developed VS strategies. Indeed, the high flexibility of the composite material coupled with the small dimensions of the scaled blade render the vibration measurements distorted and noise contaminated, thus rendering the use of system identification techniques challenging. As a result, the produced experimental modal parameters feature a discrete level of uncertainty, which complicate the model updating activities. The updated FE model thus embeds a non-negligible level of modeling errors, which inevitably influences the degree of success of the employed data assimilation methods.
The small scale composite blade is introduced in Section 9.1, along with a description of the measurement campaign, the FE model and its validation and update results obtained via a methodology developed in Simcenter^{TM} HEEDS. Section 9.2 then offers the VS results obtained during shaker testing of the small scale blade. Specifically, the STPLFM with a Wiener covariance function is hereby proposed for the task of input-state prediction in presence of distorted data. The STPLFM performance is evaluated by comparing it against the GPLFM and the state-of-the-art AKF. Next, conclusions for this chapter are drawn in Section 9.3.

9.1 Small scale composite wind turbine blade

The hereby analyzed experimental case study deals with shaker testing of the SISW-owned small scale composite WT blade in Fig. 9.1. The scaled blade has been designed and manufactured by DTU Wind Energy via a typical resin infusion process. This technology foresees the manufacturing of two shells which are then sealed together. For each shell, glass fibers are placed in a mold and resin is then injected into the mold cavity under pressure. Before welding the two surfaces together, the so-called shear webs, i.e., two reinforcements spanning 3/4 of the blade length (visible in Fig. 9.5), are glued internally to one of the halves. The small composite blade under study also features an aluminum insert at the root, which has been added for allowing the blade attachment to a scaled WT hub through a bolted connection.

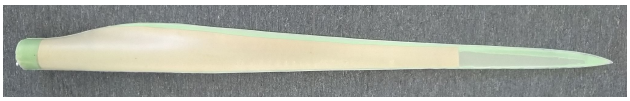

Figure 9.1: Small scale composite WT blade

9.1.1 Measurement campaign

Figure 9.2 (left) shows the setup adopted during the shaker test carried out at SISW on the small scale composite WT blade . During tests, the blade root has been clamped via a 6-bolts connection between the aluminum insert and a steel plate, while random excitation has been provided by means of a shaker positioned as in Fig. 9.2 (right). The blade response has been acquired through 10 accelerometers and 2 uniaxial strain gauges. The sensors and shaker locations are displayed in Fig. 9.3.

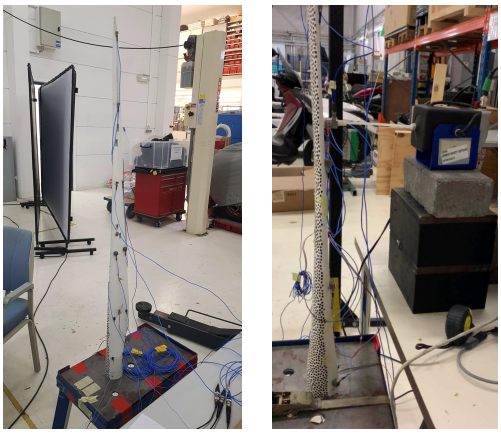

Figure 9.2: Small scale composite WT blade experimental setup

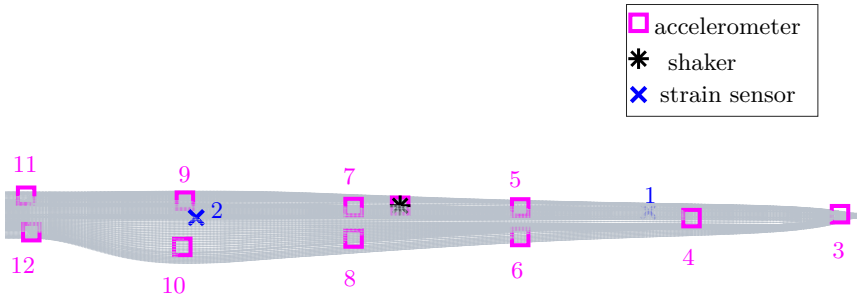

Figure 9.3: Small scale composite WT blade sensing configuration during shaker tests: strain sensors (blue), accelerometers (magenta)

Simcenter^{TM} Testlab PolyMAX has been used to determine the experimental modal parameter of the blade summarized in Tab. 9.1.

9.1.2 Numerical model: Finite Element model udpdate and Reduced Order Model

The FE model of the small scale composite blade, offered in Fig. 9.4, has been developed by DTU Wind Energy via the in-house Blade Modeling Tool and solved in MSC^{TM} Nastran. It is composed of around 87000 CHEXA elements (8 nodes) featuring solid composite properties.
A MATLAB^{TM}-based methodology has been developed to export the FE model from MSC^{TM} Nastran into NX^{TM} Nastran, to be manipulated in Simcenter^{TM} 3D and then updated through a strategy set up in Simcenter^{TM} HEEDS.

Modes	Frequency [Hz]	Damping [%]
1	15.07	1.26
2	30.80	2.53
3	47.88	1.38
4	102.04	2.95
5	117.19	2.73
6	181.85	2.68
7	225.75	4.27
8	256.11	2.36
9	295.02	1.48
10	373.59	1.49

Table 9.1: Small scale composite WT blade experimental modal frequencies and damping ratios in clamped-free conditions

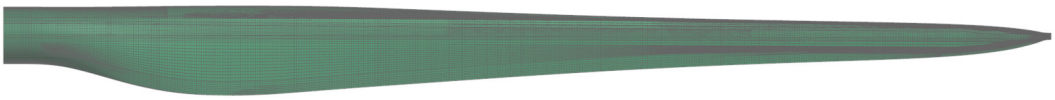

Figure 9.4: Small scale composite WT blade FE model

The developed updating method relies on experimental data collected during a preliminary test with the blade in clamped-free BCs. To reproduce the test BCs, the constraints shown in Fig. 9.5 have been defined at the blade FE model root by means of 6 RBEs with fixed independent nodes. Concentrated masses (0D elements) have been added to the FE model at the accelerometers locations to account for their presence and increase the correlation with experimental data.

Figure 9.5: Small scale composite WT blade FE model BCs

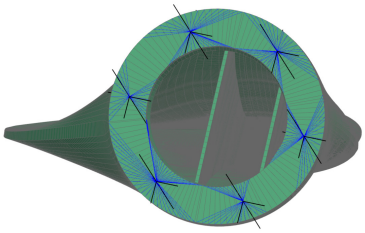

The Simcenter^{TM} HEEDS updating workflow, summarized in Fig. 9.6, consists in exploiting the SHERPA algorithm to seek for the variables values combination which best matches the optimization objectives.

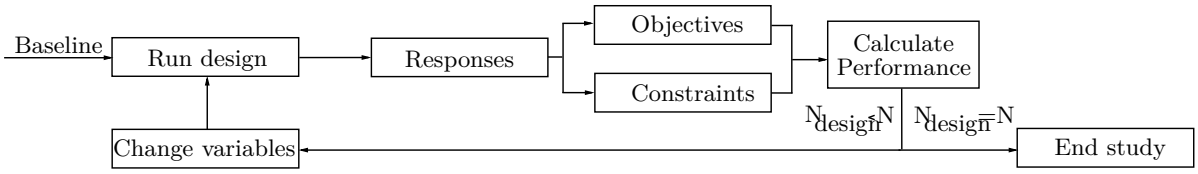

Figure 9.6: Small scale composite WT blade: FE model update workflow in Simcenter^{TM} HEEDS

For the hereby analyzed case study, the objectives consist in i) minimizing the frequency errors between the FE model natural frequencies and the experimental natural frequencies in Tab. 9.1, ii) maximizing the numerical-experimental MAC diagonal pairs, iii) minimizing the numerical-experimental MAC off-diagonal pairs. An overview of the main material properties (Young's moduli and densities) selected as design variables within the optimization is offered in Tab. 9.2, along with

a summary of the admitted variables ranges, their initial and updated values.

Table 9.2: Small scale composite WT blade FE model update: design variables initial and updated values, selected and maximum % change

Design variables	Initial value	Updated value	Selected change [%]	Max. change [%]
$\rho_{al}[kg/mm^3]$	2.70×10^{-6}	2.1×10^{-6}	-22.15	±25.00
$E_{al}[MPa]$	70000	60900	-13.05	±25.00
$\rho_{balsa}[kg/mm^3]$	1.45×10^{-6}	1.51×10^{-6}	4.00	±20.00
$E_{balsa}[MPa]$	2350	1880	-20.00	±20.00
$\rho_{biax}[kg/mm^3]$	2.00×10^{-6}	2.40×10^{-6}	20.00	±20.00
$E_{1_{biax}}[MPa]$	14520	17424	20.00	±20.00
$E_{2_{biax}}[MPa]$	14520	17424	20.00	±20.00
$E_{3_{biax}}[MPa]$	14520	17424	20.00	±20.00
$\rho_{glue}[kg/mm^3]$	1.50×10^{-6}	1.80×10^{-6}	20.00	±25.00
$E_{glue}[Pa]$	4000	4662.4	16.56	±25.00
$\rho_{UD90}[kg/mm^3]$	2.6×10^{-6}	3.12×10^{-6}	20.00	±20.00
$E_{1_{UD90}}[MPa]$	12162	11194	-7.96	±20.00
$E_{2_{UD90}}[MPa]$	41050	44613	8.68	±20.00
$E_{3_{UD90}}[MPa]$	12162	11194	-7.96	±20.00
$\rho_{uniax}[kg/mm^3]$	1.98×10^{-6}	2.1×10^{-6}	6.08	±20.00
$E_{1_{uniax}}[MPa]$	41050	32840	-20.00	±20.00
$E_{2_{uniax}}[MPa]$	12162	13471	10.76	±20.00
$E_{3_{uniax}}[MPa]$	12162	13471	10.76	±20.00

Table 9.3 shows the updating results by comparing the initial and updated numerical frequencies and MAC diagonal pairs. A substantial improvement in terms of frequency errors and diagonal MAC pairs has been achieved via the proposed strategy. These results are confirmed by the initial and updated MAC diagrams offered in Fig. 9.7. Nevertheless, Fig. 9.7 highlights that, although a diagonalization is introduced via the updating process, the final FE model still features high correlation for some off-diagonal mode pairs. These uncertainties can be ascribed to i) BCs approximation in the FE model and ii) the WT blade high flexibility, which has generated noisy signals, modes mixture between 220 and 260 Hz (torsion and high-order bending) and considerable shaker-structure interaction. These latter aspects have introduced several challenges in the selection of the experimental mode set and, consequently, a relatively high degree of uncertainty in the correlation with the numerical modal parameters.

Table 9.3: Small scale composite WT blade FE model initial and updated frequencies, frequency errors and MAC pairs

Modes	f_i^{test}[Hz]	f_i^{initial}[Hz]	f_i^{updated}[Hz]	$\text{MAC}_{ii}^{\text{initial}}$	$\text{MAC}_{ii}^{\text{updated}}$
1	15.07	16.26	14.25	0.99	0.99
2	30.80	34.60	32.97	0.96	0.97
3	47.88	53.93	47.66	0.99	0.99
4	102.04	114.54	104.85	0.88	0.96
5	117.19	127.50	117.97	0.95	0.95
6	181.85	203.18	180.53	0.96	0.97
7	225.75	269.55	243.27	0.56	0.69
8	256.11	284.00	264.98	0.35	0.68
9	295.02	306.50	280.35	0.95	0.96
10	373.59	409.05	367.79	0.95	0.95

A ROM of the composite scaled blade has been constructed following the procedure outlined in Subsection 2.1.1 by taking into account the first ten modes (frequency range of interest: 0-450 Hz) and one residual attachment mode related to the unknown force to be estimated via the chosen Bayesian estimators. For the hereby analyzed shaker tests, the residual attachment mode has been computed by applying a unitary force at the shaker location pointed out in Fig. 9.3, along the shaker stinger direction.

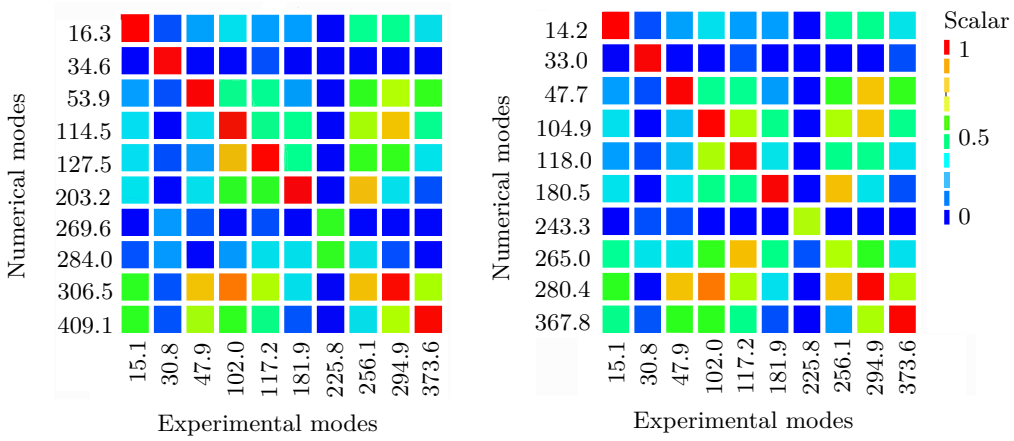

Figure 9.7: Small scale composite WT blade FE model update: initial (left) and updated (right) MAC diagram.

9.2 Joint input-state estimation through the Student-t Process Latent Force Model

This section proposes the use of VS techniques for the estimation of the QoI during shaker testing of the composite scaled WT blade. Specifically, this section evaluates and compares the performance of the GP-based and the STP-based approaches discussed in Subsection 5.2.1 for real-life data. The use of filtering only within the proposed strategies is hereby preferred to the KF and RTS smoother combination. This case study thus comprises an additional experimental validation for the use of LFMs constructed via state-space formulation of stochastic processes relying on real-time estimation only. Moreover, the analyzed data set also serves as further experimental assessment of the ad hoc selection of the estimators covariance function proposed in Subsection 5.2.1 and previously validated both numerically (Subsubsection 5.2.1.1) and experimentally (Section 8.3). The reconstructed signals are compared against the state-of-the-art AKF estimations. The hereby adopted estimators have been employed for input-state prediction using the mixed observations set (strain and acceleration) reported in Tab. 9.4, where the sensors numbers refer to the layout in Fig. 9.3. The measurements acquired at the remaining locations have been used to validate the estimations provided by the investigated methods. The chosen values for the necessary initial conditions and the process and measurement noise covariance matrices are also shown in Tab. 9.4. The latter has been retrieved from the background noise recorded by sensors during tests, while the first has been instead tuned by trial and error. For the AKF, the process noise covariance values associated to the states and the input are highlighted. To the contrary, the states process noise covariance and the Wiener covariance function initial hyperparameters are presented for the GP-based and STP-based approaches.

Table 9.4: Small scale composite WT blade random test: AKF,GPLFM and STPLFM observations sets and initialization values

Estimator	Observations	Initial state mean	Initial error cov. matrix	Input noise cov./ initial hyperparameters	Process noise cov. matrix ($\mathbf{Q}$)	Measurement noise cov. matrix ($\mathbf{R}$)
AKF	1, 3, 5, 8, 9, 13	$\hat{\mathbf{x}}^a_{0\|0} = \mathbf{0}$	$\hat{\mathbf{P}}^a_{0\|0} = 10^{-10} \times \mathrm{I}$	$\mathbf{Q}^u = 1 \times \mathrm{I}$	$\mathbf{Q}_{displ} = 10^{-11} \times \mathrm{I}$ $\mathbf{Q}_{vel} = 10^{-6} \times \mathrm{I}$	$\mathbf{R}_{\text{strain}} = 10^{-11} \times \mathrm{I}$ $\mathbf{R}_{\text{acc}} = 10^{-14} \times \mathrm{I}$
GPLFM, STPLFM	1, 3, 5, 8, 9, 13	$\hat{\mathbf{x}}^a_{0\|0} = \mathbf{0}$	$\hat{\mathbf{P}}^x_{0\|0} = 10^{-10} \times \mathrm{I}$	$\sigma^2 = 1 \times 10^7$	$\mathbf{Q}_{displ} = 10^{-11} \times \mathrm{I}$ $\mathbf{Q}_{vel} = 10^{-6} \times \mathrm{I}$	$\mathbf{R}_{\text{strain}} = 10^{-6} \times \mathrm{I}$ $\mathbf{R}_{\text{acc}} = 10^{-14} \times \mathrm{I}$

Figure 9.8 shows a comparison in both time and frequency domains between the actual force and the input predictions obtained via the AKF, the GPLFM and the STPLFM when a Wiener covariance function is adopted. During the analyzed test, the force applied by the shaker has been recorded by a force cell placed between the shaker and the structure. A quantification of the input estimations accuracy in frequency domain is reported in Tab. 9.5 (last column) by means of the FRAC estimator

formulated in Subsection 8.2.2. The frequency range 0-450 Hz has been selected for computing the FRAC. From the results reported in Fig. 9.8 and Tab. 9.5, it can be concluded that none of the tested estimators allows to reach a high level of accuracy in terms of input predictions. This is primarily due to the high shaker-structure interaction exhibited during shaker testing of the small composite blade, which resulted in a non-flat PSD of the measured force signal. This has increased the complexity of the input prediction objective, especially since the employed FE model features a level of uncertainty which is difficult to be compensated within the proposed strategies. However, a slightly higher FRAC can be achieved by employing the STPLFM. To the contrary, the GPLFM produces a predicted time history modulated by a low frequency component, which is reflected in a lower FRAC value.

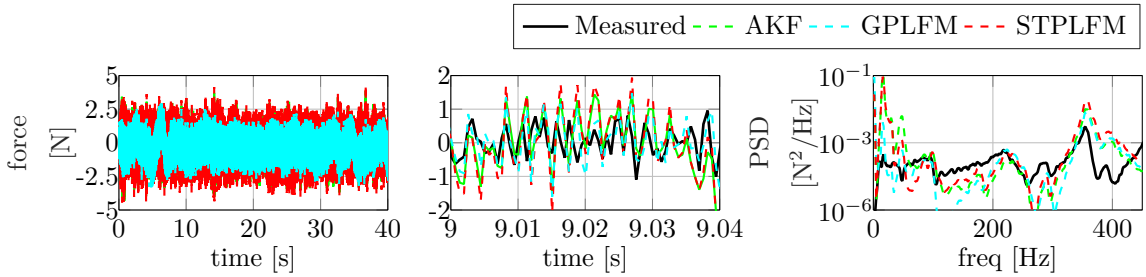

Figure 9.8: Small scale composite WT blade: measured (black) and estimated (AKF - green, GPLFM - cyan and STPLFM - red) force signals

Figures 9.9 and 9.10 present the comparison between measured and estimated signals respectively for a strain and an accelerometer that are not included in the observations set.

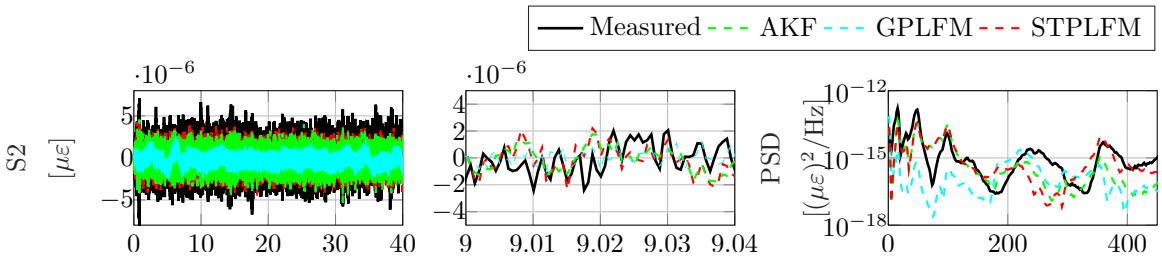

Figure 9.9: Small scale composite WT blade: measured (black) and estimated (AKF - green, GPLFM - cyan and STPLFM - red) strain at location 2

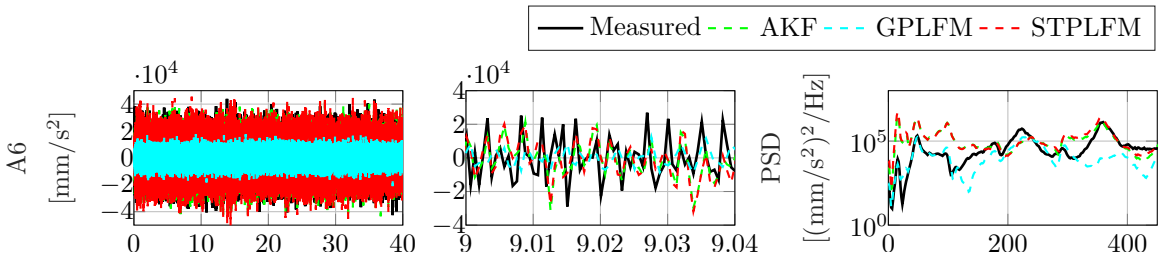

Figure 9.10: Small scale composite WT blade: measured (black) and estimated (AKF - green, GPLFM - cyan and STPLFM - red) acceleration at location 6

These results demonstrate that a good and comparable prediction accuracy can be achieved by the AKF and the STPLFM for both strain and acceleration predictions. On the other hand, the GPLFM does not match the response signals amplitude due to a lower correlation at low frequency for the strain response and at high frequency for the acceleration response. An overall information regarding the response estimation precision is reported in Tab. 9.5 and Fig. 9.11, respectively in terms of frequency content (estimated FRAC values for the entire set of responses) and amplitude (measured and estimated RMS values for the entire set of responses). The presented indicators report a lower accuracy for the GPLFM in terms of strain response prediction. The same is valid

for acceleration response, although the discrepancy is more contained for this type of sensors.

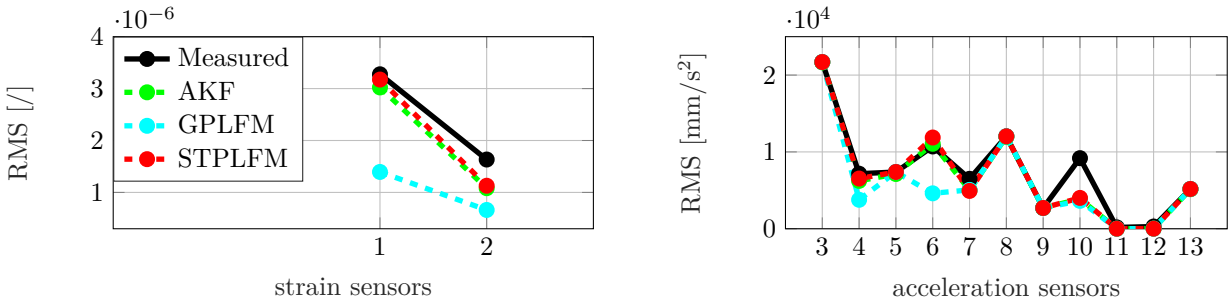

Figure 9.11: Small scale composite WT blade: measured (black) and estimated (AKF - green, GPLFM - cyan and STPLFM - red) strain (left) and acceleration (right) responses RMS values

Table 9.5: Small scale composite WT blade: FRAC values between measured and estimated (AKF,GPLFM and STPLFM) force and responses. Observations are underlined.

Estimator	1	2	3	4	5	6	7	8	9	10	11	12	13	**force**
AKF	0.994	0.710	1.000	0.400	1.000	0.280	0.650	1.000	1.000	0.877	0.086	0.230	1.000	0.0345
GPLFM	0.025	0.007	1.000	0.612	1.000	0.161	0.584	1.000	1.000	0.883	0.066	0.263	1.000	0.0210
STPLFM	1.000	0.587	1.000	0.188	1.000	0.340	0.646	1.000	1.000	0.872	0.035	0.383	1.000	0.0873

The input-response estimation results reported in this section highlight that the use of a Wiener covariance function for constructing a LFM via stochastic process regression provides results comparable with the ones achieved via the state-of-the-art AKF in presence of a mixed observations set. This proves that the use of a Wiener covariance function in such a context is equivalent to the adoption of the conventional RW equation for modeling the unknown input dynamics. However, in the STPLFM algorithm the tuning task is limited since part of the process is put in place via the training phase aimed at selecting the hyperparameters. Specifically, the STPLFM has proved to overcome the GPLFM with regards to their applicability to challenging experimental case studies. As explained in Subsection 5.2.1, STP regression allows to more easily detect outliers and it is therefore more suitable for scenarios in which noisy and distorted data (as the ones analyzed here) are employed.

9.3 Summary

This chapter presents an experimental case study concerning a small scale composite WT blade, which has served for assessing the use of STP regression alternatively to GP regression for construction of the unknown input model in an online joint input-state estimation framework. The employment of a GPLFM for online input-state estimation has been extensively tested and validated in Chapters 6 and 8, where both the options of a conventional Matérn covariance function and the alternative ad hoc covariance function selection have been explored. In Section 9.1, the STPLFM higher flexibility and ability to detect outliers in real-life data are exploited for input-state estimation during shaker testing of the small scale composite blade. For this application, a Wiener covariance function has been selected for both the GPLFM and the STPLFM, thus offering further proof of the validity of the ad hoc covariance function approach. A ROM of the blade has been constructed by means of a CMS method and employed within the analyzed Bayesian estimation strategies. The presented results show that the use of STP regression guarantees lower estimation errors in situations in which both the experimental data and the FE model features render input-response prediction a challenging task. It is thus demonstrated that the use of STPLFMs should be preferred to GPLFMs in such conditions.

10

CONCLUSIONS

This thesis treats the development of VS techniques for virtualization of structures and mechanical components subjected to dynamic loads. Dynamic virtualization of these systems, i.e., the establishment of real-time operating DTs, is addressed by constructing the so-called "virtual sensors", i.e., online predictions of unmeasured loads and responses obtained via data assimilation methods. The latters comprise the combination of observations of a system with a mechanistic model to produce an analysis of the system states as it evolves in time. The employment of data assimilation strategies for load and response estimation in dynamic loads environments introduces several modeling and methodological challenges, whose investigation builds the core of this dissertation. The content of this work is divided in two parts. The first part defines a theoretical framework and proposes new approaches for addressing the existing limitations arising from the use of joint input-state estimation algorithms in structural dynamics. The second part reports on the validation of the developed methods by means of several case studies, including small scale and large scale experiments. This chapter first summarizes the main concluding remarks of this thesis. Lastly, some recommendations for future research directions are highlighted.

10.1 Summary of the main contributions

Chapter 2 offers the theoretical principles forming the basis for the VS methods investigated in this thesis. Both deterministic and stochastic analytical tools necessary for the definition of the dynamic system models employed within VS strategies are reported. Basic deterministic concepts such as state-space modeling of dynamical systems and MOR via CMS are first presented. The stochastic framework forming the core of this dissertation is then introduced in this chapter via the concept of Bayesian dynamic modeling and the related uncertainties parameters, i.e., the measurement and process noise terms typically adopted to embed modeling uncertainties and measurement noise into the physics-based system representation. Under this perspective, the concept of Bayesian inference is outlined in Chapter 2, along with a description of the well-known KF and RTS smoother. In the third section of Chapter 2, basic knowledge of stochastic regression via GPs and STPs is proposed to complement the previously introduced modeling approaches, based on pure mechanistic assumptions, with data-driven strategies relying on observed data only. It is shown that the construction of data-driven models via the proposed strategies is usually performed via batch processing, i.e., by analyzing a set of data previously stored over a certain time period. As such, conventional formulations of these techniques i) do not allow for real-time inference and ii) demand a high computational effort. To remedy these limitations, a framework for state-space representation of both GPs and STPs is proposed in Chapter 2, where it is demonstrated that regression using these stochastic processes can be formulated and solved in a recursive fashion, thus allowing to couple the analyzed data-driven techniques to real-time Bayesian estimators derived from the standard KF. This approach is outlined for several covariance functions adopted in stochastic process regression, even those which are not typically employed within the structural dynamics domain. A thorough analysis of the SDE representation associated to each of the proposed covariance functions is provided by means of an analogy with harmonic oscillators theory. According to the latter, each covariance function produces a stochastic process whose dynamic model features specific properties

(state-space matrices, TF and related poles, i.e., eigenvalues of the system) that make it more suited to approximate certain types of signals.

In Chapter 3, the main data assimilation algorithms for response and load-response estimation are presented. A deterministic approach for response estimation, i.e., the ME method, is first outlined, followed by a description of the most common Bayesian input-state estimators. This chapter starts from highlighting the ME features and its limitations linked to the adopted sensors number and type. Next, a modification of the method is proposed under the name of CMS-ME with the purpose of embedding static deformation into the reduction basis adopted for expanding measured data. This method is particularly useful when information about the unknown input location is available, e.g. during experiments in which the excitation source position is known but cannot be measured, thus allowing to enhance the numerical reduction basis via a prior information regarding the system static response in the analyzed configuration. The CMS-ME method has been employed within the developed A-AKF algorithm described in Chapter 4, where it is proposed as a solution to the intricate task of tuning the AKF for input-state estimation in structural dynamics. By relying on CMS-ME response estimates, the A-AKF performs inference of unknown loads and responses in a near-online fashion without requiring the user intervention for selecting the most suitable time-variant process noise covariance matrix. The latter is tuned adaptively by the algorithm, which is particularly suitable for estimation of long-term monitoring data thanks to the assumption of uncertainties variability embedded in the process noise covariance matrix time-variance. The CMS-ME and A-AKF validity for input-state estimation is proved by means of two different experimental case studies: i) a large scale composite blade during pull and release tests in Chapter 7 and ii) a 3D-printed scaled titanium WT blade undergoing shaker testing in Chapter 8. For both the experiments, the CMS-ME method has proved to provide accurate response estimation, with higher accuracy than ME. The A-AKF formulation developed in Chapter 4 for the inaccuracy indicators has been thus tested for two different excitation scenarios, providing estimations featuring higher accuracy with respect to the conventional AKF. The A-AKF robustness with respect to the user's parameters choice, i.e., time window length and ranges for the process noise terms, has been proved in Chapter 7 by means of two parametric studies.

Chapter 5 elaborates on the unknown input modeling effort posed in the construction of Kalman-based input-state estimators. Specifically, the commonly adopted RW transition model is analyzed and its limitations within the context of vibration testing are highlighted. In this regard, the use of LFMs is proposed as a more comprehensive and flexible alternative to the RW model. LFMs can be constructed by exploiting the SDE representation for stochastic process regression presented in Chapter 2. The GPLFMs proposed in literature for joint input-state estimation in structural dynamics, i.e., foreseeing the use of Matérn covariance function and a combination of KF and RTS smoother for recursive regression, is presented and tested for i) environmental testing of the BARC setup (Chapter 6), ii) pull and release tests of the 3D-printed scaled WT blade and iii) shaker testing (random excitation) of the 3D-printed scaled WT blade (Chapter 8). The results achieved for the three case studies highlight that the GPLFM allows for both accurate response and load predictions, with accuracy comparable to the one achieved by more conventional estimators such as the AKF and the DKF. Additionally, the algorithm applicability for acceleration-only data sets is validated during shaker testing for both the BARC and the 3D-printed scaled blade, thus confirming to overcome the unobservability limitations of the AKF when no displacement-level sensor is available. Following the covariance functions framework presented in Chapter 2, Chapter 5 also proposes a study on the selection of ad hoc GP covariance functions for estimation of standard excitation signals in vibration measurements. The proposed study is validated via a simulated 3 DOFs example in Chapter 5 and for the 3D-printed scaled blade experimental case study in Chapter 8, where regression is performed on a single observation instead of adopting the entire set of measured responses. Additionally, the suggested framework foresees the exclusion of the RTS smoother step from the algorithm to allow for real-time inference. Both the simulated and the experimental applications show that a proper selection of the covariance function adopted for GP regression allows for a more accurate

input estimation, which features a good accuracy even when a single response measurement is used for training the covariance function hyperparameters. Moreover, the simulated example also demonstrates that the use of smoothing introduces accumulation errors in the input and response predictions. Chapter 5 further suggests the use of enhanced regression schemes, more suitable for distorted and noise-contaminated real-life data, such as STP regression for building LFMs within the context of joint input-state estimation. The employment of STPLFMs for input-state estimation is validated in Chapter 7 for an experimental case study concerning shaker testing of a small scale composite WT blade. The analyzed case study shows that the predicted random load time history is less affected by errors when STP is employed instead of GP for regression.

Chapter 6 deals with environmental testing of the BARC setup. Besides comprising an experimental validation example for the data assimilation tools developed in this thesis, this case study introduces modeling challenges derived from the BCs typically adopted during environmental testing. A CMS strategy is employed to build a ROM able to deal with the BARC rigid body motion. The effect of the employed CMS technique on the estimations achieved via the analyzed estimators is evaluated in conjunction with the use of a FE modeling alternative comprising the use of 1D elastic elements to model the BARC-shaker interaction. The response and load predictions reported in Chapter 6 show that the combination of the two modeling strategies allows for a discrete improvement of the AKF performance. The latter is initially evaluated in presence of strains-only or mixed strain and acceleration observations for the original ROM (no modeling of the shaker-BARC interaction). A comparison of the estimations achieved in the two scenarios highlights that the use of a mixed observations set significantly enhances the AKF performance. For this reason, a mixed observations set has been adopted in the case studies presented thereafter for validation of state-of-the-art estimators such as the AKF and the DKF. Specifically, Chapter 8 provides an extensive validation of both conventional and newly developed tools on a scaled WT blade made of isotropic material, thus allowing for a reduced number of modeling uncertainties influencing the results provided by the analyzed data assimilation techniques. To the contrary, Chapter 7 deals with the employment of the methodological tools developed in this thesis for a small scale and a large scale composite blade. It is shown that, despite the updating strategies developed via commercial softwares, the composite material and the limited blade dimension introduce several modeling challenges, as well as limitations in the achievable model updating results, thus influencing the VS predictions accuracy.

10.2 Limitations and recommendations for future directions

The development of VS techniques for dynamic virtualization of structures and mechanical components is treated in this thesis. Although the major challenges arising from the implementation of data assimilation techniques for VS have been addressed, a number of unresolved matters are still to be explored both from the practical and the methodological perspective.

The VS approaches presented in this thesis are valid under the assumption of LTI systems. However, the ever-growing complexity and dimensions of structures may cause nonlinearities, e.g. due to large deformations or material properties. Nonlinear structural behavior is already addressed in literature by means of Kalman-type filters specifically designed to deal with nonlinearities. Further research should consider the uncertainties and input modeling challenges touched upon in this dissertation within the context of nonlinearly-behaving systems.

This thesis adopts laboratory experiments for validating the developed methodological approaches. A future research path comprises the extension of implemented tools for in-field measurements, thereby implying the coupling of real-time operating data with physics-based models embedding information on the structures in operational conditions. This implies the use of more complex models accounting for interactions between several subparts of the systems under study, e.g. multibody models of WTs in operation. A thorough SHM strategy could be then put in place by exploiting the full-field response information produced by VS methods for damage detection algorithms constructed via ML approaches. In this view, physics-based models can be constructed for specific processes and components whose behavior can be discretized via mechanistic assumptions. On the other hand, black-box modeling can be implemented in situations in which lack of information is manifested

leveraging ML algorithms and physically recorded data. The poor availability of information particularly applies to the task of input modeling, which poses multiple challenges due to the distributed nature of loads acting on WT and spacecraft components in operation, and to their unknown locations. These major aspects could be treated within further studies by exploiting spatio-temporal stochastic process regression to produce data-driven a priori models for the unknown loads both in time and space.

An essential feature for VS in this context lies in the real-time applicability of the adopted algorithms, which aim to be as less user-dependent as possible. The methodological tools developed in this thesis could be thus adapted to and exploited in the operational setting. This is in line with the final objective of dynamic virtualization comprising the establishment of a DT from the conceptualization phase to operation and eventually, to end-of-life.

A further direction for future work comprises the combination of VS strategies with innovative sensing technologies such as optical monitoring methodologies. The latters contribute indeed to overcome conventional sensors limitations, e.g. strain gauges and accelerometers, arising from their electrical nature, which is critical for use in the field. To this end, an improved version of the A-AKF applicable for sensors fusion, could be implemented by exploiting frequency domain approaches within the time windows used in the algorithm.

11

APPENDIX

This chapter contains details on some of the tools adopted in the main text.

11.1 Appendix A

In this thesis, the performance of the analyzed data assimilation methods is measured by means of accuracy indicators. The latters are used to quantify both in time and/or frequency domains, how much a prediction resembles the corresponding physically acquired signal. Besides the standard RMSE, the TRAC and FRAC indicators are adopted within this thesis to measure the employed estimators performance. The TRAC formulation is reported in Eq. 11.1, where $\hat{\mathbf{z}}^p$ is the vector of the predicted time histories at the "unmeasured" locations and $\mathbf{z}^p$ contains the corresponding actual responses acquired by physical sensors. In Eq. 11.1, the explicit dependency with respect to time of the signals is omitted.

$$TRAC = \frac{[\mathbf{z}^{p^T}\hat{\mathbf{z}}^p]^2}{[\hat{\mathbf{z}}^{p^T}\hat{\mathbf{z}}^p][\mathbf{z}^{p^T}\mathbf{z}^p]} \tag{11.1}$$

The TRAC quantifies the correlation between the predicted and the measured time histories for a single DOF for a chosen response window. When a good correlation between the measured time signal at a certain location and its corresponding estimated time history is achieved, the TRAC assumes values close to 1. A value that is close to 0, indicates therefore poor estimation accuracy. Similarly to the TRAC, the so-called FRAC reported in Eq. 11.2, quantifies the correlation for one DOF between the estimated $\hat{\mathbf{Z}}^p$ and the measured $\mathbf{Z}^p$ frequency domain signals for the chosen frequency range. In Eq. 11.2, the explicit dependency with respect to frequency of the signals is omitted.

$$FRAC = \frac{[\mathbf{Z}^{p^T}\hat{\mathbf{Z}}^p]^2}{[\hat{\mathbf{Z}}^{p^T}\hat{\mathbf{Z}}^p][\mathbf{Z}^{p^T}\mathbf{Z}^p]}. \tag{11.2}$$

11.2 Appendix B

The state-of-the-art Bayesian estimators exploited in thesis normally require a considerable tuning effort of the process noise covariance matrix. In cases where input estimation is addressed along with state estimation, common practice consists in setting the process noise covariance associated to the system states to a very low number. The covariance of the process noise terms associated with the unknown input are instead tuned offline either via trial and error or by means of the so-called Lcurve, i.e., a regularization method which evaluates the estimator performance by means of two error indicators. The first error term, i.e., the smoothing norm, quantifies the input error estimation as follows:

$$\sum_{k=1}^{n} \|\hat{\mathbf{u}}_k\|_2^2 \tag{11.3}$$

where n is the total number of time steps and $\hat{\mathbf{u}}_k$ is the vector of estimated inputs at the specific point in time k. The error norm is instead related to the inaccuracy featured by the re-estimated

measured responses. Under the assumption of displacement-level measurements only and use of the AKF for joint input-state estimation, the error norm can be constructed as:

$$\sum_{k=1}^{n} \|\mathbf{y}_k^o - \mathbf{H}_o^a \hat{\mathbf{x}}_k^{a+}\|_2^2 \tag{11.4}$$

where $\mathbf{y}^o$ is the observations vector, $\hat{\mathbf{x}}^{a+}$ is the posterior estimate of the augmented state vector and $\mathbf{H}_o^a$ is the augmented output matrix calculated at the measured DOFs.

BIBLIOGRAPHY

[1] Bart Peeters, Herman Van der Auweraer, Patrick Guillaume, and Jan Leuridan. "The PolyMAX frequency-domain method: a new standard for modal parameter estimation?" In: *Shock and Vibration* 11.3-4 (2004), pp. 395–409.

[2] Mahmoud Elkafafy, Bart Peeters, Tim De Troyer, and Patrick Guillaume. "Polymax Plus: better estimation of the modal parameters and their confidence bounds." English. In: *In Proceedings of In Proceedings of the International Conference On Noise and Vibration Engineering (ISMA) Leuven, Belgium*. PROCEEDINGS OF ISMA2014 INCLUDING USD2014; International Conference on Noise and Vibration Engineering, ISMA2014 - USD2014 ; Conference date: 19-09-2014 Through 21-09-2014. ISMA 2014, Sept. 2014, pp. 2491–2506.

[3] BART PEETERS and GUIDO DE ROECK. "REFERENCE-BASED STOCHASTIC SUBSPACE IDENTIFICATION FOR OUTPUT-ONLY MODAL ANALYSIS." In: *Mechanical Systems and Signal Processing* 13.6 (1999), pp. 855–878. ISSN: 0888-3270. DOI: https://doi.org/10.1006/mssp.1999.1249. URL: https://www.sciencedirect.com/science/article/pii/S0888327099912499.

[4] Mahmoud Elkafafy and Bart Peeters. "Robust Identification of Stable MIMO Modal State Space Models." In: *Topics in Modal Analysis & Parameter Identification, Volume 8*. Ed. by Brandon J. Dilworth, Timothy Marinone, and Michael Mains. Cham: Springer International Publishing, 2023, pp. 81–95. ISBN: 978-3-031-05445-7.

[5] Olek C Zienkiewicz, Robert Leroy Taylor, and Jian Z Zhu. *The finite element method: its basis and fundamentals*. Elsevier, 2005.

[6] Christof Devriendt, Filipe Magalhães, Mahmoud El Kafafy, Gert De Sitter, Álvaro Cunha, and Patrick Guillaume. "Long-term dynamic monitoring of an offshore wind turbine." In: *Topics in Dynamics of Civil Structures, Volume 4: Proceedings of the 31st IMAC, A Conference on Structural Dynamics, 2013*. Springer. 2013, pp. 253–267.

[7] Christof Devriendt, Filipe Magalhães, Wout Weijtjens, Gert De Sitter, Álvaro Cunha, and Patrick Guillaume. "Structural health monitoring of offshore wind turbines using automated operational modal analysis." In: *Structural Health Monitoring* 13.6 (2014), pp. 644–659.

[8] N Dervilis, M Choi, SG Taylor, RJ Barthorpe, G Park, CR Farrar, and K Worden. "On damage diagnosis for a wind turbine blade using pattern recognition." In: *Journal of sound and vibration* 333.6 (2014), pp. 1833–1850.

[9] George Tsialiamanis, MD Champneys, Nikolaos Dervilis, David J Wagg, and Keith Worden. "On the application of generative adversarial networks for nonlinear modal analysis." In: *Mechanical Systems and Signal Processing* 166 (2022), p. 108473.

[10] Kartik Chandrasekhar, Nevena Stevanovic, Elizabeth J Cross, Nikolaos Dervilis, and Keith Worden. "Damage detection in operational wind turbine blades using a new approach based on machine learning." In: *Renewable Energy* 168 (2021), pp. 1249–1264.

[11] Imad Abdallah, V Dertimanis, H Mylonas, Konstantinos Tatsis, Eleni Chatzi, N Dervili, K Worden, and Eoghan Maguire. "Fault diagnosis of wind turbine structures using decision tree learning algorithms with big data." In: *Safety and Reliability–Safe Societies in a Changing World*. CRC Press, 2018, pp. 3053–3061.

[12] MD Champneys, G Tsialiamanis, TJ Rogers, N Dervilis, and K Worden. "On the dynamic properties of statistically-independent nonlinear normal modes." In: *Mechanical Systems and Signal Processing* 181 (2022), p. 109510.

[13] Thomas Simpson, George Tsialiamanis, Nikolaos Dervilis, Keith Worden, and Eleni Chatzi. "On the Use of Variational Autoencoders for Nonlinear Modal Analysis." In: *Nonlinear Structures & Systems, Volume 1*. Ed. by Matthew R.W. Brake, Ludovic Renson, Robert J. Kuether, and Paolo Tiso. Cham: Springer International Publishing, 2023, pp. 297–300. ISBN: 978-3-031-04086-3.

[14] Nikolaos Dervilis, Thomas E Simpson, David J Wagg, and Keith Worden. "Nonlinear modal analysis via non-parametric machine learning tools." In: *Strain* 55.1 (2019), e12297.

[15] Michael Friswell and John E Mottershead. *Finite element model updating in structural dynamics*. Vol. 38. Springer Science & Business Media, 1995.

[16] Reza Jafarkhani and Sami F Masri. "Finite element model updating using evolutionary strategy for damage detection." In: *Computer-Aided Civil and Infrastructure Engineering* 26.3 (2011), pp. 207–224.

[17] Anne Teughels, Johan Maeck, and Guido De Roeck. "Damage assessment by FE model updating using damage functions." In: *Computers & structures* 80.25 (2002), pp. 1869–1879.

[18] Bijaya Jaishi and Wei-Xin Ren. "Structural finite element model updating using ambient vibration test results." In: *Journal of structural engineering* 131.4 (2005), pp. 617–628.

[19] Adolphus Lye, Alice Cicirello, and Edoardo Patelli. "Sampling methods for solving Bayesian model updating problems: A tutorial." In: *Mechanical Systems and Signal Processing* 159 (2021), p. 107760. ISSN: 0888-3270. DOI: https://doi.org/10.1016/j.ymssp.2021.107760. URL: https://www.sciencedirect.com/science/article/pii/S0888327021001552.

[20] Lambros S Katafygiotis, Costas Papadimitriou, and Heung-Fai Lam. "A probabilistic approach to structural model updating." In: *Soil Dynamics and Earthquake Engineering* 17.7-8 (1998), pp. 495–507.

[21] Lambros S Katafygiotis and Jim L Beck. "Updating models and their uncertainties. II: Model identifiability." In: *Journal of Engineering Mechanics* 124.4 (1998), pp. 463–467.

[22] Jianye Ching and Yi-Chu Chen. "Transitional Markov chain Monte Carlo method for Bayesian model updating, model class selection, and model averaging." In: *Journal of engineering mechanics* 133.7 (2007), pp. 816–832.

[23] Thomas Simpson, Vasilis Dertimanis, Costas Papadimitriou, and Eleni Chatzi. "On the potential of dynamic sub-structuring methods for model updating." In: *Structural Health Monitoring 2019* (2019).

[24] Hector A Jensen, Eduardo Millas, D Kusanovic, and Costas Papadimitriou. "Model-reduction techniques for Bayesian finite element model updating using dynamic response data." In: *Computer Methods in Applied Mechanics and Engineering* 279 (2014), pp. 301–324.

[25] Costas Papadimitriou and Dimitra-Christina Papadioti. "Component mode synthesis techniques for finite element model updating." In: *Computers & structures* 126 (2013), pp. 15–28.

[26] Roy R Craig Jr. "A review of time-domain and frequency-domain component mode synthesis method." In: (1985).

[27] Karl Kunisch and Stefan Volkwein. "Galerkin proper orthogonal decomposition methods for parabolic problems." In: *Numerische mathematik* 90.1 (2001), pp. 117–148.

[28] Christian H Meyer and Daniel Rixen. "Global proper orthogonal decomposition for parametric model reduction of geometrically nonlinear structures." In: *PAMM* 19.1 (2019), e201900436.

[29] Gianluigi Rozza. "Fundamentals of reduced basis method for problems governed by parametrized PDEs and applications." In: *Separated representations and PGD-based model reduction*. Springer, 2014, pp. 153–227.

[30] Nikolaos Tsokanas, Thomas Simpson, Roland Pastorino, Eleni Chatzi, and B Stojadinović. "Model order reduction for real-time hybrid simulation: Comparing polynomial chaos expansion and neural network methods." In: *Mechanism and Machine Theory* 178 (2022), p. 105072.

[31] Thomas Simpson, Nikolaos Dervilis, and Eleni Chatzi. "Machine learning approach to model order reduction of nonlinear systems via autoencoder and LSTM networks." In: *Journal of Engineering Mechanics* 147.10 (2021), p. 04021061.

[32] Thomas Simpson, Nikolaos Dervilis, and Eleni Chatzi. "On the use of nonlinear normal modes for nonlinear reduced order modelling." In: *arXiv preprint arXiv:2007.00466* (2020).

[33] Thomas Simpson, Nikolaos Dervilis, Philippe Couturier, Nico Maljaars, and Eleni Chatzi. "Nonlinear Reduced Order Modelling of Soil Structure Interaction Effects via LSTM and Autoencoder Neural Networks." In: *arXiv preprint arXiv:2203.01842* (2022).

[34] Peter Avitabile and Pawan Pingle. "Prediction of full field dynamic strain from limited sets of measured data." In: *Shock and vibration* 19.5 (2012), pp. 765–785.

[35] Tulay Ercan and Costas Papadimitriou. "Optimal Sensor Placement for Reliable Virtual Sensing Using Modal Expansion and Information Theory." In: *Sensors* 21.10 (2021). ISSN: 1424-8220. URL: https://www.mdpi.com/1424-8220/21/10/3400.

[36] Alexandros Iliopoulos, Rasoul Shirzadeh, Wout Weijtjens, Patrick Guillaume, Danny Van Hemelrijck, and Christof Devriendt. "A modal decomposition and expansion approach for prediction of dynamic responses on a monopile offshore wind turbine using a limited number of vibration sensors." In: *Mechanical Systems and Signal Processing* 68 (2016), pp. 84–104.

[37] Marius Tarpø, Bruna Nabuco, Christos Georgakis, and Rune Brincker. "Expansion of experimental mode shape from operational modal analysis and virtual sensing for fatigue analysis using the modal expansion method." In: *International Journal of Fatigue* 130 (2020), p. 105280. ISSN: 0142-1123. DOI: https://doi.org/10.1016/j.ijfatigue.2019.105280. URL: https://www.sciencedirect.com/science/article/pii/S0142112319303846.

[38] Kristof Maes, A Iliopoulos, W Weijtjens, C, and Geert Lombaert. "Dynamic strain estimation for fatigue assessment of an offshore monopile wind turbine using filtering and modal expansion algorithms." In: *Mechanical Systems and Signal Processing* 76 (2016), pp. 592–611.

[39] Vasilis K Dertimanis, EN Chatzi, S Eftekhar Azam, and Costas Papadimitriou. "Input-state-parameter estimation of structural systems from limited output information." In: *Mechanical Systems and Signal Processing* 126 (2019), pp. 711–746.

[40] Costas Papadimitriou, Claus-Peter Fritzen, Peter Kraemer, and Evangelos Ntotsios. "Fatigue predictions in entire body of metallic structures from a limited number of vibration sensors using Kalman filtering." In: *Structural Control and Health Monitoring* 18.5 (2011), pp. 554–573.

[41] K.E. Tatsis, V.K. Dertimanis, C. Papadimitriou, E. Lourens, and E.N. Chatzi. "A general substructure-based framework for input-state estimation using limited output measurements." In: *Mechanical Systems and Signal Processing* 150 (2021), p. 107223. ISSN: 0888-3270. DOI: https://doi.org/10.1016/j.ymssp.2020.107223. URL: https://www.sciencedirect.com/science/article/pii/S0888327020306099.

[42] Konstantinos Tatsis, Vasilis Dertimanis, and Eleni Chatzi. "Response Prediction of Systems Experiencing Operational and Environmental Variability." In: *Computing in Civil Engineering 2019: Smart Cities, Sustainability, and Resilience*. American Society of Civil Engineers Reston, VA, 2019, pp. 468–474.

[43] Konstantinos E Tatsis, Vasilis K Dertimanis, and Eleni N Chatzi. "Adaptive Process and Measurement Noise Identification for Recursive Bayesian Estimation." In: *Model Validation and Uncertainty Quantification, Volume 3*. Springer, 2020, pp. 361–364.

[44] R Cumbo, T Tamarozzi, K Janssens, and W Desmet. "Kalman-based load identification and full-field estimation analysis on industrial test case." In: *Mechanical Systems and Signal Processing* 117 (2019), pp. 771–785.

[45] Enrico Risaliti, Tommaso Tamarozzi, Martijn Vermaut, Bram Cornelis, and Wim Desmet. "Multibody model based estimation of multiple loads and strain field on a vehicle suspension system." In: *Mechanical Systems and Signal Processing* 123 (2019), pp. 1–25.

[46] Eleni N Chatzi and Andrew W Smyth. "The unscented Kalman filter and particle filter methods for nonlinear structural system identification with non-collocated heterogeneous sensing." In: *Structural Control and Health Monitoring: The Official Journal of the International Association for Structural Control and Monitoring and of the European Association for the Control of Structures* 16.1 (2009), pp. 99–123.

[47] Stefano Mariani and Aldo Ghisi. "Unscented Kalman filtering for nonlinear structural dynamics." In: *Nonlinear Dynamics* 49.1 (2007), pp. 131–150.

[48] Konstantinos Tatsis, Long Wu, Paolo Tiso, and Eleni Chatzi. "State estimation of geometrically non-linear systems using reduced-order models." In: *Life Cycle Analysis and Assessment in Civil Engineering: Towards an Integrated Vision* (2018), pp. 219–227.

[49] E Lourens, Edwin Reynders, Guido De Roeck, Geert Degrande, and Geert Lombaert. "An augmented Kalman filter for force identification in structural dynamics." In: *Mechanical Systems and Signal Processing* 27 (2012), pp. 446–460.

[50] Frank Naets, Javier Cuadrado, and Wim Desmet. "Stable force identification in structural dynamics using Kalman filtering and dummy-measurements." In: *Mechanical Systems and Signal Processing* 50 (2015), pp. 235–248.

[51] Saeed Eftekhar Azam, Eleni Chatzi, and Costas Papadimitriou. "A dual Kalman filter approach for state estimation via output-only acceleration measurements." In: *Mechanical Systems and Signal Processing* 60 (2015), pp. 866–886.

[52] Saeed Eftekhar Azam, Eleni Chatzi, Costas Papadimitriou, and Andrew Smyth. "Experimental validation of the Kalman-type filters for online and real-time state and input estimation." In: *Journal of vibration and control* 23.15 (2017), pp. 2494–2519.

[53] Chien-Shu Hsieh. "Optimal time-delayed joint input and state estimation for systems with unknown inputs." In: *Proceedings of the 48h IEEE Conference on Decision and Control (CDC) held jointly with 2009 28th Chinese Control Conference*. IEEE. 2009, pp. 4426–4431.

[54] Chien-Shu Hsieh. "Unbiased minimum-variance input and state estimation for systems with unknown inputs: A system reformation approach." In: *Automatica* 84 (2017), pp. 236–240.

[55] Kristof Maes, Steven Gillijns, and Geert Lombaert. "A smoothing algorithm for joint input-state estimation in structural dynamics." In: *Mechanical Systems and Signal Processing* 98 (2018), pp. 292–309.

[56] Kristof Maes, E Lourens, Katrien Van Nimmen, Edwin Reynders, Guido De Roeck, and Geert Lombaert. "Design of sensor networks for instantaneous inversion of modally reduced order models in structural dynamics." In: *Mechanical Systems and Signal Processing* 52 (2015), pp. 628–644.

[57] Roberta Cumbo, Lorenzo Mazzanti, Tommaso Tamarozzi, Pavel Jiranek, Wim Desmet, and Frank Naets. "Advanced optimal sensor placement for Kalman-based multiple-input estimation." In: *Mechanical Systems and Signal Processing* 160 (2021), p. 107830.

[58] Lorenzo Mazzanti, Roberta Cumbo, Wim Desmet, Frank Naets, and Tommaso Tamarozzi. "An Improved Optimal Sensor Placement Strategy for Kalman-Based Multiple-Input Estimation." In: *Model Validation and Uncertainty Quantification, Volume 3*. Springer, 2020, pp. 181–185.

[59] Tulay Ercan, Konstantinos Tatsis, Victor Flores Terrazas, Eleni Chatzi, and Costas Papadimitriou. "Optimal Sensor Configuration Design for Virtual Sensing in a Wind Turbine Blade Using Information Theory." In: *Model Validation and Uncertainty Quantification, Volume 3: Proceedings of the 40th IMAC, A Conference and Exposition on Structural Dynamics 2022*. Springer. 2022, pp. 67–70.

[60] Tulay Ercan, Omid Sedehi, Lambros S Katafygiotis, and Costas Papadimitriou. "Information theoretic-based optimal sensor placement for virtual sensing using augmented Kalman filtering." In: *Mechanical Systems and Signal Processing* 188 (2023), p. 110031.

[61] Simon J Julier, Jeffrey K Uhlmann, and Hugh F Durrant-Whyte. "A new approach for filtering nonlinear systems." In: *Proceedings of 1995 American Control Conference-ACC'95*. Vol. 3. IEEE. 1995, pp. 1628–1632.

[62] Simon J Julier and Jeffrey K Uhlmann. "New extension of the Kalman filter to nonlinear systems." In: *Signal processing, sensor fusion, and target recognition VI*. Vol. 3068. International Society for Optics and Photonics. 1997, pp. 182–193.

[63] Behrouz Safarinejadian and Navid Vafamand. "Kalman randomized joint UKF algorithm for dual estimation of states and parameters in a nonlinear system." In: *Journal of Electrical Engineering and Technology* 10.3 (2015), pp. 1212–1220.

[64] Eleni N Chatzi and Clemente Fuggini. "Online correction of drift in structural identification using artificial white noise observations and an unscented Kalman filter." In: *Smart Struct. Syst* 16.2 (2015), pp. 295–328.

[65] Christopher K Williams and Carl Edward Rasmussen. *Gaussian processes for machine learning*. Vol. 2. 3. MIT press Cambridge, MA, 2006.

[66] Jouni Hartikainen and Simo Särkkä. "Kalman filtering and smoothing solutions to temporal Gaussian process regression models." In: *2010 IEEE international workshop on machine learning for signal processing*. IEEE. 2010, pp. 379–384.

[67] Jouni Hartikainen and Simo Sarkka. "Sequential inference for latent force models." In: *arXiv preprint arXiv:1202.3730* (2012).

[68] Simo Särkkä, Mauricio A Alvarez, and Neil D Lawrence. "Gaussian process latent force models for learning and stochastic control of physical systems." In: *IEEE Transactions on Automatic Control* 64.7 (2018), pp. 2953–2960.

[69] Mauricio A Álvarez, David Luengo, and Neil D Lawrence. "Linear latent force models using Gaussian processes." In: *IEEE transactions on pattern analysis and machine intelligence* 35.11 (2013), pp. 2693–705. DOI: 10.1109/TPAMI.2013.86.

[70] Mauricio Alvarez, David Luengo, and Neil D Lawrence. "Latent force models." In: *Artificial Intelligence and Statistics*. PMLR. 2009, pp. 9–16.

[71] Rajdip Nayek, Souvik Chakraborty, and Sriram Narasimhan. "A Gaussian process latent force model for joint input-state estimation in linear structural systems." In: *Mechanical Systems and Signal Processing* 128 (2019), pp. 497–530.

[72] TJ Rogers, K Worden, and EJ Cross. "On the application of Gaussian process latent force models for joint input-state-parameter estimation: With a view to Bayesian operational identification." In: *Mechanical Systems and Signal Processing* 140 (2020), p. 106580.

[73] Konstantinos Tatsis, Vasilis K Dertimanis, Timothy J Rogers, Elizabeth Cross, Keith Worden, and Eleni Chatzi. "A spatiotemporal dual Kalman filter for the estimation of states and distributed inputs in dynamical systems." In: *Proceedings of ISMA-USD 2020* (2020), pp. 3591–3597.

[74] Steven Gillijns and Bart De Moor. "Unbiased minimum-variance input and state estimation for linear discrete-time systems." In: *Automatica* 43.1 (2007), pp. 111–116.

[75] Peter K. Kitanidis. "Unbiased minimum-variance linear state estimation." In: *Automatica* 23.6 (1987), pp. 775–778. ISSN: 0005-1098. DOI: https://doi.org/10.1016/0005-1098(87)90037-9. URL: https://www.sciencedirect.com/science/article/pii/0005109887900379.

[76] Bernard Delyon and Qinghua Zhang. "On the optimality of the Kitanidis filter for state estimation rejecting unknown inputs." In: *Automatica* 132 (2021), p. 109793.

[77] Steven Gillijns and Bart De Moor. "Unbiased minimum-variance input and state estimation for linear discrete-time systems with direct feedthrough." In: *Automatica* 43.5 (2007), pp. 934–937.

[78] E Lourens, Costas Papadimitriou, Steven Gillijns, Edwin Reynders, Guido De Roeck, and Geert Lombaert. "Joint input-response estimation for structural systems based on reduced-order models and vibration data from a limited number of sensors." In: *Mechanical Systems and Signal Processing* 29 (2012), pp. 310–327.

[79] Konstantinos Tatsis, Vasilis Dertimanis, Imad Abdallah, and Eleni Chatzi. "A substructure approach for fatigue assessment on wind turbine support structures using output-only measurements." In: *Procedia engineering* 199 (2017), pp. 1044–1049.

[80] Nymfa Noppe, Konstantinos Tatsis, Eleni Chatzi, Christof Devriendt, and Wout Weijtjens. "Fatigue stress estimation of offshore wind turbine using a Kalman filter in combination with accelerometers." In: *Proceedings of the ISMA*. 2018, p. 9.

[81] Sofia Puerto Tchemodanova, Masoud Sanayei, Babak Moaveni, Konstantinos Tatsis, and Eleni Chatzi. "Strain predictions at unmeasured locations of a substructure using sparse response-only vibration measurements." In: *Journal of Civil Structural Health Monitoring* 11.4 (2021), pp. 1113–1136.

[82] Sergio Bittanti and Sergio M Savaresi. "On the parametrization and design of an extended Kalman filter frequency tracker." In: *IEEE transactions on automatic control* 45.9 (2000), pp. 1718–1724.

[83] Murali R Rajamani and James B Rawlings. "Estimation of the disturbance structure from data using semidefinite programming and optimal weighting." In: *Automatica* 45.1 (2009), pp. 142–148.

[84] Ka-Veng Yuen, Ka-In Hoi, and Kai-Meng Mok. "Selection of noise parameters for Kalman filter." In: *Earthquake Engineering and Engineering Vibration* 6.1 (2007), pp. 49–56.

[85] Per Christian Hansen and Dianne Prost O'Leary. "The use of the L-curve in the regularization of discrete ill-posed problems." In: *SIAM Journal on Scientific Computing* 14.6 (1993), pp. 1487–1503.

[86] Ulrika Lagerblad, Henrik Wentzel, and Artem Kulachenko. "Dynamic response identification based on state estimation and operational modal analysis." In: *Mechanical Systems and Signal Processing* 129 (2019), pp. 37–53.

[87] Raman Mehra. "Approaches to adaptive filtering." In: *IEEE Transactions on automatic control* 17.5 (1972), pp. 693–698.

[88] Charles G Hilborn and Demetrios G Lainiotis. "Optimal estimation in the presence of unknown parameters." In: *IEEE Transactions on Systems Science and Cybernetics* 5.1 (1969), pp. 38–43.

[89] R Kashyap. "Maximum likelihood identification of stochastic linear systems." In: *IEEE Transactions on Automatic Control* 15.1 (1970), pp. 25–34.

[90] Raman Mehra. "On the identification of variances and adaptive Kalman filtering." In: *IEEE Transactions on automatic control* 15.2 (1970), pp. 175–184.

[91] R Mehra. "On-line identification of linear dynamic systems with applications to Kalman filtering." In: *IEEE Transactions on Automatic Control* 16.1 (1971), pp. 12–21.

[92] Brian J Odelson, Murali R Rajamani, and James B Rawlings. "A new autocovariance least-squares method for estimating noise covariances." In: *Automatica* 42.2 (2006), pp. 303–308.

[93] Stefan Wernitz, Eleni Chatzi, Benedikt Hofmeister, Marlene Wolniak, Wanzhou Shen, and Raimund Rolfes. "On noise covariance estimation for Kalman filter-based damage localization." In: *Mechanical Systems and Signal Processing* 170 (2022), p. 108808.

[94] S.C. Rutan. "Adaptive Kalman filtering." In: *Analytical Chemistry* 63.22 (1991), pp. 1103–1109.

[95] Peter Avitabile. "Why you can't ignore those vibration fixture resonances." In: *Sound and Vibration* 33 (1999), pp. 20–27.

[96] Julie M Harvie and Randy Mayes. "Quantification of dynamic differences between boundary conditions for environment specification improvement." In: *Shock & Vibration, Aircraft/Aerospace, Energy Harvesting, Acoustics & Optics, Volume 9: Proceedings of the 34th IMAC, A Conference and Exposition on Structural Dynamics 2016*. Springer. 2016, pp. 117–131.

[97] Troy J Skousen and David Soine. *Boundary Conditions in Environmental Testing Round Robin.* Tech. rep. Sandia National Lab.(SNL-NM), Albuquerque, NM (United States), 2018.

[98] Daniel Peter Rohe. *Modal data for the BARC challenge problem Test Report.* Tech. rep. Sandia National Lab.(SNL-NM), Albuquerque, NM (United States), 2018.

[99] William Larsen, Jason R Blough, James P DeClerck, Charles D VanKarsen, David E Soine, and Richard Jones. "Initial modal results and operating data acquisition of shock/vibration fixture." In: *Topics in Modal Analysis & Testing, Volume 9*. Springer, 2019, pp. 363–370.

[100] Umberto Musella, Mariano Alvarez Blanco, Davide Mastrodicasa, Giovanni Monco, Manzato Simone, Bart Peeters, Emiliano Mucchi, Patrick Guillaume, et al. "Combining Test and Simulation to Tackle the Challenges Derived from Boundary Conditions Mismatches in Environmental Testing." In: *Sensors and Instrumentation, Aircraft/Aerospace, Energy Harvesting & Dynamic Environments Testing, Volume 7*. Springer, 2020, pp. 259–269.

[101] Daniel P Rohe, Ryan A Schultz, Tyler F Schoenherr, Troy J Skousen, and Richard J Jones. "Comparison of multi-axis testing of the BARC structure with varying boundary conditions." In: *Sensors and Instrumentation, Aircraft/Aerospace, Energy Harvesting & Dynamic Environments Testing, Volume 7: Proceedings of the 37th IMAC, A Conference and Exposition on Structural Dynamics 2019*. Springer. 2020, pp. 179–193.

[102] Daniel P Rohe, Scott Smith, Matthew RW Brake, James DeClerck, Mariano Alvarez Blanco, Tyler F Schoenherr, and Troy J Skousen. "Testing summary for the box assembly with removable component structure." In: *Sensors and Instrumentation, Aircraft/Aerospace, Energy Harvesting & Dynamic Environments Testing, Volume 7*. Springer, 2020, pp. 167–177.

[103] David E Soine, Richard J Jones, Julie M Harvie, Troy J Skousen, and Tyler F Schoenherr. "Designing hardware for the boundary condition round robin challenge." In: *Topics in Modal Analysis & Testing, Volume 9: Proceedings of the 36th IMAC, A Conference and Exposition on Structural Dynamics 2018*. Springer. 2019, pp. 119–126.

[104] Heorhi Brzhezinski, Silvia Vettori, Emilio Di Lorenzo, Bart Peeters, Eleni Chatzi, and Francesco Cosco. "On the Dynamic Virtualization of a 3D-Printed Scaled Wind Turbine Blade." In: *Model Validation and Uncertainty Quantification, Volume 3: Proceedings of the 40th IMAC, A Conference and Exposition on Structural Dynamics 2022*. Springer. 2022, pp. 31–39.

[105] International Electrotechnical Commission et al. "International standard iec 61400-23 Wind turbine generator systems–part 23: full-scale structural testing of rotor blades." In: *Wind Turbines-Part* 1 (2014).

[106] Hak Gu Lee and Jisang Park. "Static test until structural collapse after fatigue testing of a full-scale wind turbine blade." In: *Composite Structures* 136 (2016), pp. 251–257. ISSN: 0263-8223. DOI: https://doi.org/10.1016/j.compstruct.2015.10.007. URL: https://www.sciencedirect.com/science/article/pii/S0263822315009381.

[107] Jinshui Yang, Chaoyi Peng, Jiayu Xiao, Jingcheng Zeng, Suli Xing, Jiaotong Jin, and Hang Deng. "Structural investigation of composite wind turbine blade considering structural collapse in full-scale static tests." In: *Composite Structures* 97 (2013), pp. 15–29. ISSN: 0263-8223. DOI: https://doi.org/10.1016/j.compstruct.2012.10.055. URL: https://www.sciencedirect.com/science/article/pii/S0263822312005569.

[108] Peter R Greaves, Robert G Dominy, Grant L Ingram, Hui Long, and Richard Court. "Evaluation of dual-axis fatigue testing of large wind turbine blades." In: *Proceedings of the Institution of Mechanical Engineers, Part C: Journal of Mechanical Engineering Science* 226.7 (2012), pp. 1693–1704.

[109] Oscar Castro, Federico Belloni, Mathias Stolpe, Süleyman Cem Yeniceli, Peter Berring, and Kim Branner. "Optimized method for multi-axial fatigue testing of wind turbine blades." In: *Composite Structures* 257 (2021), p. 113358.

[110] Xiao Chen, Sergei Semenov, Malcolm McGugan, Steen Hjelm Madsen, Süleyman Cem Yeniceli, Peter Berring, and Kim Branner. "Fatigue testing of a 14.3 m composite blade embedded with artificial defects–damage growth and structural health monitoring." In: *Composites Part A: Applied Science and Manufacturing* 140 (2021), p. 106189.

[111] Othman Al-Khudairi, Homayoun Hadavinia, Christian Little, Gavin Gillmore, Peter Greaves, and Kirsten Dyer. "Full-scale fatigue testing of a wind turbine blade in flapwise direction and examining the effect of crack propagation on the blade performance." In: *Materials* 10.10 (2017), p. 1152.

[112] Kari Williamson. "Push and pull – testing wind turbine blades." In: *Reinforced Plastics* 56.1 (2012), pp. 26–32. ISSN: 0034-3617. DOI: https://doi.org/10.1016/S0034-3617(12)70034-6. URL: https://www.sciencedirect.com/science/article/pii/S0034361712700346.

[113] M. M. Luczak, B. Peeters, S. Manzato, E. Di Lorenzo, K. Reck-Nielsen, P. Berring, P. U. Haselbach, and K. Branner. "Research sized wind turbine blade modal tests: comparison of the impact excitation with shaker excitation." In: *Journal of Physics: Conference Series* 1102 (2018), p. 012022. DOI: 10.1088/1742-6596/1102/1/012022.

[114] Marcin Luczak, Simone Manzato, Bart Peeters, Kim Branner, Peter Berring, and Maciej Kahsin. "Dynamic investigation of twist-bend coupling in a wind turbine blade." In: *Journal of Theoretical and Applied Mechanics* 49.3 (2011), pp. 765–789.

[115] Peter Berring, Kim Branner, Christian Berggreen, and Henrik W Knudsen. "Torsional performance of wind turbine blades-Part 1: Experimental investigation." In: *16th International Conference on Composite Materials*. Vol. 43. 2007.

[116] D Todd Griffith and Thomas G Carne. "Experimental modal analysis of 9-meter research-sized wind turbine blades." In: *Structural Dynamics and Renewable Energy, Volume 1*. Springer, 2011, pp. 1–14.

[117] Sarah Reese, Daniel Todd Griffith, Miguel Casias, Todd William Simmermacher, and Gregory A Smith. *Modal testing of the TX-100 wind turbine blade*. Tech. rep. Sandia National Laboratories, 2006.

[118] GC Larsen, MH Hansen, A Baumgart, and I Carlen. "Modal Analysis of Wind Turbine Blades (Risø-R-1181 (EN))." In: *Roskilde: Riso National Laboratory* (2002).

[119] E. Di Lorenzo, S. Manzato, B. Peeters, V. Ruffini, P. Berring, P. U. Haselbach, K. Branner, and M. M. Luczak. "Modal Analysis of Wind Turbine Blades with Different Test Setup Configurations." In: *Topics in Modal Analysis & Testing, Volume 8*. Ed. by Michael L. Mains and Brandon J. Dilworth. Cham: Springer International Publishing, 2020, pp. 143–152.

[120] E di Lorenzo, S Manzato, Marcin Luczak, B Peeters, and Kim Branner. "Strain-based operational modal analysis for wind turbine blades." In: *8th International Operational Modal Analysis Conference*. IOMAC. 2019.

[121] C. Grinderslev, F. Belloni, S. G. Horcas, and N. N. Sørensen. "Investigations of aerodynamic drag forces during structural blade testing using high-fidelity fluid–structure interaction." In: *Wind Energy Science* 5.2 (2020), pp. 543–560. DOI: 10.5194/wes-5-543-2020. URL: https://wes.copernicus.org/articles/5/543/2020/.

[122] J Kullaa. "Bayesian virtual sensing in structural dynamics." In: *Mechanical Systems and Signal Processing* 115 (2019), pp. 497–513.

[123] Jyrki Kullaa. "Virtual sensing of structural vibrations using dynamic substructuring." In: *Mechanical Systems and Signal Processing* 79 (2016), pp. 203–224.

[124] Peter Avitabile. "Model reduction and model expansion and their applications–part 1 theory." In: *Proceedings of the Twenty-Third International Modal Analysis Conference, Orlando, FL, USA*. 2005.

[125] Armando Barreto, Malek Adjouadi, Francisco R. Ortega, and Nonnarit O-larnnithipong. *"Intuitive understanding of Kalman filtering with MATLAB"*. en. First edition. Boca Raton, FL: CRC Press, 2020. ISBN: 978-0-367-19135-1 978-0-367-19133-7.

[126] R CRAIG JR. "On the use of attachment modes in substructure coupling for dynamic analysis." In: *18th structural dynamics and materials conference*. 1977, p. 405.

[127] Charles Van Loan. "Computing integrals involving the matrix exponential." In: *IEEE transactions on automatic control* 23.3 (1978), pp. 395–404.

[128] R. E. Kalman. "A New Approach to Linear Filtering and Prediction Problems." In: *Journal of Basic Engineering* 82.1 (Mar. 1960), pp. 35–45. ISSN: 0021-9223. DOI: 10.1115/1.3662552. URL: https://doi.org/10.1115/1.3662552 (visited on 12/31/2021).

[129] Amar Shah, Andrew Wilson, and Zoubin Ghahramani. "Student-t processes as alternatives to Gaussian processes." In: *Artificial intelligence and statistics*. PMLR. 2014, pp. 877–885.

[130] Arno Solin and Simo Särkkä. "Explicit link between periodic covariance functions and state space models." In: *Artificial Intelligence and Statistics*. PMLR. 2014, pp. 904–912.

[131] Arno Solin and Simo Särkkä. "State space methods for efficient inference in Student-t process regression." In: *Artificial Intelligence and Statistics*. PMLR. 2015, pp. 885–893.

[132] I.I. Gikhman, A.V. Skorokhod, and S. Kotz. *The Theory of Stochastic Processes: I*. Vol. 1. Classics in Mathematics. Springer Berlin Heidelberg, 2004. ISBN: 9783540202844. URL: https://books.google.nl/books?id=HBDiMpORJkoC.

[133] Chris Chatfield. *The analysis of time series: an introduction*. Chapman and hall/CRC, 2003.

[134] Morris Tenenbaum and Harry Pollard. *Ordinary differential equations: an elementary textbook for students of mathematics, engineering, and the sciences*. Courier Corporation, 1985.

[135] Frank Naets, Jan Croes, and Wim Desmet. "An online coupled state/input/parameter estimation approach for structural dynamics." In: *Computer Methods in Applied Mechanics and Engineering* 283 (2015), pp. 1167–1188.

[136] Imad Abdallah, Konstantinos Tatsis, and Eleni Chatzi. "Fatigue assessment of a wind turbine blade when output from multiple aero-elastic simulators are available." In: *Procedia Engineering* 199 (2017), pp. 3170–3175.

[137] Matthew B Rhudy, Roger A Salguero, and Keaton Holappa. "A Kalman Filtering Tutorial for Undergraduate Students." en. In: *International Journal of Computer Science & Engineering Survey* 08.01 (Feb. 2017), pp. 01–18. ISSN: 09763252, 09762760. DOI: 10.5121/ijcses.2017.8101. URL: http://aircconline.com/ijcses/V8N1/8117ijcses01.pdf (visited on 01/18/2022).

[138] Tommaso Tamarozzi, Enrico Risaliti, Ward Rottiers, Wim Desmet, et al. "Noise, ill-conditioning and sensor placement analysis for force estimation through virtual sensing." In: *In International Conference on Noise and Vibration Engineering (ISMA2016),* KATHOLIEKE UNIV LEUVEN, DEPT WERKTUIGKUNDE. 2016, pp. 1741–1756.

[139] Silvia Vettori, Emilio Di Lorenzo, Bart Peeters, and Eleni Chatzi. "Kalman-based coupled response-input estimation during environmental tests on the box assembly with removable component structure." In: *Proceedings of the 11th International Conference on Structural Dynamics, Athens, Greece*. 2020, pp. 23–26.

[140] Konstantinos Tatsis and E Lourens. "A comparison of two Kalman-type filters for robust extrapolation of offshore wind turbine support structure response." In: *Life-Cycle of Engineering Systems: Emphasis on Sustainable Civil Infrastructure: Proceedings of the Fifth International Symposium on Life-Cycle Civil Engineering (IALCCE 2016), 16-19 October 2016, Delft, The Netherlands*. CRC Press. 2016, p. 209.

[141] Silvia Vettori, Emilio Di Lorenzo, Bart Peeters, and Eleni Chatzi. "A virtual sensing approach to operational modal analysis of wind turbine blades." In: *Proceedings of ISMA2020 International Conference on Noise and Vibration Engineering, Leuven, Belgium*. 2020.

[142] Andre G Journel and Charles J Huijbregts. "Mining geostatistics." In: (1976).

[143] Pierre Goovaerts et al. *Geostatistics for natural resources evaluation*. Oxford University Press on Demand, 1997.

[144] Theodoros Evgeniou and Massimiliano Pontil. "Regularized multi–task learning." In: *Proceedings of the tenth ACM SIGKDD international conference on Knowledge discovery and data mining*. 2004, pp. 109–117.

[145] Jay M Ver Hoef and Ronald Paul Barry. "Constructing and fitting models for cokriging and multivariable spatial prediction." In: *Journal of Statistical Planning and Inference* 69.2 (1998), pp. 275–294.

[146] Phillip Boyle and Marcus Frean. "Dependent gaussian processes." In: *Advances in neural information processing systems* 17 (2004).

[147] Mauricio A Alvarez and Neil D Lawrence. "Computationally efficient convolved multiple output Gaussian processes." In: *The Journal of Machine Learning Research* 12 (2011), pp. 1459–1500.

[148] Kristof Maes, Katrien Van Nimmen, E Lourens, A Rezayat, P Guillaume, Guido De Roeck, and Geert Lombaert. "Verification of joint input-state estimation for force identification by means of in situ measurements on a footbridge." In: *Mechanical Systems and Signal Processing* 75 (2016), pp. 245–260.

[149] Silvia Vettori, Emilio Di Lorenzo, Roberta Cumbo, Umberto Musella, Tommaso Tamarozzi, Bart Peeters, and Eleni Chatzi. "Kalman-Based Virtual Sensing for Improvement of Service Response Replication in Environmental Tests." In: *Proceedings of 38th International Modal Analysis Conference (IMAC38), Houston, TX, US*. 2019.

[150] Per Christian Hansen and Dianne Prost O'Leary. "The use of the L-curve in the regularization of discrete ill-posed problems." In: *SIAM Journal on Scientific Computing* 14.6 (1993), pp. 1487–1503.

[151] Marcin M. Luczak, Riccardo Riva, Süleyman C. Yeniceli, Steen Hjelm Madsen, and Emilio Di Lorenzo. "Identification of the test setup influence on the modal properties of a short wind turbine blade during fatigue test." In: *Measurement* 174 (2021), p. 108960. ISSN: 0263-2241. DOI: https://doi.org/10.1016/j.measurement.2020.108960. URL: https://www.sciencedirect.com/science/article/pii/S0263224120314378.

Colophon

This document was typeset in LaTeX using the typographical look-and-feel `classicthesis`. The bibliography is typeset using `biblatex`.